Waterstofgeïnduceerd mechanisch falen
van Fe-C-X-hoogsterktelegeringen

Hydrogen Induced Mechanical Degradation
of High Strength Fe-C-X Alloys

Tom Depover

Promotor: prof. dr. ir. K. Verbeken
Proefschrift ingediend tot het behalen van de graad van
Doctor in de Ingenieurswetenschappen: Materiaalkunde

Vakgroep Toegepaste Materiaalwetenschappen
Voorzitter: prof. dr. ir. J. Degrieck
Faculteit Ingenieurswetenschappen en Architectuur
Academiejaar 2015 - 2016

UNIVERSITEIT
GENT

ISBN 978-90-8578-889-8
NUR 971
Wettelijk depot: D/2016/10.500/21

Acknowledgements

I sincerely want to thank some people who helped me during these four years. Without their advice, guidance, support or friendship, this PhD would not have been accomplished. People always say that the best time of your life is while you are studying. Well, they are right and wrong as in my personal view those best years were during my PhD. I got the opportunity to dig into a subject and to study something I really like and additionally I got the chance to work with people who over the years have become friends and explore myself in my personal life, which is even of greater value.

This PhD would not have been possible without the help of many people. First of all, I want to express my gratitude to Prof. Kim Verbeken, who encouraged me during my master dissertation and opened my eyes as a potential researcher. He gave me the chance to work in his group and to explore my abilities and future opportunities, which I really appreciate! I want to thank him as well for all the time and interest in my work and especially for the guidance and scientific discussions during this PhD. Furthermore, I would like to thank Prof. Degrieck, head of the department of Materials Science and Engineering, for giving me the chance to develop this work. Finally, I would like to thank all the professors at the Department for their advice during meetings or experimental support. Special thanks go to Prof. Roumen Petrov. I also wish to acknowledge the Special Research Fund (BOF), UGent (BOF10/ZAP/121) and the Agency for Innovation by Science and Technology in Flanders (IWT) for support (Project nr SB111205).

I also would like to acknowledge my industrial supervisor from OCAS, dr. Zinedine Zermout, for giving me the opportunity to work with him and for all his advice and guidance. Additionally, I would like to thank all the people working at OCAS who helped me with the processing of the materials and the people from the hydrogen laboratory at OCAS Zwijnaarde.

Furthermore, I would like to thank Marnix and Alex for the hours of sample preparation they performed for me with the outmost care. I also really appreciate the work done by Vitaliy for the TEM images and the experimental support by the H-team, i.e. Elien, Aurélie and Emilie. Finally, I would like to thank all my close colleagues for the great atmosphere. It has always been a pleasure to come to the office. Not a single day I was not feeling like going to work again. A big part of that feeling was caused by the people who I was privileged to work with. Next to the professional side, I also had the honor to be surrounded by many wonderful friends who gave me all the love and friendship I needed to finish this work. Especially, I would like to mention Wiebren, Valérie, Matteo, Lotje, Lore, Lotte and Chloé for their care, patience and encouragements through these four years. Lastly, I would like to say a final word to my parents, brother and family. They gave me the chance to study, something I still consider a privilege. I fulfilled this opportunity with great determination and I was able to finish it in a way I am really proud of. However, I never took the chance they gave me for granted and I really want to thank them for their belief and love.

Tom

February, 2016

Summary

Hydrogen is often quoted as a clean alternative energy carrier for the finite fossil fuels as no CO_2 emissions are provoked by its combustion. Hydrogen is environmentally friendly, but commercializing it seems to be a challenge. Alternatively, lowering the fuel consumption is a very relevant approach to make transportation more ecological. High strength steels realize because of their higher strength level the possibility to create lower weight structures, resulting in a decrease of the fuel consumption. However, there are ample of opportunities for these materials to come into contact with a hydrogen containing environment and unfortunately they are reported to be more prone to hydrogen embrittlement.

The hydrogen embrittlement phenomenon was first discussed in 1875. To date, it remains far from understood as hydrogen still induces unpredictable failures. Hydrogen causes a detrimental effect on the mechanical behavior of steels. The ductility loss caused by hydrogen is considered to be the main consequence and many examples are available, i.e. hydrogen induced cracking in pipeline steel, hydrogen embrittlement of welds, delayed fracture in high strength steels, hydrogen related cracks in nuclear power plants, etc. The applicability of high strength steels is even doubted in some literature due to hydrogen embrittlement issues. The problem is of a very particular nature due to the low solubility but significant consequences of this little amount of hydrogen present in steels. Additionally, hydrogen diffuses at measurable rate at room temperature in a body centered cubic crystal lattice which makes it extremely complex to visualize hydrogen and hence to determine its position in the matrix. Therefore, only the consequences of the hydrogen presence can be observed. Non-ferrous materials and austenitic steels suffer from hydrogen embrittlement as well. Therefore, controlling the hydrogen effect is still a challenging issue for many academic and industrial material engineers. Over the last two decades, an important and renewed interest in this research field has been observed, many hydrogen related publications are published and international conferences are organized. However, the responsible mechanisms are still far from understood.

Due to the low solubility and high mobility of hydrogen in steel, a heterogeneous hydrogen distribution is present in the microstructure. Interaction between hydrogen and the different features in the microstructure results in a longer or more permanent stay of hydrogen at this specific position, i.e. hydrogen is locally trapped in the microstructure. A steel matrix offers different trapping possibilities, i.e. bainite, martensite, pearlite, precipitates, grain/lath boundaries, vacancies, dislocations,..., which all show a specific interaction with hydrogen. Carbides are considered a very important trap site and carbides present in the microstructure are the most frequently cited approach to decrease the hydrogen embrittlement sensitivity. Alternatively, non-trapped hydrogen or diffusible hydrogen significantly contributes to hydrogen induced mechanical degradation.

On many occasions, hydrogen-related research uses one of three approaches: the evaluation of the effect of hydrogen on the mechanical properties such as by tensile tests, the study of the hydrogen trapping and diffusion isothermally by hydrogen permeation tests and the determination of the activation energy of the hydrogen trapping sites by thermal desorption spectroscopy. In this work, all three approaches will be combined on both industrial high strength steels and iron-based lab cast alloys in which a carbide forming element was introduced to evaluate the carbide trapping capacity and their influence on the hydrogen induced mechanical degradation.

In this work, first the basic concepts of the hydrogen/material interaction are discussed and illustrated by some specific literature examples. Dedicated literature surveys are included in the different chapters.

In the experimental section, first of all, the effect of hydrogen charging on the mechanical properties of four industrial high strength steels was studied thoroughly. A significant hydrogen induced mechanical degradation was observed for all materials, except for the high strength low alloy steel. This was attributed to the presence of carbides, emphasizing their beneficial potential as effective hydrogen traps. Fractography of the hydrogen charged samples showed a brittle transgranular cleavage fracture near the edges, where hydrogen was introduced in the matrix, with a transition zone to some ductile features in the center. Tensile tests at lower deformation rate showed a more pronounced effect of hydrogen on the mechanical properties since hydrogen was enabled to diffuse to critical stress zones ahead of a crack tip. This increase in hydrogen embrittlement was most noticeable for dual phase steel. Therefore, this steel was examined in more detail. Variable hydrogen charging conditions were applied on this material. At first, different pre-charging times together with in-situ hydrogen charging allowed evaluating the impact of the initial hydrogen content. The degree of hydrogen embrittlement increased with pre-charging times until saturation was reached. Secondly, variable cross-head deformation speeds were also applied on uncharged samples. This ingress of hydrogen during the tensile tests and the corresponding hydrogen diffusion into the sample were visualized by a fractography study. Hydrogen induced brittle features were indeed detected over a distance equivalent to the hydrogen diffusion distance.

Although the industrial steels showed some very interesting features, their complex multiphase microstructures made a straightforward interpretation of the hydrogen/material interaction difficult. Therefore, single phase laboratory cast Fe-C alloys were processed and studied. A well-designed heat treatment allowed evaluating the interaction of the different phases such as pearlite, bainite and martensite with hydrogen. Pure iron was used as a reference material and a carbon content variation was studied for the bainitic alloys. A considerable but different hydrogen embrittlement sensitivity was observed. The pearlitic microstructure was more prone to hydrogen embrittlement compared to the bainitic and martensitic alloys, which showed a similar response upon hydrogen charging. This was attributed to the diffusible hydrogen content and the hydrogen diffusion distance during the tensile test. Pure iron showed also a high sensitivity to hydrogen charging, which was linked to possibly internal damage and the high hydrogen diffusion coefficient in a ferritic matrix. Furthermore, an increased sensitivity was observed when the carbon content doubled for the bainitic alloys due to the larger amount of diffusible hydrogen. When the tensile test speed was decreased, the hydrogen embrittlement degree increased for all materials because of the increased hydrogen diffusion distance. The increase was the lowest for the martensitic alloy due to its lower hydrogen diffusion coefficient. To evaluate the combined impact of both the amount and diffusivity of hydrogen, the bainitic alloys were studied in more detail. Although adding carbon resulted in a higher amount of diffusible hydrogen, a lower relative increase in terms of hydrogen embrittlement was obtained for the higher carbon containing alloy when lowering the tensile test speed. This was attributed to its lower hydrogen diffusion coefficient. This observation confirmed the importance of both the amount and the mobility of hydrogen.

Since carbides were often cited to improve the hydrogen embrittlement resistance, the hydrogen/carbide interaction in quenched and tempered laboratory alloys was studied next. Generic Fe-C-X alloys were cast with four different ternary alloying elements, i.e. X = Ti, Cr, Mo and V. For each carbide forming element, three

different chemical compositions, with increasing carbon content and a stoichiometric amount of X, were used to allow a trustworthy evaluation of the impact of carbides with variable strength level and to confirm their role in different Fe-C-X alloys. An appropriate heat treatment was performed to compare two conditions: i.e. an as-quenched martensitic microstructure and a quenched and tempered condition in which carbides were induced. The hydrogen trapping capacity of the carbides was evaluated and their effect on the hydrogen embrittlement sensitivity was investigated thoroughly.

The Fe-C-Ti materials showed a decreased resistance against hydrogen embrittlement in the tempered condition. Thermal desorption spectroscopy and hot/melt extraction revealed that the TiC were capable of trapping a significant amount of hydrogen, which increased sensitivity to hydrogen. A clear correlation was obtained between the degree of hydrogen embrittlement and the amount of mobile hydrogen. This type of hydrogen is assumed to be mainly trapped at the dislocations, which play an important role in hydrogen induced failure. Additionally, some irreversibly trapped hydrogen was detected as well. After keeping the sample 72 hours in vacuum, the irreversibly trapped hydrogen stayed nearly completely in the sample. The corresponding activation energies were determined with thermal desorption spectroscopy. Slightly adapted thermal treatments allowed to verify that hydrogen was most likely trapped at the interface between the precipitate and matrix and that carbides with sizes larger than 70 nm were no longer capable of trapping hydrogen electrochemically. Furthermore, a modified hydrogen charging procedure allowed to verify if TiC addition is beneficial in terms of enhancing the hydrogen embrittlement response. A similar amount of hydrogen was charged into the as-quenched and tempered materials, and the highest resistance against hydrogen embrittlement was observed for the materials which contained the 'best' carbide trapping sites, confirming the beneficial effect of carbide presence.

The tempered induced carbides in the Fe-C-Cr alloys improved the resistance against hydrogen embrittlement. Hot/melt extraction showed that a similar amount of hydrogen was charged in the as-quenched and quenched and tempered material. Thermal desorption spectroscopy, however, revealed that different trapping sites were active for both conditions. The tempered materials contained carbides which were able to trap hydrogen. Hence, their amount of mobile hydrogen decreased, which was correlated to the lower dislocation density in the tempered condition. Consequently, a nice relation between the degree of hydrogen embrittlement and the amount of mobile hydrogen was again established. A slightly modified thermal treatment allowed to verify that the carbides trapped hydrogen at the interface of the precipitate with the matrix and that carbides with sizes larger than 100 nm were not able to trap hydrogen electrochemically. Conclusively, the addition of $Cr_{23}C_6$ precipitates was confirmed to be beneficial to improve the resistance to hydrogen embrittlement.

Tempering appeared to reduce the resistance to hydrogen embrittlement for the Fe-C-Mo alloys, although overall low degrees of embrittlement were obtained for these materials. Tempered induced Mo_2C particles were able to trap hydrogen as observed by thermal desorption spectroscopy, but rather low amounts of hydrogen were detected by hot extraction. Additionally, due to the low diffusion coefficient, little mobile hydrogen was present, which can be seen as a confirmation for the low embrittlement percentages. Carbide size distribution maps showed that carbides with sizes less than 50 nm were responsible for the irreversibly trapped hydrogen. The amount of irreversibly trapped hydrogen remained the same after 72 hours of vacuum, confirming its irreversible nature. A modified charging procedure allowed to elucidate the beneficial effect of Mo_2C addition. The deepest trapping sites, associated with hydrogen at carbides, were first filled, effectively decreasing the amount of

mobile hydrogen and hence the hydrogen embrittlement susceptibility. Finally, the combined impact of both the amount of hydrogen and the hydrogen diffusivity was verified by lowering the tensile test rate. The increase of the ductility loss was more pronounced in the as-quenched materials due to their higher hydrogen diffusion coefficient compared to the tempered condition.

Also the Fe-C-V alloys showed an increased sensitivity to hydrogen embrittlement when they were tempered. The V_4C_3 precipitates were able to trap a lot of hydrogen, which could be correlated with this increase. Thermal desorption spectroscopy confirmed the trapping ability of the precipitates and for these materials no better correlation was obtained when the mobile amount of hydrogen was considered to interpret the degree of hydrogen embrittlement. Since mobile hydrogen was assumed to be related with hydrogen at dislocations, one might argue that hardly any plastic deformation occurred for these materials as they all show rather low strain levels at fracture. Hence, this limited plastic deformation indicated a limited movement of dislocations ahead of fracture. Therefore the mobile amount of hydrogen could not play its detrimental role. Additionally, 72 hours of vacuum allowed to evaluate the irreversible character of trapping at the precipitates. Although the activation energy was lower than the literature limit between reversible and irreversible trapping (60 kJ/mol), a lot of hydrogen remained detectable by thermal desorption spectroscopy. This kind of irreversible hydrogen was available in such a significant amount that it was even able to affect the mechanical properties. Tempering for two hours showed that hydrogen was most likely trapped at the interface between the precipitate and matrix. Finally, the fracture surface showed some intergranular features, correlated with the high amount of hydrogen trapped at the V_4C_3 precipitates.

Samenvatting

Waterstof wordt vaak aangehaald als een milieuvriendelijk energie alternatief voor de eindige voorraad aan fossiele brandstoffen aangezien er geen CO_2 uitstoot gepaard gaat met de verbranding ervan. Waterstof is ecologischer, maar de commercialisering blijkt een uitdaging te zijn. Het brandstofverbruik doen dalen is een alternatief om transport groener te maken. Hoogsterkte staalsoorten kunnen hier van pas komen aangezien ze een hoge sterkte combineren met een licht gewicht, wat kan leiden tot brandstofvermindering bij gebruik. Desalniettemin zijn er talloze mogelijkheden voor deze materialen om in contact te komen met een waterstof bevattende omgeving en jammer genoeg zijn ze extra gevoelig aan waterstofverbrossing.

Het fenomeen van waterstofverbrossing werd het eerst bediscussieerd in 1875. Tot op de dag van vandaag, blijft het onbegrepen aangezien waterstof nog steeds onvoorspelbare breuk veroorzaakt. Waterstof creëert een schadelijk effect op het mechanisch gedrag van staal. Het ductiliteitsverlies, gepaard met waterstof, wordt als de hoofdconsequentie beschouwd waarvan vele voorbeelden aanwezig zijn: bv. waterstof geïnduceerde scheuren in pijpleiding staal, waterstofverbrossing van lassen, onverwachte breuk in hoogsterkte staalsoorten, waterstof gerelateerde scheuren in de nucleaire kerncentrales, ect. De toepasbaarheid van hoogsterkte staal wordt zelfs in twijfel getrokken in bepaalde literatuur net door de waterstof problematiek. Deze is namelijk heel specifiek in zijn soort door zijn lage oplosbaarheid en toch drastische gevolgen wanneer slechts een beetje waterstof aanwezig is in staal. Bovendien diffundeert waterstof aan meetbare snelheid bij kamertemperatuur in een kubisch ruimtelijk gecentreerd kristalrooster. Dit maakt het extreem moeilijk om waterstof te visualiseren en zo om zijn exacte positie in de matrix te bepalen. Net daarom kunnen enkel de gevolgen van de aanwezigheid van waterstof bestudeerd worden. Niet-ferritische materialen en austenitische stalen ondervinden ook hinder van waterstofverbrossing. Daarom is het controleren van het waterstofeffect nog steeds een uitdagend probleem voor vele academische en industriële materiaalkundige ingenieurs. Tijdens de laatste twee decennia kon men een hernieuwde interesse in dit onderzoeksveld waarnemen. Veel waterstofgerelateerde artikels werden gepubliceerd en internationale conferenties werden georganiseerd. Desondanks blijven de achterliggende mechanismes ongekend en niet volledig doorgrond.

Door de lage oplosbaarheid en hoge mobiliteit van waterstof in staal ontstaat er een heterogene verdeling van waterstof in de microstructuur. Interactie tussen waterstof en de microstructuur zorgt voor een langer of meer permanent verblijf van waterstof bij een bepaalde positie. Waterstof is dan lokaal gevangen in de microstructuur, wat we een “trap” noemen. Een staal heeft verschillende trap mogelijkheden, namelijk bainiet, martensiet, perliet, precipitaten, korrel/lat grenzen, vacatures, dislocaties,... Deze hebben allemaal een specifieke interactie met waterstof. Carbides worden aanschouwd als een heel belangrijke trap positie en worden dan ook vaak geciteerd als mogelijke strategie om de gevoeligheid voor waterstofverbrossing te verminderen. Aan de andere kant, wordt niet gevangen of diffundeerbare waterstof aanschouwd als nadelig voor het waterstof geïnduceerd mechanisch falen.

Drie manieren worden aangewend om waterstofgerelateerd onderzoek uit te voeren: de evaluatie van het effect van waterstof op de mechanische eigenschappen door middel van trekproeven, de studie van waterstof traps en diffusie door waterstofpermeatie testen en de bepaling van de activatie-energie van waterstof trap posities door

thermische desorptie spectroscopie. In dit werk worden alle drie de technieken gecombineerd op zowel industriële staalsoorten als op ijzergebaseerde generische legeringen. In die laatste werd een carbide vormend element toegevoegd om de trap capaciteit van het carbide te evalueren alsook diens invloed op het waterstof geïnduceerd mechanisch falen.

In dit werk werd eerst gefocust op de basisconcepten van de interactie tussen waterstof en staal. Dit werd geïllustreerd aan de hand van een een aantal welgekozen voorbeelden uit de literatuur. Toegewijde literatuur studies over de carbides werden telkens toegevoegd bij de desbetreffende hoofdstukken.

In het eerste experimentele hoofdstuk, werd het effect van waterstofoplading op de mechanische eigenschappen van vier industriële hoogsterkte stalen grondig bestudeerd. Een significant waterstof geïnduceerd ductiliteitsverlies werd waargenomen, met uitzondering van het 'high strength low alloy' staal. Dit werd toegeschreven aan de aanwezigheid van carbides, waarmee hun potentieel voordelige invloed als efficiënte waterstof traps werd benadrukt. Fractografie werd uitgevoerd op de waterstof opgeladen materialen en een brosse transgranulaire breuk werd geobserveerd langs de zijkant, daar waar waterstof werd geïntroduceerd in het staal. Een transitiezone naar een meer ductiel breukoppervlak in het centrum kon ook worden waargenomen. Trekproeven uitgevoerd aan een lagere deformatiesnelheid toonden een groter effect aan van waterstof op de mechanische eigenschappen. Waterstof kon in dit geval meer diffunderen naar kritische spanningszones voor een scheurtip, wat zijn schadelijk effect verder versterkte. Deze stijging in waterstofverbrossing werd het meest opgemerkt voor 'dual phase' staal. Dit materiaal werd dan ook verder onderzocht. Veranderlijke oplaadcondities werden opgelegd aan dit materiaal. Ten eerste werden verschillende voor-oplaadtijden gebruikt samen met in-situ waterstof oplading. Dit liet toe het effect van de initiële hoeveelheid waterstof te evalueren. De graad van waterstofverbrossing steeg met stijgende voor-oplaadtijden tot saturatie bekomen werd. Ten tweede, werden veranderlijke deformatiesnelheden opgelegd aan onopgeladen materialen. De intrede van waterstof tijdens de trekproef en zijn corresponderende diffusie-afstand in het materiaal kon zo worden gevisualiseerd door een fractografiestudie. Waterstof geïnduceerde brosse zones werden inderdaad gedetecteerd bij een afstand gelijk aan de waterstof diffusie afstand.

Hoewel de industriële stalen enkele heel interessante aspecten aantoonden, maakte hun complexe multifase microstructuur het moeilijk om de interactie tussen waterstof en het materiaal te interpreteren. Daarom werden éénfasige generische Fe-C legeringen geproduceerd en bestudeerd. Een goed ontwikkelde hittebehandeling stond toe om de interactie van de verschillende fases, namelijk bainiet, perliet en martensiet, met waterstof te evalueren. Zuiver ijzer werd gebruikt als een referentiemateriaal en een koolstofvariatie werd aangebracht voor de bainitische materialen. Een aanzienlijke doch verschillende gevoeligheid voor waterstofverbrossing werd waargenomen. De perliet microstructuur was het meest gevoelig vergeleken met bainiet en martensiet, die wat gelijkaardige verbrossingsgraden vertoonden. Dit werd toegeschreven aan de diffundeerbare hoeveelheid waterstof en de waterstofdiffusie afstand die kon worden overbrugd tijdens de trekproef. Puur ijzer vertoonde ook een lage weerstand tegen waterstofoplading en dit werd verklaard door mogelijk wat interne schade en de hoge diffusie coëfficiënt van waterstof in een ferrietmatrix. Verder werd er een verhoogde gevoeligheid waargenomen wanneer de hoeveelheid koolstof verdubbelde voor de bainiet microstructuren. Dit werd gelinkt aan de hogere hoeveelheid diffundeerbare waterstof. Wanneer de trekproef snelheid werd verlaagd, steeg de graad van waterstofverbrossing voor alle materialen door de grotere diffusieafstand van waterstof tijdens deze

trage trekproef. Deze stijging was het laagst voor het martensiet materiaal door zijn lage diffusie coëfficiënt. Net om de gecombineerde impact van zowel de hoeveelheid diffundeerbare waterstof als de waterstof diffusiviteit te evalueren, werden de bainitische materialen verder onderzocht. Ondanks dat koolstoftoename resulteerde in een hogere hoeveelheid aan diffundeerbare waterstof, bleek dat het materiaal met de hoogste hoeveelheid koolstof een lagere relatieve stijging in waterstofverbrossing onderging wanneer de snelheid van de trekproef daalde. Dit werd toegeschreven aan de lagere diffusiecoëfficiënt van dat materiaal, door zijn hogere hoeveelheid koolstof. Deze observatie bevestigde het belang van zowel de waterstof hoeveelheid als de waterstof mobiliteit.

Aangezien carbides vaak werden geciteerd om de weerstand tegen waterstofverbrossing te verbeteren, werd de interactie tussen waterstof en carbides vervolgens onderzocht in quenched en tempered generische legeringen. Lab Fe-C-X legeringen werden gegoten met vier verschillende ternaire legeringselementen, namelijk Ti, Cr, Mo en V. Voor elk carbidevormend element werden drie verschillende chemische samenstellingen voorzien, telkens met stijgende hoeveelheid koolstof en een stoichiometrische hoeveelheid X. Deze aanpak werd gevolgd om een betrouwbare evaluatie van het effect van carbides te maken met een variabel sterkte niveau en om hun rol in verschillende Fe-C-X legeringen te bevestigen. Een gepaste hittebehandeling werd opgelegd om twee verschillende condities te vergelijken: namelijk een as-quenched martensiet microstructuur en een quenched en tempered toestand waarin carbides werden geïntroduceerd. De waterstof trap capaciteit van de carbides werd geëvalueerd en hun effect op de gevoeligheid voor waterstofverbrossing werd grondig bestudeerd.

De Fe-C-Ti materialen vertoonden een verminderde weerstand tegen waterstofverbrossing wanneer ze getemperd werden. Thermische desorptie spectroscopie en warmte/smelt extractie toonde aan dat de TiC een aanzienlijke hoeveelheid waterstof kon trappen, waardoor de gevoeligheid om te verbrossen steeg. Een mooie correlatie ontstond tussen de graad van waterstofverbrossing en de hoeveelheid mobiele waterstof. Dit type waterstof werd voornamelijk gelinkt aan waterstof gevangen bij de dislocaties, aangezien deze een belangrijke rol spelen bij waterstofgeïnduceerd falen. Bovendien werd wat irreversibele waterstof gevonden. Na 72 uur in vacuüm, bleef deze irreversibele waterstof zo goed als compleet in het materiaal aanwezig. De corresponderende activatie energie werd bepaald door thermische desorptie spectroscopie. Licht aangepaste hittebehandelingen lieten toe om te verifiëren dat waterstof hoogstwaarschijnlijk gevangen zit aan de grens tussen het precipitaat en de matrix. Bovendien konden carbides met een grootte boven de 70 nm geen waterstof meer opnemen wanneer het materiaal elektrochemisch opgeladen werd. Verder werd een aangepaste oplaadprocedure opgelegd aan het materiaal om te onderzoeken indien toevoegen van TiC voordelig is om de weerstand tegen waterstofverbrossing te verhogen. Een gelijkaardige hoeveelheid waterstof werd geïnduceerd voor zowel de as-quenched als de quenched en tempered materialen. De hoogste weerstand werd waargenomen voor de materialen die de beste carbide traps bevatte. Dit bevestigde het positieve effect van de aanwezigheid van carbides.

De door temperen geproduceerde carbides in de Fe-C-Cr legeringen zorgden voor een verbeterde weerstand tegen waterstofverbrossing. Warmte/smelt extractie toonde aan dat een gelijkaardige hoeveelheid waterstof werd opgeladen in beide condities. Desalniettemin toonde thermische desorptie spectroscopie aan dat verschillende soorten trap plaatsen aanwezig waren voor beide condities. De getemperde materialen bevatten carbides die waterstof konden vangen. Hierdoor daalde hun hoeveelheid mobiele waterstof. Dit werd gecorreleerd met de

lagere dislocatiedichtheid van de getemperde conditie. Als gevolg werd er een treffende relatie gevonden tussen de graad van verbrossing en de hoeveelheid mobiele waterstof. Een licht aangepaste thermische behandeling liet toe om te bepalen dat waterstof hoogstwaarschijnlijk gevangen zit aan de grens tussen precipitaat en matrix. Bovendien konden carbides met een grootte boven de 100 nm geen waterstof meer vangen. Als conclusie kon worden gezegd dat de toevoeging van $Cr_{23}C_6$ precipitaten voordelig was om de weerstand tegen waterstofverbrossing te verhogen.

Tempering bleek de gevoeligheid voor waterstofverbrossing te doen stijgen voor de Fe-C-Mo legeringen. Alhoewel lage verbrossingsgraden werden waargenomen voor deze materialen. Thermische desorptie spectroscopie toonde aan dat de geïnduceerde Mo_2C deeltjes waterstof konden vangen, maar lage hoeveelheden waterstof werden gedetecteerd door warmte-extractie. Bovendien was er slechts weinig mobiele waterstof aanwezig door de lage diffusiecoëfficiënt. Dit verklaarde de lage verbrossingsgraden. Carbide grootte distributies toonden aan dat carbides met een grootte kleiner dan 50 nm verantwoordelijk waren voor de irreversibel gevangen waterstof. De hoeveelheid van deze waterstof bleef constant na 72 uur in vacuüm, wat zijn irreversibel karakter bevestigde. Een aangepaste oplaadprocedure liet toe om te verifiëren of de toevoeging van Mo_2C voordelig was. De diepste trap posities, die gelinkt met waterstof bij de carbides, werden eerst gevuld. Dit verlaagde de hoeveelheid mobiele waterstof drastisch, waardoor ook de verbrossingsgraad daalde. Uiteindelijk werd de gecombineerde impact van zowel de hoeveelheid waterstof als de waterstofdiffusiviteit onderzocht door de snelheid van de trektest te verlagen. De stijging van het ductiliteitsverlies was meer uitgesproken in het as-quenched materiaal vergeleken met het getemperde materiaal door zijn hogere diffusie coefficient.

De Fe-C-V legeringen toonden ook een verhoogde gevoeligheid voor waterstofverbrossing wanneer ze getemperd waren. De V_4C_3 precipitaten konden heel goed waterstof vangen, wat de stijging kon verklaren. Thermische desorptie spectroscopie bevestigde de trap mogelijkheid van de precipitaten. Hoewel, voor deze materialen werd geen betere correlatie waargenomen wanneer de mobiele hoeveelheid waterstof in rekening werd gebracht om de verbrossingsgraad te interpreteren. Aangezien verondersteld werd dat mobiele waterstof gelinkt was met dislocaties, kan men argumenteren dat bijna geen plastische vervorming ontstond voor deze materialen aangezien ze allemaal lage verlengingsgraden bij breuk vertoonden. Vervolgens impliceerde deze gelimiteerde hoeveelheid plastische vervorming dat slechts een gelimiteerde beweging van dislocaties kon plaatsvinden voor breuk. Hierdoor kon de mobiele hoeveelheid waterstof zijn schadelijke rol niet uitoefenen. Bovendien werd 72 uur vacuüm opgelegd aan de materialen om het irreversibel karakter van de carbide traps te evalueren. Hoewel de activatie energie lager was dan de door de literatuur opgelegde grens tussen reversibel en irreversibel (60 kJ/mol), bleef heel wat waterstof aanwezig in het materiaal. Dit kon worden gedetecteerd door thermische desorptie spectroscopie. Dit type waterstof was in een aanzienlijke hoeveelheid aanwezig zodat het zelfs de mechanische eigenschappen kon aantasten. Tempering voor twee uur toonde aan dat waterstof hoogstwaarschijnlijk gevangen zit aan de grens tussen het precipitaat en de matrix. Uiteindelijk toonde breukoppervlak analyse aan dat er intergranulaire zones ontstonden. Deze werden gecorreleerd met de hoge hoeveelheid waterstof die gevangen zat bij de V_4C_3 precipitaten.

List of publications

Journals

1. Depover T, Verbeken K, Evaluation of the effect of V_4C_3 precipitates on the hydrogen induced mechanical degradation in Fe-C-V alloys, Materials Science and Engineering (2016), submitted.
2. Depover T, Verbeken K, The effect of TiC on the hydrogen induced ductility loss and trapping behavior of Fe-C-Ti alloys, Corrosion Science (2016), submitted.
3. Depover T, Verbeken K, Hydrogen trapping and hydrogen induced mechanical degradation in lab cast Fe-C-Cr alloys, Materials Science and Engineering A (2016), accepted with minor revisions.
4. Depover T, Verbeken K, Evaluation of the role of Mo_2C in hydrogen induced ductility loss in Q&T Fe-C-Mo alloys, International Journal of Hydrogen Energy (2016), accepted with minor revisions.
5. Depover T, Wallaert E, Verbeken K, On the synergy of diffusible hydrogen and hydrogen diffusivity in the mechanical degradation of laboratory cast Fe-C alloys, Materials Science and Engineering A 664 (2016) 195-205.
6. Depover T, Van den Eeckhout E, Verbeken K, The impact of hydrogen on the ductility loss of bainitic Fe-C alloys, Materials Science Technology (2016), accepted, DOI: 10.1080/02670836.2015.1137387.
7. Depover T, Wallaert E, Verbeken K, Fractographic analysis of the role of hydrogen diffusion on the hydrogen embrittlement susceptibility of DP steel, Materials Science and Engineering A 649 (2016) 201-208.
8. Laureys A, Depover T, Petrov R, Verbeken K, Microstructural characterization of hydrogen induced cracking in TRIP-assisted steel by EBSD, Materials Characterization 112 (2016) 169-179.
9. Laureys A, Depover T, Petrov R, Verbeken K, Characterization of hydrogen induced cracking in TRIP-assisted steel, International Journal of Hydrogen Energy 40 (2015) 16977-16984.
10. Depover T, Monbaliu O, Wallaert E, Verbeken K, Effect of Ti, Mo and Cr based precipitates on the hydrogen trapping and embrittlement of Fe-C X Q&T alloys, International Journal of Hydrogen Energy 40 (2015) 16977-16984.
11. Depover T, Pérez Escobar D, Wallaert E, Zermout Z, Verbeken K, Effect of hydrogen charging on the mechanical properties of advanced high strength steels, International Journal of Hydrogen Energy 39 (2014) 4647-4656.
12. Wallaert E, Depover T, Arafin M, Verbeken K, Thermal desorption spectroscopy evaluation of the hydrogen-trapping capacity of NbC and NbN precipitates, Metallurgical and Materials Transactions A 45 (2014) 2412-2420.
13. Laureys A, Depover T, Petrov R, Verbeken K, Microstructural characterization of hydrogen induced cracking in TRIP steels by EBSD, Advanced Materials Research 922 (2014) 412-417 , not yet available at Web of Science on 15/02.
14. Depover T, Van den Eeckhout E, Wallaert E, Zermout Z, Verbeken K, Evaluation of the effect of TiC precipitates on the hydrogen trapping capacity of Fe-C-Ti alloys, Advanced Materials Research 922 (2014) 102-107, not yet available at Web of Science on 15/02.

15. Pérez Escobar D, Depover T, Wallaert E, Duprez L, Verhaege M, Verbeken K, Thermal desorption spectroscopy study of the interaction between hydrogen and different microstructural constituents in lab cast Fe-C alloys, Corrosion Science 56 (2012) 199-208.
16. Pérez Escobar D, Depover T, Duprez L, Verbeken K, Verhaege M, Combined thermal desorption spectroscopy, differential scanning calorimetry, scanning electron microscopy and X-ray diffraction study of hydrogen trapping in cold deformed TRIP steel, Acta Materialia 60 (2012) 2593-2605.
17. Depover T, Wallaert E, Zermout Z, Verbeken K, Evaluation of the effect of in-situ charging on the mechanical properties of iron-based alloys (2012), proceedings of the 2012 International Hydrogen Conference, Wyoming (USA), 165-172, not yet available at Web of Science on 15/02.
18. Wallaert E, Depover T, Pieters B, Arafin MA, Verbeken K, TDS evaluation of the hydrogen trapping capacity of NbC precipitates (2012), proceedings of the 2012 International Hydrogen Conference, Wyoming (USA), 575-584, not yet available at Web of Science on 15/02.

Conferences

1. Depover T, Van den Eeckhout E, Verbeken K, Comparison of the role of four different carbides in the hydrogen induced mechanical degradation of lab cast Fe-C-X alloys, International Hydrogen Conference, Wyoming (USA) (2016) submitted.
2. Laureys A, Depover T, Deseranno T, Claeys L, Petrov R, Verbeken K, EBSD characterization of hydrogen induced cracking in generic Fe-C-Ti and Fe-C-V alloys, International Hydrogen Conference, Wyoming (USA) (2016) submitted.
3. Depover T, Wallaert E, Zermout Z, Verbeken K, The impact of carbides on the hydrogen trapping and embrittlement of Fe-C-X quenched and tempered alloys, Hydrogen in Metals Conference, Berlin (2015)
4. Depover T, Van den Eeckhout E, Wallaert E, Zermout Z, Verbeken K, Evaluation of the effect of TiC precipitates on the hydrogen trapping capacity and the mechanical properties of Fe-C-Ti alloys, Steely Hydrogen Conference (2014)
5. Depover T, Wallaert E, Duprez L, Verbeken K, Verhaege M, In-situ mechanical evaluation of hydrogen embrittlement for TRIP, FB, DP and HSLA steels, Steely Hydrogen Conference (2011)

Table of contents

List of symbols

As_2O_3	arsenic trioxide
C	carbon
C_H	hydrogen solubility
Cr	chromium
D	diffusion coefficient
D_{app}	apparent diffusion coefficient
e^-	electron
E_a	activation energy for detrapping
E_b	binding energy of a trap
E_{ch}	minimal energy for chemisorption
E_d	diffusional energy
E_f	minimal energy for fysisorption
E_s	activation energy for trapping
Fe	iron
H	hydrogen atom
H^+	hydrogen proton
H_2	hydrogen gas
H_2S	hydrogen sulphide
H_2SO_4	sulphuric acid
H_{abs}	absorbed hydrogen
H_{ads}	adsorbed hydrogen
K	equilibrium value of Sieverts's law
L	material thickness
M	Molar
M	metal
Mn	manganese
Mo	molybdenum
M_s	martensitic transformation start temperature
NaOH	sodium hydroxide
N_2	nitrogen gas
Nb	niobium
Ni	nickel
P	phosphorus
p_{H2}	partial pressure of hydrogen gas
R	universal gas constant
$SC(NH_2)_2$	thiourea
Si	silicon
T_{max}	peak temperature

Ti	titanium
V	vanadium
wt%	weight percent
X	a specific alloying element
X_{ch}	distance in the chemisorption state
X_f	distance in the fysisorption state
α'	martensite
α_w	widmanstätten ferrite
ε_{ch}	elongation of the charged sample
ε_{un}	elongation of the uncharged sample
γ	austenite
Φ	heating rate [°C/min]
σ_{max}	maximum tensile strength
σ_y	yield stress
%HE	percentage of hydrogen embrittlement

List of abbreviations

AIDE	adsorption-induced dislocation-emission
As-Q	as-quenched
BCC	body centered cubic
BCT	body centered tetragonal
CCT	continuous cooling transformation
CERT	constant extension rate test
DP	dual phase
EAC	environmental assisted cracking
EDX	energy-dispersive X-ray analysis
FB	ferrite-bainite
FCC	face centered cubic
FSD	forward scatter detector
HE	hydrogen embrittlement
HEAC	hydrogen environmental assisted cracking
HEDE	hydrogen-enhanced decohesion
HELP	hydrogen-enhanced localized plasticity
HIC	hydrogen induced cracking
HSLA	high strength low alloy
HV	Vickers hardness
IHAC	internal hydrogen assisted cracking
LOM	light optical microscopy
Q&T	quenched and tempered
RD	rolling direction
SADP	selected area diffraction pattern
SCC	stress corrosion cracking
SEM	scanning electron microscopy
TDS	thermal desorption spectroscopy
TEM	transmission electron microscopy
TRIP	transformation induced plasticity
TTT	time-temperature-transformation
wppm	weight parts per million

CHAPTER I

Introduction

I.1 Basics on the hydrogen/material interaction

I.1.1 Hydrogen in metals

Due to the estimated increase in population and average standard of living, the limited fossil resources, the concerns about nuclear power and above all the global warming issues, scientists all over the world are triggered to come up with solutions. One of the suggested replacements for fossil fuels is hydrogen gas. Hydrogen is by far the most abundant element in the universe and is a safe and clean fuel gas, available in unlimited quantities by the electrolysis of water. Under atmospheric conditions, hydrogen is present as hydrogen gas: H_2. The combustion of this gas only generates water, so no greenhouse gasses are emitted in the atmosphere. Electrolysis of water and steam at high temperatures is one of the most efficient and cost-effective ways to produce hydrogen [1]. Despite these advantages, hydrogen has a negative connotation for many people due to explosion and ignition dangers. A lot of other incidents that happened in the past (caused by e.g. a lack of hydrogen detection or equipment failure) indicate the danger of this gas [2]. Lowering the fuel consumption is a different approach to make transportation by car more ecological. The use of high strength steels, which combine a high strength with a similar density as construction steel, lowers the weight and thus the fuel consumption of the vehicle significantly. High strength steel alloys are widely used in many applications thanks to their excellent mechanical properties, such as high strength and sufficient toughness. Unfortunately, hydrogen has been reported to be detrimental for the mechanical behaviour of those high strength steels [3] [4] [5]. Frequent opportunities for contact with a hydrogen containing environment are available. Hydrogen can enter the material during processing or in use, as for instance during the steel production process, galvanizing, welding and when in contact with aqueous solutions or H_2 containing gases. Another widely studied topic is sulphide stress corrosion cracking of pipeline steels in H_2S environments [6] [7].

Johnson [8] was the first to describe the effect of hydrogen on the properties of iron. He discovered *a remarkable change in some of the physical properties of iron caused by its temporary immersion in hydrochloric and sulphuric acids.* A temporary loss of ductility was observed. This work has inspired a lot of researchers to continue investigating this subject resulting in many reference works and international conferences [9] [10] [11] [12] [13] [14] [15] [16] [17] [18] [19] [20]. Recently, the attention got reinforced by the development of numerous applications of high strength steels involving hydrogen interaction, such as oil and gas pipelines, vehicles, storage tanks, offshore structures, welds, etc. [6] [7] [21]. The phenomenon of temporary ductility loss implies so called hydrogen embrittlement (HE), which leads to unpredictable failure with non-ductile characteristics. The ductility loss caused by hydrogen is considered as the main consequence of HE. Absorbed and dissolved hydrogen diffuses through the metal, introducing extra stresses at potential crack initiation sites

and/or facilitating crack propagation. High strength steels are very susceptible to HE because of the high stress level present in the metal as well as the great number of potential fracture initiation sites [22]. Moreover, this HE phenomenon is not only observed in iron-based alloys, but also in non-ferrous metals [23] [24] [25]. Consequently, the potential and safe application of hydrogen still offers major challenges to the materials engineer and clearly a renewed interest in this research field occurred during the last decade in both industrial and scientific communities.

In this introductory chapter, the focus will be first on the general aspects of hydrogen/steel interaction in section I.2. The adsorption, absorption and diffusion of hydrogen will be described. Furthermore, the different possible trapping sites will be presented and several important trapping sites for this work will be included in the overview by means of relevant literature data. A literature overview related to the specific topics of the experimental chapters will be included in these chapters, as this will immediately allow discussing the obtained experimental data with the literature. Additionally, the experimental techniques used in hydrogen related research will be described briefly in this chapter. The underlying mechanisms to explain the hydrogen embrittlement phenomenon will be discussed in section I.3. Finally, some relevant results from the work of Diana Perez Escobar [26] will be presented in section I.4 to illustrate the concept of how the hydrogen/material interactions will be studied in this work. The scope of this work will be presented in section I.5.

I.1.2 Interaction of hydrogen with steel

The presence of hydrogen in steel is detrimental to its mechanical performance. Therefore, the different steps that result in this actual ductility loss are described here. Hydrogen first has to enter the material, whereupon transport through the lattice takes place. This diffusion process plays a decisive role in understanding the embrittlement mechanisms, together with the hydrogen solubility and the trapping possibilities. The interaction between hydrogen and metals consists of four steps. The first step is the adsorption of hydrogen on the metal surface, where a distinction can be made between adsorption from a gaseous or an electrochemical hydrogen source. Further, hydrogen can be absorbed in the metal which is followed by hydrogen diffusion. Finally, the interaction between hydrogen and the microstructural features of the metal can induce hydrogen trapping.

I.1.2.1 Adsorption at the surface

Hydrogen can be introduced in metals in different ways depending on the hydrogen source, there is electrolytic hydrogen charging from an aqueous solution and gaseous hydrogen charging [27]. Molecular hydrogen (H_2), as present in the gaseous phase, is too large to enter a solid material via the surface [28]. This makes dissociation into single hydrogen atoms necessary. Since transport of hydrogen in a gas phase at normal pressures is a very fast process because of the high surface collision rate of this ultra-light molecule, the dissociative reaction will be the rate-determining step of the adsorption process [29]. Adsorption through the gaseous phase, also called chemisorption, results in dissociation and adsorption of the hydrogen atoms (H_{ads}) on the metal surface (M). The complete process can be summarized by the following reaction:

$$M + \frac{1}{2}H_2(g) \leftrightarrow MH_{ads} \qquad \text{(I-1)}$$

The hydrogen molecule is initially attracted by the metal surface, driven by weak van der Waal's forces. At a certain distance X_f from the surface (see Figure I-1) a local minimum in energy E_{ph} is reached, the molecule is now in the physisorption state. At distances closer than X_{ph}, repulsive interaction forces give rise to an increasing energy status. However, for molecules consisting of multiple atoms, an even stronger interaction, and

accordingly lower potential, is possible by breaking the bonds of the molecule and form a bond with the surface atoms. At a certain distance, the dissociation energy for the hydrogen molecule is exceeded by the adsorption energy. This results in a dissociation into two atoms, each chemisorbed on the surface with a lower minimal energy E_{ch} at a distance X_{ch}.

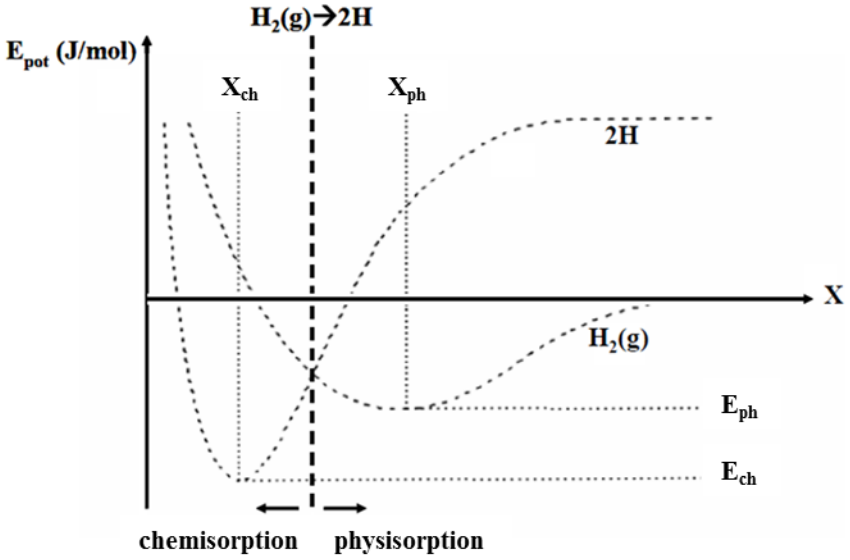

Figure I-1: Dissociative chemisorption of a hydrogen molecule on a metal surface, energy as a function of distance X to the surface [28].

Other than by gaseous charging, hydrogen can also adsorb on the surface via electrochemical charging [27]. Protons (H^+) from an aqueous electrolyte are converted to atomic hydrogen (H). This type of interaction results in the main uptake of hydrogen in steel. The conversion into atomic hydrogen by applying an electrical current occurs via the following reduction reaction:

$$H^+ + e^- \leftrightarrow H \tag{I-2}$$

The previous reaction allows adsorption of the atomic hydrogen on the metal surface:

$$H + M \leftrightarrow MH_{ads} \tag{I-3}$$

Parameters such as temperature, electrolyte, current density, charging time etc. should be taken into account. Choosing inappropriate charging conditions can result in damage as for example blisters or micro-cracks might be introduced during charging when the current density or the charging time is too high [30] [31]. This has a negative effect on the test results as mechanical tensile tests for instance on damaged material are useless.

I.1.2.2 Absorption in the metal

When hydrogen atoms are adsorbed at the surface, they can either recombine to hydrogen gas, giving rise to a release of H_2, or enter into the metal matrix [32]. The yield of hydrogen absorption is dependent on the concentration of hydrogen just below the surface. For charging in a gaseous environment, Sieverts described that the solubility of a diatomic gas (hydrogen in this case) in metal (C_H) is proportional, with equilibrium value K, to the square root of the partial pressure of the gas (p_{H_2}) in thermodynamic equilibrium [33]:

$$C_H = K \cdot \sqrt{p_{H_2}} \tag{I-4}$$

Sieverts's law allows direct calculation of dissolved hydrogen, which is a major advantage over electrochemical charging. The equilibrium reaction for absorption of hydrogen gas can be written as:

$$M + \frac{1}{2}H_2(g) \leftrightarrow MH_{abs} \quad \text{(I-5)}$$

For absorption from an aqueous solution, a relation is found between solubility and the applied current density during electrochemical charging. Research illustrated that this solubility is proportional to the square root of the current density [32]. If the adsorbed hydrogen does not recombine but is absorbed into the metal matrix, this can lead to hydrogen embrittlement. In order to perform research on this HE effect, it is desirable to prevent recombination as much as possible. This can be achieved by the use of chemicals such as H_2S, As_2O_3 or thiourea ($SC(NH_2)_2$). For more detailed data about the evolution of the hydrogen content as a function of time, the possible occurrence of blisters and internal cracks,…, the author refers to the PhD of Pérez Escobar [26].

I.1.2.3 Transport in bulk

Hydrogen migrates in the microstructure after absorption in the metal. Diffusion can be divided into substitutional and interstitial diffusion [34]. The conditions to dissolve an element interstitially in a metal are given by the ratio of the atomic diameter of the solute and the metal atom, which should be between 0.41 and 0.59. The lower boundary is determined by the geometrical condition for an interstitial atom to touch the adjacent atoms in the hard-sphere unit cell. If below 0.41, the dissolved atom is not hold by the lattice and diffuses rapidly. This is the case for hydrogen; it can be transported through the metal matrix interstitially. Due to its fast diffusion rate through the lattice, a hydrogen atom can even diffuse at room temperature. The diffusivity and solubility of hydrogen in the material are the main parameters to describe the way of transport. The diffusivity is expressed by the diffusion coefficient D (m²/s); a higher diffusion coefficient indicates a faster diffusion rate. According to Deluccia and Berman the diffusion coefficient of hydrogen in steel is given by [35]:

$$D = L^2 / 4\, t_{max} \quad \text{(I-6)}$$

where L is the thickness of the material (m) and t_{max} is the time to reach the saturation (s).

The diffusivity and solubility of hydrogen are mainly influenced by temperature, chemical composition and crystal structure. Hadam and Zakroczymski [36], for example, demonstrated that adding about 1% carbon to a pure iron matrix resulted in a rise in the hydrogen solubility with a factor 70, whereas the hydrogen diffusion decreased with a factor 280. Interstitial hydrogen is located in the interstitial sites in the matrix, which are different for body centered cubic (bcc) and face centered cubic (fcc) metal structures (Figure I-2). In bcc lattices, hydrogen is mainly trapped in the tetrahedral interstitial sites whereas in fcc lattices the octahedral interstitial sites are occupied more often [37]. This influences the diffusivity and solubility, i.e. in austenite, the mobility of hydrogen is lower and the solubility is higher compared to ferrite or martensite.

BCC

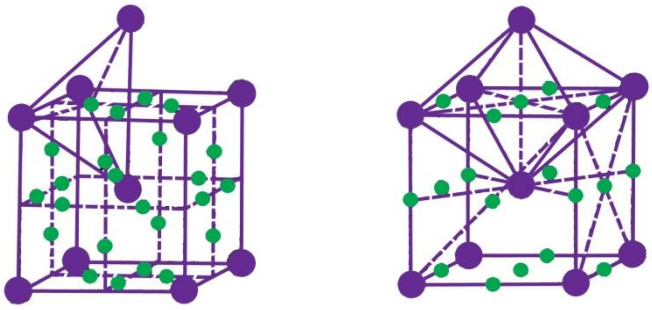

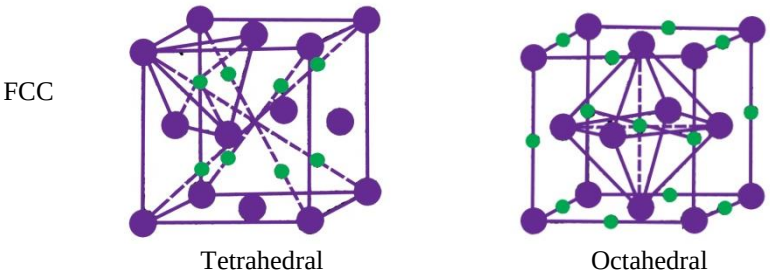

Figure I-2: Tetrahedral and octahedral sites for interstitials in bcc and fcc lattices [38]**.**

I.1.2.4 Hydrogen trapping

In a metal lattice, hydrogen can either be present at interstitial positions in the lattice or reside at microstructural heterogeneities in the material. At these positions, hydrogen can stay for a longer time than at a normal interstitial position. Therefore, hydrogen in considered to be trapped at those sites. These trapping sites can be all kinds of microstructural features, such as dislocations, vacancies, substitutional or interstitial solute atoms, grain boundaries, phase boundaries, precipitates etc. [39]. Figure I-3 gives an overview of the possible trapping sites for hydrogen in steel [40].

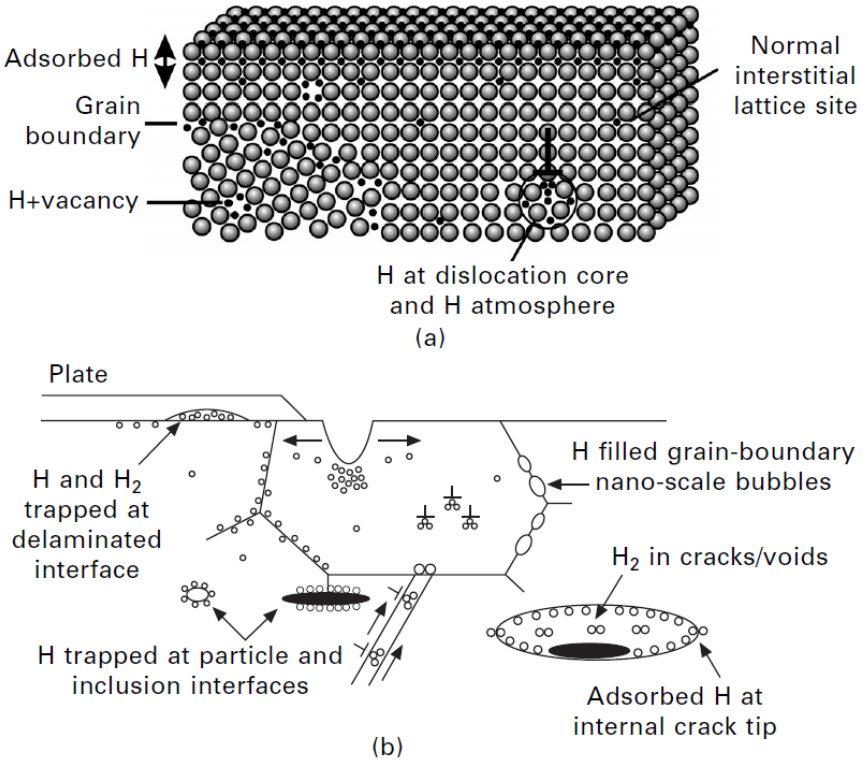

Figure I-3: Schematic illustrations of sites and traps for hydrogen in materials on the atomic scale (a) and on a microscopic scale [16]**.**

Contrary to the interstitial positions, traps are considered as more energetically favourable sites for the hydrogen atoms. There, hydrogen is bound to the defect, slowing down its mobility in the metal. When hydrogen encounters a trapping site, this will act as a potential well and attract the hydrogen (Figure I-4). E_D is the necessary energy for diffusion through a perfect lattice. When reaching a saddle point, the hydrogen will only

need an energy $E_S < E_D$ to be bond in the trap with a binding energy E_B. Trapping will thus be favoured over diffusion. The activation energy E_A is the energy needed for hydrogen to escape from the trap. An increased temperature or an applied stress can provide this energy.

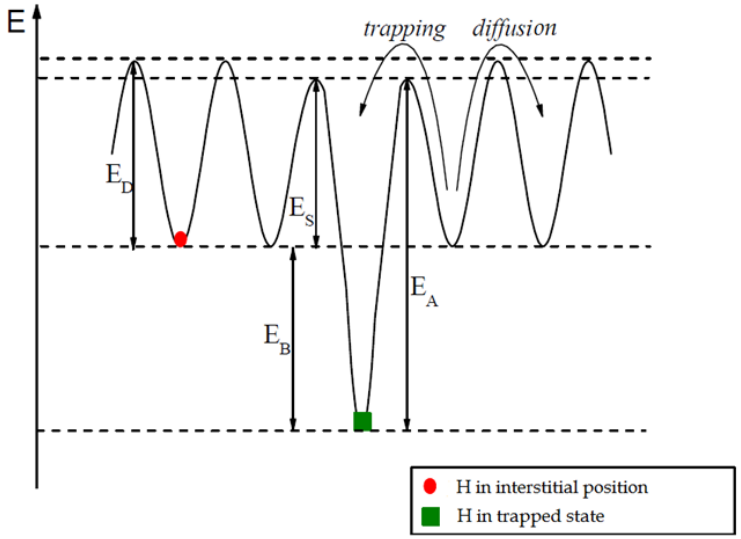

Figure I-4: Potential energy of hydrogen in interstitial position and trapped, with E_D the diffusional energy, E_S the activation energy for trapping, E_B the binding energy of the trap and E_A the activation energy for desorption of the hydrogen from the trap.

Hydrogen, to which a certain mobility is attributed, is in literature often called diffusible hydrogen. It is important to mention that this concept has multiple definitions in literature. Hadam *et al.* [36] defined it as the hydrogen present in the interstitial lattice sites, Loidl [5] defined it as the hydrogen that desorbs below 1000°C, Bergers *et al.* [41] set the temperature at 450°C, Scully *et al.* [42] as the hydrogen release below 190°C, Wang *et al.* [43] at 327°C and Akiyama *et al.* at 300°C [44]. This definition mainly depends on the working temperature of the materials and actually means that hydrogen trapped in what are commonly described as irreversible trapping sites, can even be considered as diffusible if the working temperature is high enough for the hydrogen to be released from those traps.

Generally, two kinds of traps are considered; reversible traps and irreversible traps. In literature, traps with a activation energy less than 60 kJ/mol are often called reversible, while those with higher activation energy are irreversible traps. Hydrogen in reversible traps, such as grain boundaries, dislocations and interstitial solute atoms, is subject to a low interaction energy and consequently has a high probability to be released from the trap. Because of the lower required energy to enter the trap, hydrogen will be easily trapped in those sites during electrochemical charging. The residence time in the trap is low, so hydrogen can escape even after the slightest application of stress or elevated temperature or after some time at room temperature. After escaping, hydrogen is again free to diffuse through the material. The reversible traps can thus act as storage for diffusional hydrogen, which is detrimental for the mechanical properties, as it can migrate to low potential crack initiation sites, resulting in crack growth and unpredictable fracture [45]. Irreversible traps are sites that exert a large attractive force on the hydrogen atoms, binding them with higher energies. These traps are stable at room temperatures and even at slightly elevated temperatures. Hydrogen trapping in irreversible traps can only be undone when a substantial amount of energy is added to the material [46]. Examples are TiC, retained austenite, NbC and MnS.

The process of hydrogen trapping and hydrogen being released from traps determines to a great extent the embrittlement characteristics of the material. The border of reversible and irreversible trapping of 60 kJ/mol may be considered an arbitrary choice as will be discussed in **Chapter V-VIII.**

The determination of an accurate activation energy for a certain trapping site is difficult, not only due to the limitations in experimental possibilities, but also due to the simultaneous effect of the different trapping sites of each microstructure. Two different kinds of measurements methods exist to date. The first group assesses the binding energy isothermally, i.e. the permeation [47] technique. The second groups applies different heating rates to determine similar data non-isothermally and is called thermal desorption spectroscopy (TDS). Both will be used in this work, although only the latter will be used to determine activation energies. The first one will be used to determine the hydrogen diffusion coefficient. Both techniques are described in section I.2 of this chapter. Atomistic simulations using computational quantum mechanical modelling to determine theoretically the hydrogen diffusion and trapping characteristics are possible as well [48] [49]. Although they can offer very valuable information, they are not included in this work as they were considered to be out of scope due to the experimental nature of this work. Illustratively, some activation energies reported in literature are summarized in Table I-1.

Table I-1: Activation energy for different microstructural features and the corresponding literature source. Multiple activation energy values can be found for most traps.

Trapping site	Activation energy (kJ/mol)	Ref.	Trapping site	Activation energy (kJ/mol)	Ref.
Austenite	40.4	[50]	Fe_3C	67.5 – 77.2	[51]
Lath bainite	28.1	[50]	TiC	61	[52] [53]
Lath martensite	27	[54]	TiC	86.9	[55]
Microvoids	27.6 – 35.15	[56]	TiC	136-152	[57]
Voids	28.9	[51] [58]	TiC	95	[59]
Vacancy clusters	40-70	[60]	TiC	55.8	[61]
Dislocations	29	[54]	Incoherent TiC	85.7	[62]
Dislocations	19.2	[56]	Incoherent TiC	68-116	[62]
Dislocations	24.1 – 29.9	[51]	Coherent TiC	46-59	[62]
Dislocations	21.6	[63]	Coherent NbC	23-48	[64]
Dislocations	21.9	[62]	Incoherent NbC	63-68	[64]
Dislocations	20.2	[10]	NbC	28-56	[65]
Triple junctions	> 77.2	[51]	NbN	100-143	[64]
γ grain boundary	62.2-180	[58] [66]	M_2C precipitates	11.4-11.6	[67]
Grain boundary	29 – 58	[54]	VC	33-35	[68]

Grain boundary	20.5	[56]		MnS	77	[69]
Grain boundary	28.9 – 57.9	[51]		MnS	84	[70]
Grain boundary	32	[62]				

A lot of scientific literature on hydrogen trapping has been published recently due to the potential of the strategy of using traps as possible obstacles for diffusible hydrogen and to prevent hydrogen transport to dislocations, voids and crack tips, which consequently limits possible damage or degradation of the mechanical properties. A uniform distribution of fine irreversible hydrogen traps is reported to result in the maximal resistance against hydrogen embrittlement according to Pressouyre and Bernstein [59]. They retard the fracture and the degree of the hydrogen induced ductility loss. The sensitivity to HE decreases with more irreversible traps [71]. However, large irreversible traps are reported to be the most detrimental ones and thus increase the degree of HE [11].

With respect to the hydrogen/carbide interaction, the work of Wei and Tsuzaki on TiC is very often quoted in literature [61]. The hydrogen trapping effect of semi-coherent and coherent TiC was extensively studied by means of TDS. The coherent, semi-coherent and incoherent precipitates showed a different behaviour regarding their hydrogen capacity, the interaction energy with hydrogen and the available locations for hydrogen. Disc-shaped TiC precipitates are able to trap hydrogen in their broad (semi-)coherent interface with an activation energy for desorption of 55.8 kJ/mol during cathodic charging at room temperature. As the carbide grows, the interface gradually loses its coherency, resulting in a proportional increase in the binding and desorption activation energy. At a certain size, electrolytic charging is no longer possible; hydrogen then needs to be introduced in the material during production at elevated temperature or gaseous charging. According to Wei and Tsuzaki [61] the amount of hydrogen trapped by coherent or semi-coherent TiC particles depends on the surface area of the carbide, indicating that hydrogen is located at the particle-matrix interface. Those small, (semi-)coherent precipitates are formed at lower temperatures during tempering, where the matrix has a ferritic (or sometimes martensitic) microstructure. Here, the interstitial sites in the particle are tetrahedral, which results in a low energy trapping site for hydrogen. Those metastable sites are thus a lot less energetically favourable with respect to the trapping sites at the particle-matrix interface, where hydrogen preferably will be trapped (see Figure I-5 (a)). For larger, incoherent precipitates, the volume rather than the surface area determines the hydrogen content of the carbide, which means that the hydrogen should be trapped inside the incoherent particle. The octahedral carbon vacancies of the particle that was formed during the austenitization state does indeed offer a deeper trap for hydrogen (Figure I-5 (b)). The activation energy to enter this internal trap will be a lot higher than for trapping at the interface.

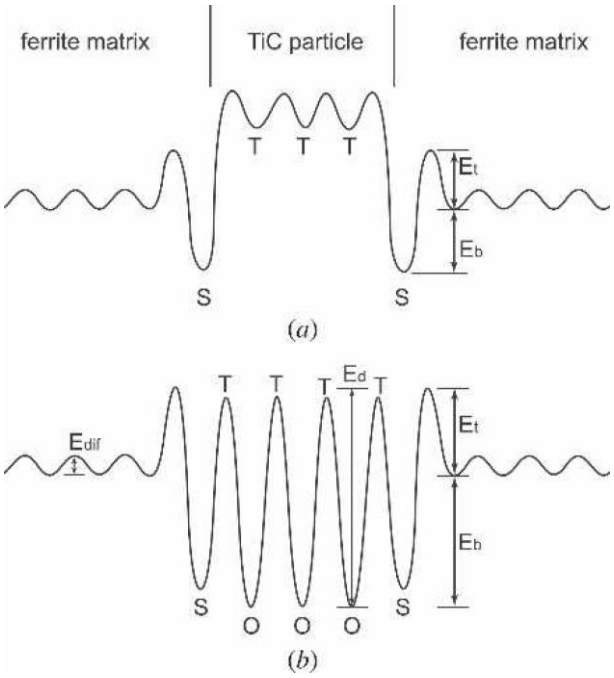

Figure I-5: Illustration of the energy level of hydrogen around a (semi-)coherent (a) and an incoherent (b) TiC-particle, with E_d the desorption activation energy, E_b the binding energy, E_t the trapping activation energy and E_{diff} the diffusion activation energy. T, O and S represent respectively a tetrahedral interstitial site, an octahedral carbon vacancy and a trap site at the interface between the TiC particle and the ferrite matrix [61]**.**

Later on, Wei *et al.* [62] calculated the E_a for hydrogen desorption from incoherent TiC in a 0.05C-0.22Ti-2.0Ni-steel as being 85.7 kJ/mol. For steel with a higher carbon grade (0.42C-0.30Ti-steel) an E_a of 116 kJ/mol is found for interaction of hydrogen with the coarse TiC present in the material when tempered at 650°C and 700°C. This value decreases with decreasing tempering temperature, as shown in Figure I-6. Concerning coherent precipitates, the activation energy also varies with tempering temperature, reaching values between 46 and 59 kJ/mol. Grain boundaries and dislocations trap hydrogen with an energy of about 30 kJ/mol.

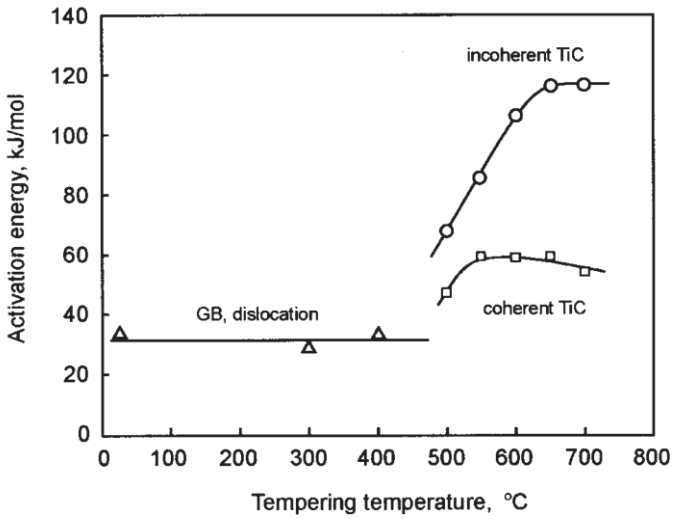

Figure I-6: Changes in activation energy for desorption of hydrogen in grain boundaries, dislocations and incoherent and coherent TiC with tempering temperature [62]**.**

I.1.3 Mechanisms of hydrogen embrittlement

Hydrogen embrittlement is correlated with localized hydrogen concentrations at (sub-) surface sites at internal or external crack tips [72], at interfaces (particle/matrix, grain boundaries,..), at interstitial sites subjected to triaxial stresses and at dislocations. There seems to be a relation between these sites and the fracture mode. When the hydrogen concentration at these stress sites becomes too high, crack initiation and propagation might occur [73]. The mechanism according to which this embrittlement occurs is of significant importance. A good understanding of this subject is indeed vital to be able to design materials which are not suffering from hydrogen induced cracking (HIC).

However, thoroughly performed research data have not been able to give a clear and unarguable understanding of the hydrogen embrittlement mechanism. Several researchers developed theories on the responsible mechanism of HE on a microscopic scale, resulting in three general mechanisms [74], next to hydride-forming mechanisms. These degradation theories are based on decohesion, locally enhanced plasticity and adsorption. The first theory – hydrogen-enhanced decohesion (HEDE) – has been studied for over 45 years and was presented by Troiano [75] and Oriani [76]. It involves weakening of interatomic bonds in regions of high hydrogen concentrations (crack tips, high triaxial stress regions ahead of crack tips and interfaces) resulting in brittle fracture. The hydrogen-enhanced localized-plasticity (HELP) mechanism is more recent and was first introduced by Beachem [77] and later promoted by Birnbaum *et al.* [78]. It involves easier dislocation movement when dislocations and obstacles to them are surrounded by hydrogen atmospheres. Finally, according to Lynch [79], HE can occur via a mechanism called adsorption-induced dislocation-emission (AIDE). This involves weakening of interatomic bonds at crack tips due to 'adsorbed' hydrogen.

Although Lynch [79] claims that these mechanisms can be separately responsible for hydrogen induced cracking, other authors, such as Liu [80], counter this assertion and believe that a combination of the mechanisms is always the cause. These proposed mechanisms are all supported by a large number of experimental confirmations. One reasonable aspect of this controversy is that there are several viable mechanisms of hydrogen-related failure. Currently, it is assumed that a combination of the mechanisms is responsible for the different cases of HIC, but one mechanism is always the dominant failure mechanism, dependent on the fracture mode. There appears to be some consensus that cleavage fractures are mainly promoted by AIDE, brittle intergranular fractures probably occur mainly by HEDE, and slip band fractures plausibly involve HELP [81]. The parameters that influence the susceptibility to HE are [82]:

- the kinetics of hydrogen diffusion and trapping: they can affect the extent of the hydrogen enriched zone as well as the crack propagation rate;
- the amount and distribution of hydrogen present in the material;
- previous and current stresses and strains exerted on the material: this controls the accumulation and local concentration of hydrogen in the material.

I.1.3.1 Hydrogen-Enhanced Decohesion (HEDE)

Oriani [76] was the first to evolve a full theory of lattice decohesion caused by hydrogen, based on assumptions made by Troiano [75]. It considers the increase in hydrogen solubility in a tensile strain field, for instance on the tip of a crack or in areas with internal tensile strain or in the tension field of edge dislocations, as presented in Figure I-7. Solute hydrogen atoms create a decrease in the cohesive forces of the lattice atoms, due to an increase

in the atomic distance. Brittle material fracture can occur if this local hydrogen concentration exceeds a critical level [74] [82].

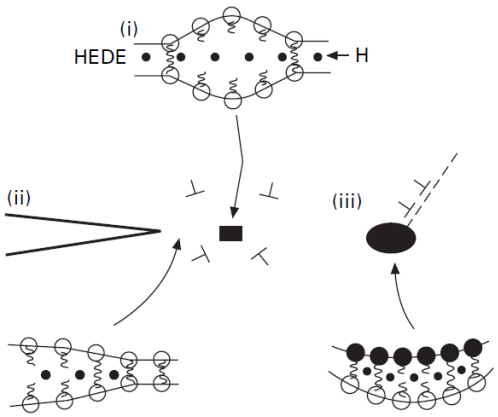

Figure I-7: Schematic diagrams illustrating the HEDE mechanism, involving tensile separation of atoms owing to weakening of interatomic bonds by (i) hydrogen in the lattice (ii) adsorbed hydrogen and (iii) hydrogen at particle/matrix interfaces [40]**.**

Regions that are sensitive to this pile-up of hydrogen are regions of triaxial stress, such as ahead of a crack tip. The existing hydrogen atoms, driven to these places by stress-assisted lattice diffusion [83], cause a dilatation of the lattice at the tip of the crack. When the interatomic bonding strength, weakened by the presence of hydrogen, is overcome by the elastic tensile stress at the crack tip, premature micro-cracks are created and crack growth will occur. As the material ahead of the crack tip is always addressed and then weakened at its atomic bonds, the crack will propagate discontinuously. Crack propagation is facilitated along grain boundaries, interfaces and cleavages.

I.1.3.2 Hydrogen-Enhanced Localized Plasticity (HELP)

In contrary to the HEDE theory, the HELP mechanism stipulated by Beachem [77] is in fact a ductile mechanism, at least on the microstructural scale. Birnbaum *et al*. [78] proposed a complete picture for this model, where hydrogen increases the ease of dislocation movement or generation, or both. They state that hydrogen atmospheres around dislocations and other microstructural features reduce the repulsive elastic interactions between these obstacles. The dislocations are thus shielded from each other by the hydrogen atoms, facilitating their movement [79] (cf. Figure I-8). Therefore, a local dislocation movement will already take place at low level of shear stress, which is caused by a local drop of yield stress due to hydrogen.

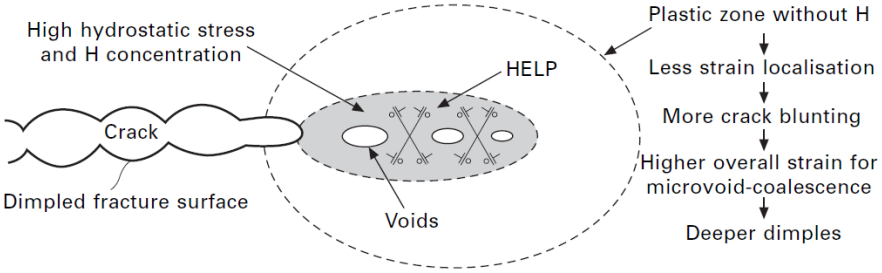

Figure I-8: Schematic diagram illustrating the HELP mechanism, involving a microvoid-coalescence process, with plasticity localised and facilitated in regions of hydrogen concentrations [40]**.**

The definition of hydrogen fracture as a brittle fracture is based on the loss of macroscopic ductility. However, fractographic studies show that HE is related with locally enhanced plasticity at the crack tip. This plasticity is only local, as hydrogen is only locally accumulated at the stress zone ahead of the crack tip and thus non-uniformly distributed. The result of this highly localized plastic flow is a local softening which leads to fracture with limited ductility, i.e. a lower total elongation, on a macroscopic scale [74].

I.1.3.3 Adsorption-Induced Dislocation Emission (AIDE)

Lynch [79] introduced the AIDE mechanism as a combination of HEDE and HELP. Hydrogen is adsorbed on the surface and influences only the first few atomic layers of the material. The interatomic bonds of the lattice are weakened, similar to the HEDE mechanism, facilitating the nucleation of dislocations, like in the HELP mechanism. The dislocations then move away from the crack tip, making the crack propagate. The whole procedure of dislocation nucleation and subsequent transfer away from the crack tip is defined as dislocation emission. This gives rise to a localized plastic flow, which results in a macroscopic lower ductility of the material.

I.1.4 Illustration on hydrogen/material interaction in high strength steel

The interaction of high strength steels with hydrogen has been investigated thoroughly during the last decade, e.g. [3] [30] [43] [84] [85] [86] [87] [88] [89]. As an illustration of such a study and an introduction to **Chapter II**, some of our recent work will be presented here on four industrial high strength steels, i.e. a dual phase (DP), a transformation induced plasticity (TRIP), a high strength low alloyed (HSLA) called S550MC and a ferrite bainite (FB) alloy. Pure iron served as a reference material. Pérez Escobar *et al.* [90] studied the available trapping sites and their trapping capacity by performing thermal desorption spectroscopy (TDS) and hot extraction on these materials. They observed that the steels trapped a different amount of hydrogen after electrochemical charging and that a different amount of diffusible hydrogen effused from the material as a function of increasing desorption times in vacuum. TRIP steel contained the highest amount of diffusible hydrogen as determined by hot extraction. However, TDS revealed that S550MC contained more hydrogen compared to TRIP steel (cf. Figure I-9). The difference between hot extraction and TDS can be explained based on the differences between both techniques as one hour of desorption time is necessary to guarantee a sufficiently low pressure in the analysis chamber ahead of the TDS measurement. During this time, a certain amount of hydrogen is able to effuse from the sample and apparently TRIP lost more hydrogen compared to S550MC as observed in Figure I-9. The S550MC behavior was attributed to the presence of Ti- and Nb- carbo nitrides in this HSLA steel.

In a next step, the samples were kept for longer times at low pressure before the start of the TDS measurement. Self-evidently, the amount of detected hydrogen decreased with desorption time as illustrated in Figure I-10 for the HSLA steel. The degree of decrease with desorption time was slowest for the HSLA steel compared to the other commercial steels, which was again attributed to the presence of the carbides. This confirms the results by Duprez *et al.* [91] where a different amount of ductility recovery for these materials was observed when hydrogen charged tensile samples were left one week in air before actually testing them. The hydrogen induced mechanical degradation of these materials will be discussed in **Chapter II** [3] and a visualization of the impact of both the amount and diffusivity of hydrogen in DP steel will be investigated in **Chapter III** with a detailed

fractography study [84]. The effect of the deformation speed on the hydrogen embrittlement sensitivity will also be discussed in more detail in these chapters.

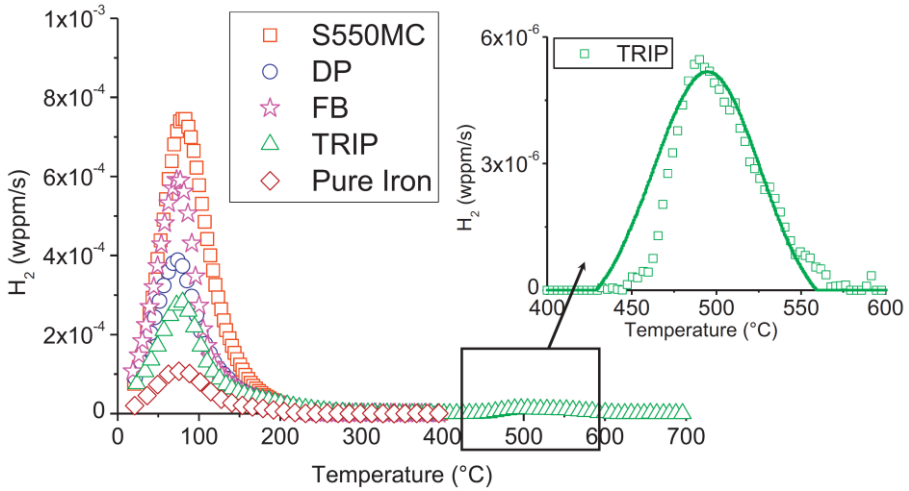

Figure I-9: TDS spectra of S550MC, DP, FB, TRIP and Pure Iron at heating rate of 200°C/h [90]**.**

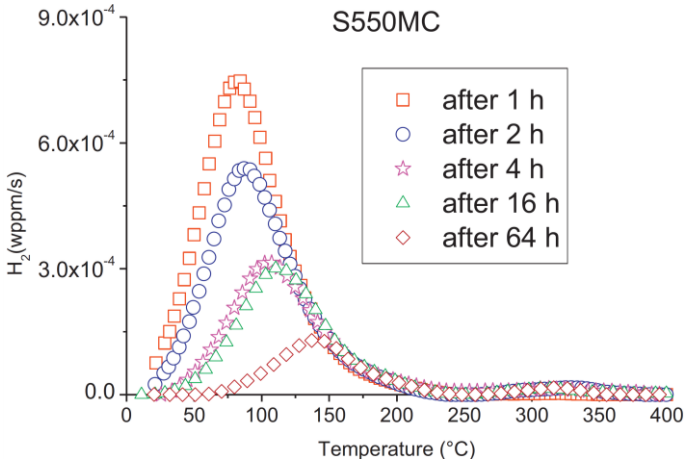

Figure I-10: TDS spectra of S550MC after different desorption times at heating rate of 200°C/h [90]**.**

However, the obtained activation energies for the different traps in these multiphase high strength steels were all in the same range, making it very difficult to attribute a certain peak to a specific microstructural feature. This clearly showed that the complex correlation between a certain microstructural feature and a specific obtained desorption peak complicated the study of the hydrogen/material interaction in these materials a lot. Therefore, generic single-phased alloys will be considered and discussed in **Chapter IV** to study the interaction between hydrogen and several microstructural constituents such as bainite and martensite and to study the role of different carbides in the rest of this PhD.

When evaluating the TDS spectra in Figure I-9 [90], it was observed that only TRIP steel showed a high temperature peak with an E_a of 90 kJ/mol which was proved to come from hydrogen trapped in the retained austenite. Proof was generated by applying different degrees of cold deformation to the TRIP steel. Cold deformation caused a strain induced transformation of the retained austenite into martensite and consequently reduced the retained austenite fraction in the material. The high temperature peak decreased correspondingly in

intensity with increasing degree of cold deformation as shown in Figure I-11 [92]. Consequently, the link between this peak and the retained austenite was demonstrated.

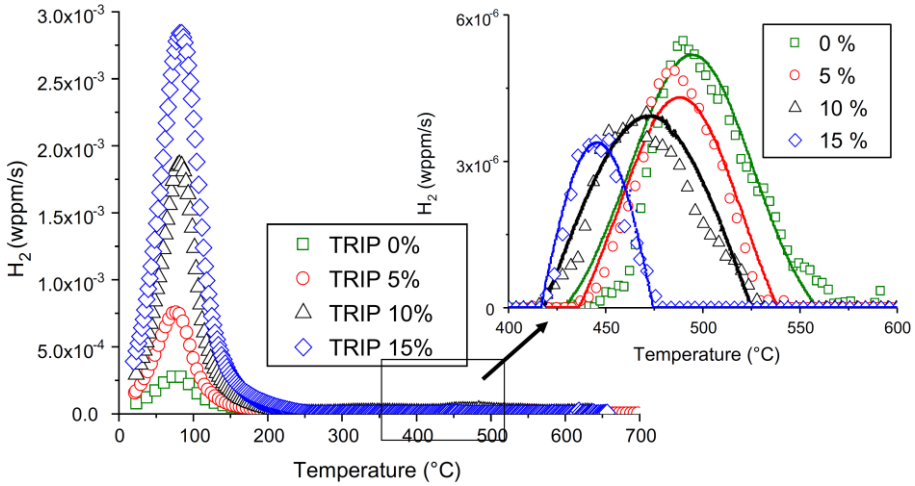

Figure I-11: TDS spectra of TRIP steels with different % of cold deformation at heating rate of 200°C/h [92]**.**

As already mentioned above, the hydrogen induced failure mechanisms are not yet completely understood. Hydrogen in steel is a particular problem because the hydrogen atom is highly mobile and can both diffuse through the lattice and affects the movement of dislocations. It is known that the interaction of hydrogen with microstructural features such as lattice defects, grain boundaries, lath boundaries, dislocations, vacancies, etc. play an important role in this phenomenon [93]. They can trap hydrogen, possibly influencing the susceptibility to hydrogen embrittlement. Moreover, the low hydrogen solubility and the fact that is almost impossible to visualize hydrogen [94] significantly contribute to the complexity of hydrogen in steels. As indicated above, one of the most suggested solutions for this problem is the introduction of small carbides in the steel, which can act as hydrogen trapping sites. In this way, the resistance to brittle fracture caused by the presence of hydrogen can be improved. This will be the main scope of this work and is the focus of **Chapter V-VIII** for Ti, Cr, Mo and V based carbides, respectively. Literature sources on these specific carbides are considered in the introduction part of each chapter.

I.2 Experimental procedure of the hydrogen characterization techniques

In this work, the amount of diffusible hydrogen will be determined by hot extraction and a temperature of 300°C was chosen in this work, which is the same definition for diffusible hydrogen as proposed by Akiyama *et al.* [44]. The total amount of hydrogen can be measured by melt extraction at 1600°C. For both, a GALILEO G8 ON/H (Bruker AXS) device was used. The system comprises a pulse furnace in which a pre-weighted sample is heated as fast as possible in a nitrogen atmosphere. The metal is heated till the desired temperature and releases its hydrogen as gaseous H_2. The latter is taken up by a nitrogen flow and the mixture of N_2 and H_2 is directed to a thermal conductivity measuring cell. The thermal conductivity of the mixture relies on the H_2 concentration because of the significant variance in conductivity of H_2 and N_2. The software determines the hydrogen concentration of the sample based on the thermal conductivity difference.

The permeation technique was used to determine the hydrogen diffusion coefficient, for which the Devanathan and Stachurski method [47] was applied. The two compartments were filled with 0.1 M NaOH solution and the polished specimen of typically 1 mm thickness was clamped in between. The hydrogen entry side acted as the cathode by applying a current density of 3 mA/cm^2, and the hydrogen exit side (anode) was potentiostatically kept at - 500 mV according to a Hg/Hg_2SO_4 reference electrode. This electrolyte differs from the one used for the other hydrogen related characterization techniques as the high current density and long duration of the permeation test are very likely to cause hydrogen induced damage such as blisters which would make the obtained results invalid. The solutions in the compartments were both stirred with nitrogen bubbling and temperature was maintained constant at 25°C. The apparent hydrogen diffusion coefficient was calculated from the permeation transient using the following formula [95]:

$$D_{app} = \frac{L^2}{7.7\ t}\ (m^2/\ s) \tag{I-7}$$

where t is the time (s) when the normalized steady state value has reached 0.1 and L is the sample thickness (m).

TDS was done in this work to identify both the hydrogen trapping sites and their corresponding activation energy. Hydrogen was introduced in the materials by electrochemical charging using a 1g/L thiourea in a 0.5 M H_2SO_4 solution. The conditions were chosen in such a way that they did not create blisters or any internal damage and it was verified that a complete saturation of the materials was ensured. Three different heating rates (200°C/h, 600°C/h and 1200°C/h) were applied. The used experimental procedure required one hour between the end of hydrogen charging and the start of the TDS measurement as the mass spectrometer requires a sufficiently low pressure in the analysis chamber before the TDS measurement could start. In order to determine the E_a of hydrogen traps related to the peaks observed in the TDS spectra, the method based on the work of Lee *et al.* [96] [97] [98] was used. Equation (I-8) is a simplification of the original formula of Kissinger [99]:

$$\frac{d(\ln\frac{\Phi}{T_{max}^2})}{d(\frac{1}{T_{max}})} = -\frac{E_a}{R} \tag{I-8}$$

where Φ is the heating rate (K/min), T_{max} (K) the TDS peak temperature, E_a (J/mol) the detrapping activation energy for the specific hydrogen trap associated with T_{max} and R ($JK^{-1}mol^{-1}$) the universal gas constant. After TDS measurements were performed using different heating rates, the spectra were deconvoluted and the corresponding peak temperatures for a trap were determined. Plotting $\ln(\Phi/T_{max}^2)$ vs. $(1/T_{max})$ allows to obtain the E_a corresponding to that specific trap. One of the contras of TDS is the fact that hydrogen diffusion is not included in the proposed methodology for data analysis. The sample thickness is therefore a very important feature, especially when the materials show a low D_{app}. Consequently, a constant sample thickness of 1 mm was used. Additionally, no hydrogen retrapping is considered, i.e. every trap is an isolated microstructural feature. However, one of the pros is obviously the deconvolution method which results in the possibility to make a distinction between several peaks that can be linked to specific microstructural features.

The hydrogen induced ductility loss was determined in this work by comparing tensile tests performed in air with tests done on in-situ hydrogen charged samples. In-situ charging meaning that hydrogen charging and the tensile test could be performed simultaneously. Hydrogen was introduced in the sample in the same way as for the TDS measurements, while in-situ charging indeed continued during the tensile test. The reference tensile

tests were performed at a cross-head deformation speed of 5 mm/min, with a corresponding strain rate of 1.11 x 10^{-3} s^{-1}, similar to Zhao *et al.* [100]. To compare the sensitivity of the hydrogen induced mechanical degradation, the percentage hydrogen embrittlement (%HE) is defined as [3] [84]:

$$\%HE = 100 \cdot \left(1 - \frac{\varepsilon_{ch}}{\varepsilon_{un}}\right) \tag{I-9}$$

with ε_{ch} and ε_{un} being the elongation at fracture of the charged and uncharged sample, respectively. Hence, the %HE varies between 0 and 1, with 0 meaning that there is no ductility loss and that the material is insensitive to HE. When an index of 1 is obtained, the ductility drop is 100% and HE is maximal.

The tensile samples were machined with their tensile axis parallel to the rolling direction. For the tensile specimens tested in Chapter II, III and IV, notched tensile samples were used and their geometry is shown in Figure I-12. This was done in order to control the position of crack initiation as our previous work, where no in-situ hydrogen charging was applied, indicated that the tensile samples tend to break at the interface between the electrolyte and air due to a different type of corrosion. Consequently, the notch, which introduced locally a triaxial stress condition and reduction, was induced to guarantee that fracture occurred in the central part of the specimen, which was kept inside the electrolyte during charging. This geometrical discontinuity gives rise to a local stress concentration expressed by a stress concentration factor K_t of 4.2 for the used tensile sample geometry. Initially, this sample geometry was maintained for this work, for which the in-situ charging cell was used. The tensile tests in **Chapter II, III and IV** were performed on the notched specimens.

However, this work focused on ductility loss. Ductility is the possibility to strain in the absence of stress concentrations. Consequently, a non-notched tensile specimen is preferred for this purpose (cf. Figure I-13). Therefore, in **Chapter V, VI, VII and VIII** the notch was removed as it was verified that failure occurred in the central region inside the electrolyte when the in-situ hydrogen charging cell was used. Finally, the surface of the samples was sandblasted to remove possible oxides remaining from processing.

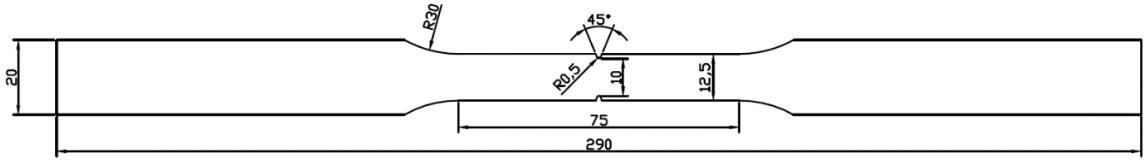

Figure I-12: Geometry of the tensile specimen in Chapter II, III and IV.

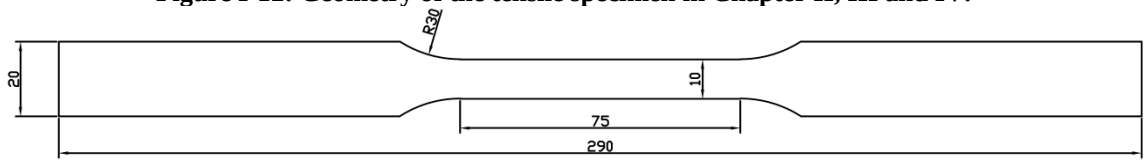

Figure I-13: Geometry of the tensile specimen in Chapter V, VI, VII and VIII.

The stress and strain level was determined using the concepts of conventional engineering stress and strain definitions as accurate as possible, taking into account the experimental limitations of the tensile test set-up. The actual overall (i.e. specimen as well as the tensile testing equipment) deformation was recorded in mm as the crosshead displacement. No local determination of the deformation was possible for these experiments as the in-situ charging cell is surrounding the tensile specimen for the hydrogen charged samples. The use of an extensometer was as such impossible. Therefore, it was chosen to rely on the deformation recorded by the tensile machine for all the performed tensile tests and hence the determination of the actual Young's modulus cannot be performed. The strain was calculated using the definition presented in Eq. I-10, where L_0 is the gauge length (i.e. 75 mm in the present case) and Δ L is the crosshead displacement. Additionally, the stress level of the materials

was determined as well by the tensile machine since the software documented the forces applied on the samples. By using the definition for engineering stress (Eq. I-11), the software determined the stress level, where A_0 was the initial area, i.e. the width of 10 mm multiplied by the thickness of the materials.

$$\varepsilon = \Delta L / L_0 \quad \text{(I-10)}$$

$$\sigma = F / A_0 \quad \text{(I-11)}$$

Since soon after necking failure occurred, the strain at fracture calculated using Eq. I-10 is representative for the failure strain. Obviously, for the notched specimens the strain will localize around the notch and the actual strain will there be significantly higher than the average strain calculated by Eq. I-10.

I.3 Scope of the present work

The fact that hydrogen/material interaction can have a detrimental effect on the mechanical properties of that material is well-known for years. Although, numerous research studies have been published on this topic, a full understanding of the mechanism behind is lacking since hydrogen induced failure still occurs unpredictably since the process of failure is not well understood. Recently, the use of high strength steels has gained a lot of interest due their large applicability and their high strength vs. weight ratio makes them of an interesting alternative for the automotive industry to both lower the vehicle's weight and reduce the polluting CO_2 emissions with even increased safety. Unfortunately, these materials are more prone to HE, which renewed the attention in the research field of H/material interactions.

The detrimental effect of hydrogen on the mechanical properties is clear and well described. In addition, the interaction between precipitates and hydrogen, when both present in a metallic microstructure, has also captured considerable interest and Table I-1 showed the corresponding activation energy for hydrogen trapped by these precipitates. Additionally, a vast amount of literature exists on how precipitates affect the mechanical properties as a result of precipitation strengthening of the material. Consequently, one-by-one links are well-known between hydrogen, mechanical properties and precipitates, however, hardly any study combines all three features in a systematic and consistent way. This is exactly the aim of the present work, as illustrated in Figure I-14, where the combined effect of the presence of hydrogen and precipitates on the mechanical properties of high strength steels will be studied.

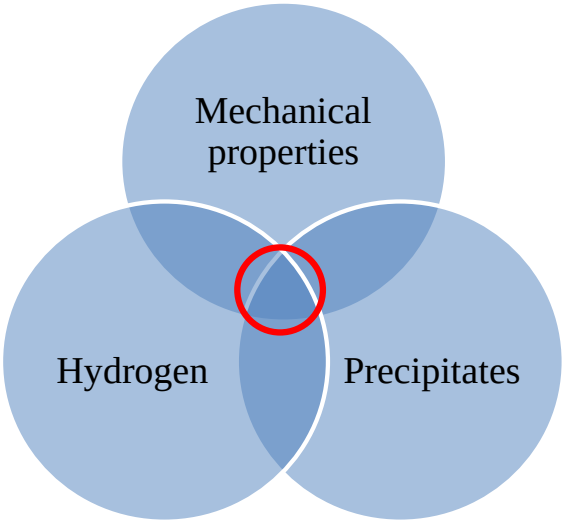

Figure I-14: Illustration of the aim of this work.

Due to the low solubility of hydrogen in steels, together with its high mobility the hydrogen related research is a challenging topic. Additionally, visualization is far from evident, which makes it hard to evaluate the effects of hydrogen. Basically, hydrogen related research can be divided into three different types of tests: the evaluation of the hydrogen induced mechanical degradation by tensile testing, the hydrogen diffusion by isothermal tests such as the permeation technique and the determination of the hydrogen trapping sites and their corresponding activation energy by TDS.

In this work, the hydrogen embrittlement susceptibility and trapping behaviour of both industrial high strength steels and iron-based lab cast materials will be studied using these techniques. The effect of hydrogen on the mechanical properties of high strength steels will be studied in **Chapter II**, whereas the synergetic detrimental effect of both the amount and diffusivity of hydrogen in DP steel will be visualized by scanning electron microscopy and elaborated in a detailed fractography study in **Chapter III**. Due to the complex microstructure of these multiphase high strength steels, a separate study of the different constituents would be more convenient. Therefore, a specific microstructural constituent, i.e. pearlite, bainite and martensite, will be induced in lab cast Fe-C alloys, where pure iron will be used as reference material. The effect of hydrogen on the hydrogen induced ductility loss in these lab cast alloys will be discussed in **Chapter IV**. The effect of hydrogen diffusivity on the sensitivity to hydrogen embrittlement will be included for the bainitic alloys.

As mentioned before, carbides are often reported to be beneficial trapping sites to enhance the response to hydrogen embrittlement. The interaction between hydrogen and carbides has been studied already in the literature by multiple TDS studies. The influence of hydrogen on the mechanical properties is also studied in detail just as it is well-known that carbides strengthen the material when the effect of hydrogen is not taken into account. However, a dedicated study focusing on all aspects of the combined effect of the presence of carbides and hydrogen in a high strength steel matrix using mechanical tests, TDS and hydrogen permeation has hardly been reported in literature so far. Moreover, a systematic study studying all these aspects for different carbide forming elements has not been done. Therefore, in this work, quenched and tempered Fe-C-X lab cast materials will be produced and their interaction with hydrogen will be studied thoroughly. As carbide forming elements Ti, Cr, Mo and V are chosen, which will be discussed in **Chapter V – VI – VII – VIII,** respectively.

As high strength steels are reported to be more susceptible to HE, the material with the highest strength level will be selected for all Fe-C-X alloys and the different kind of carbides will be compared with each other in **Chapter IX**. Finally, the conclusions will be given in **Chapter X**, and some suggestions for future research will be described there as well.

I.4 References

[1] Hauch A, Ebbesen SD, Jensen SH, Mogensen M, „Highly efficient high temperature electrolysis," *Journal of materials chemistry,* vol. 18, pp. 2331-2340, 2008.

[2] Woodtli J, Kieselbach R, „Damage due to hydrogen embrittlement and stress corrosion cracking," *Eng Fail Anal,* vol. 7, pp. 427-450, 2000.

[3] Depover T, Pérez Escobar D, Wallaert E, Zermout Z, Verbeken K, „Effect of in-situ hydrogen charging on the mechanical properties of advanced high strength steels," *Int Journal of Hydrogen Energy,* vol. 39, pp. 4647-4656, 2014.

[4] Hilditch TB, Lee SB, Speer JG, Matlock DK, „Response to Hydrogen Charging in High Strength Automotive Sheet Steel Products," *SAE Technical Paper,* 2003, http://dx.doi.org/10.4271/2003-01-0525.

[5] Loidl M, Kolk O, BMW Group, Germany, „Hydrogen embrittlement in HSSs limits use in lightweight body," *Adv Mat Process,* vol. 169, pp. 22-25, 2011, BMW Group, Germany.

[6] Revie RW, Sastri VS, Elboujdaii M, Ramsingh RR, Lafrenière Y, „Hydrogen-induced cracking of line pipe steels used in sour service," *Corrosion,* vol. 49, pp. 531-536, 1993.

[7] Chawla KK, Rigsbee JM, Woodhouse JB, „Hydrogen-induced cracking in two linepipe steels," *Journal Mater Sci,* vol. 21, pp. 3777-3782, 1986.

[8] Johnson WH, „On some remarkable change produced in iron and steel by the action of hydrogen and acids.," *Proceedings of the Royal Society of London,* vol. 23, pp. 168-179, 1875.

[9] Staehle RW, Hochmann J, McCright RD, Slater JE (eds.), Stress corrosion cracking and hydrogen embrittlement of iron base alloys, Houston, TX: NACE, 1977.

[10] Hirth JP, „Effects of Hydrogen on the Properties of Iron and Steel," *Metallurgical Transactions A,* vol. 11A, pp. 861-890, 1980.

[11] Oriani RA, Hirth JP, Smialowski M, Hydrogen degradation of ferrous alloys, New Jersey: Noyes Publications, 1985.

[12] Louthan MR Jr, „The effect of hydrogen on metals," in *Corrosion Mechanisms,* New York, 1987, pp. 329-365.

[13] Gangloff RP, Ives MB (eds), Environment-induced cracking of metals, Houston, TX: NACE, 1990.

[14] Vehoff H, „Hydrogen related material properties," *Topics in appl phys,* vol. 73, pp. 215-278, 1997.

[15] Sofronis P, „Special issue on recent advances in engineering aspects of hydrogen embrittlement," *Engineering Fracutre Mechanics,* p. 68, 2001.

[16] Pundt A, Kirchheim R, „Hydrogen in metals: microstructural aspects," *Ann Rev Mater Res,* vol. 36, pp. 555-608, 2006.

[17] Gangloff RP, „Hydrogen assisted cracking of high strength alloys," in *Comprehensive structural integrity,* Amsterdam, Elsevier, 2003, pp. 31-101.

[18] Somerday B, Sofronis P, Jones R, „Effects of hydrogen on materials," in *Proc. of the 2008 Int. Hydrogen Conf,* Wyoming, USA, 2008.

[19] Somerday B, Sofronis P, Jones R, „Hydrogen-materials interactions," in *Proc. of the 2012 Int Hydrogen Conf*, Wyoming, USA, 2012.

[20] Gangloff P, Somerday B, Gaseous hydrogen embrittlement of materials in energy technologies, Cambridge: Woodhead, 2012.

[21] Maroef I, Olson DL, Eberhart M, Edwards GR, „Hydrogen trapping in ferritic steel weld metal," *Inter Mater Rev,* vol. 47, pp. 191-223, 2002.

[22] Eliaz N, Shachar A, Tal B, Eliezer D, „Characteristics of hydrogen embrittlement, stress corrosion cracking and tempered martensite embrittlement in high-strength steels," *Engineering Failure Analysis,* vol. 9, nr. 2, pp. 167-184, 2000.

[23] Petroyiannis PV, Pantelakis SG, Haidemenopoulos GN, „Protective role of local Al cladding against corrosion damage and hydrogen embrittlement of 2024 aluminum alloy specimens," *Theor Appl Fract Mech,* vol. 44, pp. 70-81, 2005.

[24] Smith SW, Scully JR, „The identification of hydrogen trapping sites in an Al-Li-Cu-Ze alloy using thermal desorption spectroscopy," *Metall Mater Trans A,* vol. 31, pp. 179-193, 2000.

[25] Zielinski A, „Hydrogen-assisted degradation of some non-ferrous metals and alloys," *Mater Process Tech,* vol. 109, pp. 206-214, 2001.

[26] Pérez Escobar D, PhD: Evaluation of hydrogen trapping in iron-based alloys by thermal desorption spectroscopy, Ghent: Ghent University, 2012.

[27] Perng TP, Wu JK, „A brief review note on mechanisms of hydrogen entry into metals," *Materials Letters,* vol. 57, pp. 3437-3438, 2003.

[28] Carter TJ, Cornish LA, „Hydrogen in metals, Engineering Failure Analysis," *Engineering Failure Analysis,* vol. 8, nr. 2, pp. 113-121, 2001.

[29] McLellan RB, Harkins CG, „Hydrogen interactions with metals," *Mat Sci and Eng A,* vol. 18, pp. 5-35, 1975.

[30] Pérez Escobar D, Miñambres C, Duprez L, Verbeken K, Verhaege M, „Internal and surface damage of multiphase steels and pure iron after electrochemical hydrogen charging," *Corrosion Science,* vol. 53, p. 3166–3176, 2011.

[31] Pérez Escobar D, Depover T, Wallaert E, Duprez L, Verhaege M, Verbeken K, „Thermal desorption spectroscopy study of the interaction between hydrogen and different microstructural constituents in lab cast Fe-C alloys," *Corrosion Science,* vol. 65, pp. 199-208, 2012.

[32] Iyer RN, Pickering HW, Zamanzadeh M, „Analysis of Hydrogen Evolution and Entry into Metals for the Discharge-Recombination Process," *Journal of The Electrochemical Society,* vol. 136, nr. 9, pp. 2463-2470, 1989.

[33] Oriani RA, The Physical and Metallurgical Aspects of Hydrogen in Metals, Minneapolis: The University of Minnesota, 1993.

[34] Porter DA, Easterling KE, Phase transformation in metals and alloys, London, UK: Chapman & Hall, 1992.

[35] Deluccia JJ, Berman DA, „An electrochemical technique to measure diffusible hydrogen in metals," *ASTM special technical publication,* vol. 227, pp. 269-281, 1981.

[36] Hadam U, Zakroczymski T, „Absorption of hydrogen in tensile strained iron and high carbon steel studied by electrochemical permeation and desorption techniques," *Int Journal of Hydrogen Energy,* vol. 34, pp. 2449-2459, 2009.

[37] Da Silva JRG, Stafford SW, McLellan RB, „Thermodynamics of the H-Fe system," *Journal Less-Comm Met,* vol. 49, pp. 407-420, 1976.

[38] Shao H, Relationship study of hydrogen storage property and material structure, [Online], Available: http://i2cner.kyushu-u.ac.jp/..

[39] Tal-Gurelmacher E, Eliezer D, Abramov E, „Thermal desorption spectroscopy (TDS) – Application in quantitative study of hydrogen evolution and trapping in crystalline and non-crystalline materials", Materials Science and Engineering A, vol. 445-446,," *Mat Sci and Eng A,* vol. 445, pp. 625-631, 2007.

[40] Lynch SP, Hydrogen embrittlement phenomenon and mechanism, Australia: Woodhead, 2011.

[41] Bergers K, Thomas I, Flock J, „Determination of hydrogen in steel by thermal desorption mass spectroscopy," in *Proc. of the 8th Inter. workshop on progress in analytical chemistry and materials characterization in the steel and metal industries,* 2011.

[42] Scully JR, Dogan H, Gangloff RP, „Controlling hydrogen embrittlement in ultra-high strength steels," in *Proc. on the conference on corrosion,* 2004.

[43] Wang M, Akiyama E, Tsuzaki K, „Effect of hydrogen on the fracture behavior of high strength steel during slow strain rate test," *Corrosion Science,* vol. 49, pp. 4081-4097, 2007.

[44] Akiyama E, Matsukado K, Wang M, Tsuzaki K, „Evaluation of hydrogen entry into high strength steel under atmospheric corrosion," *Corrosion Science,* vol. 52, pp. 2758-2765, 2010.

[45] Kim WK, Koh SU, Yang BY, Kim KY, „Effect of environmental and metallurgical factors on hydrogen induced cracking of HSLA steels," *Corrosion Science,* vol. 50, pp. 3336-3342, 2008.

[46] Dadfarnia M, Sofronis P, Neeraj T, „Hydrogen interaction with multiple traps: Can it be used to mitigate embrittlement?," *Int Journal of Hydrogen Energy,* vol. 36, pp. 10141-10148, 2011.

[47] Devanathan MAV, Stachurski Z, „The adsorption and diffusion of electrolytic hydrogen in palladium," *Proc Roy Soc A,* vol. 270, pp. 90-101, 1962.

[48] Di Stefano D, Mrovec M, Elsässer C, „First-principles investigation of hydrogen trapping and diffusion at grain boundaries in nickel," *Acta Mat,* vol. 98, pp. 306-312, 2015.

[49] Winzer N, Rott O, Thiessen R, Thomas I, Mraczek K, Höche T, Wright L, Mrovec M, „Hydrogen diffusion and trapping in Ti-modified advanced high strength steels," *Materials & Design,* vol. 92, pp. 450-461, 2016.

[50] Gu JL, Chang KD, Fang HS, Bai BZ, „Delayed fracture properties of 1500 MPa bainite/martensite dual-phase high strength steel and its hydrogen traps," *ISIJ Inter,* vol. 42, pp. 1560-1564, 2002.

[51] Pressouyre GM, „Classification of hydrogen traps in steel," *Metall Trans A,* vol. 10A, pp. 1571-1573, 1979.

[52] Asaoka T, Lapasset G, Aucouturier M, Lacombe P, „Observations of hydrogen trapping in Fe-0.15 wt. pct Ti alloy by high resolution autoradiography," *Corros NACE,* vol. 1978, pp. 39-47, 1978.

[53] Asaoka T, Daggbert C, Aucouturier, M, Galland, J, „Quantitative study on capture of hydrogen in ferrite Fe-0.15%-Ti using high resolution autoradiography and degassing at different temperatures," *Scripta Metallurgica,* vol. 11, pp. 467-472, 1977.

[54] Thomas LSR, Li D, Gangloff RP, Scully JR, „Trap-governed hydrogen diffusivity and uptake capacity in ultrahigh strength aermet 100 steel," *Met Mat Trans A,* vol. 33A, pp. 1991-2004, 2002.

[55] Lee HG, Lee JY, „Hydrogen trapping by TiC particles in iron," *Acta Metall,* vol. 32, pp. 131-136, 1984.

[56] Choo WY, Lee JY, „Thermal analysis of trapped hydrogen in pure iron," *Metall Trans A,* vol. 13A, pp. 135-140, 1982.

[57] Pérez Escobar D, Wallaert E, Duprez L, Atrens A, Verbeken K, „Thermal Desorption Spectroscopy Study of the Interaction of Hydrogen with TiC Precipitates," *Met Mater Int,* vol. 19, pp. 741-748, 2013.

[58] Dogan H, Lo D, Scully JR, „Controlling hydrogen embrittlement in precharged ultrahigh-strength steel," *Corrosion Science,* vol. 63, pp. 689-703, 2007.

[59] Pressouyre GM, Bernstein IM, „A quantitative analysis of hydrogen trapping," *Metall Trans A,* vol. 9A, pp. 1571-1580, 1978.

[60] Nagumo M, Nakamura M, Takai K, „Hydrogen Thermal Desorption Relevant to Delayed-Fracture Susceptibility of High-Strength Steels," *Met Mat Trans A,* vol. 32, nr. 2, pp. 339-347, 2001.

[61] Wei FG, Tsuzaki K, „Quantitative Analysis on hydrogen trapping of TiC particles in steel," *Met Mat Trans A,* vol. 37A, pp. 331-353, 2006.

[62] Wei FG, Hara T, Tsuzaki K, „Precise determination of the activation energy for desorption of hydrogen in two Ti-added steels by a single thermal-desorption spectrum," *Met Mat Trans B,* vol. 35B, pp. 587-97, 2004.

[63] Takai K, Chiba Y, Noguchi K, Nozue A, „Visualization of the hydrogen desorption process from ferrite, pearlite and graphite by secondary ion mass spectroscopy," *Met Mat Trans A,* vol. 33A, pp. 2659-2665, 2002.

[64] Wallaert E, Depover T, Arafin MA, Verbeken K, „Thermal desorption spectroscopy evaluation of the hydrogen trapping capacity of NbC and NbN precipitates," *Met Mat Trans A,* vol. 45, pp. 2412-2420, 2014.

[65] Ohnuma M, Suzuki JI, Wei FG, Tsuzaki K, „Direct observation of hydrogen trapped by NbC in steel using small-angle neutron scattering," *Scripta Mater,* vol. 58, pp. 142-145, 2008.

[66] Mizuno M, Anzai H, Aoyama T, Suzuki T, „Determination of hydrogen concentration in austenitic stainless steels by thermal desorption spectroscopy," *Mat Trans JIM,* vol. 35, p. 703, 1994.

[67] Li D, Gangloff RP, Scully JR, „Hydrogen trap states in ultrahigh-strength AERMET 100 steel," *Met Mat Trans A,* vol. 35, nr. 3, pp. 849-864, 2004.

[68] Asahi H, Hirakami D, Yamasaki S, *ISIJ Intl,* vol. 43, pp. 527-533, 2003.

[69] Lee JY, Lee JL, Choo WY, „Current solutions to hydrogen problems in steel," *ASM,* p. 423, 1982.

[70] lino M, „Evaluation of hydrogen-trap binding enthalpy," *Met Trans A,* vol. 18, pp. 1559-1564, 1987.

[71] Serna S, Martinez H, Lopez SY, Gonzalez-Rodriguez JG, Albarran JL, „Electrochemical technique applied to evaluate the hydrogen permeability in microalloyed steels," *Int Journal of Hydrogen Energy,* vol. 30, pp. 1333-1338, 2005.

[72] Lynch SP, „Environmentally assisted cracking: overview of evidence for an adsorption-induced localised-slip process," *Acta metallurgica,* vol. 36, nr. 10, pp. 2639-2661, 1988.

[73] Ćwiek J, Michalska-Ćwiek J, „Evaluation of hydrogen degradation of high-strength weldable steels," *Journal of Achievements in Materials and Manufacturing Engineering,* vol. 42, nr. 1-2, pp. 103-110, 2010.

[74] Liu Q, Irwanto B, Atrens A, „The influence of hydrogen on 3.5NiCrMoV steel studied using the linearly increasing stress test," *Corrosion Science,* vol. 67, pp. 193-203, 2013.

[75] Troiano AR, „The role of Hydrogen and Other Interstitials in the Mechanical Behaviour of Metals," *Trans. ASM,* vol. 52, pp. 54-80, 1960.

[76] Oriani RA, „A Mechanistic Theory of Hydrogen Embrittlement of Steels," *Berichte der Bunsengesellschaft für physikalische Chemie,,* vol. 76, pp. 848-857, 1972.

[77] Beachem CD, „A new Model for Hydrogen-Assisted Cracking," *Met Trans A,* vol. 3, pp. 437-451, 1972.

[78] Bimbaum HK, Sofronis P, „Hydrogen-enhanced localized plasticity – a mechanism for hydrogen related fracture," *Mat Sci and Eng A,* vol. 176, nr. 1-2, pp. 191-202, 1994.

[79] Lynch SP, „Comments on "A unified model of environment-assisted cracking"," *Scripta Materialia,* vol. 61, pp. 331-334, 2009.

[80] Liu HW, „Reply to comments on "A unified model of environment assisted cracking"," *Scripta Materialia,* vol. 61, nr. 3, pp. 335-337, 2009.

[81] Lynch SP, „Mechanisms of hydrogen-assisted cracking," in *Hydrogen effects on material behavior and corrosion deformation interactions,* 2003, pp. 449-466.

[82] Marchetti L, Herms E, Laghoutaris P, Chêne J, „Hydrogen embrittlement susceptibility of tempered 9%Cr-1%Mo steel," *Int Journal of Hydrogen Engery,* vol. 36, pp. 15880-15887, 2011.

[83] Toribo J, „Hydrogen-plasticity interactions in pearlitic steel: a fractographic and numerical study," *Mat Sci and Eng A,* vol. 219, pp. 180-191, 1996.

[84] Depover T, Wallaert E, Verbeken K, „Fractographic analysis of the role of hydrogen diffusion on the hydrogen embrittlement susceptibility of DP steel," *Mat Sci and Eng A,* vol. 649, pp. 201-208, 2016.

[85] Ronevich JA, Speer JG, Matlock DK, „Hydrogen embrittlement of commercially produced advanced high strength steels," *SAE Int Journal Mater Manuf,* vol. 3, pp. 255-267, 2010.

[86] Koyama M, Tasan CC, Akiyama E, Tsuzaki K, Raabe D, „Hydrogen-assisted decohesion and localized plasticity in dual-phase steel," *Acta Mat,* vol. 70, pp. 174-187, 2014.

[87] Wang M, Akiyama E, Tzuzaki K, „Effect of hydrogen and stress concentration on the notch tensile strength of AISI 4135 steel," *Mat Sci and Eng A,* vol. 398, pp. 37-46, 2005.

[88] Laureys A, Depover T, Petrov R, Verbeken K, „Characterization of hydrogen induced cracking in TRIP-assisted steels," *Int Journal of Hydrogen Energy,* vol. 40, nr. 47, pp. 16901-16912, 2015.

[89] Laureys L, Depover T, Petrov R, Verbeken K, „Microstructural characterization of hydrogen induced cracking in TRIP-assisted steel by EBSD," *Materials Characterization,* vol. 112, pp. 169-179, 2016.

[90] Pérez Escobar D, Verbeken K, Duprez L, Verhaege M, „Evaluation of hydrogen trapping in high strength steels by thermal desorption spectroscopy," *Mat Sci and Eng A,* vol. 551, pp. 50-58, 2012.

[91] Duprez L, Verbeken K, Verhaege M, „Effect of hydrogen on the mechanical properties of multiphase high strength steels," in *Proc. of the 2008 Int. Hydrogen Conf.,* Jackson, Wyoming, USA, 2008.

[92] Pérez Escobar D, Depover T, Wallaert E, Duprez L, Verbeken K, Verhaege M, „Combined thermal desorption spectroscopy, differential scanning calorimetry, scanning electron microscopy and X-ray diffraction study of hydrogen trapping in cold deformed TRIP steel," *Acta Mat,* vol. 60, p. 2593, 2012.

[93] Takasugi T, „Hydrogen-lattice defect interaction in embrittlement of L12 ordered intermetallics: a review," *Elsevier Science Limited,* vol. 4, pp. 181-187, 1995.

[94] Takahashi J, Kawakami K, Kobayashi Y, Tarui T, „The first direct observation of hydrogen trapping sites in TiC precipitation-hardening steel through atom probe tomography," *Scripta Mat,* vol. 63, pp. 261-264, 2010.

[95] McBreen, Nanis L, Beck W, „A method for determination of the permeation rate of hydrogen through metal membranes," *Journal of Electrochemical Society,* vol. 113, pp. 1218-1222, 1966.

[96] Lee SM, Lee JY, „The trapping and transport phenomena of hydrogen in nickel," *Metal Trans A,* vol. 17A, pp. 181-187, 1986.

[97] Lee JY, Lee SM, „Hydrogen trapping phenomena in metals with bcc and fcc crystal structures by the desorption thermal-analysis technique," *Surface and Coatings Technology,* vol. 28, pp. 301-314, 1986.

[98] Lee JL, Lee JY, „Hydrogen trapping in AISI-4340 steel," *Metal Science,* vol. 17, pp. 426-432, 1983.

[99] Kissinger HE, „Reaction kinetics in differential thermal analysis," *Analytical Chemistry,* vol. 29, pp. 1702-1706, 1957.

[100] Zhao MC, Liu M, Atrens A, Shan YY, Yang K, „Effect of applied stress and microstructure on sulfide stress cracking resistance of pipeline steels subject to hydrogne sulfide," *Mat Sci and Eng A,* vol. 478, pp. 43-47, 2008.

CHAPTER II

Effect of hydrogen charging on the mechanical properties of advanced high strength steels*

II.1 Introduction

Hydrogen is often quoted to be the future energy carrier as it might offer an alternative for the scarce fossil fuels. However, the commercialization of hydrogen has proven to be a challenge. A significant difficulty from the steel point of view appears to be the high diffusivity of hydrogen, as this element may give rise to embrittlement in the steel components. Therefore, further investigation of the possibilities to store and transport hydrogen and of the material-hydrogen interactions is inevitable and thus required.

In hydrogen-powered vehicles, gaseous hydrogen has to be stored at a pressure up to 70 MPa to achieve sufficient gravimetric and volumetric energy density [1]. Nowadays, stable nickel-based austenitic stainless steels are commonly used for structural applications such as fittings, pipes and valve housings. Nevertheless, these materials are too expensive for automotive mass production. Aluminum alloys are feasible alternatives for valve housing, resulting in a cost and weight reduction. Unfortunately, parts such as springs, fittings and pipes, cannot be made of aluminum alloys, due to incompatible strength, wear and fatigue characteristics. Therefore, the application of steel in the automotive industry remains unavoidable [2].

In the automotive industry, one of the main goals is weight reduction while retaining the same strength and stiffness level at the lowest possible cost. Aluminum has the drawback of a lower stiffness and a higher cost compared to steels. Therefore, excellent candidates to attain these necessary requirements are high strength steels since they combine light weight and high strength. Unfortunately, high strength steels are more sensitive to hydrogen embrittlement [3]. This embrittlement has a substantial influence on the mechanical material characteristics, causing a brittle and unpredictable fracture which can have severe consequences. In order to be able to understand and predict the potential hydrogen damage, detailed research on the effect of the interaction between hydrogen and high strength steels is necessary.

Among the advanced high strength steels, Dual Phase (DP), Transformation Induced Plasticity (TRIP), Complex Phase (CP), Ferritic Bainitic (FB), High Strength Low Alloy (HSLA) and martensitic steels are the most important ones. DP steel consists of a dispersion of martensitic islands in a ferrite matrix and combines low yield strength with high tensile strength. TRIP steel possesses both superior strength and good formability as a result of the transformation of a small volume fraction of metastable retained austenite to martensite during deformation. The microstructure of CP steel consists of very fine ferrite and a higher volume fraction of hard phases which can be further strengthened by fine precipitates obtained by adding small quantities of niobium, titanium and/or vanadium. The FB steel consists of fine ferrite and bainite regions. The HSLA steel used in this

* This chapter is based on the following publication: Depover T, Pérez Escobar D, Wallaert E, Zermout Z, Verbeken K, *International Journal of Hydrogen Energy*, vol. 39, pp. 4647-4656, 2014.

research consists of a ferrite/cementite microstructure containing Ti and Nb, which makes precipitation strengthening possible. In martensitic steels, the high temperature austenite almost entirely transforms into martensite during quenching. Furthermore, these steels are often subjected to post-quench tempering to improve ductility.

Although the impact of hydrogen on high strength steel has already been confirmed by many research groups, little data are available about the interaction between hydrogen and TRIP steels, except for the early work of McCoy *et al*. [4], and the recent studies of Hilditch *et al.* [3] and Ronevich *et al.* [5]. Recently, the mechanical properties of four different high strength steels, including TRIP, have been studied by Duprez *et al.* [6]. They performed, among others, tensile tests on TRIP samples immediately after electrochemical charging and on samples that were atmospherically discharged for one week. Their results showed that the ductility loss after charging is reversible. A large part of the ductility is recovered after discharging the sample for one week. These tests prove that damage that is observed after charging is caused by the intrinsic presence of mobile hydrogen and not due to an irreversible damage mechanism caused by hydrogen charging. Other high strength steels appeared to be less sensitive to the ductility loss immediately after charging, while it was also observed that not all steels recovered their initial ductility by waiting one week in between hydrogen charging and tensile testing due to irreversible damage.

As mentioned before, TRIP steel contains metastable austenite, which transforms to martensite during deformation. The effects of a martensitic microstructure on the hydrogen content and diffusivity have been studied by a number of researchers [2] [7] [8] [9] [10] [11]. Chan *et al.* [9] found that the observed variations in hydrogen content and diffusivity did not only depend on the carbon content, but also on the different martensite morphologies and the effects of the presence of retained austenite. Sakamoto and Mantani [10] pointed out that minimum diffusivity and maximum solubility of hydrogen are obtained when the steel has an as-quenched martensitic structure, as opposed to tempered martensite. Other work of Chan *et al.* [11] shows that a higher amount of hydrogen is present in steels (especially for high carbon steels) which still contain retained austenite.

In the present study, the influence of hydrogen on the mechanical properties of four multiphase steels was investigated by performing tensile tests on in-situ charged samples. Correlations were made with previously published [12] hot extraction and thermal desorption spectroscopy measurements where possible. Some tensile tests were also performed at different cross-head deformation speeds in order to elucidate the impact of the diffusible hydrogen on the embrittlement.

II.2 Experimental procedure

In this study, the mechanical properties of four multiphase, advanced high strength steels under various conditions were investigated. These industrial materials contained different constituents, such as martensite, bainite, pearlite and retained austenite. The thickness of the TRIP steel sheets was 0.7 mm, while the FB, DP and HSLA steels had a thickness of 1.1 mm. These thicknesses were reached after hot and cold rolling, followed by subsequent annealing via industrial annealing parameters necessary to obtain the desired microstructure. Chemical compositions are summarized in Table II-1. The samples were ground using a Ziersch and Baltrusch surface grinder, rotating at 3342 rpm. After grinding, notched tensile samples were made by spark erosion, the tensile axis being parallel to the rolling direction. Finally, the surface and edges of the samples were sand blasted.

Table II-1: Chemical compositions in wt%.

Material/ Element	C	Mn	Si	Other
TRIP	0.17	1.60	0.40	1%-2% Al 0.04%-0.1% P
FB	0.07	1.00	0.10	0.5%-1.0% Cr
DP	0.07	1.50	0.25	0.4%-0.8% Cr+Mo
HSLA	0.07	0.95	0.00	0.08%-0.12% Ti+Nb

To characterize the material by the optical microscopy, it was ground, polished and etched. For the TRIP steel a 4% Picral solution was used and for the FB, DP and HSLA steel a 2% Nital solution was used as an etchant. The amount of retained austenite was quantified by XRD measurements. The retained austenite volume fraction was determined with the direct comparison method [13] using the integrated intensity of the $(200)_\alpha$, $(112)_\alpha$, $(220)_\gamma$ and $(311)_\gamma$ peaks. The carbon content was determined according to the method of Cullity [13].

In order to study the influence of hydrogen embrittlement, the tensile properties of the four alloys were measured in air (uncharged) and in hydrogen charged conditions. Each test was performed twice in order to get an indication on the reproducibility of the results: two identical test conditions will be labeled as "A" and "B". In case of charged samples, hydrogen was introduced by cathodic charging using 1 g/L of thiourea in a 0.5 M H_2SO_4 solution. The materials were charged for 2 hours at a current density of 2.65 mA/cm², these two hours of pre-charging ensured complete hydrogen saturation of the samples [6] [12] and are significantly more severe than real-life conditions, but are required to visualize the hydrogen effect on a relatively short term. After two hours of charging, the tensile test is started. In order to control crack initiation, notched tensile samples (cf. Figure II-1), which locally introduced a triaxial stress condition, were used. This geometrical discontinuity gives rise to a local stress concentration expressed by a stress concentration factor K_t of 4.2 for the used tensile sample geometry.

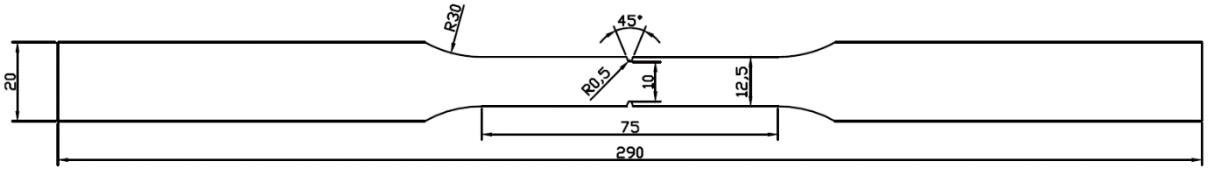

Figure II-1: Geometry of the tensile specimen.

Tensile tests were performed using two different cross-head deformation speeds; namely 5 mm/min, similar to Zhao *et al.* [14] and 0.05 mm/min. The latter was done to evaluate the possible effect of hydrogen diffusion during the slower tensile test. In order to evaluate the impact of hydrogen embrittlement on the ductility, an embrittlement index (EI) was defined as:

$$EI = \frac{\text{Elongation in Air - Elongation when Charged}}{\text{Elongation in Air}} \quad \text{(II-1)}$$

Hence, the embrittlement index can vary between 0 and 1, with 0 meaning that there is no ductility drop and the material appears to be insensitive to hydrogen embrittlement. When an index of 1 is obtained, the ductility drop is 100% and the hydrogen embrittlement is maximal.

To obtain a confirmation of the results obtained with the embrittlement index described above, another index (EI_{RA}) based on the reduction of area (RA), which was determined based on Scanning Electron Microscope (SEM) images, was used:

$$EI_{RA} = \frac{RA_{Air} - RA_{Charged}}{RA_{Air}} \quad \text{(II-2)}$$

II.3 Materials characterization

Optical microscopy allowed the identification of the different constituents present. In Figure II-2, the phases present in the materials were indicated. The TRIP steel contained ferrite, martensite, bainite and retained austenite. The amount of retained austenite, quantified by XRD, was 9.6%. The carbon content of the retained austenite was 1.2 wt%. The FB grade contained ferrite and 3.4% bainite. The DP steel consisted of ferrite and 23.6% martensite. In the HSLA steel, cementite (Fe_3C) was observed in the ferrite matrix, while although they were not visible here, this steel also contained Ti and Nb based carbonitrides.

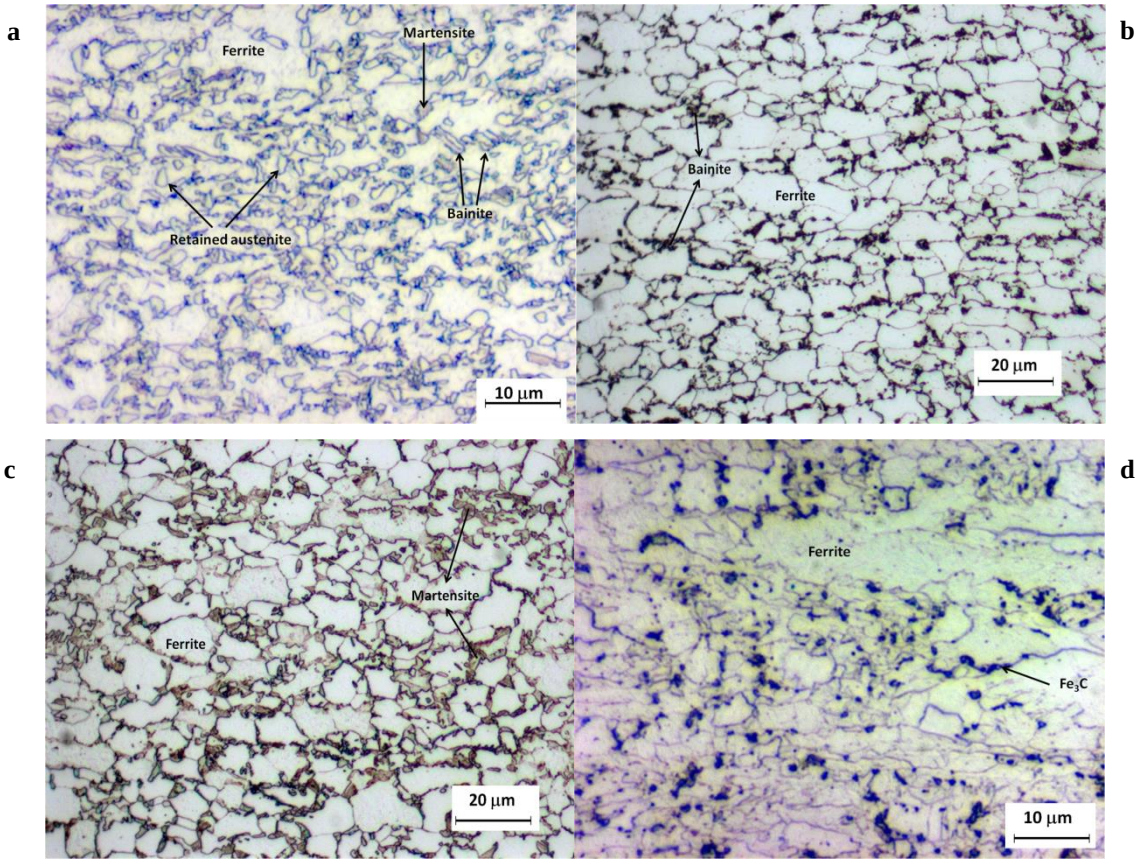

Figure II-2: Optical micrograph of the TRIP (a), FB (b), DP (c) and HSLA (d) grade.

II.4 Tensile tests at 5 mm/min

The results of the tensile test with a deformation rate of 5 mm/min performed on both charged and uncharged samples were summarized in Figure II-3 and Table II-2. The curves of the samples measured under the same conditions were nearly identical, confirming the good reproducibility of the test. The highest embrittlement index was measured for the TRIP steel, meaning that the hydrogen charging had more effect on the TRIP steel ductility in comparison to the other steel grades. The ductility of the DP steel dropped for instance 54%, while the FB steel had an embrittlement index of 37%. Interesting results were obtained for the HLSA steel. This high strength alloy containing Nb and Ti precipitates showed almost no effect of hydrogen embrittlement after charging. Although it was found that hydrogen caused for most investigated steels a considerable loss in ductility, which was not the same for every material, it should be taken into account that the charging conditions are far more severe than the real conditions in which the material will be employed.

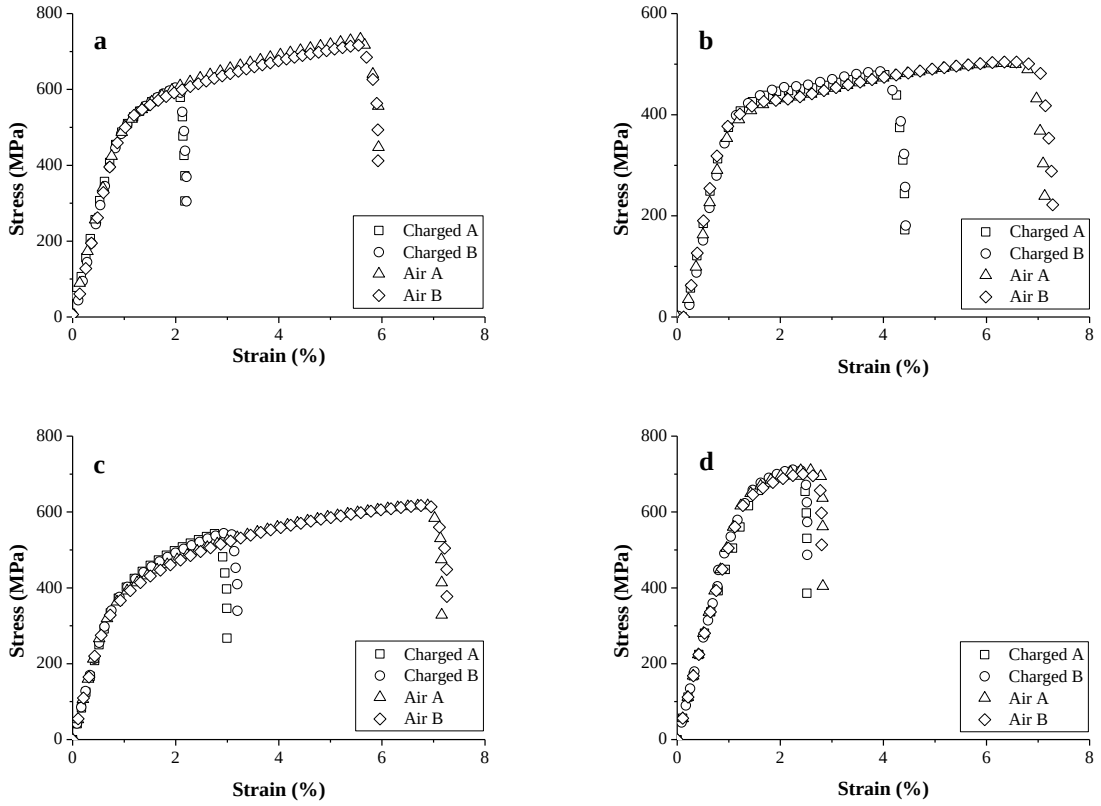

Figure II-3: Stress-strain curves for TRIP (a), FB (b), DP (c) and HSLA (d), with similar tests indicated with "A" and "B".

Table II-2: Summary of the tensile tests performed on the TRIP, FB, DP and HSLA steels at a deformation rate of 5 mm/min.

	TRIP		FB		DP		HSLA	
	In air	**After charging**	**In air**	**After charging**	**In air**	**After charging**	**In air**	**After charging**
Average maximum elongation (mm)	5.81	2.30	7.14	4.47	7.12	3.24	2.79	2.56
Average tensile strength (MPa)	726	607	503	482	608	550	705	709
Average yield strength (MPa)	438	442	360	372	313	335	611	630
Embrittlement index EI	0.60		0.37		0.54		0.08	

Several reasons might cause the larger ductility drop in the TRIP steel. At first, it must be mentioned that this steel had a higher tensile strength and the hydrogen effect is more pronounced with increasing strength of the steel, as was reported by Oriani [15], Troiano [16], Bernstein and Thompson [17] [18] and others [19] [20], and as schematically shown in Figure II-4. However, the HSLA steel clearly did not follow this trend as its tensile strength in air was similar to the one of the TRIP steel but the ductility loss for the HSLA steel was minimal. This discrepancy might be related to, on the one hand, that the elongation in air was considerably lower for the HSLA steel and, on the other hand, that the trapping capacity of the precipitates present in the HSLA might play a role as discussed in more detail below.

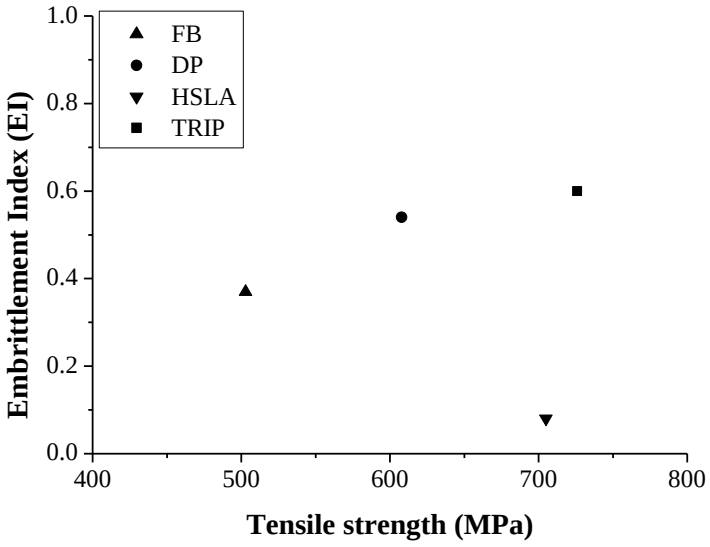

Figure II-4: Schematic of the index vs tensile strength for the FB, DP, HSLA and TRIP steel.

Secondly, as mentioned before, the strain induced transformation of the retained austenite caused martensite formation. The effect of the presence of martensite in the microstructure was also illustrated by the relatively high index for the DP steel. The similarity of the strain-stress curves between TRIP and DP steel might be

related to their microstructural features due to the transformation of retained austenite to martensite in the TRIP steel during the tensile test. The hardness of martensite, in comparison to the retained austenite, is much higher and the volume change, caused by the transformation, gave rise to plastic deformation of the surrounding ferrite, leading to a local strengthening of the grade [21] [22]. This strengthening effect retarded further deformation in this area and transferred the martensite formation to other regions in the material. This slowed down necking and gave rise to high values for the elongation. Consequently, during the tensile tests the microstructure changed and the effect of the martensitic phase became increasingly important. Moreover, this brittle martensite fraction is formed from the retained austenite which is demonstrated to contain some hydrogen [23]. Additionally, it should be taken into account that the solubility of hydrogen in a face centered cubic (FCC) crystal lattice is higher than in a body centered cubic lattice, this might affect the embrittlement effect of the TRIP steel, which contains retained austenite. Additionally it was demonstrated that the ductility loss after charging TRIP steels is reversible [6]. Alternatively, McCoy *et al.* [4] evaluated the austenite to martensite transformation in TRIP steel and its impact on hydrogen embrittlement. Their tests were conducted on cathodically charged TRIP specimens, of which some had endured plastic deformation prior to charging. In their experiment, no hydrogen induced delayed brittle failures were observed. Apparently, the strain-induced martensite was not causing any significant crack propagation. Although it should be mentioned that there is no evidence that their electrochemical charging also effectively charged the retained austenite. Our previous experiments indicated the opposite [23]. This could possibly explain why there was no effect measured.

Thirdly, another possible explanation correlates the ductility with the chemical composition. On the one hand the presence of a higher amount of carbon in the TRIP samples might play a role. They contained 0.17% of carbon in comparison to 0.07% in the other grades. Moreover, the carbon content in retained austenite was determined to be 1.2%, which implies that the strain induced martensite also contained a considerable amount of carbon which also affected the embrittlement. The carbon content also had an impact on the hydrogen saturation level of the BCC phases. Thermal desorption spectroscopy of lab cast Fe-C alloys with 0.2% and 0.4% of carbon demonstrated a higher amount of hydrogen for the 0.4% C containing material, as presented in [24]. On the other hand, TRIP steel contained a high amount of Si and some Al. Ciszewski *et al*. [25] and French *et al.* [26] demonstrated that mixed oxide inclusions, containing Si and Al, were favorable for void nucleation. As voids are considered to be excellent hydrogen traps, the high embrittlement index for TRIP steel and the chemical composition could be correlated. Other groups concluded that large MnS inclusions immediately trapped hydrogen in voids, causing weak sites in the microstructure [27]. Perez Escobar *et al.* [28] also indicated the possible detrimental effect of MnS second phase particles as well as the role of Mn segregations, when a crack was revealed near Mn segregations, as illustrated in Figure II-5. The amount of Mn in the TRIP steel is quite high, which also could have a detrimental influence on the embrittlement index.

Finally, one must also take into account that TRIP had a thickness of 0.7 mm while the others had a thickness of 1.1 mm. Since industrial processing conditions were applied on the material, this difference in thickness could not be avoided. The possible significance of the difference in thickness on variations in ductility still needs to be further elaborated.

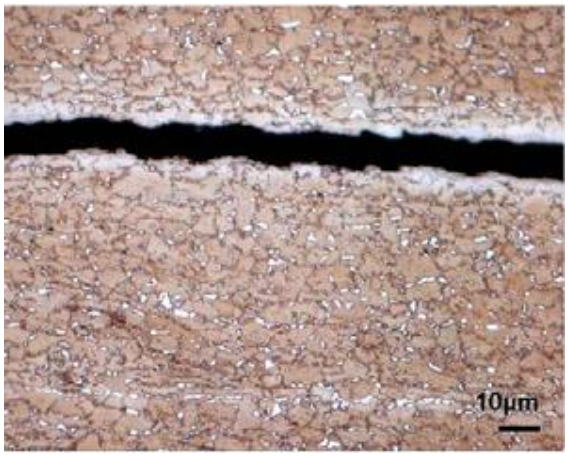

Figure II-5: Mn segregation related crack revealed by LePera etching in the TRIP steel [27].

For the FB grade, the embrittlement was lower than for the TRIP and DP steel. An important difference between this steel and the other multiphase steels was the low amount of secondary phase. All steels had a ferrite based matrix, but FB only contained 3.4% bainite, while DP had 23.6% martensite and TRIP 9.6% retained austenite additional to some martensite and about 35% of bainite. As the occurrence of multiple phases and the associated phase boundaries has an important and often detrimental effect in the presence of hydrogen, this is believed to play here a significant role as well.

Remarkable were the results for the HSLA steel grade. This micro-alloyed high strength steel with Nb and Ti precipitates showed almost no sign of hydrogen embrittlement after charging. It should also be mentioned that the elongation of the uncharged tests was significantly lower in comparison with the FB, TRIP and DP steel, leading for the latter steels to possibly higher embrittlement indices. A plausible explanation for this behavior is the presence of precipitates that act as strong hydrogen traps. Ti forms TiC, a strong, irreversible trap with high activation energy. Pressouyre and Bernstein [29] [30] determined that titanium additions greatly reduced degradation by providing strong traps for hydrogen and preventing it from reaching more damaging second phase particles sites or reaching trap site that catch hydrogen reversibly. Wei and Tsuzaki [31] demonstrated the influence of the coherence of TiC precipitates. Semi coherent and incoherent TiC precipitates showed a considerable difference in trapping capacity and in activation energy for hydrogen detrapping: 55.8 kJ/mol and 87-95 kJ/mol [31], respectively. According to these authors, the amount of hydrogen kept in incoherent particles depended on their volume which strongly indicated that hydrogen was dissolved inside these particles. However, a conclusion with absolute certainty was not possible as the interface of incoherent particles seemed to be more attractive to trap hydrogen when the particles were growing. It should be added that the precipitates were formed in the austenitic region and after phase transformation only incoherent boundaries can be obtained. Escobar *et al.* [32] observed similar behavior; the activation energy of semi-coherent TiC precipitates was lower than for incoherent particles. Pressouyre and Bernstein [33] mentioned in their work that the binding energy of TiC traps decreased with increasing degree of coherency with the matrix. Next to Ti, Nb can also form irreversible NbC [34]. As mentioned in the section on material characterization, the HSLA steel also contained Fe_3C, being a possible irreversible trap for hydrogen with an activation energy of 84 kJ/mol [35]. The precipitates of the HSLA

steel were mainly formed in the austenite region and after phase transformation only incoherent boundaries occurred.

Research done by *Escobar et al.* [12] showed that the HSLA steel gave the highest thermal desorption spectroscopy (TDS) peak at low temperature compared to TRIP, DP and FB. TDS was used to calculate the activation energy of corresponding different trapping sites by measuring the hydrogen desorption flux under controlled temperature conditions. Furthermore, these authors performed hot extraction on these materials to evaluate the hydrogen saturation time under identical charging conditions as the TDS measurements. TRIP steel contained the highest amount of hydrogen present after charging (approximately 4 wppm), while the three other industrial alloys contained a lower though similar amount of hydrogen (about 2 wppm). The main difference between both techniques was the necessity of a vacuum chamber for TDS analysis. During the required time to reach this vacuum condition, diffusible and consequently weakly trapped hydrogen was able to escape from the material. As the HSLA steel had the highest thermal desorption peak, the desorption kinetics were slower for this grade, which was related to its microstructural features such as the presence of Ti- and Nb- based precipitates, leading to higher solubility and lower effusion kinetics. TRIP steel, on the contrary, showed the lowest thermal desorption peak and the highest hydrogen saturation level and hence, this grade contained a lot of diffusible hydrogen. Moreover, Duprez *et al.* [6] showed that the HSLA steel was not that sensitive to the loss of ductility, indicating a weak effect of the diffusible or more weakly trapped hydrogen. This observation as well could be correlated with the existence of Ti- and Nb- based particles.

Apart from the approach to determine the effect of hydrogen by an index based on the reduction of elongation, another parameter EI_{RA} was used to investigate the influence of hydrogen on the material ductility based on the reduction of area. The index based on the reduction of area (Eq. II-2) was calculated from the difference in necking between the charged and uncharged sample. In Table II-3, this index was calculated for the four different materials and a good agreement between both EI and EI_{RA} was found. This similarity implies that both indices are valid to express the degree of hydrogen embrittlement. As an illustration, the difference between the reduction of area for the uncharged and charged sample was shown in Figure II-6a and II-7a. In Figure II-6a, the fracture surface of the uncharged sample showed fine dimples indicating that a ductile fracture with considerable necking occurred. A detailed image of the uncharged sample, indicating the fine dimples was shown in Figure II-6b. In Figure II-7a, the fracture surface of the charged sample was depicted. The necking was clearly smaller due to the embrittlement caused by hydrogen charging. A transition zone from brittle transgranular cleavage fracture near the edges to a more ductile zone in the centre was observed, as illustrated in Figure II-8. These observations can be correlated to the ones presented by Liu *et al*. in [36]. Additionally, they claimed that there was no influence of hydrogen up to the yield stress of the steel. A detailed image of the fracture surface of the charged sample in the center was shown in Figure II-7b, which clearly indicated the more ductile zone in the centre. Hydrogen caused a change from a ductile, microvoid coalescence failure, to a predominantly faceted, brittle transgranular cleavage failure after hydrogen charging, which is in good agreement with the results obtained in [3].

Table II-3: Summary of the indices measured with the tensile tests and SEM images.

Material	tensile test index (EI)	reduction of area index (EI_{RA})
TRIP	0.60	0.60
DP	0.54	0.52
FB	0.37	0.36
HSLA	0.08	0.12

a

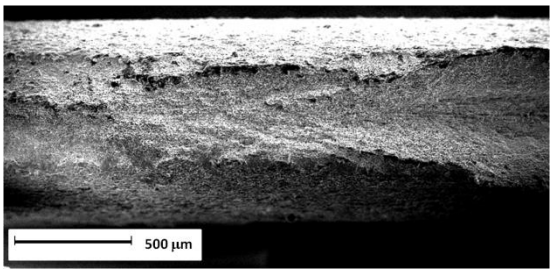

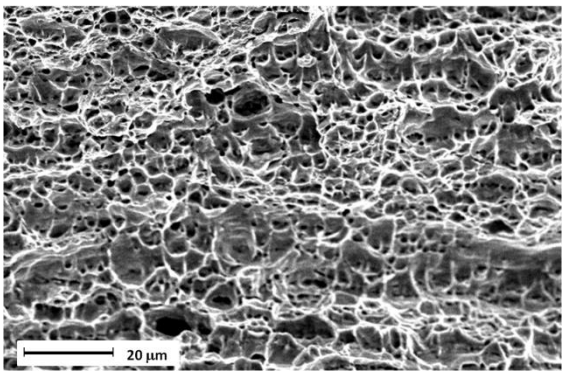

b

Figure II-6: SEM images of the DP surface fracture for the uncharged sample, (a) and (b) more in detail.

a

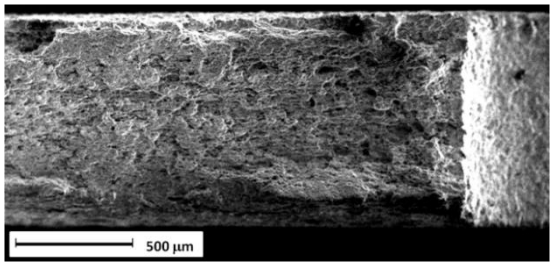

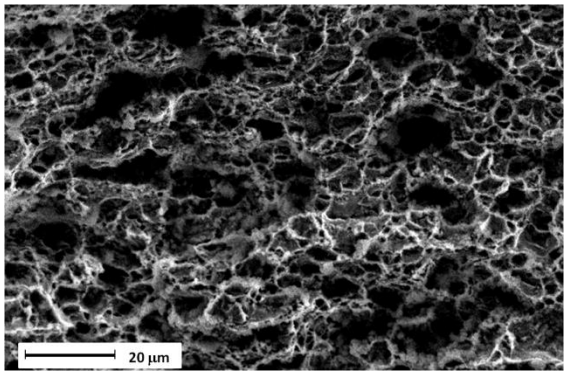

b

Figure II-7: SEM images of the DP fracture surface for the charged sample, (a) and (b) more in detail.

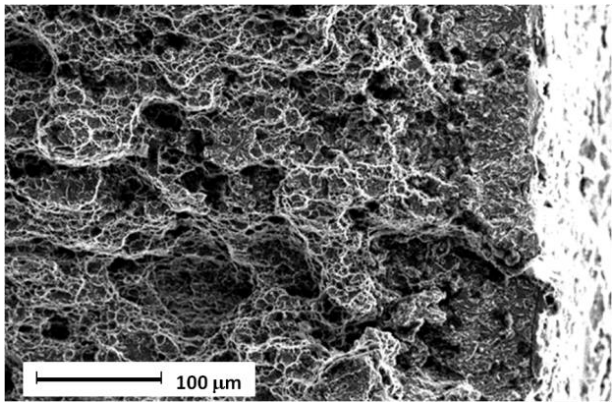

Figure II-8: SEM image of the DP surface fracture for the charged sample near the edge.

II.5 Tensile tests at 0.05 mm/min

As mentioned above, diffusible hydrogen is expected to play a major role in hydrogen embrittlement because of its interactions with dislocations, crack formation and growth. Since at the slower deformation rate diffusible hydrogen has more time to migrate towards the crack tip, this type of tests was conducted. Tensile tests were performed at a lower cross-head deformation speed of 0.05 mm/min. The influence of the deformation rate was already confirmed by Toh and Baldwin [37], who demonstrated that the RA (reduction of area) decreased with increasing deformation rate. The results of the tensile tests with a deformation rate of 0.05 mm/min were shown in Figure II-9, where just one curve of the identical tests with deformation rate of 5 mm/min is presented, and in Table II-4. Tests were performed for all steels and are compared with those obtained at 5 mm/min. Generally, the sensitivity of the elongation to the strain rate for steels is or not very high, or the lower the strain rate, the larger the elongation at fracture [38]. However, in the present case, the materials show the opposite tendency. Huh *et al.* [39] reported similar observations for TRIP and DP steels and attributed this to the fact that local strain rate hardening restrains the progress of necking and elongation propagates in the adjacent region. The strain rate at the necking region and the flow stress in the necking region exceeds the flow stress in the other region due to the high strain rate. Consequently, the necking region becomes stronger than the neighboring region despite thinning in the necking region. Peixinho *et al.* [40] and Choi *et al.* [41] also detected similar results indicating that the ductility of TRIP and DP does not decrease with increasing tensile test speed. Moreover, this phenomenon was more remarkable for TRIP steel compared to DP steel. This might be attributed to the deformation induced phase transformation, hindering the dislocation mobility.

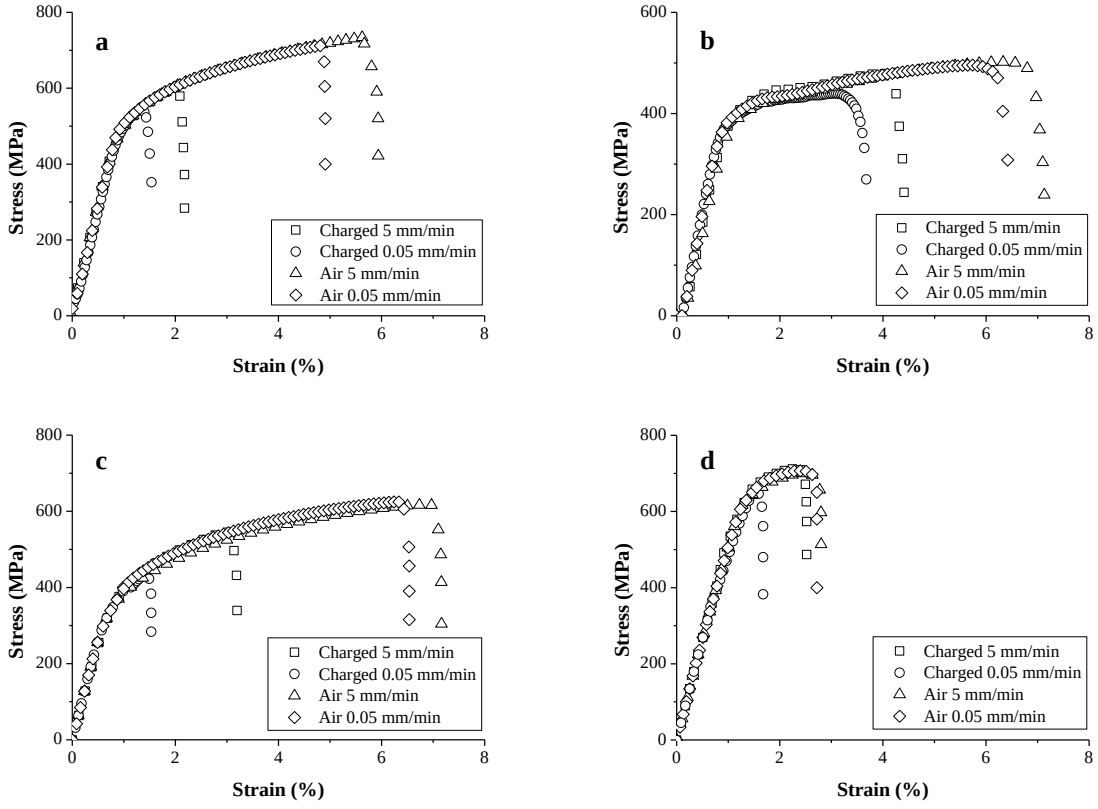

Figure II-9: Stress-strain curves for the TRIP (a), FB (b), DP (c) and HSLA (d) steel performed at deformation rate of 5 mm/min and at a lower one of 0.05 mm/min.

Table II-4: Summary of the tensile tests performed on the TRIP, FB, DP and HSLA steels at a deformation rate of 0.05 mm/min.

	TRIP		FB		DP		HSLA	
	In air	**After charging**	**In air**	**After charging**	**In air**	**After charging**	**In air**	**After charging**
Maximum elongation (mm)	4.85	1.63	6.19	3.69	6.31	1.68	2.54	1.72
Tensile strength (MPa)	713	513	496	431	625	436	707	634
Yield strength (MPa)	430	435	366	363	315	322	609	615
Embrittlement index EI	0.66		0.40		0.73		0.32	

The reproducibility of the obtained data suggested that the observed differences were significant to assume that the deformation rate had a clear effect on the hydrogen embrittlement of the steel. The results showed that the index for the low deformation rate tests was higher than the one of the high deformation rate tests. For the TRIP steel the ductility loss increased from 60% to 66%, while the change in deformation rate caused an increase in the embrittlement index for the FB grade from 37% to 40%. Remarkable results were obtained for the DP steel, where the index raised from 54% to 73% and for the HSLA steel, which was at high deformation rate almost unaffected by hydrogen charging (8%), while at lower deformation rate a clear ductility loss was observed (32%).

In the previous section, the differences in embrittlement for both steels at 5 mm/min ($EI_{\mathrm{TRIP}} > EI_{\mathrm{DP}}$) were discussed based on the lower strength and the lower Si, Mn or C content for the DP grade in comparison with the TRIP steel. The present data indicated that the DP steel was more susceptible to hydrogen embrittlement than TRIP at 0.05 mm/min ($EI_{\mathrm{DP}} > EI_{\mathrm{TRIP}}$). Clearly, the deformation rate affected the sensitivity to hydrogen embrittlement for each type of steel differently. Hilditch *et al.* [3] gave a possible explanation for this phenomenon. Since they traced fracture initiation at the martensite-ferrite interfaces, it can be assumed that hydrogen preferentially migrates to such interfaces during charging. The martensite fraction of about 23% in DP steel tends to form larger "islands" while in TRIP steel the martensite regions are much smaller in size and less in amount (5%). Moreover, martensite in TRIP steel is mostly embedded in the 9.6% retained austenite present. Therefore, TRIP steel contains a significantly lower fraction of martensite-ferrite interfaces than DP steel. Consequently, the mechanism proposed by Hilditch *et al.* [3] can assist hydrogen cracking in DP steel and apparently, this mechanism gained importance at lower cross-head deformation speed, where diffusible hydrogen is enabled to diffuse to critical highly stressed regions during the tensile test. Therefore, it could be concluded that at 0.05 mm/min, the effect of hydrogen located at the interface of martensite with ferrite dominated the embrittling behavior ($EI_{\mathrm{DP}} > EI_{\mathrm{TRIP}}$). Additionally, the diffusivity of hydrogen through DP steel was higher compared to TRIP steel due to the presence of retained austenite in the latter steel. Escobar *et al.* [23] calculated the diffusion coefficient for TRIP steel, which was about 3.9 x 10^{-7} cm^2/s, while for a similar DP steel a diffusion coefficient about 7.46 x 10^{-7} cm^2/s was obtained [42]. The distance *x* (cm) hydrogen can diffuse at a

cross-head deformation speed of 0.05 mm/min, can be calculated by taken the square root of the product of the diffusion coefficient D (cm^2/s) and the time t (s) of the test, i.e. $x = (D \times t)^{1/2}$. The distances hydrogen can diffuse at 0.05 mm/min were about 0.25 mm and 0.35 mm for respectively TRIP and DP steel, which showed the increased importance of diffusible hydrogen at lower cross-head deformation speed for DP steel compared to TRIP steel and consequently might account for the higher embrittlement index for DP at 0.05 mm/min.
Moreover, Duprez *et al.* [6] already emphasized the importance of the diffusible hydrogen for DP and TRIP steel by evaluating the ductility loss immediately after charging and testing after one week. A complete recovery in terms of ductility was observed for these materials after one week.

The FB grade showed little effect on the change of deformation rate, this could be attributed to the lower amount of diffusible hydrogen and hence lower impact on the variation of the deformation rate [6] [12]. The HSLA steel was no longer unaffected by hydrogen charging. This could be explained by the fact that diffusible hydrogen can diffuse to the crack tip during the tensile test. Another possibility is that the irreversibly trapped hydrogen in the precipitates was released due to the external applied strain during the tensile test. This released hydrogen will diffuse, causing an enhanced hydrogen embrittlement.

II.6 Conclusion

Tensile tests with in-situ hydrogen charging were performed on four high strength steels. The experiments showed a considerable ductility loss of these materials due to hydrogen pick-up, although the degree of embrittlement varied considerably between the grades. The tests at a cross-head deformation speed of 5 mm/min showed that TRIP steel was most prone to hydrogen embrittlement (EI of 60%), followed by DP, FB and finally the HSLA grade (EI of 8%), which was almost unaffected by the hydrogen charging. The correlation between the strength of the material and the degree of hydrogen embrittlement was confirmed, except for the HSLA steel where additional effects, concerning the presence of carbides, played a crucial role.
The established index based on the elongation was in good agreement with the one based on the reduction of area. The fracture surface of the uncharged samples showed a considerable ductile necking zone, while the hydrogen charged samples showed a brittle transgranular cleavage failure near the edges, with transition zone to some ductile features in the centre.
Tensile tests performed at a lower cross-head deformation speed of 0.05 mm/min allowed to evaluate the impact of cross-head deformation speed and consequently the effect of diffusible hydrogen on the mechanical properties. It was demonstrated that the additional ductility loss could be attributed to the role played by diffusible hydrogen, which was most noticed for the DP steel (EI from 54 to 73%), as this material contains hydrogen susceptible regions at the martensitic/ferrite highly stressed interfaces, where hydrogen can diffuse to. TRIP steel was less dependent on the variation of cross-head deformation speed (EI from 60 to 66%), which was attributed to the lower diffusion coefficient.

II.7 References

[1] Helmolt RV, Eberle U, „Fuel cell vehicles: Status 2007," *J Power Sources*, vol.165, pp. 833-843, 2007.

[2] Michler T, Naumann J. „Microstructural aspects upon hydrogen environment embrittlement of various bcc steels," *Int Journal of Hydrogen Energy*, vol. 35, pp.821-832, 2010.

[3] Hilditch TB, Lee S-B, Speer JG, Matlock DK, „Response to hydrogen charging in high strength automotive sheet steel products," *SAE Technical Paper* 2003-01-0525, 2003, http://dx.doi.org/10.4271/2003-01-0525.

[4] McCoy RA, Gerberich WW, Zackay VF, „On the resistance of TRIP steel to hydrogen embrittlement," *Met Trans*, vol. 1, pp. 2031-2034, 1970.

[5] Ronevich JA, Speer JG, Matlock DK, „Hydrogen embrittlement of commercially produced advanced high strength steels," *SAE Int J Mater Manuf*, vol. 3, pp. 255-267, 2010.

[6] Duprez L, Verbeken K, Verhaege M, „Effect of hydrogen on the mechanical properties of multiphase high strength steels," in *Proc. of the 2008 Int. Hydrogen Conf.*, Jackson, Wyoming, USA, 2008.

[7] Marder AR, Benscoter AO, „Microcracking in Fe-C acicular martensite," *Trans ASM*, vol.61, pp. 293-299, 1968.

[8] Robert CS. „Effect of carbon on the volume fractions and lattice parameters of retained austenite and martensite," *TMS-AIME*, vol. 197, pp. 203-210, 1953.

[9] Chan SLI, Lee HL, Yang JR. „Effect of retained austenite on the hydrogen content and effective diffusivity of martensitic structure," In: *Proceedings 4th International Conference on the effect of hydrogen on the behavior of materials*; 1990, pp. 145-155.

[10] Sakamoto Y, Mantani T „Effect of quenching and tempering on diffusion of hydrogen in carbon steel," *Trans JIM*, vol.17, pp. 734-748, 1976.

[11] Chan SLI, Lee HL, Yang JR, „Effect of retained austenite on the hydrogen content and effective diffusivity of martensitic structure," *Met Trans A*, vol. 22A, pp. 2579-2586, 1991.

[12] Pérez Escobar D, Verbeken K, Duprez L, Verhaege M, „Evaluation of hydrogen trapping in high strength steels by thermal desorption spectroscopy," *Mat Sci and Eng A*, vol.551, pp. 55-58, 2012.

[13] Cullity BD , Stock SR, Elements of X-ray Diffraction, New York: Prentice Hall, 2001.

[14] Zhao M-C, Liu M, Atrens A, Shan Y-Y, Yang K, „Effect of applied stress and microstructure on sulfide stress cracking resistance of pipeline steels subject to hydrogen sulfide," *Mat Sci and Eng A*, vol. 478, pp. 43-47, 2008.

[15] Oriani RA, „Hydrogen embrittlement of steels," *Ann Rev Mater Sci*, vol. 8, pp. 327-357, 1978.

[16] Troiano AR, „Hydrogen embrittlement of high strength FCC alloys," In: *Hydrogen in Metals*, ASM, Metals Park, OH, 1974, pp. 3-16.

[17] Bernstein IM, Thompson AW, „Behavior of metals," *Trans ASM*, vol. 52, pp. 54-80, 1960.

[18] Thompson AW, Bernstein IM, Effect of hydrogen on behavior of materials, New York: TMS-AIME; 1976.

[19] Matsuoka S, Homma N, Tanak H, Fukushima Y, Murakim Y, „Effect of hydrogen on the tensile properties of 900 MPa-class JIS-SCM435 low-alloy steel for use in storage cylinder of hydrogen station," *J Jpn Inst Metals* vol. 70, pp. 1002-1011, 2006.

[20] San Marchi C, Somerday BP, „Effects of high-pressure gaseous hydrogen on structural metals," *Journal of Materials and Manufacturing*, vol. 116, pp. 94-110, 2007.

[21] Jacques PJ, Furnémont Q, Lani F, Pardoen T, Delannay F, „Multiscale mechanics of TRIP-assisted multiphase steels: I. Characterization and mechanical testing," *Acta Mat*, vol. 55, pp. 3681-3693, 2007.

[22] Lani F, Furnémont Q, Van Rompaey T, Delannay F, Jacques PJ, Pardoen T, „Multiscale mechanics of TRIP-assisted multiphase steels: II. Micromechanical modelling," *Acta Mat*, vol. 55, pp. 3695-3705, 2007.

[23] Pérez Escobar D, Depover T, Duprez L, Verbeken K, Verhaege M, „Combined thermal desorption spectroscopy, differential scanning calorimetry, scanning electron microscopy and X-ray diffraction study of hydrogen trapping in cold deformed TRIP steel," *Acta Mat*, vol. 60, pp. 2593-2605, 2012.

[24] Pérez Escobar D, Depover T, Wallaert E, Verbeken K, Duprez L, Verhaege M, „Thermal desorption spectroscopy study of the interaction between hydrogen and different microstructural constituents in lab cast Fe-C alloys," *Corrosion Science*, vol. 65, pp. 199-208, 2012.

[25] Ciszewsku A, Radowski T, Smialowski M, Stress corrosion cracking and hydrogen embrittlement of iron bas alloys, Houston, TX: NACE-5. 1977.

[26] French IE, Weinrich PF, Weaver CW, „Tensile fracture of free machining brass as a function of hydrostatic pressure", *Acta Met*, vol.21, pp. 1045-1049, 1973.

[27] Goldenberg T, Mee TD, Hirth JP, „Ductile fracture of U-notched bend specimens of spheroidized AISI 1095 steel," *Met Trans A*, vol. 9A, pp. 1663-1671, 1978.

[28] Pérez Escobar D, Miñambres C, Duprez L, Verbeken K, Verhaege M, „Internal and surface damage of multiphase steels and pure iron after electrochemical hydrogen charging," *Corrosion Science*, vol.53, pp. 3166-3176, 2011.

[29] Pressouyre GM, Bernstein IM, „A kinetic trapping model for hydrogen induced cracking," *Acta Met*, vol. 27, pp. 89-100, 1979.

[30] Pressouyre GM, Role of trapping on hydrogen transport and embrittlement (PhD Thesis), Carnegie-Mellon University, Pittsburgh, PA, 1977.

[31] Wei FG, Tsuzaki K, „Quantitative analysis on hydrogen trapping of TiC particles in steel," *Met Mat Trans A*, vol. 37A, pp.331-353, 2006.

[32] Pérez Escobar D, Wallaert E, Duprez L, Atrens A, Verbeken K, „Thermal desorption spectroscopy study of experimental Ti/S containing steels," *Met Mater Int*, vol.19(4), pp. 741-748, 2013.

[33] Pressouyre GM, Bernstein IM, *Metall Trans A*, vol. 9, pp. 1571-1579, 1978.

[34] Wallaert E, Depover T, Arafin M, Verbeken K, „Thermal desorption spectroscopy of NbC and NbN precipitates" *Met Mat Trans A*, vol.45A, pp. 2412-2420, 2014.

[35] Gibala R, De Miglio DS, Hydrogen effects in metals, TMS Warrendale, 1981.

[36] Liu Q, Irwanto B, Atrens A, „The influence of hydrogen on 3.5 NiCrMoV steel studied using the linearly increasing stress test," *Corrosion Science*, vol. 67, pp. 193-203, 2013.

[37] Toh T, Baldwin WM, „Stress corrosion cracking and embrittlement," In: *Stress Corrosion Cracking and Embrittlement*. New York : Wiley; 1956, pp. 176-186.

[38] Dieter GE, Mechanical Metallurgy, McGraw-Hill Book Company, New York, 1961.

[39] Huh H, Kim, S-B, Song J-H, Lim J-H, „Dynamic tensile characteristics of TRIP-type and DP-type steel sheets for an auto-body," *International Journal of Mechanical Sciecens,* vol. 50, pp. 918-931, 2008.

[40] Peixinho N, Pinho A, „Dynamic material properties of dual-phase and TRIP steels and constitutive equation," In: *Proceedings of Eurodyn;* 2005, pp. 1767-1771.

[41] Choi ID, Son DM, Kim SJ, Matlock DK, Speer JG, „Strain rate effects on mechanical stability of restrained austenite in TRIP sheet seels," *SAE Technical Paper*, 2006-01-1434, 2006.
[42] Hadzipasic AB, Malina J, Malina M, „The influence of microstructure on hydrogen diffusion and embrittlement of multiphase fine-grained steels with increased plasticity and strength," *Chem Biochem Eng Q*, vol. 25(2), pp. 159-169, 2011.

CHAPTER III

Fractographic analysis of the role of hydrogen diffusion on the hydrogen embrittlement susceptibility of DP steel*

III.1 Introduction

Hydrogen is often quoted as a potential energy carrier and as an alternative for the finite fossil fuels. Combustion of hydrogen leads to H_2O, while fossil fuels produce CO_2, having a detrimental effect in terms of global warming. So far, commercializing has proven to be a challenge, since transport and storage of hydrogen is risky as hydrogen leads to an embrittlement of the metal resulting in an unpredictable failure. A significant difficulty from the steel substrate point of view appears to be the high diffusivity of hydrogen. The possible consequences of such an unpredictable fracture may certainly be dramatic. Therefore, further investigation of the hydrogen-material interactions is inevitable and thus vital.

A second important aspect is the desire of the automotive industry to lower weight together with an increase in strength and stiffness level (safety issues) at the lowest possible cost, in order to minimalize fuel consumption and meet the stringent CO_2-emission regulations. Aluminum has the drawback of a lower stiffness and a higher cost in comparison to steels. Therefore, excellent candidates to fulfill the requirements still remain the high strength steels since they combine a high strength level with lower weight, but unfortunately they are more prone to hydrogen embrittlement (HE) [1] [2]. The abovementioned ductility loss is considered as the main consequence of the presence of hydrogen in a material. BMW therefore even doubts the use of high-strength materials for automotive applications [3]. They point out that steels with a tensile strength higher than 1000 MPa, for instance Dual Phase (DP), Complex Phase (CP), martensitic phase and Tranformation Induced Plasticity (TRIP) steels, may fail due to hydrogen embrittlement under certain conditions which hinders the use of the highest strength steels for body-in-white applications.

Among the advanced high strength steels, DP, TRIP, CP, Ferritic Bainitic (FB), High Strength Low Alloy (HSLA) and martensitic steels are the main ones. The present authors already evaluated the hydrogen induced ductility loss of these steels in a previous study (cf. Chapter II) where the embrittlement index (EI) was defined as:

$$EI = \frac{\text{Elongation in Air - Elongation when Charged}}{\text{Elongation in Air}} \quad \text{(III-1)}$$

Hence, EI can vary between 0 and 1, with 0 indicating no ductility drop and the material appears to be insensitive to hydrogen embrittlement. When an index of 1 is obtained, the ductility drop is 100% and the hydrogen embrittlement is maximal.

* This chapter is based on the following publication: Depover T, Wallaert E, Verbeken K, *Materials Science and Engineering A*, vol. 649, pp. 201-208, 2016.

The HSLA steel gave the lowest ductility loss due to cathodic hydrogen pre-charging with an embrittlement index of about 8%, which was correlated with the presence of carbides, whereas DP steel embrittled with 54%, TRIP 60% and FB 37%. Additionally, the mechanical properties of these four different high strength steels have also been studied by Duprez *et al.* [4]. They performed, among others, tensile tests immediately after electrochemical charging and on samples that were atmospherically discharged for one week. Their results on TRIP and DP steel showed that the ductility loss after charging is reversible. A large part of the ductility is recovered after discharging the sample for one week, whereas the difference between immediate and after one week testing was limited for FB and HSLA. These observations nicely correlate with the findings presented by Escobar *et al.* [5], where a thermal desorption spectroscopy (TDS) study was performed on the same four high strength steels. These authors applied different times in vacuum before the TDS measurement started and observed that hydrogen present in the TRIP and DP steel was mainly diffusible, leaving the material easily during discharging, whereas the opposite observations and conclusions could be made for FB and HSLA.
Straightforward conclusions are difficult to draw from the results of the multiphase steels since all the present microstructural phases behave differently in contact with hydrogen. Single-phase lab cast materials were produced and studied by the present authors as well [6]. A martensitic, bainitic and pearlitic structure was introduced in a 0.2% C grade and all three materials showed a different response to the presence of hydrogen. The combined effect of both the amount of diffusible hydrogen and the hydrogen diffusivity in a certain microstructure was set responsible to explain the varying hydrogen embrittlement susceptibility. The crucial role of diffusible hydrogen in terms of degradation in the mechanical properties is widely studied in many scientific works [7] [8].

Dual phase steels in particular have been developed with appropriate properties for automotive applications. This material offers an excellent strength/ductility combination and work hardening features when compared to conventional high strength steels of comparable tensile strength. The typical characteristics of DP steel are determined by thermo-mechanical processing and the volume fraction of austenite islands that transform into martensite. The strength level is primarily dependent on the volume fraction and hardness of the martensite in the dual phase structure [9] [10]. This microstructure is of fundamental importance for its mechanical properties. Avramovic-Cingara *et al.* [11] focused on the effect of the martensite distribution in DP600 dual phase steels and concluded that DP steels with a uniform distribution of martensite exhibited a slower rate of damage growth in non-hydrogen charged conditions, whereas center-lined martensite formation showed accelerated void growth with hence detrimental consequences. However, the high mechanical contrast between both phases introduces certain risks, especially in the presence of hydrogen as showed by Davies [12] and in Chapter II of this work.

Due to the industrial applications, and because of its complex microstructural characteristics [13], DP steel has been subject of several scientific studies to elucidate its particular interaction with hydrogen. Gu *et al.* [14] studied the delayed fracture properties of a hydrogen charged 1500 MPa bainite/martensite DP high strength steel and demonstrated that its crack growth rate is less than that of conventional quenched and tempered high strength steels. They attributed this to the fine dual phase microstructure and the lath boundaries which may act as beneficial hydrogen traps, slowing down segregation and diffusion of hydrogen to the crack tip. However, according to Sun *et al.* [15], the relative high susceptibility of dual phase steels to hydrogen embrittlement may

be attributed to sub-structural changes, since cracks initiated along the interface and lath boundaries if hydrogen charging was applied. Recently, Koyama *et al.* [16] investigated the micro-cracking behavior in martensite-ferrite DP steels in the presence of hydrogen. They clearly observed that hydrogen influenced considerably the damage evolution process. Basically, they attributed both the hydrogen-enhanced decohesion (HEDE) and hydrogen-enhanced localized plasticity (HELP) mechanisms to contribute the damage evolution in DP steels leading to an unpredictable hydrogen embrittlement failure. Moreover, similar studies have been performed on TRIP steels as well. Laureys *et al.* [17] showed that crack initiation started in the freshly formed martensitic phase for TRIP steels and McCoy *et al.* [18] found that cracks followed along paths of the martensite plates of this material.

The associated hydrogen related behavior has not been fully understood, but the role of diffusible hydrogen can be expected to be of crucial importance for these high strength steels. The aim of this work is to get a better understanding on the role of diffusible hydrogen in a specific dual phase steel grade. The influence of diffusible hydrogen on the DP600 steel was investigated by putting specific variations in the experimental variables of the performed mechanical tests. A clear link between the diffusion distance of hydrogen during the tensile tests and an in-depth fractography study was performed and correlations with new and previously published [2] [4] [5] [19] hot extraction and thermal desorption spectroscopy measurements on the same material were made as well.

III.2 Experimental procedure

In this study, the hydrogen related ductility loss of a DP steel was investigated. The DP steel had a thickness of 1.1 mm. This thickness was reached after hot and cold rolling, followed by subsequent annealing via industrial annealing parameters necessary to obtain the desired microstructure. The chemical composition is summarized in Table III-1. The samples were ground using a Ziersch and Baltrusch surface grinder, rotating at 3342 rpm. After grinding, tensile samples were machined, the tensile axis being parallel to the rolling direction. In order to control crack initiation, these tensile samples were notched, which locally introduced a triaxial stress condition. This geometrical discontinuity gives rise to a local stress concentration expressed by a stress concentration factor K_t of 4.2 for the used tensile sample geometry (cf. Chapter II, Figure II-1). Finally, the surface and edges of the samples were sand blasted with the sample reaching a final thickness of about 1 mm.

Table III-1: Chemical composition in wt%.

Material/ Element	C	Mn	Si	Other
DP	0.07	1.50	0.25	0.4%-0.8% Cr+Mo

In order to characterize the material by optical microscopy, it was ground, polished and etched. A 2% Nital solution was used as an etchant and samples were immediately cleaned with methanol and acetone.

To study the hydrogen saturation of the DP steel, hot/melt extraction was used to determine the diffusible and total amount of hydrogen as a function of the electrochemical pre-charging time. Hydrogen was introduced, without internal damage [19], by cathodic charging using 1 g/L of thiourea in a 0.5 M H_2SO_4 solution at a current density of 0.8 mA/cm^2. The system comprises a pulse furnace in which a pre-weighted sample is heated up to 1600°C for melt and 300°C for hot extraction, which is equal to the definition of diffusible hydrogen

proposed by Akiyama *et al.* [20] [21]. The metallic sample releases its hydrogen as gaseous H_2, and the latter is taken up by a nitrogen flow and the mixture (N_2-H_2) is sent to a thermal conductivity measuring cell. The thermal conductivity of the mixture depends on the H_2 concentration because of the significant difference in conductivity between H_2 and N_2. The software calculates the hydrogen concentration of the sample based on the thermal conductivity variation.

The hydrogen induced ductility loss was studied by performing tensile tests in air (uncharged), on hydrogen saturated and for partially charged samples while using the abovementioned charging parameters. Each test was performed twice in order to check its reproducibility and a good reproducibility was found. The impact of hydrogen was quantified by the embrittlement index as defined in Eq. (III-1).

First of all, HE was studied by tensile tests performed at a cross-head deformation speed of 5 mm/min, similar to Zhao *et al.* [22]. These tests were performed on both hydrogen saturated and partially charged samples. It must be mentioned that during the actual tensile test charging continued, which was done to avoid hydrogen loss into the environment during the actual test. The observations were correlated with those obtained by the hot/melt extraction.

In a next step, the influence of the cross-head deformation speed was evaluated for two different experimental charging procedures. On the one hand, tests were performed on hydrogen saturated samples with continued in-situ charging during the test, using three different cross-head deformation speeds; namely 5 mm/min, 0.5 mm/min and 0.05 mm/min. The latter was done to evaluate the possible effect of hydrogen diffusion during the slower tensile test. On the other hand, tensile tests were also executed on in-situ hydrogen charged samples that were not pre-charged. Here, charging started at the same moment as the tensile test started in order to evaluate the effect of the hydrogen diffusion distance into the sample from the edges during the tensile test which could be varied by varying the cross-head deformation speed.

III.3 Materials characterization

Optical microscopy allowed the identification of the different constituents present. In Figure III-1, the phases present in the materials were indicated. The DP steel is a ferritic-martensitic dual phase steel with approximately 23% of martensite and a grain size of about 7 μm for the ferritic phase and about 2 μm for the martensitic phase.

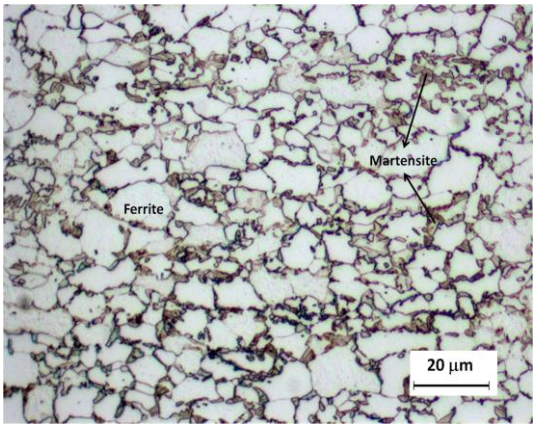

Figure III-1: Optical microscopic image of DP600 steel.

III.4 The effect of hydrogen level on the hydrogen embrittlement susceptibility

At first, the time needed to saturate this dual phase steel was determined by charging and subsequent hot/melt extraction. Secondly, the effect of the initial hydrogen content was evaluated by tensile tests performed after different pre-charging times. The evolution in the amount of hydrogen is presented in Figure III-2 and a total hydrogen saturation level of about 6.3 wppm was obtained after two hours of hydrogen pre-charging, which appeared to be the time needed for saturation. At saturation, 2.3 wppm was diffusible hydrogen. These results were in good agreement to the ones obtained by Pérez Escobar [5]. Figure III-3 presents the tensile test results for different hydrogen pre-charging times at a cross-head deformation speed of 5 mm/min. This fast speed minimized hydrogen diffusion during the tensile test. The embrittlement indices of each test are presented in Table III-2. As a general trend, the embrittlement raises with hydrogen pre-charging time before saturation, which can be linked with a higher amount of hydrogen introduced during cathodic charging.

A similar EI of about 50% was obtained for the tests performed with a pre-charging time of two and three hours, meaning that maximal ductility loss is reached after two hours of cathodic hydrogen pre-charging. No additional embrittlement was observed when charged one extra hour, indicating that the hydrogen effect is the largest for the hydrogen saturated samples. This EI value is also in good agreement with previously published results by the present authors [2] [5] (cf. Chapter II). Moreover, Escobar *et al.* [19] demonstrated that no internal damage or blisters were present for this combination of current density and charging time. The identical results after two and three hours of charging confirm this hypothesis.

Remarkable is the relative high EI of the non-pre-charged sample. Even without hydrogen pre-charging a ductility loss of about 22% was achieved due to in-situ charging during the tensile test. Hydrogen diffusion during the tensile test, despite its limited duration of about one minute, clearly had a significant impact on the obtained result for non-hydrogen-saturated samples. This striking observation will be elaborated in detail in a next section of this paper.

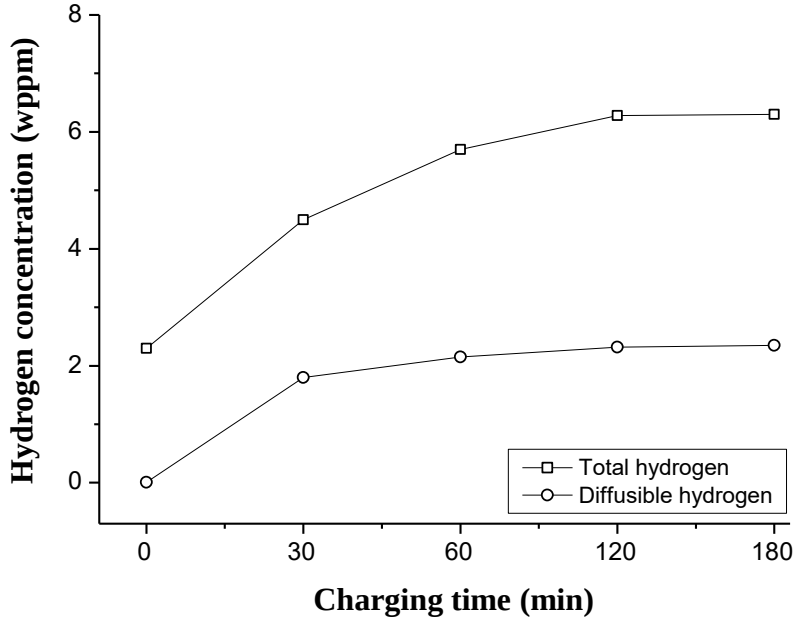

Figure III-2: Hot/melt exaction results of DP steel with variable hydrogen pre-charging times.

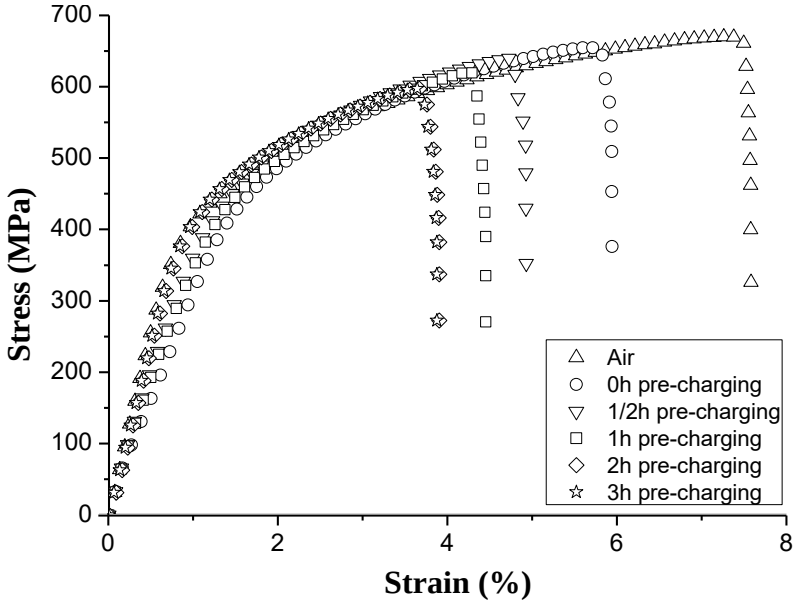

Figure III-3: Stress-strain curves for DP steel with varying hydrogen pre-charging times, with ongoing in-situ hydrogen charging during the tensile test.

Table III-2: Overview of the EI for DP steel with different hydrogen pre-charging times, with ongoing in-situ hydrogen charging during the tensile test.

Pre-charging time	Average maximum elongation (%)	Embrittlement index EI
0h	5.95	22%
1/2h	4.92	35%
1h	4.45	41%
2h	3.91	49%
3h	3.88	49%

III.5 Effect of cross-head deformation speed

Since the role of diffusible hydrogen is of crucial importance in order to understand the hydrogen embrittlement phenomenon [6], an in-depth study on the effect of cross-head deformation speed was performed as this parameter determines the duration of the tensile test and as such the time hydrogen can diffuse during the test. The influence of the deformation rate was already indicated by Toh and Baldwin [23], who demonstrated that the RA (reduction of area) decreased with increasing deformation rate and by the present authors on multiphase high strength steels (cf. Chapter II) and lab cast single-phase Fe-C alloys (cf. Chapter IV).

At first, these tests were done on samples which were pre-charged till saturation, i.e. two hours, while charging continued in-situ during the tensile test. Secondly, tensile tests were also executed on non-pre-charged samples again with in-situ charging during the test. This allowed evaluating the role of the actual diffusion distance of hydrogen into the sample during a tensile test. As mentioned above, tensile tests were performed at three different cross-head deformation speeds, i.e. at 5 mm/min, 0.5 mm/min and 0.05 mm/min.

Figure III-4 represents the stress-strain curves of hydrogen pre-charged and non-pre-charged DP steel at different cross-head deformation speeds. The uncharged tests in air gave similar ductile behavior for the different tensile

test speeds, whereas a clear effect of the variation in cross-head deformation speed could be observed for both pre-charged and non-pre-charged specimens. The embrittlement index results are summarized in Table III-3.

For the hydrogen pre-charged samples, the EI of the different tests increases with lower cross-head deformation speeds, from 49% for the highest rate, to 69% and finally even to 79% for the test at 0.05 mm/min. A possible correlation was investigated with the distance hydrogen can diffuse during the tensile test when stress is applied. During the test, mobile hydrogen can diffuse to highly stressed regions ahead of the crack tip, hence facilitating crack propagation. Even reversibly trapped hydrogen can escape and become mobile when stress is applied, whereas newly generated trapping sites are created by the microstructural defects caused by the tensile stress as reported by Kim *et al.* [24]. They reported that a high level of stress can be concentrated at the tip of an inclusion or precipitate. Consequently, a triaxial stress field can be generated where hydrogen will preferentially diffuse to. At lower cross-head deformation rates, hydrogen has the time to do so. The findings of Laureys *et al.* [17], Otsuka *et al.* [25] and Yamada *et al.* [26] support these conclusions.
The diffusion coefficient for a similar DP steel was about 7.46×10^{-7} cm^2/s, as obtained in [27]. The hydrogen distance x (cm) at different cross-head deformation speeds can be calculated by taking the square root of the product of the diffusion coefficient D (cm^2/s) and the test time t (s), i.e. $x = (D \times t)^{1/2}$. The distances hydrogen can diffuse at 5, 0.5 and 0.05 mm/min were about 53 μm, 145 μm and 390 μm, respectively, which confirms the increased importance of hydrogen diffusion at lower deformation speeds.

For the non-pre-charged samples, a clear effect of the cross-head deformation speed could be detected as well. Again, the EI of the different tests increases with lower cross-head deformation speeds, from 22% for the highest tensile test speed, to 55% and finally even to 76% for the test at 0.05 mm/min. Remarkable was the 76% ductility loss for the slowest tensile test without pre-charging, which was almost similar to the 79% HE of the two hours pre-charged sample. Both tests took approximately half an hour while in-situ charging was applied. According to the hot extraction results (Figure III-2) on the amount of diffusible hydrogen, the saturation level of diffusible hydrogen is almost reached when charged for half an hour, which emphasizes the crucial role of this diffusible hydrogen during a low cross-head deformation speed tensile test. The increase in EI could again be correlated with the distance hydrogen can diffuse to during the tensile test, as shown in Table III-3. The results presented so far suggest a correlation between the EI and the hydrogen diffusion distance during the tensile test. It could be expected that this correlation could be possibly visualized by a detailed investigation of the fracture surfaces of the non-pre-charged specimens. This investigation is therefore presented in the next section.

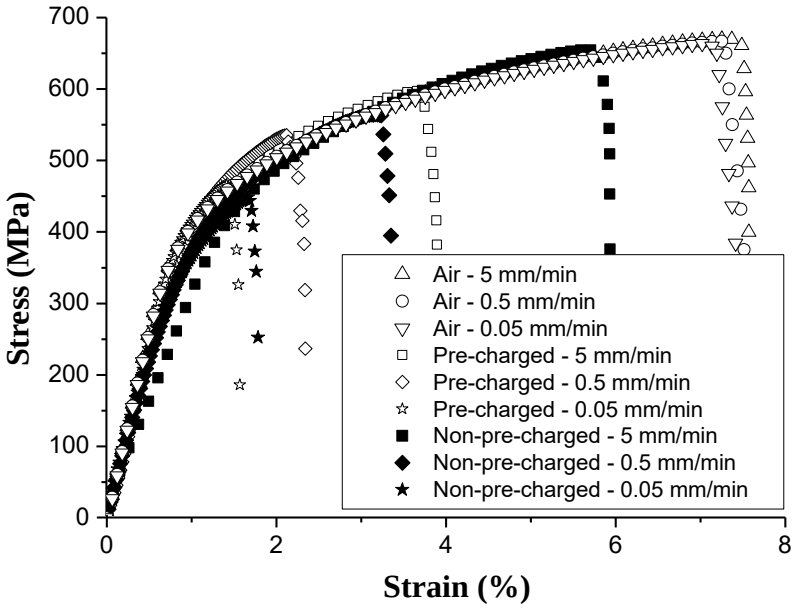

Figure III-4: Stress-strain curves of hydrogen pre- and non-pre-charged DP steel at varying cross-head deformation speeds.

Table III-3: Hydrogen embrittlement summary together with the distance *x* hydrogen can diffuse during a tensile test of hydrogen pre-charged (2 hours) and non-pre-charged DP steel at different cross-head deformation speeds.

Cross-head deformation speed	Diffusion distance *x* (μm)		Embrittlement index EI	
	Pre - charged	Non-pre-charged	Pre-charged	Non-pre-charged
5 mm/min	53	65	49%	22%
0.5 mm/min	145	168	69%	55%
0.05 mm/min	390	410	79%	76%

III.6 Fractography study on the non-pre-charged samples

Figure III-5 gives an overall view of the fracture surface for the sample tested at 5 mm/min. At both sides a brittle zone can be detected. The central part of the fracture surface is still ductile. When having a closer look at both sides in Figure III-6 (a) and (b), the two different fracture zones can be clearly observed. The brittle zone extends approximately 60-70 μm from the edge of the sample, which is exactly the calculated hydrogen diffusion distance at 5 mm/min, as given in Table III-3. Consequently, a clear correlation is demonstrated between the distance over which hydrogen can exhibit its detrimental effects for the specific testing conditions of this sample and the region with brittle features of the fracture surface.

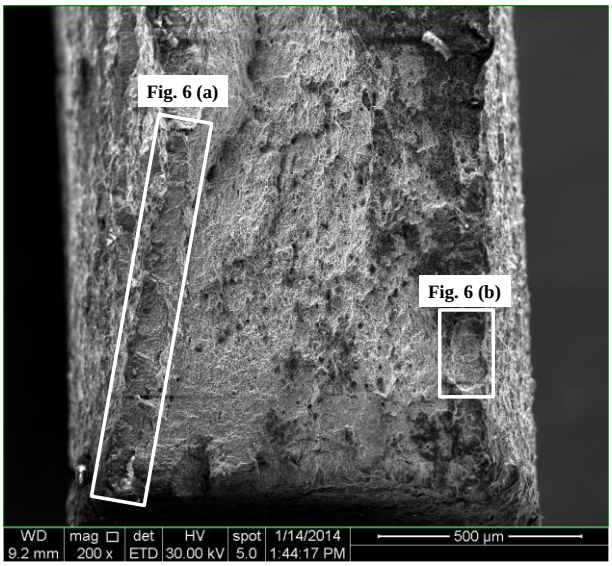

Figure III-5: SEM image of fracture surface, which was non-pre-charged and tested at cross-head deformation speed of 5 mm/min.

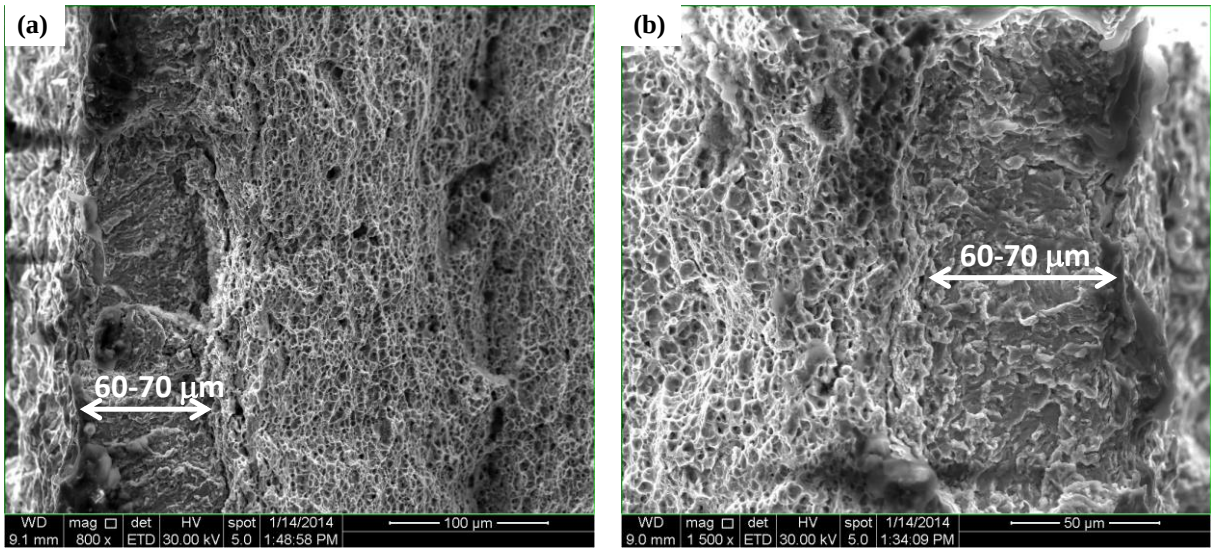

Figure III-6: Detailed SEM image of both left (a) and right (b) side of Figure III-5, with the hydrogen diffusion distance indicated.

Confirmation of this observation was searched for in the samples with the lower deformation rates. Detailed SEM images of both the left and right fracture surface of the sample which was tensile tested at cross-head deformation speed of 0.5 mm/min are depicted in Figure III-7 (a) and (b), respectively. Again a clear distinction between a brittle hydrogen influenced zone and a ductile region can be observed. The width of the brittle zone is about 160-170 µm which again corresponds nicely to the calculated diffusion distance of hydrogen at this deformation test speed, as shown in Table III-3.

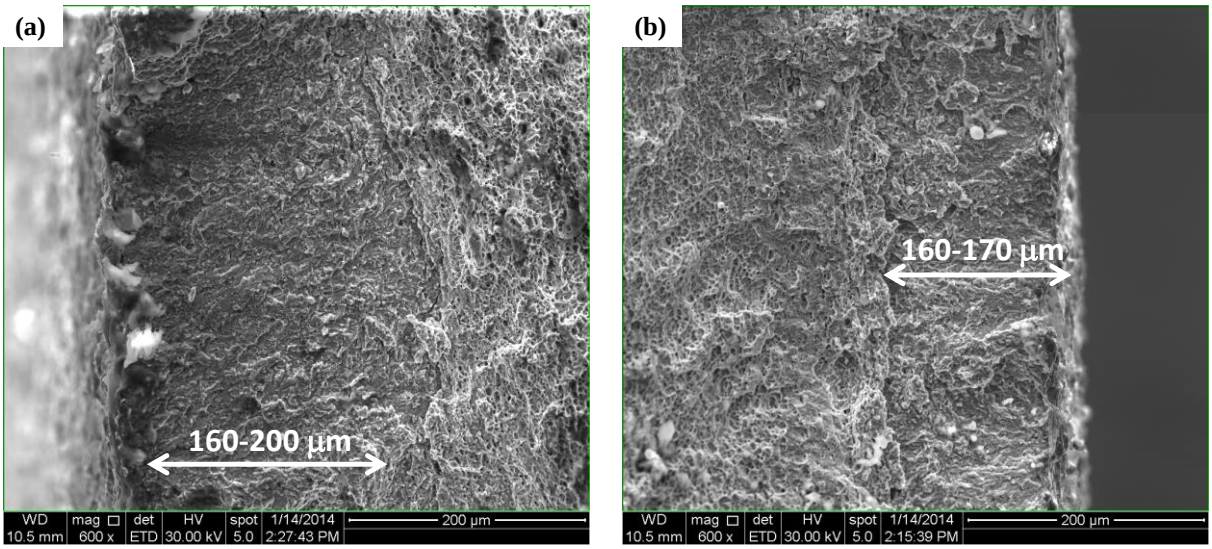

Figure III-7: Detailed SEM image of both left (a) and right (b) side of the fracture surface of the sample tested at cross-head deformation speed of 0.5 mm/min without H pre-charging. The brittle zone is shown.

At a cross-head deformation speed of 0.05 mm/min, a slightly more complex behavior is observed. When having a closer look at the fracture surface in Figure III-8 and III-9, the distinction between both zones is less obvious. The hydrogen diffusion distance for this sample is about 410 µm as presented in Table III-3. As hydrogen enters from both sites of the sample, this implies that hydrogen diffuses along the larger part of the total thickness during the test. This could hinder to make the distinction between the hydrogen affected zone and the non-affected zone as was done for the other cross-head deformation speeds. Indeed, rather large dimples are detected (Figure III-8 (b)) in the expected ductile region, which could be linked with an effect of hydrogen. In addition, the central region in Figure III-9 (a) looks embrittled which also hinders the ability to differentiate between the different zones in the fracture surface. A detailed SEM image is shown in Figure III-9 (b) and indicates clear brittle features in this central region. This brittle central region was not observed at higher cross-head deformation speed. A more detailed analysis was performed to determine the reason behind this observation.

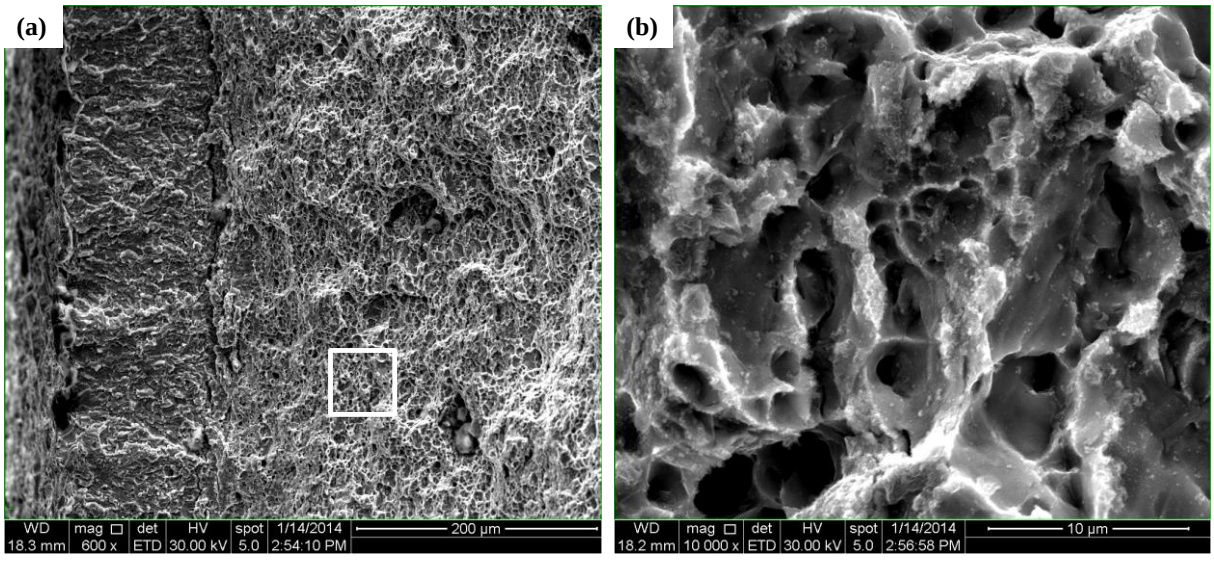

Figure III-8: SEM images of fracture surface of non-pre-charged DP steel at cross-head deformation speed of 0.05 mm/min. Detailed SEM image from the indicated zone is depicted at the right.

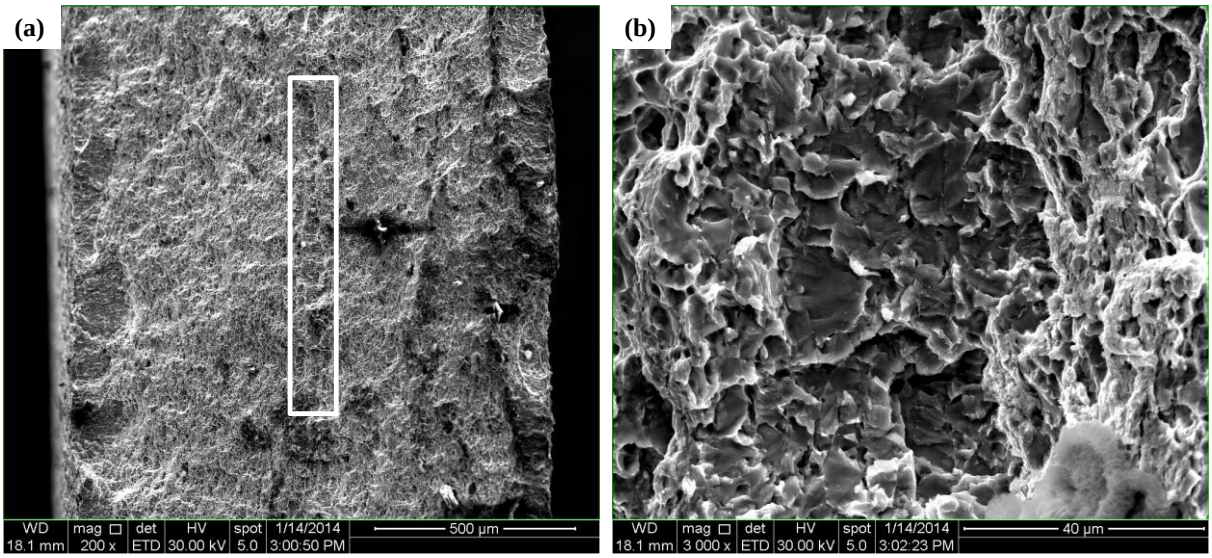

Figure III-9: SEM images of fracture surface of non-pre-charged DP steel at cross-head deformation speed of 0.05 mm/min. Detailed SEM image from the indicated zone in (a) is depicted in (b).

As reported by Escobar *et al.* [19], this DP steel contains a Mn-rich segregation line in the center of the material, which gave rise to MnS precipitates and was considered to be responsible for crack formation. This Mn segregation was confirmed by optical microscopy (Figure III-10), when a LePera etching was used as described in [28]. Escobar *et al.* [19] also performed an energy dispersive X-ray spectroscopy (EDX). EDX mappings clearly demonstrated the presence of MnS inclusions in the crack. Several studies link hydrogen induced cracking with these inclusions [29] [30] [31] [32].

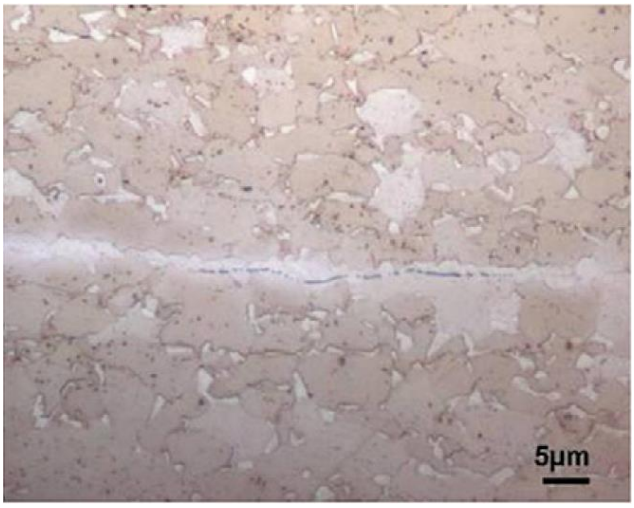

Figure III-10: Optical microscopy image of MnS inclusion with LePera etching of DP steel [19].

As the embrittled zone was only observed for the lowest cross-head deformation speed, it can be assumed that hydrogen was able to diffuse to this central part and embrittle the segregation line. However, the calculated diffusion distance was approximately 410 µm from both sides, indicating hydrogen was not able to reach this central zone. Several arguments might be able to clarify this apparent contradiction. At first, the the applied stress might have an impact on the diffusion coefficient, increasing diffusion kinetics. However, in literature, there is no conclusive answer on the effect of stresses on hydrogen diffusion as both a decrease [33] and an

increase [34] of the diffusion coefficient under loading condition are reported. For dual phase steel, this correlation has not been reported so far. Secondly, an increase of the diffusion coefficient with higher dislocation densities was suggested by Pressouyre [35], as dislocations were in this work considered to be pathways for faster hydrogen diffusion and self-evidently, the dislocation density increases during a tensile test, while the lowest test rate allows this effect to be more pronounced. Moreover, the importance of enhanced dislocation mobility, i.e. the HELP mechanism, was reported to assist the hydrogen induced damage evolution in dual-phase steels [16]. Additionally, the diffusion coefficient used in this work is an approximate value and any possible deviation has a more outspoken effect at a lower cross-head deformation speed because of the increased test time.

III.7 Conclusion

The susceptibility to hydrogen embrittlement of a dual phase steel was investigated by tensile tests under variable hydrogen charging conditions. The pre-charging time to reach hydrogen saturation was determined. Subsequently, different pre-charging times were applied together with in-situ hydrogen charging at a cross-head deformation speed of 5 mm/min to evaluate the impact of the initial hydrogen content. The ductility loss increased with pre-charging times until a maximal embrittlement of 50% was found after two hours of pre-charging, i.e. for a hydrogen saturated sample. An additional charging did not result in an additional embrittlement, whereas in-situ charging during the tensile test caused a ductility loss of 22% for samples that were uncharged before the start of the tensile test.

The influence of the cross-head deformation speed on hydrogen saturated samples, i.e. pre-charged for two hours, was considered to evaluate the effect of hydrogen diffusion during the test. Hydrogen embrittlement increased when lowering the test speed, as hydrogen was enabled to diffuse to critical regions ahead of the crack tip during the test.

Different cross-head deformation speeds were also applied on uncharged samples. These tests allowed to visualize the effective diffusion distance of hydrogen into the sample during the test. A fractography study indeed proved that the brittle hydrogen induced features were present over a distance equivalent to the distance hydrogen can diffuse during the test. Tests at the lowest speed, also showed that the central region of the sample had a brittle cleavage appearance. At 0.05 mm/min, hydrogen reached this central part of the material and embrittled the MnS segregation line, which is prone to hydrogen induced fracture.

III.8 References

[1] Hilditch TB, Lee SB, Speer JG, Matlock DK, „Response to Hydrogen Charging in High Strength Automotive Sheet Steel Products," *SAE Technical Paper*, 2003, http://dx.doi.org/10.4271/2003-01-0525.

[2] Depover T, Pérez Escobar D, Wallaert E, Zermout Z, Verbeken K, „Effect of in-situ hydrogen charging on the mechanical properties of advanced high strength steels," *Int Journal of Hydrogen Energy*, vol. 39, pp. 4647-4656, 2014.

[3] Loidl M, Kolk O, „Hydrogen embrittlement in HSSs limits use in lightweight body," *Adv Mat Process*, pp. 22-25, 2011, BMW Group, Germany.

[4] Duprez L, Verbeken K, Verhaege M, „Effect of hydrogen on the mechanical properties of multiphase high strength steels," in *Proc. of the 2008 Int. Hydrogen Conf.*, Jackson, Wyoming, USA, 2008.

[5] Pérez Escobar D, Verbeken K, Duprez L, Verhaege M, „Evaluation of hydrogen trapping in high strength steels by thermal desorption spectroscopy," *Mat Sci and Eng A*, vol. 551, pp. 50-58, 2012.

[6] Depover T, Pérez Escobar D, Wallaert E, Verbeken K, *Mat Sci and Eng A.*, submitted.

[7] Novak P, Yuan R, Somerday BP, Sofronis P, Ritchie RO, „A statistical, physical-based, micro-mechanical model of hydrogen-induced intergranular fracture in steel," *Journal of Mechanics and Physics of Solids*, vol. 58, pp. 206-226, 2010.

[8] Luppo MI, Ovejero-Garcia J, „The influence of microstructure on the trapping and diffusion of hydorgen in a low carbon steel, *Corrosion Science*, vol. 32, pp. 1125-1136, 1991.

[9] Oliver S, Jones TB, Fourlaris G, „Dual phase versus TRIP steels: Microstructural changes as a consequence of quasi-static and dynamic tensile testing," *Materials Characterization*, vol.58, pp. 390-400, 2007.

[10] Mapelli C, Barella S, Venturini R, „Characterization of the relation among the mechanical behavior and the texture features in high martensitic dual phase steels," *ISIJ Int*, vol.45, pp. 1727-1735, 2005.

[11] Hadzipasic AB, Malina J, Malina M, „The influence of microstructure on hydrogen diffusion and embrittlement of multiphase fine-grained steels with increased plasticity and strength," *Chem Biochem Eng Q*, vol. 25(2), pp. 159-169, 2011.

[12] Davies RG, „Influence of martensite content on the hydrogen embrittlement of dual-phase steels," *Scripta Mat*, vol. 17, pp. 889-892, 1983.

[13] Waterschoot T, Verbeken K, De Cooman BC, „Tempering kinetics of the martensitic phase in DP steel, *ISIJ Int*.," vol. 46 pp. 138-146, 2006.

[14] Gu JL, Chang KD, Fang HS, Bai BZ, „Delayed fracture properties of 1500 MPa bainite/martensite dual-phase high strength steel and its hydrogen traps," *ISIJ Int*., vol.42, pp. 1560-1564, 2002.

[15] Sun S, Gu J, Chen N, „The influence of hydrogen on the sub-surface of the martensite and ferrite dual-phase steel," *Scripta Mat*, vol. 23, pp. 1735-1738, 1989.

[16] Koyama M, Tasan CC, Akiyama E, Tsuzaki K, Raabe D, „Hydrogen-assisted decohesion and localized plasticity in dual-phase steel," *Acta Mat*, vol. 70, pp. 174-187, 2014.

[17] Laureys L, Depover T, Petrov R, Verbeken K, „Microstructural characterization of hydrogen induced cracking in TRIP-assisted steel by EBSD," *Materials Characterization*, vol. 112, pp. 169-179, 2016..

[18] McCoy RA, Gerberich WW, Zackay VF, „On the resistance of TRIP steel to hydrogen embrittlement," *Met Trans*, vol. 1, 2031-2034, 1970.

[19] Pérez Escobar D, Miñambres C, Duprez L, Verbeken K, Verhaege M, „Internal and surface damage of multiphase steels and pure iron after electrochemical hydrogen charging," *Corrosion Science,* vol. 53, p. 3166–3176, 2011.

[20] Wang M, Akiyama E, Tsuzaki K, „Effect of hydrogen on the fracture behavior of high strength steel during slow strain rate test," *Corrosion Science,* vol. 49, pp. 4081-4097, 2007.

[21] Akiyama E, Matsukado K, Wang M, Tsuzaki K, „Evaluation of hydrogen entry into high strength steel under atmospheric corrosion," *Corrosion Science,* vol. 52, pp. 2758-2765, 2010.

[22] Zhao MC, Liu M, Atrens A, Shan YY, Yang K, „Effect of applied stress and microstructure on sulfide stress cracking resistance of pipeline steels subject to hydrogen sulfide," *Mat Sci and Eng A,* vol. 478, pp. 43-47, 2008.

[23] Toh T, Baldwin WM, „Stress corrosion cracking and embrittlement," In: *Stress Corrosion Cracking and Embrittlement*. New York : Wiley; 1956, pp. 176-186.

[24] Kim SJ, Yun DW, Jung HG, Kim KY, „Determination of hydrogen diffusion parameters of ferritic steel from electrochemical permeation measurement under tensile loads," *Journal of the Electrochemical Soc*., vol. 161 (12), pp. 173-181, 2014.

[25] Otsuka T, Hanada H, Nakashima H, Sakamoto K, Hayakawa M, Hashizume K, Sugisaki M, „Observation of hydrogen distribution around nonmetallic inclusions in steels with tritium microautoradiographyl," *Fusion Science and Technology,* vol. 48, pp. 708-711, 2005.

[26] Yamada H, Tsurudome M, Asano Y, Ogasawara N, Horikawa K, „Visualization of hydrogen evolution during fatigue deformation in 7075 aluminum alloy," in *International Symposium on Advanced Science and Technology in Experimental Mechanics*, Taiwan, 2012.

[27] Hadzipasic AB, Malina J, Malina M, „The influence of microstructure on hydrogen diffusion and embrittlement of multiphase fine-grained steels with increased plasticity and strength," *Chem Biochem Eng Q*, vol. 25(2), pp. 159-169, 2011.

[28] LePera FS, „Improved Etching technique for the determination of percent martensite in high-strength dual-phase steels," *Metallography*, vol. 12, pp. 263-268, 1979.

[29] Hardie D, Charles EA, Lopez AH, „Hydrogen embrittlement of high strength pipeline steels," *Corrosion Science*, vol. 48, pp. 4378-4385, 2006.

[30] Wilde BE, Kim CD, Phelps EH, „Some observations on the role of inclusions in the hydrogen induced blister cracking of linepipe steels in sulfide environments," *Corrosion*, vol. 36, pp. 625-632, 1980.

[31] Domizzi G, Anteri G, Ovejero-Garcia J, „Influence of Sulphur content and inclusion distribution on the hydrogen induced blister cracking in pressure vessel and pipeline steels," *Corrosion Science,* vol.43, pp. 325-339, 2001.

[32] Ren XC, Chu WY, Li JX, Sun YJ, Qiao LI, „The effects of inclusions and second phase particles on hydrogen-induced blistering in iron," *Mater Chem Phys*, vol. 107, pp. 231-235, 2008.

[33] Kim SJ, Jung HG, Kim KY, „Effect of tensile stress in elastic and plastic range on hydrogen permeation of high-strength steel in sour environment," *Electrochimica Acta*, vol.78 pp. 139-146, 2012.

[34] Kim SJ, Yun DW, Suh DW, Kim KY, „Electrochemical hydrogen permeation measurement through TRIP steel under loading condition of phase transition," *Electrochemistry Comm*., vol. 24, pp. 112-115, 2012.

[35] Pressouyre GM, „Trap theory of hydrogen embrittlement," *Acta Met*., vol.28, pp. 895-911, 1980.

CHAPTER IV

On the synergy of diffusible hydrogen and hydrogen diffusivity in the mechanical degradation of laboratory cast Fe-C alloys*

IV.1 Introduction

As an alternative for the scarce fossil fuels, hydrogen is often quoted to be the future energy carrier. Hydrogen combustion only produces water from which it was initially derived. Hence, this non-polluting substitute could avoid CO_2 emissions, which are a major cause for global warming, since CO_2 is considered to be the main greenhouse gas. Additionally, no environmental issues concerning acid rain, smog or ground water pollution are relevant when using hydrogen instead of fossil fuels. However, the commercialization of hydrogen has proven to be a challenge, including some material related issues. A significant difficulty arises from the high diffusivity of hydrogen in the body centered cubic crystal structure of most steels, and the embrittlement of the steel components which are in contact with a hydrogen environment. Numerous examples of the potential dramatic consequences of hydrogen are available in literature, e.g. [1]. Therefore, further investigation on the possibilities to store and transport hydrogen and on the material-hydrogen interactions is of great scientific and technological value and interest.

Next to the ecologic driving force to use hydrogen instead of fossil fuels, the phenomenon of hydrogen embrittlement (HE) is a concern for the automotive industry as well, where one of the main goals is to reduce the car's weight while retaining the same strength and stiffness level at the lowest possible cost. Aluminum has the drawback of a lower stiffness and a higher material and production cost as compared to steels. Therefore, excellent candidates to attain the needed requirements are high strength steels, since they combine low weight with high strength. Unfortunately, these high strength steels are more sensitive to HE [2] [3], causing a brittle and unpredictable fracture which might have severe consequences. Moreover, a paper authored by the automotive industry recently claimed that the possible HE-related failure of steels with a tensile strength above 1000 MPa impedes their use in the body in white design [4]. Therefore, in order to be able to understand and predict the potential hydrogen damage, detailed research on the effect of the interaction between hydrogen and high strength steels is necessary. However, the characteristic complex microstructure of these high strength steels is a complicating issue.

No complete understanding of the mechanisms behind HE has been realized so far, although it was already discussed by Johnson in 1875 [5]. The detrimental influence of hydrogen on the mechanical properties has been described in several reference works by Bernstein [6], Oriani [7] and Troiano [8]. The loss of ductility is considered the main consequence of HE and conventional plasticity characteristics, such as elongation and area

* This chapter is based on the following publications: Depover T, Verbeken K, *Materials Science and Engineering A*, vol. 664, pp. 195-205, 2016 and Depover T, Van den Eeckhout E, Verbeken K, *Materials Science Technology*, DOI: 10.1080/02670836.2015.1137387.

reduction are significantly decreased due to hydrogen. Nevertheless, up to now, the responsible mechanisms remain under debate and are subject of a lot of recent scientific work.

Chan [9] presented an overview concerning the HE-susceptibility of different steel microstructures. He emphasized that an as-quenched martensitic structure has the lowest HE-resistance, while tempered bainite or martensite shows the best resistance when hydrogen charged. Moreover, the as-quenched martensite has the lowest hydrogen diffusivity [10] [11] [12]. The pearlitic structure and alloys with a homogeneous distribution of fine carbides [13] perform in between the two extremes.

Furthermore, Chan [9] described the effect of the carbon content on the hydrogen trapping capacity in ferrite-pearlite steels and found that the hydrogen saturation level increased with carbon content up to 0.69%C. When the carbon content exceeded 0.69% carbon (i.e. near the eutectoid composition), the hydrogen content decreased. This observation was correlated with, and correspondingly highlighted, the importance of the pearlite/ferrite interface [14]. In another study [15], a martensitic phase with variable carbon content was studied. The high carbon sample (0.93%) contained the highest amount of hydrogen, followed by the low carbon (0.23%) grade, whereas the medium carbon steel (0.44%) contained the lowest amount of hydrogen. This observation was attributed to differences in the martensite morphology.

Chan [16] also compared different microstructural constituents with each other and found that martensite demonstrated the highest hydrogen solubility together with the lowest hydrogen diffusivity. These observations matched the ones found by the present authors [17], where an increased amount of transformation induced martensite in a transformation induced plasticity (TRIP) steel also reduced the apparent hydrogen diffusivity. However, a low hydrogen solubility does not always correspond to a high hydrogen diffusivity. In the case of the ferrite/pearlite structure, it was observed that the hydrogen diffusivity was lower compared to upper and lower bainite. This was ascribed to the carbide distribution, which consisted of cementite lamellae in the pearlite/ferrite microstructure and effectively retarded hydrogen diffusion, while the fine carbide distribution in the bainitic structures less hindered hydrogen diffusion through the sample.

The susceptibility to the hydrogen induced ductility loss has been reported to be less for bainitic steels compared to other microstructural phases for certain environments causing HE and corrosion fatigue [18] [19] [20] [21] The mechanical degradation was analyzed by performing slow strain rate tensile tests and it was observed that lower bainite showed the highest resistance against HE when compared to quenched and tempered martensite, normalized ferrite/pearlite, spheroidized microstructures and untempered martensite.

Luppo *et al.* [22] correlated the HE sensitivity with the hydrogen diffusivity and desorption kinetics in a low carbon steel in which several microstructures are induced by an appropriate heat treatment. They found that the desorption kinetics were minimum and for an as-quenched martensitic structure, whereas the amount of desorbed hydrogen was maximal. Moreover, they saw that the HE susceptibility could be correlated with the amount of desorbed hydrogen. This meant that diffusible hydrogen could be set responsible for the hydrogen induced ductility loss, which is in good correspondence to already published results [3] [23] [24] [25].

Tau *et al.* [26] studied three different tempered martensitic and bainitic structures and observed that the carbides characteristics influenced the hydrogen diffusivity. Moreover, the carbides in bainite may even play a determinant factor in retarding the hydrogen transport, which explained why samples with very fine carbides showed the highest amount of hydrogen. The very specific characteristics of the interaction between hydrogen and other carbide forming elements such as Ti and Nb has been demonstrated as well [25] [27] [28] [29].

The hydrogen/material interaction has also been investigated previously by the authors for industrial high strength steels with a complex combination of different microstructural constituents [3] [17] [30] (cf. Chapter II). These materials are obtained by rolling and subsequent heat treatments, which all have a large influence on the final microstructure and hence the mechanical properties. It is widely accepted that the susceptibility to hydrogen embrittlement is dependent on the microstructure. In the work of Duprez *et al.* [23], the influence of diffusible hydrogen on the mechanical properties of four different high strength steels was studied. Tensile tests performed immediately after electrochemical charging and on samples that were allowed to discharge in air for one week indicated that the ductility loss after charging was reversible. Indeed, a large part of the ductility was recovered after discharging which proved that the observed ductility drop after charging was caused by the intrinsic presence of mobile hydrogen and not due to an irreversible damage mechanism caused by hydrogen charging. It was also observed that the extent of ductility recovery was not the same for all steels. Recently, Koyama *et al.* [31] studied the hydrogen induced cracking behavior for dual phase steels. They showed that both the hydrogen-enhanced decohesion (HEDE) and hydrogen-enhanced localized plasticity (HELP) mechanisms contributed to the damage evolution. Additionally, Laureys *et al.* [32] [33] studied the crack formation for TRIP steel and revealed that crack initiation started in the martensitic phase. However, the specific multiphase microstructure of these high strength steels is a complicating issue in correlating the effect of hydrogen with microstructural characteristics. Even in the detailed study on TRIP steel [17], no conclusive interpretation of all thermal desorption spectroscopy peaks to a certain microstructural constituent was possible. Therefore, in the present work, simplified Fe-C alloys were evaluated.

The present study investigates the effect of hydrogen on the mechanical properties of three sets of generic Fe-C alloys by tensile tests on in-situ hydrogen charged samples and comparison of the obtained results with uncharged specimens. In order to be able to evaluate the hydrogen interaction with specific microstructural constituents, laboratory cast Fe-C alloys were submitted to well-designed thermal cycles to introduce constituents, such as bainite, martensite and pearlite separately, instead of having to deal with the complexity of multiphase alloys. This allowed to gain relevant insights on the behavior of each phase. Additionally, the effect of hydrogen diffusion is evaluated by varying the cross-head deformation speed at which the tensile test is done.

IV.2 Experimental procedure

IV.2.1 Material characterization

The lab cast generic alloys were “pure iron” (cf. composition in Table IV-1) and two Fe-C based materials containing 0.2% and 0.4% of carbon, respectively. This difference in carbon content will allow evaluating and analyzing the impact of the carbon content on HE. The chemical composition is given in Table IV-1.

Table IV-1: Chemical composition of the used materials in wt%.

Material/Element	C	Mn	Si	Other
“Pure Iron”	0.0015	0.0003	0.00	<0.02% Al, P
0.2% C	0.199	0.004	< 0.0002	< 0.0008 P, N
0.4% C	0.374	0.002	< 0.0001	< 0.0007 P, N

The lab cast alloys were produced in a Pfeiffer VSG100 vacuum melting and casting unit, operating under an argon gas protective atmosphere. The materials were hot rolled till 8 mm and then cold rolled to achieve a final thickness of 1.6 mm for the 0.2% and 0.4% C samples and 1.8 mm for pure iron. Pure iron was further annealed at 750°C for 10 minutes in an air furnace and cooled in air. Different heat treatments were applied on the Fe-C grades to induce a bainitic, martensitic or pearlitic structure. Temperature vs. time graphs of the used heat treatments are presented in Figure IV-1. In order to obtain a bainitic structure, both Fe-C grades were in a first stage brought to 900°C in a salt bath for 10 minutes and immediately transferred to a second salt bath, where they were hold at 400°C for 10 minutes (Fig. IV-1a). The grade was then air cooled, resulting in a slow cooling rate, to prevent formation of a martensitic structure. The martensitic structure was created by bringing the grade up to 900°C for 10 minutes in a salt bath followed by water quenching (Fig. IV-1b). Pearlite was obtained in two steps; heating at 900°C for 10 minutes was followed by keeping the material at 700°C for another 10 minutes and air cooling (Fig. IV-1c).

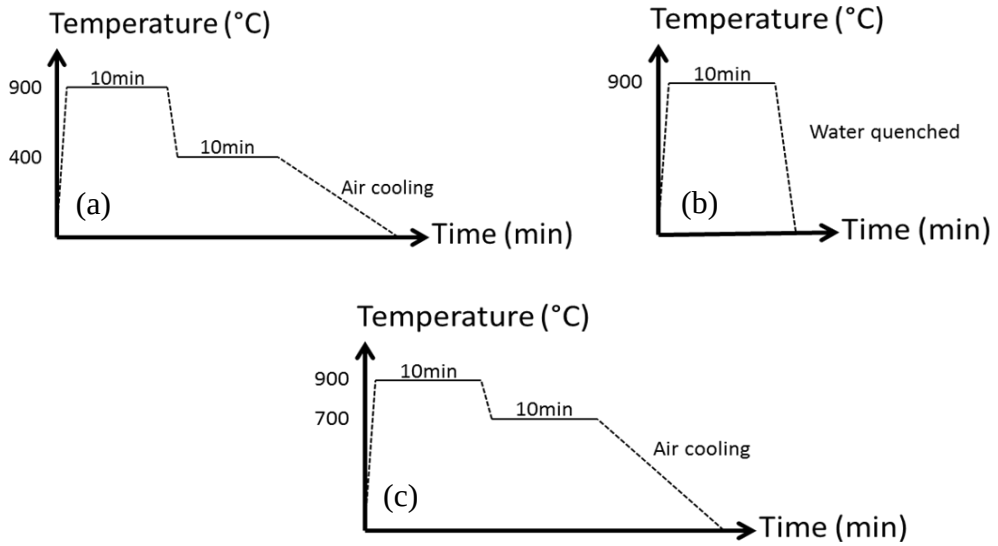

Figure IV-1: Temperature-time graphs of the different heat treatments to induce: (a) bainite, (b) martensite and (c) pearlite.

All samples were then ground and tensile samples were machined with their tensile axis parallel to the rolling direction. Finally, the surface and edges of the sample were sandblasted to remove possible remaining oxides. After sandblasting another 0.1 mm of material was removed till final thickness was reached, which was 1.5 mm for the 0.2% and 0.4% C samples and 1.7 mm for pure iron.

For light optical microscopy (LOM), sample surfaces were ground, polished and finally etched with 2% Nital for 10 s. The phase content of each lab cast material was determined by an image analysis program (Image J®). This is important to be able to evaluate the impact of the introduced phases on the HE resistance. An average of five images gave an approximate value of each phase.

Emphasis was mainly put on the comparison of different microstructural constituents, i.e. bainite, martensite and pearlite, and their response to HE for a 0.2% C lab cast grade, whereas pure iron was used as a reference material. Additionally, in order to analyze the impact of the carbon content on the embrittlement behavior, a bainitic microstructure was also induced in a 0.4% C grade.

IV.2.2 Mechanical characterization

The effect of HE on the mechanical behavior was determined by comparing tensile tests in air (uncharged) with tests performed on hydrogen charged samples. Each test was performed twice to check the reproducibility of the results: two tests performed under the same conditions will be labeled as "A" and "B". Hydrogen was introduced by cathodic charging using 1 g/L of thiourea in a 0.5 M H_2SO_4 solution. The materials were pre-charged for two hours at a current density of 2.65 mA/cm², while in-situ charging continued during the actual tensile test. These conditions are much more severe than real-life conditions, but are required to have an accelerated test procedure. Moreover, these charging conditions were chosen in such a way that they did not create hydrogen blisters or internal damage in the sample and were based on results presented in a previous work [34] [35]. It was verified that pre-charging ensured complete hydrogen saturation of the samples [30] [34]. Notched tensile samples (cf. Figure IV-2), which due to the notch locally introduce a triaxial stress state, were used to control crack initiation. This geometrical discontinuity leads to a local stress concentration, which is expressed by a stress concentration factor K_t of 4.2.

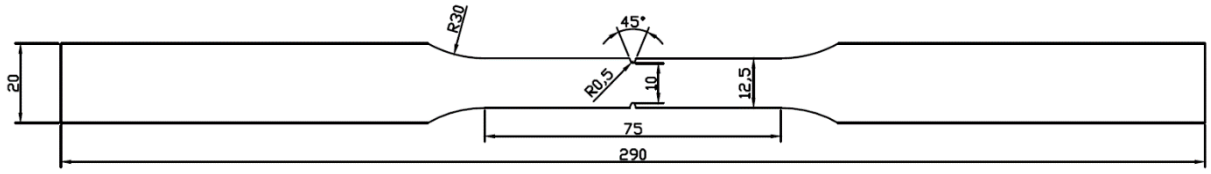

Figure IV-2: Geometry of the tensile specimen.

Tensile tests were performed using two different cross-head deformation speeds; namely 5 mm/min, similar to Zhao *et al.* [36], and 0.05 mm/min, with a corresponding strain rate of 1.11 x 10^{-3} s^{-1} and 1.11 x 10^{-5} s^{-1} respectively. This variation in tensile test speed allowed to evaluate the possible effect of hydrogen diffusion during the actual test. An embrittlement index (EI) is established in order to evaluate the impact of hydrogen on the ductility of the different grades and defined as:

$$EI = \frac{\text{Elongation in Air - Elongation when Charged}}{\text{Elongation in Air}} \quad \text{(IV-1)}$$

Hence, the EI varies between 0 and 1, with 0 meaning that there is no ductility loss and the material is insensitive to HE. When an index of 1 is obtained, the ductility drop is 100% and HE is maximal.

IV.2.3 Determination of the hydrogen/material interaction

The hydrogen content and the hydrogen diffusion coefficient was determined as described in Chapter I section I.2.4.

IV.3 Material characterization

Figure IV-3 presents the LOM images of pure iron (a) and the material with 0.2% C, with bainitic and ferritic (b), martensitic (c) and pearlitic and ferritic (d) microstructure, respectively. Figure IV-4 shows the 0.4% C alloy, where bainite was induced. Rolling and normal directions are shown on the image. Additionally, the phase content was calculated using the abovementioned procedure to obtain an indication of the amount of the introduced martensite, bainite or pearlite, as shown in Table IV-2.

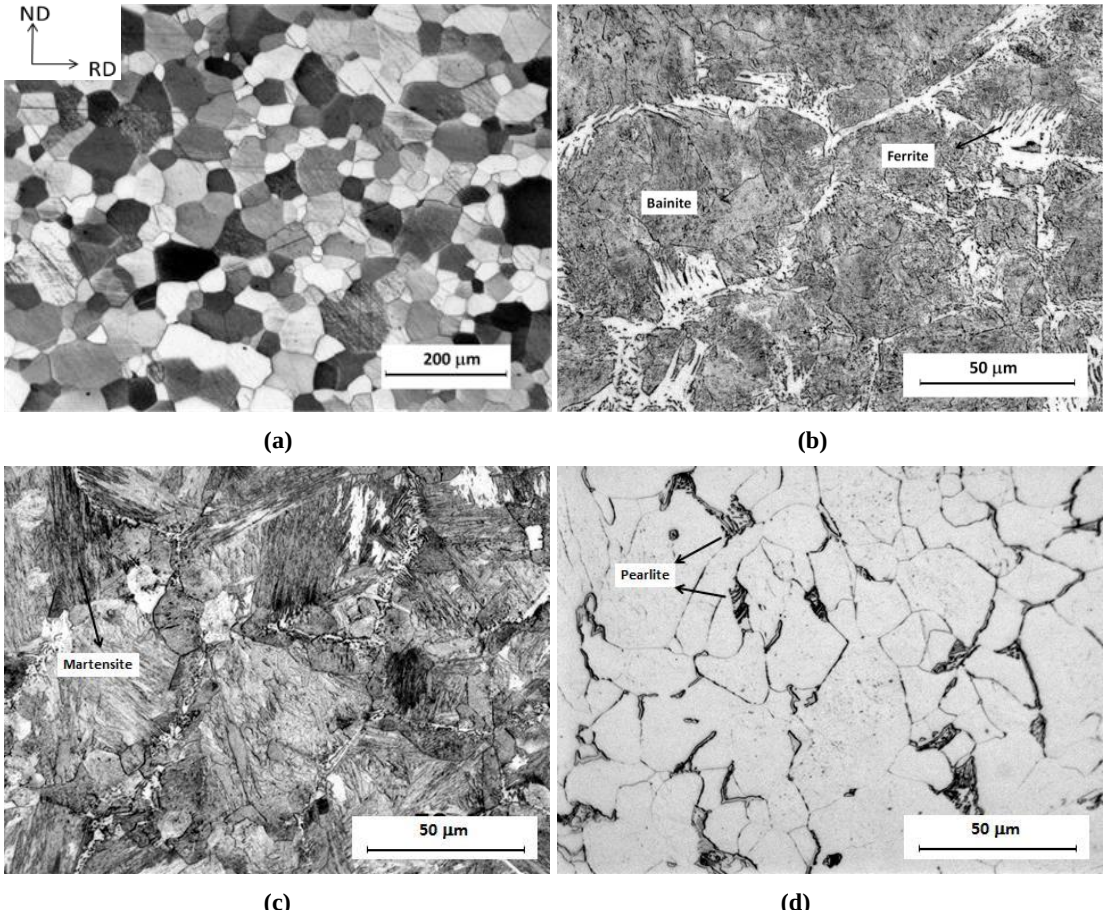

Figure IV-3: Optical microstructures of pure iron (a), and Fe-0.2% C, bainite and ferrite (b), martensite (c) and ferrite and pearlite (d).

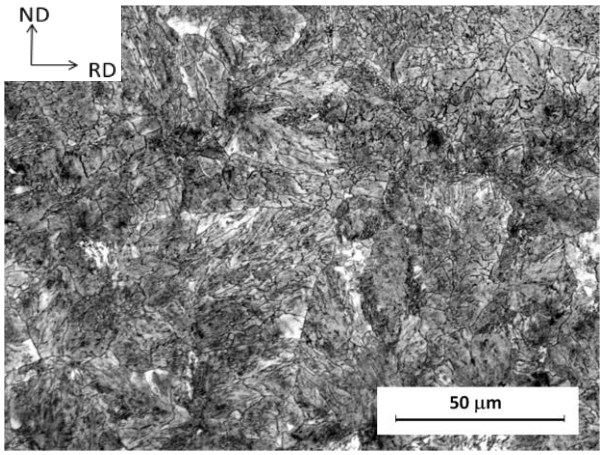

Figure IV-4: Optical microstructure of Fe-0.4% C, bainite.

Table IV-2: Average phase content determined based on the average of 5 micrographs of the used materials.

Material		Phase content (%)
Pure Iron	Pure Iron (PI)	Ferritic
Fe-0.2% C	Pearlite (P2)	6.8% pearlite + 93.2% ferrite
	Bainite (B2)	89.2% bainite + 10.8% ferrite
	Martensite (M2)	93.3% martensite + 6.7% ferrite
Fe-0.4% C	Bainite (B4)	98.1% bainite + 1.9% ferrite

The desired microstructural constituents are clearly present in Figure IV-3 and IV-4. Pure iron (PI) consists of a 100% ferritic matrix with a grain size of 37 μm, while the Fe-0.2% C alloy with pearlite (P2) contains 6.8% pearlite and has a ferrite grain size of 19 μm, which was determined by the linear intercept method. It should be mentioned that pearlite also contains a certain ferrite fraction since pearlite contains both cementite and ferrite. Alternatively, the bainitic and martensitic alloys clearly contained a significantly higher fraction of the desired constituent being a nearly 100% bainitic material for Fe-0.4% C. The amount of the different phases present is a factor which will be taken into account while analyzing HE in the different materials.

A noticeable feature is present in the B2 microstructure (Figure IV-3(b)), which could be related to the presence of Widmanstätten ferrite (α_w). This microstructural feature is produced in the higher temperature region of the bainitic transformation region, as illustrated in Figure IV-5. B4 does not contain Widmanstätten ferrite. The bainitic transformation curves in a temperature-time-transformation diagram move to the right when the carbon content increases, meaning that more time becomes available to cool the material till the desired temperature for bainite formation, which is 400°C in this case. Since the same heat treatment was applied for both grades, the Widmanstätten ferrite zone (Figure IV-5) got intersected in the case of B2, resulting in some ferrite in the microstructure in contrast to B4 which had a homogeneous bainitic structure.

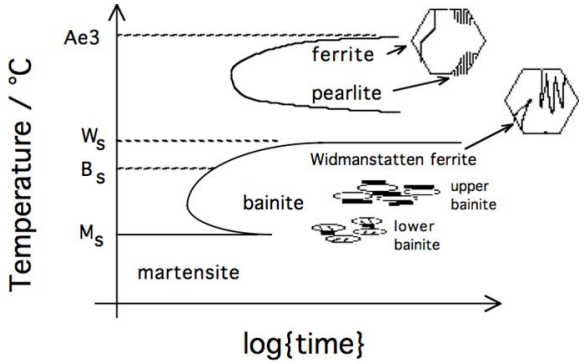

Figure IV-5: Temperature-time-transformation diagram in which Widmanstätten ferrite is indicated [37].

IV.4 Tensile tests at 5 mm/min

Figure IV-6 shows the results of the tensile tests performed on the different materials at a cross-head deformation speed of 5 mm/min in uncharged condition (air) and after hydrogen charging. As is clear from the figure, the reproducibility of the different tests was very good. The results shown of Figure IV-6 are summarized in Table IV-3.

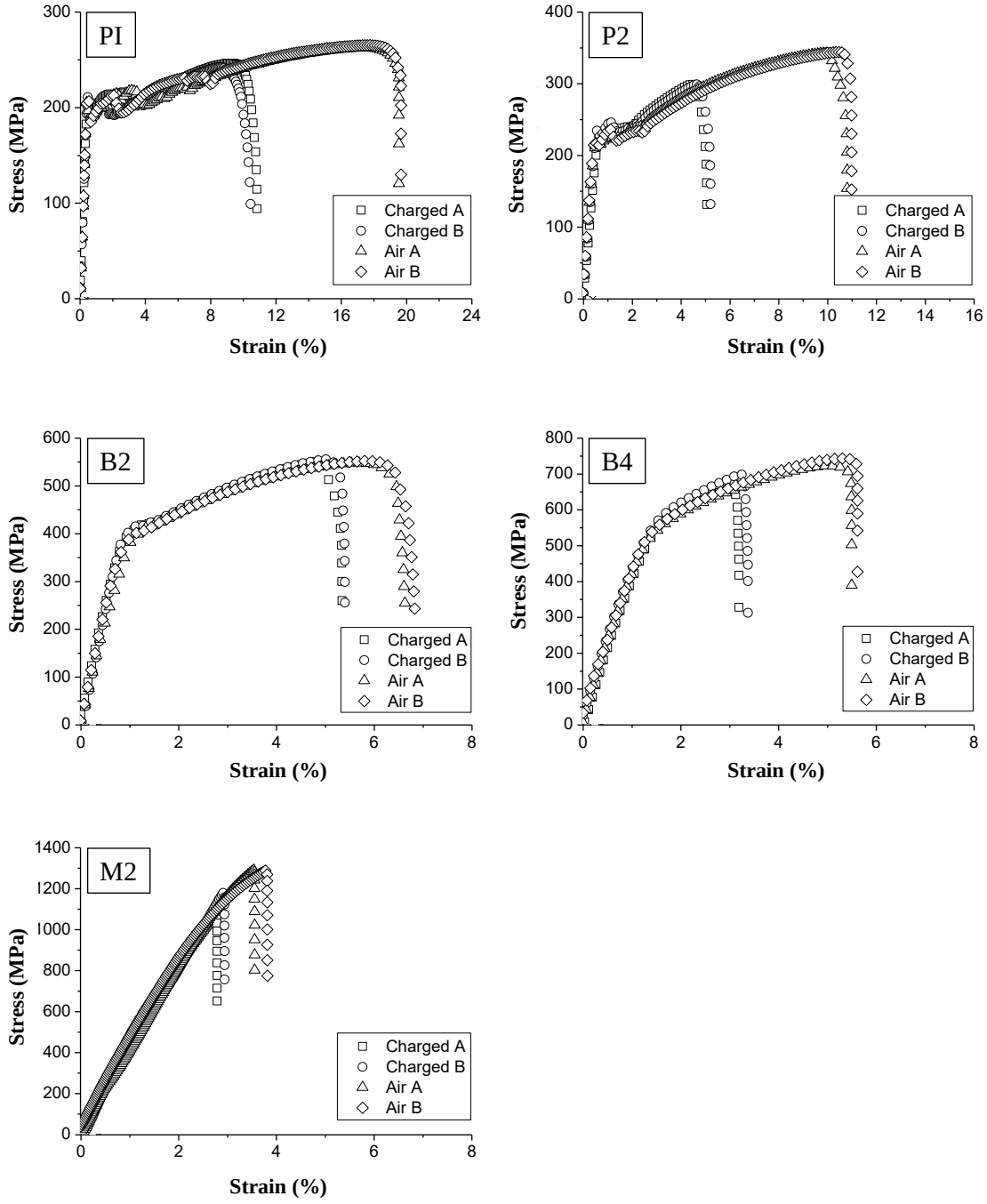

Figure IV-6: Stress-strain curves at cross-head deformation speed of 5 mm/min for PI, P2, B2, B4 and M2, with similar tests indicated with "A" and "B".

Table IV-3: Summary of the tensile tests performed at a cross-head deformation speed of 5 mm/min.

Material	PI		P2		B2		B4		M2	
	air	**charged**	**air**	**charged**	**air**	**charged**	**air**	**charged**	**air**	**charged**
Average elongation (%)	19.6	10.6	10.88	5.17	6.75	5.36	5.55	3.31	3.69	2.88
Average tensile strength (MPa)	264	245	343	299	550	553	733	693	1274	1122
Average yield strength (MPa)	205	207	217	232	371	378	508	538	/	/
Embrittlement index EI	0.46		0.52		0.21		0.40		0.22	

The lowest strength level was achieved for pure iron, whereas the Fe-0.2%C materials showed an increasing strength level going from pearlite, over bainite to martensite. B4 had an augmented strength level compared to B2 due to the higher carbon content. From Table IV-3, it is observed that the yield strength (YS) increased consistently when the samples got charged. This was also seen by Duprez *et al.* [23], where the increase in yield strength was attributed to a solid solution strengthening effect caused by the interstitial hydrogen. Considering the hydrogen content as determined by melt extraction, a strain hardening was obtained in the range of 25000 MPa per mass% hydrogen [23]. A similar tendency was found in this study, since the increase in yield strength (ΔYS PI < ΔYS B2 < ΔYS P2 < ΔYS B4) was in the same order as the increase of the total hydrogen content (PI < B2 < P2 < B4) for which the values are given in the next section.

At first sight, this observation of an increased yield strength level is in contradiction to the statement made by Liu *et al.* [38], where no influence of hydrogen up to the yield stress of the steel was mentioned. This was concluded from the observation that only surface cracks were detected in the necked region, while none were spotted in the uniformly deformed part of the specimen. It should however be noted that this conclusion was made from a macroscopic surface evaluation of the samples, where no internal damage or hydrogen assisted strengthening was taken into account. Moreover, in the present case, a recent study [32] revealed that surface cracks were observed prior to necking.

When considering the EI's, the most notable value was seen for pure iron (0.46). Although, it should be emphasized that the total elongation in air should be taken into account as well. A hydrogen charged sample of pure iron was still more ductile than uncharged specimens of the other materials (only P2 showed a similar ductility). According to literature, the susceptibility to hydrogen degradation increases in the order of bainite, quenched martensite and pearlite [13]. The same order was found here, although at a cross-head deformation speed of 5 mm/min, the martensitic and bainitic alloys behaved similarly. In addition, at this cross-head deformation speed, the test duration was only about 30 seconds to 1 minute for these samples. Therefore, a limited effect of hydrogen diffusion during the test could be expected and it will be verified whether this effect was more outspoken for a test performed at a lower strain rate.

The ductility drop for pure iron after hydrogen charging was about 46%. This is remarkable as pure iron only contains a limited amount of traps such as grain boundaries, vacancies or dislocations and therefore a rather low amount of total and diffusible hydrogen as shown in the next section. Previous, work of Escobar *et al.* [34] [35] allowed evaluating for which conditions of electrochemical charging internal damage, i.e. crack initiation, and surface damage, i.e. blister formation occurred. Blister maps were made by evaluating the surface damage when varying the current density and charging time for the same electrolyte as the one used here. These showed that the used charging conditions were close to those for blister formation for pure iron, whereas they were safe for the Fe-C alloys. Although no visible blisters appeared at the surface of pure iron, it is likely that during a tensile test, and because of the corresponding stresses, crack initiation occurred more rapidly, which could be correlated with the high EI for pure iron. Besides, Ren *et al.* [39] did identify the occurrence of blisters in industrial pure iron and recently a three-dimensional imaging of hydrogen blisters in iron was performed by neutron tomography [40], which implies that the results found by the authors in [34] support their conclusion that the presence of a second phase is not a condition for blister formation.

The comparable EI values for P2 (EI = 52%) and PI (EI = 46%) can be related to the similarities in microstructure. The pearlitic sample (Figure IV-3(d)) consisted mainly of ferrite (6.8% Pe + 93.2% α) and the slightly higher EI could be linked with the higher carbon content, introduced in the microstructure as cementite. It was also shown that adding carbon, and consequently secondary phase constituents, increased the amount of diffusible hydrogen [9] [34].

For the bainitic grades B2 and B4, a higher EI was achieved for the latter one. This could be correlated with the higher amount of secondary phase in B4 (98% B) compared to B2 (89% B). An almost fully bainitic microstructure was obtained for B4, while some Widmanstätten ferrite arose in B2, as shown in respectively Figure IV-4 and Figure IV-3(b). In addition, the amount of hydrogen is higher for B4 due to the higher carbon content since generally the hydrogen uptake capacity increases with carbon content [9]. Additionally, Hadam *et al.* [41] studied the absorption of hydrogen in relation to the carbon content in gradually strained Armco iron (0.05% C) and high carbon steel (1.00% C) using electrochemical permeation and thermal desorption spectroscopy. They found that the lattice diffusivity of hydrogen in the low carbon alloy was higher than in the high carbon steel. Moreover, they found a considerable higher amount of hydrogen in the high carbon alloy, which was in correspondence with the results presented further in this work and described previously by the authors in [34] and by Chan in [9] [15].

Considering the martensite grade, M2 showed no yielding as martensite is a brittle, hard structure, resulting in a low extension. The obtained EI at a cross-head deformation speed of 5 mm/min was in the same range as for B2. This will be further discussed with respect to the hydrogen uptake capacity of both microstructures in the next section.

IV.5 Determination of the hydrogen uptake capacity

The hydrogen uptake capacity was studied based on hot/melt extraction results. With respect to the hydrogen uptake capacity, it is important to make a distinction between the amount of diffusible hydrogen and the total amount of hydrogen in the samples, since the diffusible hydrogen has been argued to play a crucial role in hydrogen induced cracking [22] [24]. The results are presented in Table IV-4.

Table IV-4: Melt (1600°C) and hot (300°C) extraction results for hydrogen saturated samples in wppm.

	Total hydrogen (wppm)	**Diffusible hydrogen (wppm)**
PI	2.64 +/- 0.18	0.71 +/- 0.11
B2	8.71 +/- 0.54	3.82 +/- 0.12
M2	10.53 +/- 0.92	4.72 +/- 0.29
P2	9.69 +/- 0.76	5.10 +/- 0.08
B4	14.65 +/- 0.74	8.73 +/- 0.52

A correlation between the amount of diffusible hydrogen and the embrittling behavior was expected. However, an important remark should be made when linking the amount of diffusible hydrogen with the EI. Generally, the embrittlement increases with diffusible hydrogen content. However, the hydrogen diffusion coefficient should also be incorporated in this discussion. Consequently the distance x (m) hydrogen can diffuse in a certain microstructure at a certain cross-head deformation speed, i.e. during the tensile test, can be correlated with the observed EI's.

For instance, when taking a closer look to the results for pure iron, no large embrittlement was expected considering the low amount of diffusible hydrogen (Table IV-4). As above mentioned, the high EI was correlated with some possible hydrogen induced damage of the sample [34] [35] during charging, which caused faster crack formation during the tensile test. Moreover, it was observed here that, even at a cross-head deformation speed of 5 mm/min, hydrogen was able to diffuse through the lattice of pure iron due to its high diffusion coefficient, which was supposed to be about 1.28×10^{-8} m^2/s [41]. The distance x (m) over which hydrogen can diffuse, can be calculated by taken the square root of the product of the diffusion coefficient D (m^2/s) and the time t (s) of the test, i.e. $x = (D \times t)^{1/2}$ [31]. In this specific case, hydrogen can diffuse over a distance of 1.1 mm during the test, which is about the sample thickness and consequently sufficient to assist hydrogen related ductility loss.

When considering the grades containing 0.2% C (B2, M2 and P2), no straightforward tendency could be detected between the degree of embrittlement at a cross-head deformation speed of 5 mm/min (presented in Table IV-3) and the total amount of hydrogen (Table IV-4). Remarkable was the case of P2, where the total amount of hydrogen is in between B2 and M2, whereas its embrittlement is a lot higher (about 50%), compared to approximately 20% for B2 and M2. However, this trend could be understood in terms of the diffusible hydrogen content, which was the highest for P2 (5.10 wppm) compared to M2 (4.7 wppm) and B2 (3.8 wppm). This clearly shows how crucial the diffusible hydrogen is when evaluating hydrogen induced degradation.

Furthermore, as described for pure iron, the diffusion coefficient of the P2 (with 93.2% ferrite) microstructure is assumed to be higher than for the martensitic or bainitic microstructures, leading to a higher distance x (m)

hydrogen can diffuse through during this tensile test. Similar reasoning can be made when comparing the embrittlement indices of B2 (21%) and P2 (52%), where diffusible hydrogen alone cannot explain the observed EI but the hydrogen diffusion coefficient which is significantly lower in B2, due to the large amount of secondary phase in this alloy, is expected to play a decisive role as well.

Moreover, when having a closer look at the martensitic grade M2, the EI was quite low. However, at a cross-head deformation speed of 5 mm/min, hydrogen can only diffuse approximately 0.035 mm, since the diffusion coefficient in a martensitic structure was assumed to be about 4.24 x 10^{-11} m^2/s [9]. Hence, the effect of hydrogen diffusion was negligible in this case, which explains the lower obtained embrittlement index for M2 (22%) compared to PI (46%) and P2 (52%).

Concerning the bainitic materials tested at a cross-head deformation speed of 5 mm/min, the higher embrittling behavior of B4 (40%) compared to B2 (21%) could also be correlated with the amount of diffusible hydrogen introduced by electrochemical charging, which is 8.73 and 3.82 wppm respectively. To evaluate the effect of hydrogen diffusion in this case, the actual hydrogen diffusion distance can be determined and correlated with the observed hydrogen induced ductility loss. Therefore, hydrogen permeation tests were performed and the results are presented in Figure IV-7. The calculated diffusion coefficients, determined as described in Chapter I, are summarized in Table IV-5.

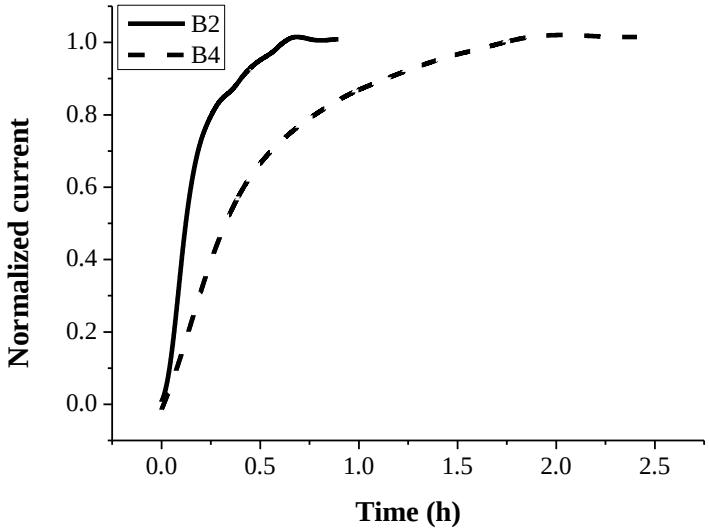

Figure IV-7: Hydrogen permeation curves for B2 and B4.

Table IV5: Hydrogen diffusion coefficient for B2 and B4.

	Hydrogen diffusion coefficient (m^2/s)
B2	6.71 x 10^{-10}
B4	3.40 x 10^{-10}

The hydrogen diffusion coefficient is significantly lower for B4 due to the higher amount of bainite compared to B2 and the higher amount of carbon which impedes hydrogen diffusion, which is in correspondence with the work of Hadam *et al.* [41], who also mentioned that the lattice diffusivity of hydrogen in the low carbon alloy was higher than in the high carbon steel. When these curves are compared to the ideal Fick's law, the transient is less steep and more extended. This is attributed to the presence of hydrogen trapping sites which delay the experimental transient compared to the theoretical curve described by Fick's law which assumes ideal diffusion.

At this cross-head deformation speed, the effect of the distance hydrogen can diffuse plays a negligible role since the actual distances hydrogen can diffuse to at this deformation speed is just 0.18 mm for B2 and 0.10 mm for B4, which is considered too low to influence significantly the HE susceptibility.

In conclusion, a clear tendency was observed that two parameters played an important role: the amount of diffusible hydrogen mattered and the ability of hydrogen to reach a critical region, which was correlated with the hydrogen diffusion coefficient through a certain microstructure. A confirmation for this tendency was envisaged by performing tensile tests at a cross-head deformation speed which is 100 times lower.

IV.6 Tensile tests at 0.05 mm/min

In order to further demonstrate and confirm the combined role of both the amount of diffusible hydrogen and the distance it can diffuse; tensile samples were tested at a significantly lower cross-head deformation speed of 0.05 mm/min. Hence, diffusible hydrogen had more time to diffuse to the crack tip and play its detrimental role. The influence of the deformation rate was already confirmed by Toh and Baldwin [42], who demonstrated that the RA (reduction of area) decreased with increasing deformation rate, and by the present authors for some advanced high strength steels (cf. Chapter II and III). Each test was performed twice to guarantee reproducible results. The mechanical investigation at this lower rate was done on pure iron and for the B2, B4 and M2 alloys and is summarized in Figure IV-8. For the sake of clarity only one of two performed tests is shown. The different EI's are given in Table IV-6.

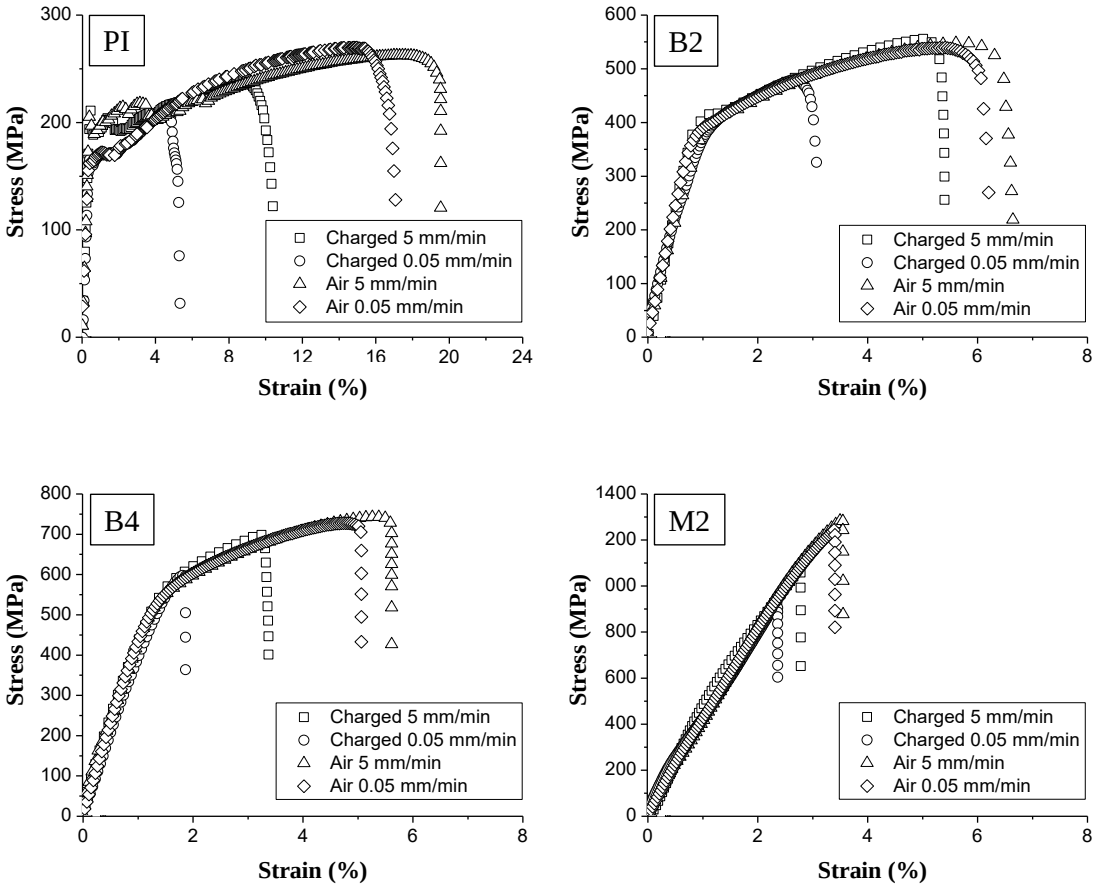

Figure IV-8: Stress-strain curves for pure iron, B2, B4 and M2 at cross-head deformation speed of 5 and 0.05 mm/min.

Generally, the degree of embrittlement increased with lower cross-head deformation speed. This could be nicely correlated with the role of the diffusible hydrogen which could diffuse over a larger distance *x*, reach the critical stress zone ahead of the crack tip, and enhance crack propagation. In order to analyze the effect of diffusible hydrogen when lowering the cross-head deformation speed, the embrittlement indices together with the amount of diffusible hydrogen and the approximate distance *x* over which hydrogen can diffuse during the tensile test are presented in Table IV-6.

Table IV-6: The embrittlement indices at 5 and 0.05 mm/min together with the amount of diffusible hydrogen and the distance *x* hydrogen can diffuse during a tensile test at 5 and 0.05 mm/min.

	EI (5 mm/min)	**EI (0.05 mm/min)**	**Diff H (wppm)**	***x* at 5 mm/min (mm)**	***x* at 0.05 mm/min (mm)**
PI	0.46	0.69	0.71	1.1	7.9
B2	0.21	0.50	3.82	0.18	1.36
M2	0.22	0.30	4.72	0.033	0.3
B4	0.40	0.63	8.73	0.10	0.76

The additional mechanical degradation was the lowest for M2 (EI from 22 to 30%), while the effect for B2 (21 to 50%) was higher than for B4 (40 to 63%). In order to explain the increased embrittlement, the combined effect of both the amount of diffusible hydrogen and the hydrogen diffusion distance *x* during the tensile test was investigated at this lower deformation rate.

This combined role is clearly shown when comparing B2 and M2 at a cross-head deformation speed of 0.05 mm/min. On the one hand, the amount of diffusible hydrogen in these grades was approximately similar (3.82 and 4.72 wppm respectively); on the other hand, the increased embrittling behavior of B2 (EI from 21 to 50%) at the lower deformation speed, was a lot higher compared to M2 (EI from 22 to 30%). This emphasized the importance of the hydrogen diffusion coefficient since the present phases have a clear impact on the diffusion phenomena. The martensitic constituents hindered diffusion of hydrogen more than bainitic structures, as observed by the hydrogen diffusion coefficients of both microstructural features [9] [43]. More specific, at a cross-head deformation speed of 0.05 mm/min, hydrogen is enabled to diffuse approximately 0.3 mm in the martensitic phase, whereas hydrogen could move 0.93 mm in the bainitic phase (Table IV-6).

The combined effect of the amount of diffusible hydrogen and the hydrogen diffusivity is also nicely demonstrated when comparing B2 and B4 at a cross-head deformation speed of 0.05 mm/min. Indeed, the effect of lowering the cross-head deformation speed was more pronounced in B2 (EI from 21 to 50%) compared to B4 (EI from 40 to 63%), even though the amount of diffusible hydrogen was higher for B4. This observation is a consequence of the larger distance *x* that the diffusible hydrogen can migrate during the test in B2 (cf. Table IV-6). Diffusible hydrogen is expected to play a major role in hydrogen embrittlement because of its interactions with dislocations, its role during crack initiation and propagation. Additionally, hydrogen is attracted to highly stressed zones ahead of the crack tip. The ability to more easily reach these critical stress zones assists crack propagation at lower cross-head deformation speed, which results in an increase of the hydrogen induced ductility loss. The lower diffusion coefficient in B4 explains the lower increase in EI for this material when lowering the tensile test speed. Alternatively, at the higher cross-head deformation speed, only a limited diffusion could take place and therefore, the amount of diffusible hydrogen plays a more prominent role in the observed EI for both materials.

Similar reasoning could be made for the behavior of PI considering that this material contained the lowest percentage diffusible hydrogen, but has a high EI. Nevertheless, pure iron did not contain that many defects or microstructural constituents, which decreased the diffusion coefficient. This enabled hydrogen to diffuse fast through the lattice, leading to a considerable embrittlement at both deformation rates.

As a general conclusion, this section nicely confirmed the proposed reasoning that a direct link between the measured amount of diffusible hydrogen and the increased embrittling behavior when lowering the tensile test speed is impossible without also incorporating the hydrogen diffusion coefficient of that specific microstructure into the discussion.

IV.7 Conclusion

Tensile tests combined with in-situ hydrogen charging were performed on generic Fe-C alloys. Different phases, such as pearlite, bainite and martensite were induced in a 0.2 %C Fe-C alloy by an appropriate heat treatment. Pure iron was used as a reference material and a variation in the carbon content up to 0.4% was established for the bainitic grade. The experiments showed a considerable ductility loss due to hydrogen pick-up, although the degree of embrittlement varied considerably between the grades. The tests at a cross-head deformation speed of 5 mm/min showed that pure iron was very sensitive to hydrogen embrittlement (EI of 46%), which was correlated to possibly internal damage and a high hydrogen diffusion coefficient in the ferrite. For the 0.2% C Fe-C alloys, the pearlitic microsctructure was more susceptible to HE compared to the bainitic and martensitic grade, which exhibited a similar HE response. This could also be understood in terms of diffusible hydrogen and the distance by which hydrogen can diffuse during the tensile test. Increasing the carbon content up to 0.4% for the bainitic microstructure resulted in an increased HE due to the larger amount of diffusible hydrogen, respectively 3.82 and 8.73 wppm hydrogen for B2 and B4. The influence of the diffusion coefficient was negligible at this cross-head deformation speed of 5 mm/min.

The yield strength of the materials was affected by hydrogen charging due to solid solution strengthening caused by the interstitial hydrogen as the increase in yield strength could be correlated with the total amount of hydrogen charged into the sample.

Tensile tests performed at a lower cross-head deformation speed of 0.05 mm/min allowed to further elaborate the combined effect of both the amount of diffusible hydrogen and the hydrogen diffusion distance during the test. An additional ductility loss was observed, which was least noticed for the martensitic grade (EI from 22 to 30%), as this material showed the lowest hydrogen diffusion coefficient. It could also be concluded that, although adding carbon resulted in a higher amount of diffusible hydrogen, a lower increase in terms of HE was obtained for B4 (EI from 40 to 63%) compared to B2 (EI from 21 to 50%) when lowering the cross-head deformation speed. This was related to the lower hydrogen diffusion coefficient of B4.

IV.8 References

[1] Woodtli J, Kieselbach R, „Damage due to hydrogen embrittlement and stress corrosion cracking," *Eng Fail Anal*, vol. 7, pp. 427-450, 2000..

[2] Hilditch TB, Lee SB, Speer JG, Matlock DK, „Response to Hydrogen Charging in High Strength Automotive Sheet Steel Products," *SAE Technical Paper*, 2003, http://dx.doi.org/10.4271/2003-01-0525.

[3] Depover T, Pérez Escobar D, Wallaert E, Zermout Z, Verbeken K, „Effect of in-situ hydrogen charging on the mechanical properties of advanced high strength steels," *Int Journal of Hydrogen Energy*, vol. 39, pp. 4647-4656, 2014.

[4] Loidl M, Kolk O, „Hydrogen embrittlement in HSSs limits use in lightweight body," *Adv Mat Process*, pp. 22-25, 2011, BMW Group, Germany.

[5] Johnson WH, „On some remarkable change produced in iron and steel by the action of hydrogen and acids.," *Proceedings of the Royal Society of London*, vol. 23, pp. 168-179, 1875.

[6] Bernstein IM, „The role of hydrogen in the embrittlement of iron and steel," *Mater Sci Eng*, Vol. 6, pp. 1-19, 1970.

[7] Oriani RA, „Hydrogen embrittlement of steels," *Ann. Rev Mater Sci*, vol. 8, pp. 327-357, 1978.

[8] Troiano AR, „Hydrogen embrittlement of high strength FCC alloys," in:, *Hydrogen in Metals*, ASM, Metals Park, OH, 1974, pp. 3-16.

[9] Chan SLI, „Hydrogen trapping ability of steels with different microstructures," *Journal Chin Inst Eng*, vol. 22, pp. 43-53, 1999.

[10] Snape E, „Roles of composition and microstructure in sulfide cracking of steel," *Corrosion*, vol. 24, pp. 261-282, 1968.

[11] Hudson RM, Stragand GL, „Effect of cold drawing on hydrogen behavior in steel," *Corrosion*, vol.16, pp. 253-258, 1960.

[12] Marandet B, „Effect of cold work on the dissolution and the diffusion of hydrogen in unalloyed carbon steels," in: *Proceedings of the International Conference on Stress Corrosion Cracking and Hydrogen Embrittlement of Iron Base Alloys*, NACE-5, NACE, Houston, TX, 1977, pp. 774–787.

[13] Thompson AW, Bernstein IM, „The role of metallurgical variables in hydrogen-assisted environmental fracture," in: *Advances in Corrosion Science and Technology*, vol. 7, Plenum Press, New York, 1980, pp. 53–175.

[14] Chan SLI, Charles JA, „Effect of carbon content on hydrogen occlusivity and embrittlement of ferrite-pearlite steels," *Mater Sci Technol*, vol. 2, pp. 956-962, 1986.

[15] Chan SLI, Lee HL, Yang JR, „Effect of carbon content and martensitic morphology on hydrogen occlusivity and effective hydrogen diffusivity," in: *Proceedings of the 4th International Conference on the Effect of Hydrogen on the Behavior of Materials*, PA, 1990, pp. 145–155.

[16] Chan SLI, Charles JA, „Hydrogen occlusivity of steels with different microstructures," in: *Proceedings of 5th Asian-Pacific Corrosion Control Conference*, vol. 2, Melbourne, Australia, 1987.

[17] Pérez Escobar D, Depover T, Wallaert E, Duprez L, Verbeken K, Verhaege M, „Combined thermal desorption spectroscopy, differential scanning calorimetry, scanning electron microscopy and X-ray diffraction study of hydrogen trapping in cold deformed TRIP steel," *Acta Mat*, vol. 60, pp. 2593-2605, 2012.

[18] Kerns GE, Wang MT, Staehle TW „Stress corrosion cracking and hydrogen embrittlement in high strength steels," in *Stress corrosion cracking and hydrogen embrittlement of iron base alloys*, NACE-5, Houston, TX, 1977, pp. 700-735.

[19] Fujita T, Yamada Y, „Physical metallurgy and SCC in high strength steels', in *Stress corrosion cracking and hydrogen embrittlement of iron base alloys*, NACE-5, Houston, TX, 1977, pp. 736-746.

[20] Bernstein IM, Thompson AW, „Hydrogen in materials," in *Advances in corrosion science and technology*, New York, Plenum Press, vol. 7, 1988, pp. 53.

[21] Akbasoglu FC, Edmonds DV, „Rolling contact fatigue and fatigue crack propagation in 1C–1.5Cr bearing steel in the bainitic condition," *Metall Trans A*, vol. 21, pp. 889-893, 1990

[22] Luppo MI, Ovejero-Garcia J, „The influence of microstructure on the trapping and diffusion of hydrogen in a low carbon steel," *Corrosion Science*, vol. 32, pp. 1125– 1136, 1991.

[23] Duprez L, Verbeken K, Verhaege M, „Effect of hydrogen on the mechanical properties of multiphase high strength steels," in *Proc. of the 2008 Int. Hydrogen Conf.*, Jackson, Wyoming, USA, 2008.

[24] Novak P, Yuan R, Somerday BP, Sofronis P, Ritchie RO, „A statistical, physical-based, micro-mechanical model of hydrogen-induced intergranular fracture in steel," *Journal of Mechanics and Physics of Solids*, vol. 58, pp. 206-226, 2010.

[25] Depover T, Pérez Escobar D, Wallaert E, Zermout Z, Verbeken K, „Effect of in-situ hydrogen charging on the mechanical properties of advanced high strength steels," *Int Journal of Hydrogen Energy*, vol. 39, pp. 4647-4656, 2014.

[26] Tau L, Chan SLI, Shin CS, „Hydrogen enhanced fatigue crack propagation of bainitic and tempered martensitic steels," *Corrosion Science*, vol. 38, pp. 2049–2060, 1996.

[27] Wallaert E, Depover T, Arafin MA, Verbeken K, „Thermal desorption spectroscopy evaluation of the hydrogen trapping capacity of NbC and NbN precipitates," *Met Mat Trans A*, vol. 45, pp. 2412-2420, 2014.

[28] Pérez Escobar D, Wallaert E, Duprez L, Atrens A, Verbeken K, „Thermal Desorption Spectroscopy Study of the Interaction of Hydrogen with TiC Precipitates," *Met Mater Int*, vol. 19, pp. 741-748, 2013.

[29] Depover T, Van den Eeckhout E, Wallaert E, Zermout Z, Verbeken K, „Evaluation of the effect of TiC precipitates on the hydrogen trapping capacity of Fe-C-Ti alloys," *Adv Mat Research*, vol. 922, pp. 102-107, 2014.

[30] Pérez Escobar D, Verbeken K, Duprez L, Verhaege M, „Evaluation of hydrogen trapping in high strength steels by thermal desorption spectroscopy," *Mat Sci and Eng A*, vol. 551, pp. 50-58, 2012.

[31] Koyama M, Tasan CC, Akiyama E, Tsuzaki K, Raabe D, „Hydrogen-assisted decohesion and localized plasticity in dual-phase steel," *Acta Mat*, vol. 70, pp. 174-187, 2014.

[32] Laureys A, Depover T, Petrov R, Verbeken K, „Characterization of hydrogen induced cracking in TRIP-assisted steels," *Int Journal of Hydrogen Energy*, vol. 40, nr. 47, pp. 16901-16912, 2015.

[33] Laureys L, Depover T, Petrov R, Verbeken K, „Microstructural characterization of hydrogen induced cracking in TRIP-assisted steel by EBSD," *Materials Characterization*, vol. 112, pp. 169-179, 2016..

[34] Pérez Escobar D, Depover T, Wallaert E, Duprez L, Verhaege M, Verbeken K, „Thermal desorption spectroscopy study of the interaction between hydrogen and different microstructural constituents in lab cast Fe-C alloys," *Corrosion Science*, vol. 65, pp. 199-208, 2012.

[35 Pérez Escobar D, Miñambres C, Duprez L, Verbeken K, Verhaege M, „Internal and surface damage of multiphase steels and pure iron after electrochemical hydrogen charging," *Corrosion Science,* vol. 53, p. 3166–3176, 2011.

[36] Zhao MC, Liu M, Atrens A, Shan YY, Yang K, „Effect of applied stress and microstructure on sulfide stress cracking resistance of pipeline steels subject to hydrogne sulfide," *Mat Sci and Eng A,* vol. 478, pp. 43-47, 2008.

[37] Bhadeshia HKDH, „Interpretation of the Microstructure of Steel," University of Cambridge. Available from: http://www.msm.cam.ac.ik/phase-trans/2008/Steel_Microstructure/SM.html/.

[38] Liu Q, Irwanto B, Atrens A, „The influence of hydrogen on 3.5NiCrMoV steel studied using the linearly increasing stress test," *Corrosion Science,* vol. 67, pp. 193-203, 2013.

[39] Ren XC, Zhou QJ, Shan GB, Chu WY, Li JX, Su YJ, Qiao LJ, „A nucleation mechanism of hydrogen blister in metals and alloys," *Met Mat Trans A*, vol. 39, pp. 87-97, 2008.

[40] Griesche A, Dabah E, Kannengiesser T, Kardjilov N, Hilger A, Manke I, „Three-dimensional imaging of hydrogen blister in iron with neutron tomography," *Acta Mat*., vol.78, pp. 14-22, 2014.

[41] Hadam U, Zakroczymski T, „Absorption of hydrogen in tensile strained iron and high carbon steel studied by electrochemical permeation and desorption techniques," *Int Journal of Hydrogen Energy,* vol. 34, pp. 2449-2459, 2009.

[42] Toh T, Baldwin WM, „Stress corrosion cracking and embrittlement," In: *Stress Corrosion Cracking and Embrittlement*. New York, Wiley, 1956, pp. 176-186.

[43] Depover T, Van den Eeckhout E, Verbeken K, „The impact of hydrogen on the ductility loss of bainitic Fe-C alloys," *Materials Science Technology* 2016, DOI: 10.1080/02670836.2015.1137387.

CHAPTER V:

The effect of TiC on the hydrogen induced ductility loss and trapping behavior of Fe-C-Ti alloys*

V.1 Introduction

During the development of recent steel alloys, a relevant topic of study has been the role of carbides, for instance in the strengthening and toughening of micro-alloyed steels [1] where carbide forming elements allow to take benefit of the precipitation strengthening phenomenon. On the other hand, an increased strength level in steels is desired as it allows the construction of lighter structures meeting more stringent safety regulations. However, steels with a high strength level are considered to be more prone to hydrogen embrittlement [2] [3], posing issues to their applicability [4].

Apart from their strengthening effect, carbides are often cited as beneficial in terms of hydrogen trapping ability as well. Since a limited amount of diffusible hydrogen might be sufficient to cause a catastrophic failure, well-designed hydrogen trapping sites might be a relevant strategy to enhance the resistance against hydrogen embrittlement (HE). Although, thermal desorption spectroscopy (TDS) studies demonstrated the hydrogen trapping ability of several carbides [5] [6] [7] [8] [9] [10] [11] [12] [13], literature integrating their effect on the mechanical properties in combination with the presence of hydrogen are limited [14] [15].

When studying high strength steels, carbides are only one aspect of a large set of microstructural features such as grain boundaries, martensite lath boundaries, dislocations, interfaces between carbide and matrix, other precipitates, vacancies, etc. which can all trap hydrogen in a reversible or irreversible way. The interaction of these high strength steels with hydrogen has been investigated thoroughly during the last decade [16] [17]. Recently, our group presented some results on four industrial high strength steels, i.e. a dual phase (DP), a transformation induced plasticity (TRIP), a high strength low alloyed (HSLA) and a ferrite bainite (FB) alloy.

Pérez Escobar *et al.* [18] studied the available trapping sites and their trapping capacity by performing TDS and hot extraction. They observed that the steels trapped a different amount of hydrogen after electrochemical charging and that a different amount of diffusible hydrogen effused from the material as a function of increasing desorption times in vacuum. This confirms results by Duprez *et al.* [19] since a different amount of ductility recovery for these materials was observed when hydrogen charged tensile samples were left one week in air before actually testing them. Additionally, the obtained activation energies in [18] for the different traps in these high strength steels were in the same range, indicating the complex correlation between a certain microstructural feature and a specific obtained desorption peak. Only the TRIP steel showed a high temperature peak with an E_a of 90 kJ/mol which was proved to come from hydrogen trapped in the retained austenite [20]. Furthermore, a

* This chapter is based on the following publication: Depover T, Verbeken K, *Corrosion Science* (2016), submitted.

detailed microstructural analysis was performed on this material by Laureys *et al.* [21] [22] showing that crack initiation occurred in the martensitic islands and that crack propagation was mainly stress driven. Additionally, the impact of hydrogen diffusion was recently visualized in DP steel by studying the fracture surfaces of an in-situ charged tensile specimen [23]. In this work, the calculated diffusion distance matched perfectly with the observed transition between hydrogen induced brittle and ductile fracture (cf. Chapter III).
The mechanical properties of these steels were investigated as well (cf. Chapter II) and a significant hydrogen induced ductility loss was observed, except for the HSLA steel, which was attributed to the presence of Ti- and Nb- carbo-nitrides. Moreover, Pérez Escobar *et al*. [24] found that this HSLA steel had the highest resistance to hydrogen cracking produced by electrochemical hydrogen charging, while TDS [18] demonstrated that hydrogen was more strongly trapped in the HSLA steel, which was also attributed to the presence of the Ti-Nb carbo-nitrides.

Because of their potential, recently more and more emphasis is put on the addition of carbides as hydrogen trapping sites. Wei and Tsuzaki performed various in-depth investigations on the interaction of hydrogen with Ti based precipitates. Hydrogen was deeply trapped by semi-coherent TiC precipitates, located at the broad face of the disc-like TiC precipitate [8] [13]. Precipitation can generate various trap sites; the precipitate/ferrite interface, the coherency strain region surrounding the precipitate and crystal defects in the precipitate. Takahashi *et al*. [25] confirmed the presence of hydrogen at the precipitate/matrix interface with an atomic-scale observation of deuterium atoms trapped at the surfaces of nanosized TiC, using atom probe tomography. In another work [8], the hydrogen trapping behavior of TiC changed according to its coherent or incoherent interfacial character. Semi-coherent precipitates demonstrated different hydrogen trapping features than incoherent particles. Semi-coherent interfaces of the TiC precipitate did not trap hydrogen during tempering, but trapped hydrogen during cathodic charging at room temperature, for which a desorption activation energy of 55.8 kJ/mol was obtained. The interface lost coherency with carbide growth, which resulted in an increase in trapping activation energy. Consequently, hydrogen trapping was more difficult during cathodic charging at room temperature due to the high energy barrier that needed to be overcome by hydrogen to get trapped. Therefore, an incoherent TiC was not capable to internally trap hydrogen during cathodic charging at room temperature, but absorbed hydrogen during its heat treatment or when charged gaseously at elevated temperature. The amount of hydrogen trapped by incoherent TiC depended mainly on its volume. Consequently, they concluded that hydrogen was trapped within the precipitate, rather than at particle/matrix interface. Carbon vacancies were assumed to be the hydrogen trap sites here. Wei and Tsuzaki further studied the effect of TiC in [9]. The E_a for hydrogen desorption from the incoherent TiC in a 0.05C-0.22Ti-2.0Ni steel was about 85.7 kJ/mol. Alternatively, a higher activation energy of 116 kJ/mol was obtained for the coarse incoherent TiC particles in a 0.42C-0.30Ti steel tempered at 650°C and 700°C, which decreased to 68 kJ/mol when the material was tempered at 500°C. The TiC coherent precipitates in the latter steel showed an E_a from 46 to 59 kJ/mol, depending on tempering temperature as well.

Pérez Escobar *et al.* [10] investigated by means of TDS measurements the interaction of hydrogen with TiC in a 0.025C – 0.09Ti ferritic material. After annealing at elevated temperature in a hydrogen atmosphere, a high temperature peak was observed, which was attributed to irreversible trapping by TiC precipitates with an E_a of

145 kJ/mol. A combination of gaseous with electrochemical hydrogen charging resulted in an additional low temperature peak, which originated from reversible traps from hydrogen at grain boundaries.
Pressouyre and Bernstein [7] reported that coherent TiC were less effective in terms of trapping compared to incoherent precipitates. Additionally, they found that the activation energy increased with precipitate size. These observations were also obtained by Lee and Lee [6] by TDS analysis. They found a low temperature peak corresponding to hydrogen trapped at grain boundaries, a second peak correlated with semi-coherent interfaces, and a high temperature peak, which increased with the size of the incoherent particles and activation energies similar to other literature data.

Generally, trapping diffusible hydrogen using nano-sized carbides as hydrogen traps is one of the main strategies to enhance the resistance against HE. Wei *et al*. [13] estimated that coherent and semi-coherent TiC, VC and NbC were all able to trap hydrogen during cathodic charging at room temperature, whereas only for TiC also the incoherent precipitates trapped hydrogen. Consequently, carbides are assumed to be effective as hydrogen traps and beneficial in increasing resistance to the hydrogen induced degradation of the mechanical properties [14]. Moreover, Ren and Zeng [26] found that a TiC film on a 304 stainless steel significantly decreased its corrosion rate and Hirohata *et al*. [27] found that a TiO_2/TiC coating reduced hydrogen absorption. Alternatively, Todoshchenko *et al.* [28] studied the hydrogen effects on fracture of high-strength steels and revealed that hydrogen induced cracking initiated at TiN/TiC particles.

One common observation from most literature data is that the complex microstructure of multiphase high strength steels hinders linking a certain observed hydrogen related result to a specific microstructural feature. Therefore, laboratory Fe-C alloys with a carbon content of 0.2 and 0.4 wt% together with pure iron as a reference material were studied in [29] and in Chapter IV. Different microstructural phases; i.e. pearlite, bainite and martensite, were induced. The sensitivity of the microstructures to hydrogen damage was studied by evaluating the tendency for blister formation [30]. No correlation was found between the carbon content and the appearance of blisters, whereas pure iron appeared to be most prone to blister formation. They concluded that the microstructure played a more important role than the amount of carbon in terms of hydrogen induced damage. Furthermore, in another work [31], the hydrogen induced ductility loss on several bainitic materials could be linked to a higher amount of charged hydrogen. However, pure iron showed again the highest susceptibility to HE, which was attributed to its high hydrogen diffusivity [32]. The combined effect of both the amount of hydrogen and the hydrogen diffusivity was demonstrated by decreasing the strain rate during the tensile test. The degree of HE increased when the cross-head deformation speed was reduced due to the impact of hydrogen diffusion (cf. Chapter II-IV).
The goal of this chapter was to study the interaction between hydrogen and TiC precipitates, using simplified Fe-C-Ti martensitic steels designed to contain only TiC particles, in order to be able to study in detail the characteristics of this type of precipitate embedded in a quenched and tempered microstructure in terms of hydrogen embrittlement, trapping capacity and ability. An industrially relevant high strength level was aimed for.

V.2 Experimental procedure

V.2.1 Material characterization

Three generic Fe-C-Ti alloys, containing about 0.1, 0.2 and 0.3 wt% C, were laboratory cast with a stoichiometric amount of the ternary alloying element Ti. The carbon variation will allow a trustworthy evaluation of the impact of the carbides on a different strength level and to confirm their role in different Fe-C-Ti alloys. The chemical composition is given in Table V-1.

Table V-1: Chemical composition of the used materials in wt%.

Material/Element	C	Ti	Other
Alloy A	0.099	0.380	200-300 ppm Al
Alloy B	0.202	0.740	
Alloy C	0.313	1.340	

The materials were cast in a Pfeiffer VSG100 incremental vacuum melting and casting unit under an argon gas atmosphere. The materials were hot and cold rolled to obtain a final thickness of 1 mm. An appropriate heat treatment was applied in order to obtain two main conditions; one as-quenched (as-Q) state with as little precipitates as possible and one quenched and tempered (Q&T) state where free carbon is enabled to precipitate with Ti during tempering. A temperature vs. time graph of the used heat treatment is presented in Figure V-1. All materials were austenitized at 1250°C for 10 minutes to obtain a full austenitic microstructure and to dissolve the carbides from the processing. These materials were then quenched in brine water (7wt% NaCl) to obtain a full martensitic structure. This is the first condition which will be further referred to as as-Q.

Next to the as-Q condition, a second condition was prepared by tempering the quenched material at a certain temperature for 1 hour in order to generate, in a controlled way, TiC precipitates, followed again by brine water quenching. Tempering was performed at different temperatures to determine at which temperature the secondary hardening effect, due to the generation of small TiC, was most outspoken.

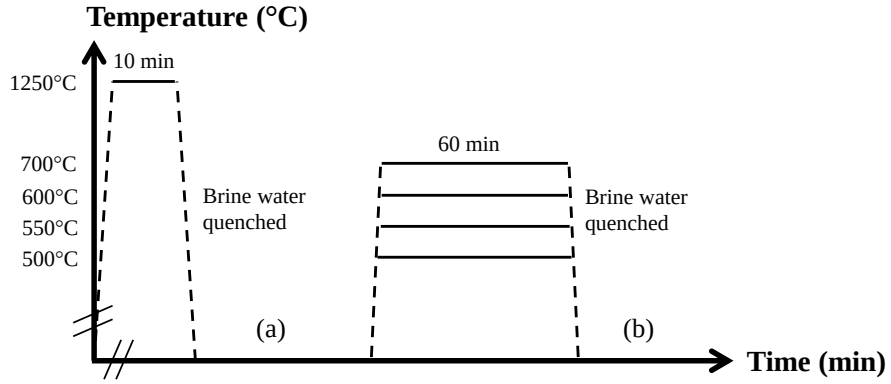

Figure V-1: Temperature-time graph of the heat treatments to induce: (a) as-Q, (b) Q&T condition.

All materials were further ground and tensile samples were machined with their tensile axis parallel to the rolling direction and the specimen geometry is shown in Figure V-2. Finally, the surface of the samples was sandblasted to remove possible oxides remaining from processing.

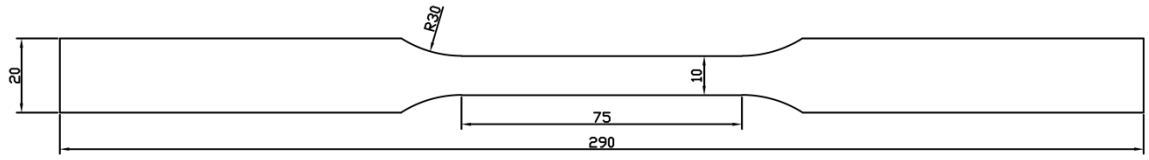

Figure V-2: Tensile sample geometry in mm.

Vickers hardness measurements were performed to determine the as-Q hardness level and the tempering temperature at which secondary hardening was most effective. A weight of 2 kg and a pyramidal diamond tip was used.

The microstructure was first investigated by light optical microscopy (LOM), for which grinding, polishing and etching with 4% Nital for 10 seconds was done. Secondly, high resolution scanning electron microscopy (HRSEM) and transmission electron microscopy (HRTEM) allowed to characterize carbides in terms of their size, size distribution and morphology. Therefore, carbon replica's and thin foils were prepared.

V.2.2 Hydrogen induced mechanical degradation

The hydrogen induced ductility loss was determined by comparing tensile tests performed in air with tests done on hydrogen charged samples. Hydrogen was introduced in the materials by electrochemical pre-charging using a 1g/L thiourea in a 0.5 M H_2SO_4 solution at a current density of 0.8 mA/cm² for 1 hour, while in-situ charging continued during the tensile test. The conditions were chosen in such a way that they did not create blisters or any internal damage, as shown further and reported on similar alloys in [30], and that a complete saturation of the materials was ensured as demonstrated in Figure V-3 for the as-Q condition (cf. section V.2.3 for the technique used to obtain this Figure).

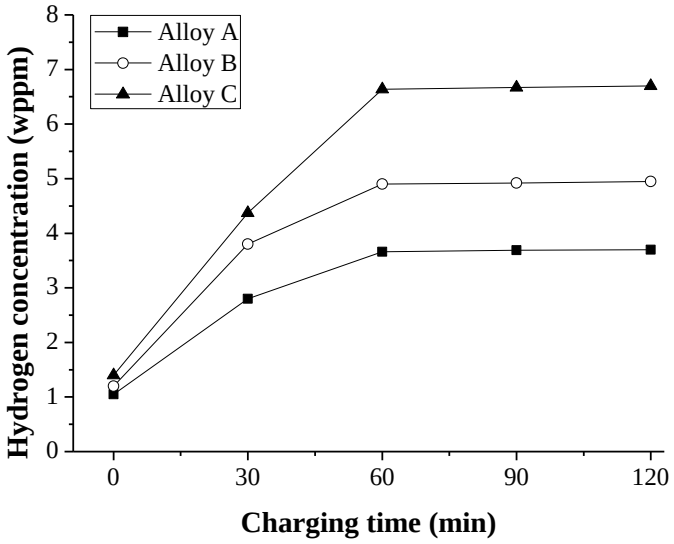

Figure V-3: Hydrogen concentration vs. charging time.

The tensile tests were performed at a cross-head deformation speed of 5 mm/min, with a corresponding strain rate of 1.11 x 10^{-3} s^{-1}, similar to Zhao *et al.* [33]. To compare the sensitivity of the hydrogen induced mechanical degradation, the percentage hydrogen embrittlement (%HE) is defined as [2] [23]:

$$\%HE = 100 \cdot \left(1 - \frac{\varepsilon_{ch}}{\varepsilon_{un}}\right) \quad \text{(V-1)}$$

with ε_{ch} and ε_{un} being the elongation of the charged and uncharged sample, respectively. Hence, the %HE varies between 0 and 1, with 0 meaning that there is no ductility loss and the material is insensitive to HE. When an index of 1 is obtained, the ductility drop is 100% and HE is maximal.

V.2.3 Determination of diffusible and total hydrogen content

In order to determine the hydrogen saturation level, melt/hot extraction was used. To determine the hydrogen content, samples were charged electrochemically using the same conditions as for the HE characterization. Measurements were done at 1600°C for the total hydrogen and at 300°C for the diffusible hydrogen content, which is the same definition for diffusible hydrogen as proposed by Akiyama *et al.* [34] [35].

The system comprises a pulse furnace in which a pre-weighted sample is heated. At this temperature, the metallic sample heats up and releases its hydrogen as gaseous H_2. The latter is taken up by a nitrogen flow and the mixture (N_2–H_2) is sent to a thermal conductivity measuring cell. The thermal conductivity of the mixture depends on the H_2 concentration because of the significant difference in conductivity of H_2 and N_2. The software calculates the hydrogen concentration of the sample based on the thermal conductivity variation.

However, it should be added that calibration modus was different for the both kind of extractions. A sample mass calibration was used for the total amount of hydrogen, whereas a gas calibration was performed to determine the diffusible hydrogen content.

V.2.4 Determination of hydrogen trapping capacity

Thermal desorption spectroscopy analysis was performed to identify both the hydrogen trapping sites and their corresponding activation energy. The samples were hydrogen charged and three different heating rates (200°C/h, 600°C/h and 1200°C/h) were used. The applied experimental procedure required one hour between the end of hydrogen charging and the start of the TDS measurement as a sufficient vacuum level is necessary in the analysis chamber before the TDS measurement could start. In order to determine the E_a of hydrogen traps related to the peaks observed in the TDS spectra, the method based on the work of Lee *et al.* [36] [37] [38] was used. Equation (V-2) is a simplification of the original formula of Kissinger [39]:

$$\frac{d(\ln\frac{\Phi}{T_{max}^2})}{d(\frac{1}{T_{max}})} = -\frac{E_a}{R} \qquad \text{(V-2)}$$

where Φ is the heating rate (K/min), T_{max} (K) the TDS peak temperature, E_a (J/mol) the detrapping activation energy for the specific hydrogen trap associated with T_{max} and R ($JK^{-1}mol^{-1}$) the universal gas constant. After TDS measurements were performed using different heating rates, the spectra were deconvoluted and the corresponding peak temperatures for a trap were determined. Plotting $\ln(\Phi/T_{max}^2))$ vs. $(1/T_{max})$ allows to obtain the E_a corresponding to that specific trap.

V.2.5 Determination of hydrogen diffusion coefficient

To determine the hydrogen diffusion coefficient, hydrogen electrochemical permeation tests were performed using the Devanathan and Stachurski method [40]. The two compartments were filled with 0.1 M NaOH solution and the polished specimen of 1 mm was clamped in between. The hydrogen entry side acted as the cathode by

applying a current density of 3 mA/cm^2, and the hydrogen exit side (anode) was potentiostatically kept at - 500 mV according to a Hg/Hg_2SO_4 reference electrode. The solutions in the compartments were both stirred with nitrogen bubbling and temperature was maintained constant at 25°C. The apparent hydrogen diffusion coefficient was calculated from the permeation transient using the following formula [41]:

$$D_{app} = \frac{L^2}{7.7\ t}\ (m^2/s) \tag{V-3}$$

where t is the time (s) when the normalized steady state value has reached 0.1 and L is the specimen thickness (m).

V.3 Material characterization

Figure V-4 represents the hardness results for the three alloys in the as-quenched condition and for the different applied tempering temperatures. A distinct secondary hardening peak can clearly be observed after tempering at 600°C, which could be attributed to the precipitation of small TiC particles. These results are in good agreement with the findings of Wei and Tsuzaki on similar alloys [8].

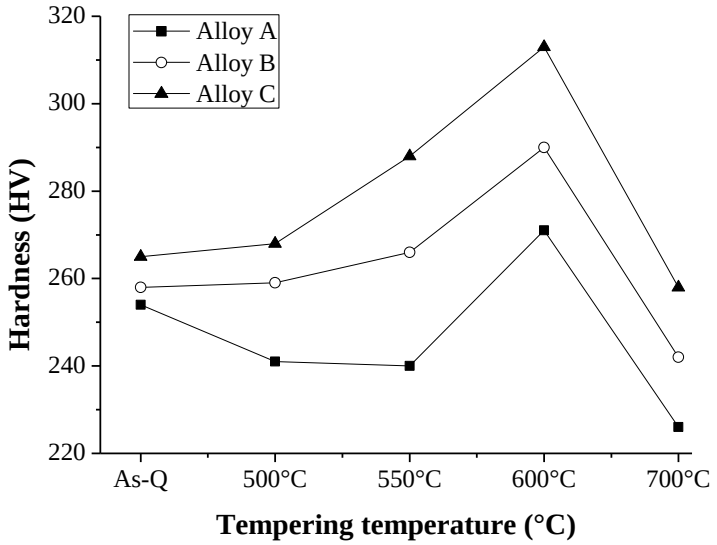

Figure V-4: Hardness vs. tempering temperature evolution for the three Fe-C-Ti alloys.

Remarkable are the small differences between the alloys in the as-quenched condition, since a rather large carbon variation was present. However, the amount of dissolved carbon at an austenization temperature of 1250°C for these stoichiometric compositions can be calculated according to the solubility product for TiC [42]. The thermo-dynamical calculations to determine the amount of dissolved carbon, as defined in Eq. V-4, and are shown in Figure V-5.

$$log_{10}\ \frac{M^m X^n}{MX}\ =\ -\frac{A}{T} + B \tag{V-4}$$

Where, M_mX_n is the precipitate considered, M and X the alloy contents (wt%), T the temperature (K) and A and B constants of the solubility product which are 7000 and 2.75 respectively for TiC according to Irvine [42]. In the present case, only 400-500 ppm carbon is free in the as-quenched condition for alloy A, B and C. As the as-Q hardness level mainly depends on the solute carbon content, this explains the small differences in hardness.

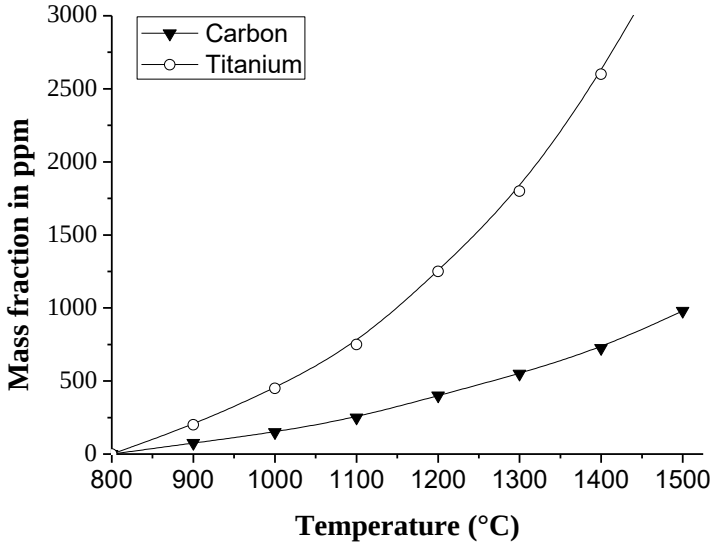

Figure V-5: Mass fraction of carbon and titanium vs. temperature that can be kept in solid solution at each temperature for stoichiometric total content of C and Ti.

The LOM images are shown in Figure V-6 for the as-Q and the Q&T condition when the materials got tempered at 600°C. A martensitic matrix can be observed and in-depth HRSEM and HRTEM were performed to analyze the TiC particles. Results are shown for alloy C. Forward scatter detection (FSD) images of carbon replicas are represented in Figure V-7, whereas TEM bright field images of thin foils are given in Figure V-8 for both the as-Q and Q&T condition. An electron backscatter detector (EBSD) scan, next to an energy dispersive X-ray (EDX) spectrum were also taken in order to confirm cubic TiC particles are indeed present in the microstructure as shown in Figure V-9.

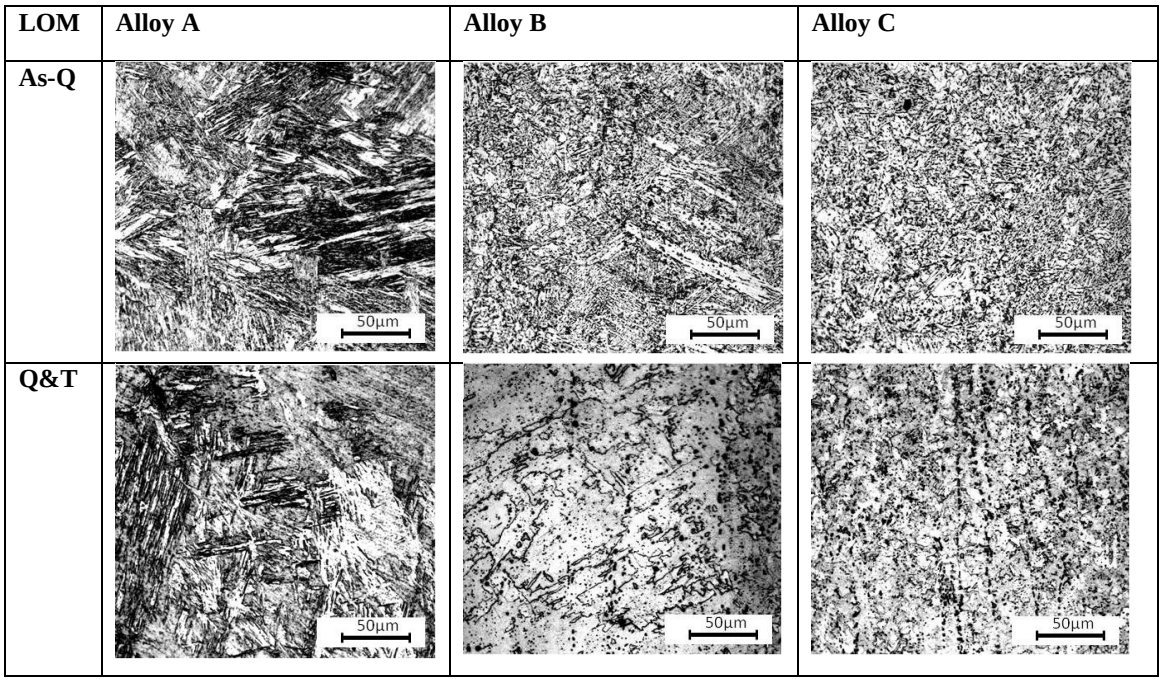

Figure V-6: LOM images of alloy A, B and C in the as-Q and Q&T condition.

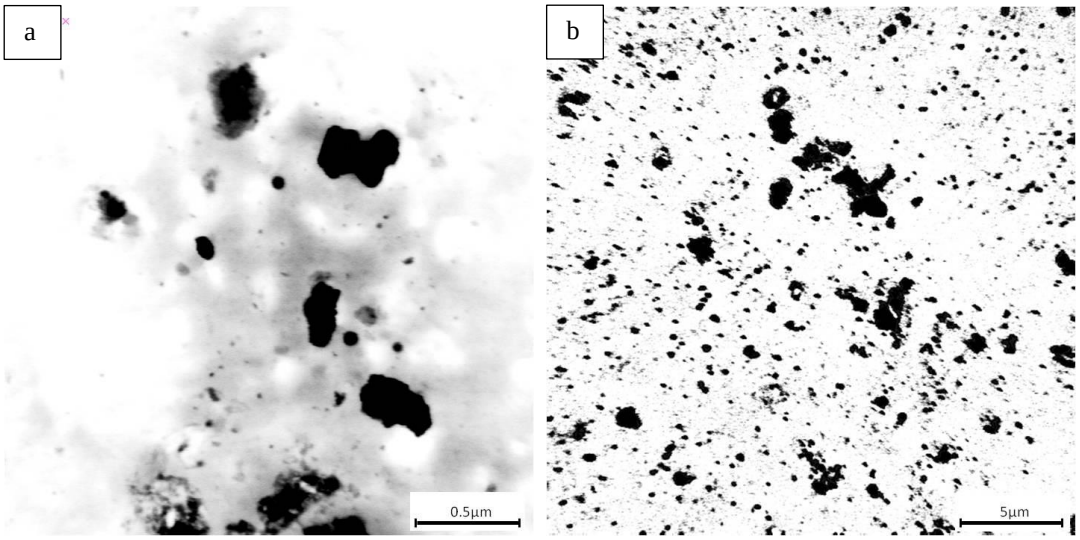

Figure V-7: FSD images of carbon replica's taken from alloy C in the as-Q (a) and Q&T (b) condition.

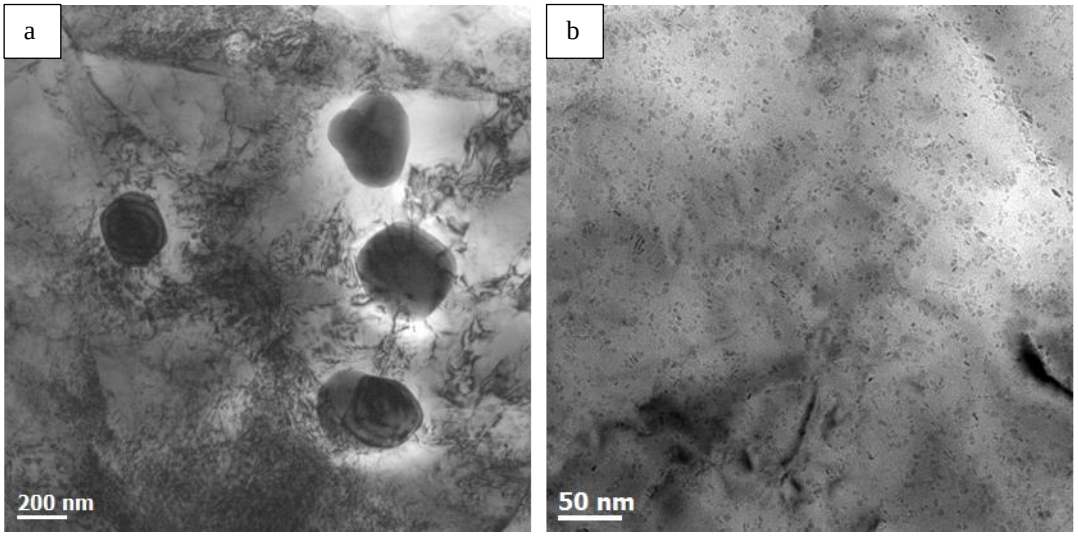

Figure V-8: TEM bright field images of thin foils taken from alloy C in the as-Q (a) and Q&T (b) condition.

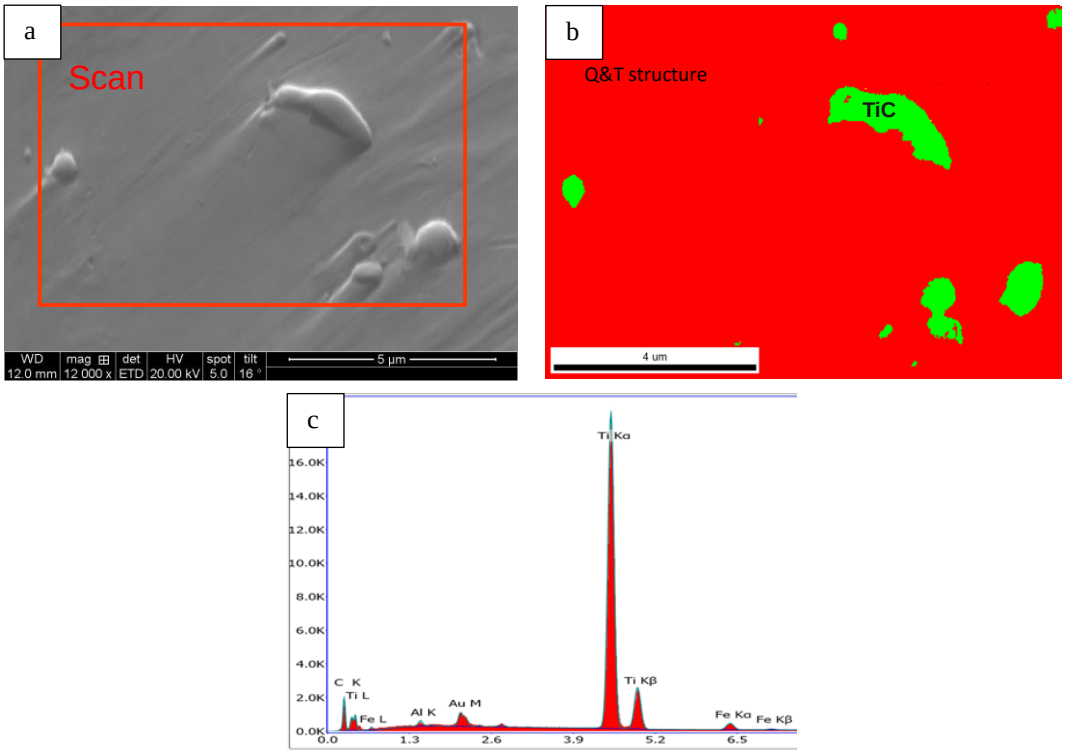

Figure V-9: SEM image (a), phase map obtained from EBSD data (b), EDX spectrum (c) of alloy C Q&T.

Additionally, diffraction patterns from a selected area in the bright field image were taken for alloy C in the Q&T condition and analyzed to confirm TiC particles are indeed present in the microstructure, as shown in Figure V-10. The selected area diffraction in Figure V-10 (a) revealed the existence of the TiC crystal structure with a zone axis along [101]. A dark field image (Figure V-10 (b)) was recorded using the diffraction spot circled in black to confirm TiC were present.

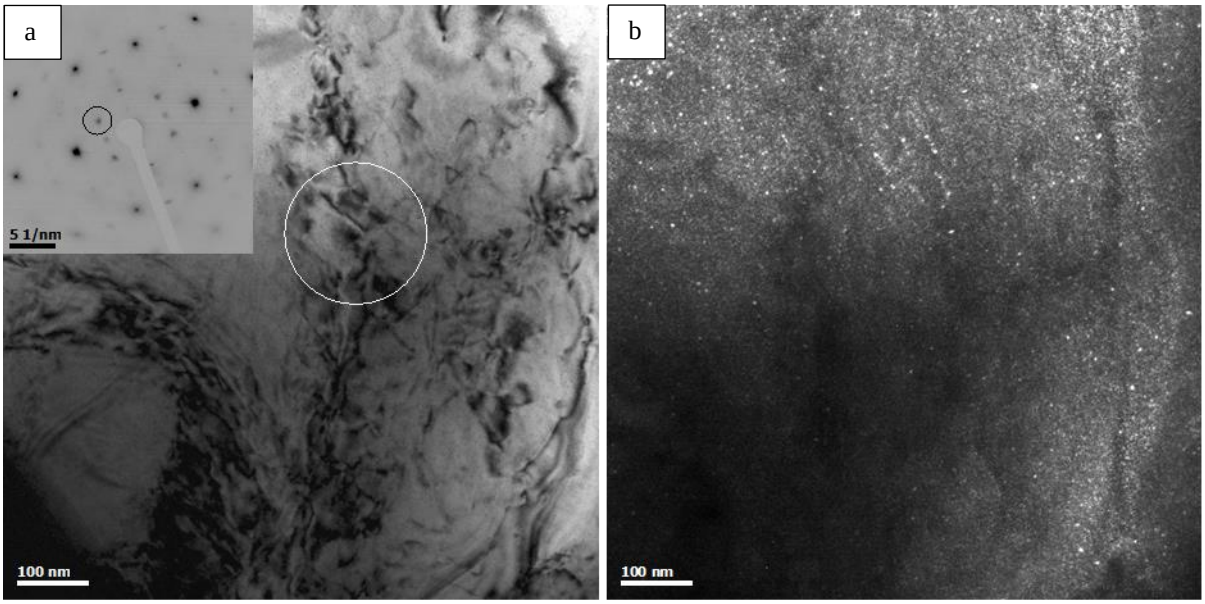

Figure V-10: TEM bright field image of alloy C Q&T (a), of which a selected area diffraction pattern was taken (white circle) and presented within (a). Dark field image (b) taken from the diffraction spot indicated by the black circle in (a).

V.4 Hydrogen induced mechanical degradation

Figure V-11 shows the results of the tensile tests performed at a cross-head deformation speed of 5 mm/min for alloy A, B and C for the as-Q and Q&T state, in uncharged condition and after hydrogen charging. The hydrogen charged results are indicated in bold. Multiple tests were performed which confirmed high reproducibility of the tests. For sake of clarity only one test result is shown for each condition. The mechanical properties are summarized in Table V-2.

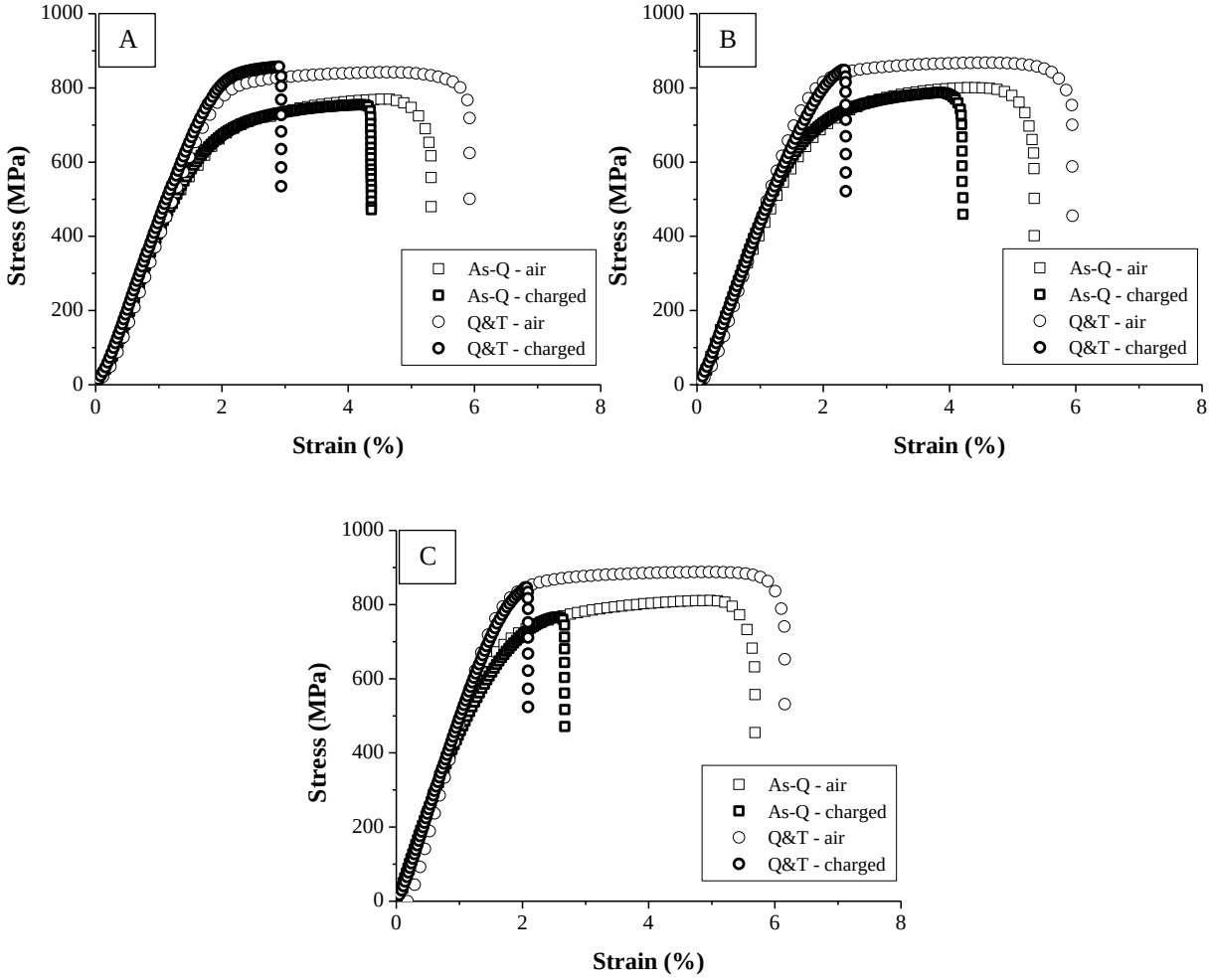

Figure V-11: Stress-strain curves of alloy A, B and C in the as-Q and Q&T condition.

Table V-2: Summary of the mechanical properties.

Mechanical properties	**Alloy A**		**Alloy B**		**Alloy C**	
	As-Q	Q&T	As-Q	Q&T	As-Q	Q&T
Tensile strength (MPa)	770	842	800	868	811	888
%HE	18	50	21	60	53	66

A slightly increasing strength level was obtained for alloy A – B – C, which is in good agreement with the hardness measurements and could be attributed to the higher amount of carbon. Additionally, tempering induced a secondary hardening effect due to the precipitation of carbides, leading to both a higher tensile strength and ductility for the uncharged Q&T materials, which is in correspondence with the HV results as well (cf. Fig. V-4).

A significant hydrogen induced ductility loss was observed for all materials, which augmented with increasing carbon content both in the as-Q and Q&T condition. Remarkably, the Q&T materials showed a considerably higher hydrogen susceptibility, despite the confirmed presence of TiC particles. A thorough hydrogen related characterization of the materials is needed to further elaborate these observations.

V.5 Determination of the hydrogen uptake and trapping capacity

The diffusible and total hydrogen content as obtained by hot/melt extraction after hydrogen charging under the same conditions as for the tensile tests are presented in Figure V-12. The hydrogen contents increased with carbon content, which was also observed previously [29] [30] [31] [32] (cf. Chapter IV). Additionally, the Q&T materials trapped almost double the amount of hydrogen compared to the as-Q alloys. Tempering induced small coherent TiC, which were responsible for the distinct hardness increase at 600°C, and these are able to trap a significant amount of hydrogen. The diffusible hydrogen content, i.e. the amount of hydrogen released by the material at 300°C, is considerably lower than the total hydrogen content, but followed the same trend. These results show a clear correlation with the obtained HE% in section V.4 as the HE susceptibility increased, on the one hand, with carbon content and, on the other hand, when tempered. However, it is not as straightforward that the total/diffusible hydrogen content alone can explain the degree of HE in an alloy as will be demonstrated below.

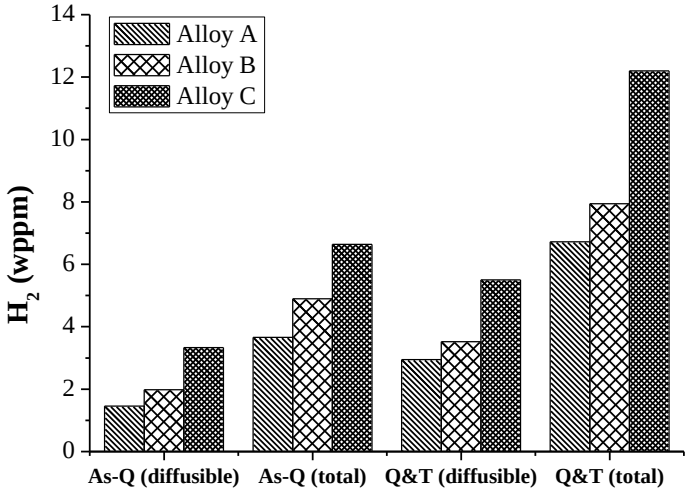

Figure V-12: The total and diffusible amount of hydrogen after electrochemical charging for alloy A, B and C in the as-Q and Q&T condition.

Another noteworthy observation from Figure V-12 is the rather high amount of hydrogen for alloy C Q&T. It was verified whether internal damage, such as small cracks, which might serve as a hydrogen reservoir, originated from charging or not. This was done by, on the one hand, a SEM evaluation and, on the other hand, by tensile testing a charged specimen after discharging it for 72 hours in vacuum. The results are shown in Figure V-13 and V-14, respectively.

Figure V-14 clearly demonstrates that a full ductility recovery was obtained after 72 hours of discharging. In addition, SEM analysis (Figure V-13) did confirm the absence of internal cracks. Since cracks or internal damage cause permanent damage to the sample, which should affect the tensile test results even after discharging, this full ductility recovery indicated that diffusible hydrogen was responsible for the obtained HE%

and that no cracks were present after electrochemical hydrogen charging. In another study [30], comparable laboratory cast alloys with similar carbon content did not show any hydrogen blisters or damage either.

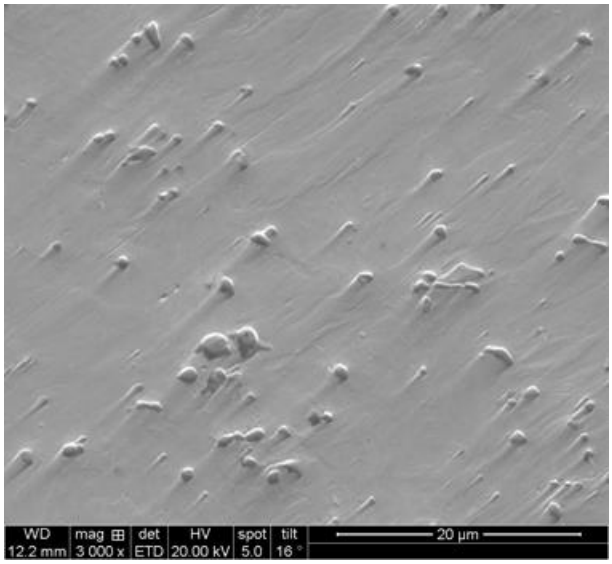

Figure V-13: SEM investigation of alloy C in the Q&T condition.

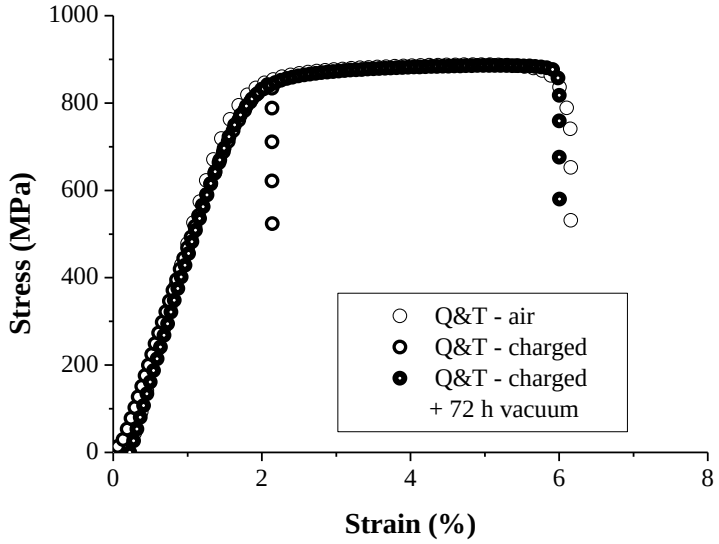

Figure V-14: Stress-strain curves of alloy C - Q&T in the uncharged, charged and charged + 72 hours of vacuum condition.

Within a material, hydrogen trapping is important as it can accommodate a specific amount of otherwise diffusible hydrogen. Therefore, and in order to attribute the trapped hydrogen to a certain microstructural constituent, TDS measurements were performed. The results are shown in Figure V-15 and the corresponding activation energies are summarized in Table V-3. The TDS spectra clearly showed that additional trapping sites were active after tempering. When small TiC precipitates were introduced by tempering, extra peaks were indeed observed, which are therefore linked to the presence of these carbides. Moreover, the presence of extra traps was already clear from hot/melt extraction (cf. Figure V-12) as the Q&T samples contained significantly more hydrogen than the as-Q ones, which is also visible in the TDS spectra.

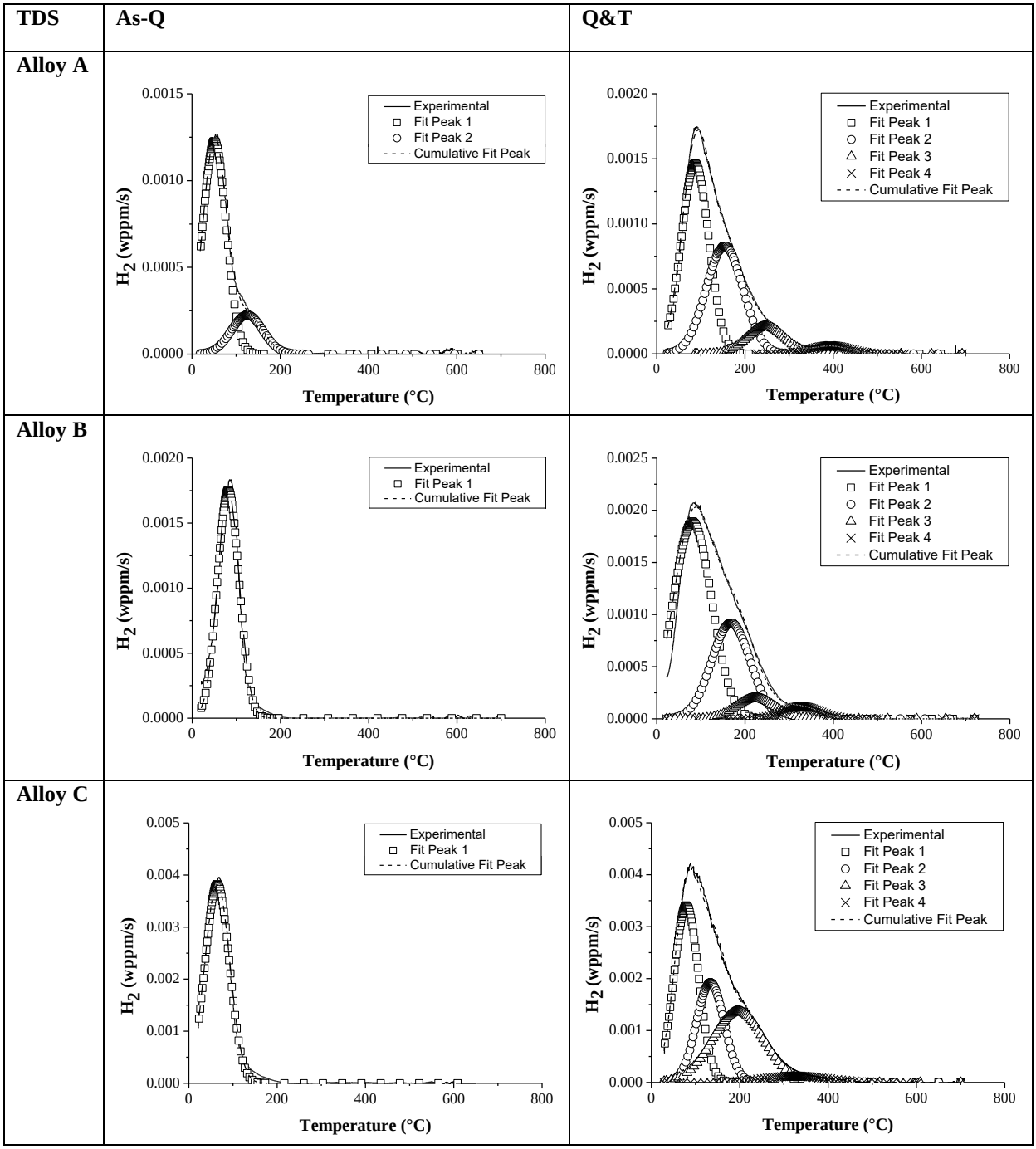

Figure V-15: TDS spectra of alloy A, B and C in the as-Q and Q&T (600°C – 1h) condition after hydrogen charging at a heating rate of 600°C/h.

Table V-3: Summary of the corresponding activation energies for the deconvoluted peaks.

Activation energy (kJ/mol)	Alloy A		Alloy B		Alloy C	
	As-Q	Q&T	As-Q	Q&T	As-Q	Q&T
Peak 1	26	42	30	42	33	48
Peak 2	42	40	/	50	/	53
Peak 3	/	52	/	44	/	47
Peak 4	/	117	/	71	/	60

For the as-Q condition, one main peak was present for all alloys. This first peak corresponded to an activation energy of about 30 kJ/mol, which has been argued to be hydrogen trapped at martensitic lath boundaries [43]. However, hydrogen trapped at dislocations has an E_a in the same range [9] [44] [45] [46], but Pérez Escobar *et al.* [20] demonstrated that hydrogen trapped by dislocations largely left the material before starting up the TDS measurement. Although a distinction between dislocations and lath boundaries could not be made based on the E_a, the first peak is assumed to be largely related to hydrogen trapped at martensite lath boundaries. In addition, the increasing amount of detected hydrogen by TDS for A → B → C was in good agreement with the hot/melt extraction results (cf. Figure V-12) and could be linked to the increasing carbon content of the alloys [29] [30] [31] [32] .

Next to the first peak, alloy A presented a clear shoulder in the desorption spectra which was deconvoluted in an additional peak with an E_a of about 42 kJ/mol. This peak was less obvious for alloy B and C, although it could not be excluded that a small additional peak was also present for these alloys. When attributing this peak to a microstructural feature, a first possibility are the carbides present in the as-Q condition. Based on the carbide characterization presented in Figure V-7 and V-8 and the solubility calculations from Figure V-5, it is demonstrated that insoluble carbides were still present after austenitization of these alloys. However, these large incoherent carbides, resulting from the processing of the materials, are not expected to trap a significant amount of electrochemically charged hydrogen as reported by Wei and Tsuzaki [8] [47] and confirmed by Pérez Escobar *et al.* [10]. When searching for an explanation for the 2nd peak a detailed TEM investigation on the present carbides conducted. Next to the large incoherent carbides resulting from processing, which were present in all alloys, alloy A also showed cluster of smaller TiC precipitates which were about 60-100 nm in size (cf. Figure V-16). These clusters were not found in alloy B and C (cf. Figure V-8) and might account for the 2nd peak in the TDS spectrum of alloy A in the as-Q condition. The corresponding E_a of 42 kJ/mol supports this hypothesis.

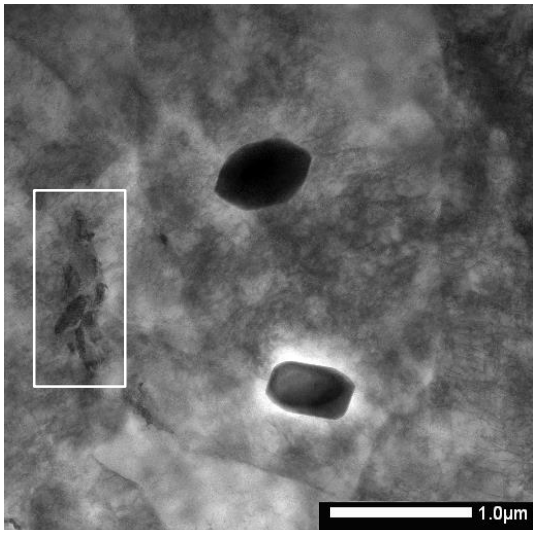

Figure V-16: STEM bright field image of alloy A in the as-Q condition, where two large incoherent carbides are observed together with a cluster of smaller TiC precipitates as indicated by the white square.

All Q&T desorption spectra could be deconvoluted into four peaks. The first deconvoluted peak can again mainly be attributed to hydrogen trapped at the martensitic lath boundaries, whereas the three additional peaks were considered to be induced by the TiC precipitates formed during tempering. The second and third peak originated from the broad hydrogen desorption shoulder in the spectra and showed E_a's of approximately 40-50 kJ/mol. These values are in good agreement with those obtained by Wei and Tsuzaki [9] who also observed E_a's around 46-59 kJ/mol for hydrogen trapped at the interface between coherent TiC and the matrix.
The fourth peak, found at a considerably higher temperature of around 350°C-400°C, corresponded to E_a's of 117, 71 and 60 kJ/mol for alloy A, B and C, respectively. This 4^{th} peak was associated with semi-coherent carbides since the E_a was considerably higher [6] [7] [9]. As the border between reversible – irreversible trapping was proposed to be 60 kJ/mol according to Dafarnia *et al.* [48], the trap is of a more irreversible nature for alloy A and B.

In order to validate the irreversible nature of 4^{th} peak, TDS measurements were also performed after putting the sample 72 hours in vacuum. During this period, reversibly trapped hydrogen could effuse out of the sample and would be consequently no longer detectable by TDS. The results are shown in Figure V-17 and the original 4^{th} peak from the regular TDS measurements (cf. Figure V-15) is included in Figure V-17 as well. The first three reversible peaks disappeared after 72 hours of vacuum whereas the small 4^{th} peak, corresponding to irreversibly trapped H, was still detectable.
However, some differences became apparent as for alloy A the 4^{th} peak kept its intensity, while a small decrease was observed for alloy B and a significant lower amount of hydrogen was measured for alloy C. Consequently, a nice correspondence was demonstrated between the strength of the trap as indicated by the E_a and the intensity of this peak in the spectrum after 72 hours of vacuum. This test also supported the often quoted irreversible nature of traps with E_a above 60 kJ/mol [48].

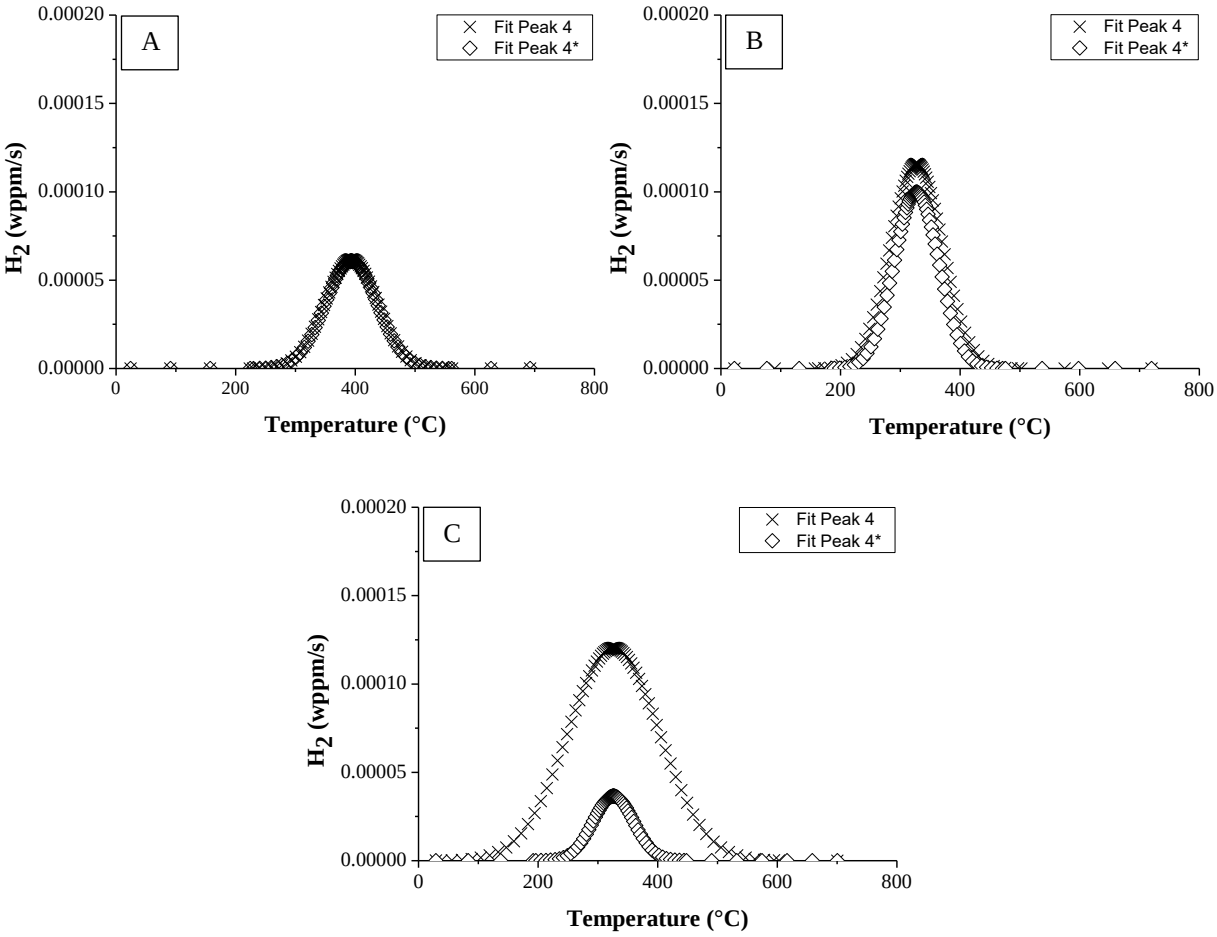

Figure V-17: TDS spectra of alloy A, B and C Q&T of which the 4th peak of Figure V-15 is shown (Fit Peak 4) together with the peak measured after 72 h of vacuum (Fit Peak 4*).

The Q&T samples contained more hydrogen compared to the as-Q materials as shown in both Figure V-12 and V-15. Although tempering induced TiC precipitates which trap hydrogen, the degree of HE (cf. Table V-2) also increased for all alloys when tempered. However one important difference has to be noted here as well. Hot/melt extraction differs from TDS since one hour is needed before the TDS measurement to assure the required low pressure in the analysis chamber. During this hour, a certain amount of the hydrogen is released from the material and consequently is no longer detectable during the TDS measurement. This type of hydrogen will be further referred to as mobile hydrogen. A summary of the amount of diffusible hydrogen, measured by hot extraction, and the integrated hydrogen content detected by TDS together with the amount of mobile hydrogen, which is the difference between the diffusible hydrogen and the amount of hydrogen detected by TDS till 300°C, is presented in Table V-4.

Table V-4: Summary of the hydrogen contents for alloy A, B and C in the as-Q and Q&T condition.

Hydrogen content (wppm)	**Alloy A**		**Alloy B**		**Alloy C**	
	As-Q	Q&T	As-Q	Q&T	As-Q	Q&T
diffusible hydrogen	1.46	2.95	1.98	3.52	3.33	5.50
hydrogen under TDS curves	0.56	1.32	1.00	1.84	1.65	3.90
mobile hydrogen	0.90	1.65	0.98	1.72	1.68	1.79

As the hydrogen diffusivity has been argued to play an important role in HE, the correlation between the different types of hydrogen in the material and the %HE was investigated. The correlation between the %HE and the amount of hydrogen is plotted in Figure V-18. The total, diffusible and mobile hydrogen content are considered and R^2 – values are included to assess the different possible correlations.

The best fit is clearly observed when the amount of mobile hydrogen is considered, which indicates a lower HE sensitivity for a lower amount of mobile hydrogen. Apart from the hydrogen content, the hydrogen diffusion coefficient plays an important role in the hydrogen induced mechanical degradation. Depover *et al.* [23] [29] [31] presented already some studies on the combined effect of the amount and diffusivity of hydrogen on the hydrogen embrittlement susceptibility (cf. Chapter IV).

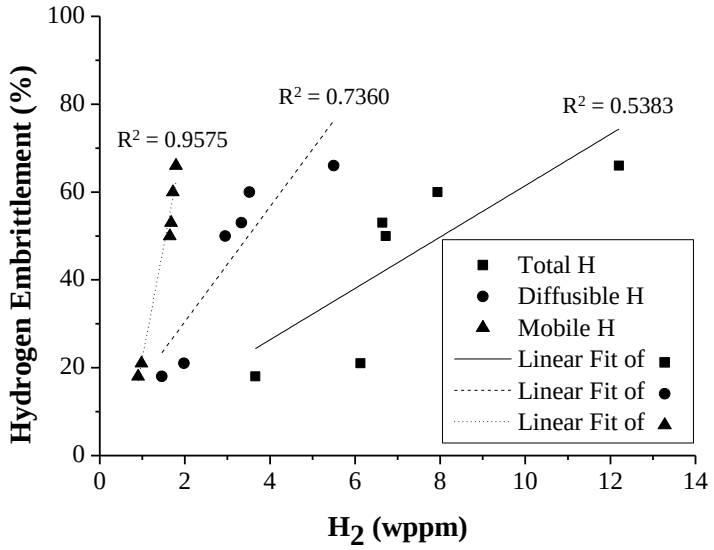

Figure V-18: Degree of hydrogen embrittlement vs. hydrogen content.

As hydrogen diffusion plays an important role, hydrogen permeation tests have been performed on alloy C for both conditions. The permeation curves are shown in Figure V-19. A remarkably slower hydrogen permeation was obtained after tempering which was due to the presence of numerous TiC precipitates, leading to hydrogen diffusion coefficients of 1.14×10^{-10} and 3.02×10^{-12} m^2/s for the as-Q and Q&T condition, respectively. This explained why only a small additional amount of mobile hydrogen effused out of the Q&T condition for alloy C, whereas the latter sample contained a significant higher amount of diffusible hydrogen compared to the as-Q condition (cf. Table V-4), and consequently also why this alloy is more sensitive to hydrogen embrittlement as demonstrated by the mechanical tests.

Although tempering reduces the dislocation density [49] [50], the amount of mobile hydrogen, which has been mentioned above to be mainly linked to hydrogen trapped at dislocations, increased for the Q&T material. However, tempering not only reduced the dislocation density, it also induced precipitates and as such new traps are created as well. The formed TiC also induce an elastic stress field in the matrix surrounding the particle, which is capable of trapping hydrogen as well [8] [45] [47]. This kind of hydrogen trap has a rather low E_a as reported by [8] [51] [52] and might therefore also contribute to the fraction of mobile H as will be further discussed below.

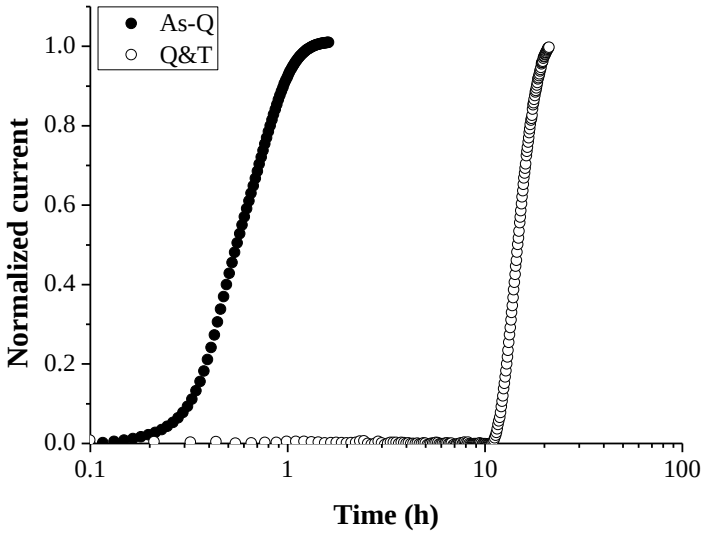

Figure V-19: Hydrogen permeation curves of alloy C in the as-Q and Q&T condition.

Although a good correlation between mobile hydrogen and %HE was demonstrated, some other material features will also play a role in the hydrogen sensitivity of a material. At first, different strength levels are observed for the different materials in the as-Q and Q&T conditions and the alloy strength level is often quoted to play a role in hydrogen embrittlement. Moreover, differences in the carbide characteristics could be expected due to the different levels of alloying elements in the three Fe-C-Ti alloys. As these carbides characteristics have a major influence on their hydrogen trapping capacity, this also needs to be addressed. Consequently, changes in the heat treatment parameters were applied on the materials to investigate both the effect of the strength level and carbides characteristics.

V.6 The influence of tempering time and carbide size on the HE susceptibility

V.6.1 Influence of the strength level

High strength steels are generally quoted to be more prone to hydrogen embrittlement and often a correlation between the HE susceptibility and the strength level is reported in literature [3] [4] [46], although contradictory observations have been published as well (cf. Chapter II). In order to exclude the possible effect of the strength level on the hydrogen induced ductility loss in the present work, different tempering times were applied to achieve a similar strength level in the Q&T material as for the as-Q condition. As such, an evaluation of the impact of carbides can be made regardless the possible influence of strength level. Tempering was performed for longer times, on the one hand, to decrease the tensile strength and, on the other hand, to let the carbides grow to enable them to trap hydrogen with a higher activation energy, since the latter increases with decreasing coherency [9], and hence impact the HE sensitivity. Hardness measurements were performed to find out for which tempering time a similar strength level was obtained as the as-Q condition. Results are presented in Figure V-20. Tempering for two hours (Q&T 120) showed a similar strength level compared to the as-Q material. Tensile tests were performed under similar hydrogen charging conditions as discussed before and are presented in Figure V-21 and summarized in Table V-5. As a reference, also the results after one hour of tempering are included in this representation.

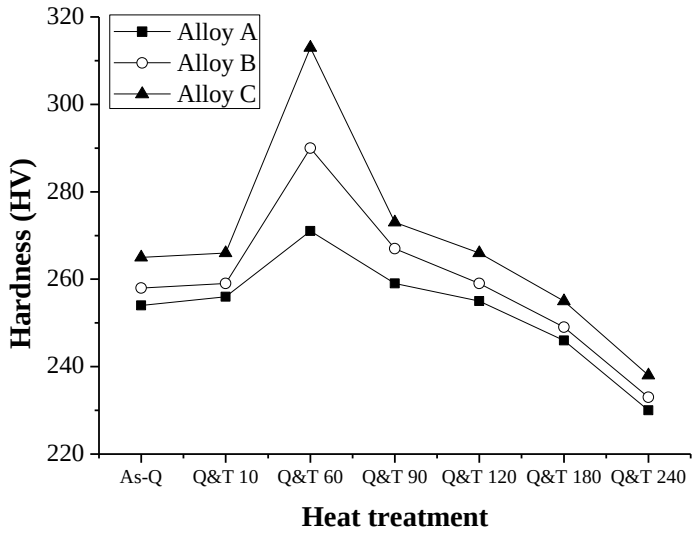

Figure V-20: Hardness vs. applied heat treatment with Q&T xx where xx corresponds with temper times in min.

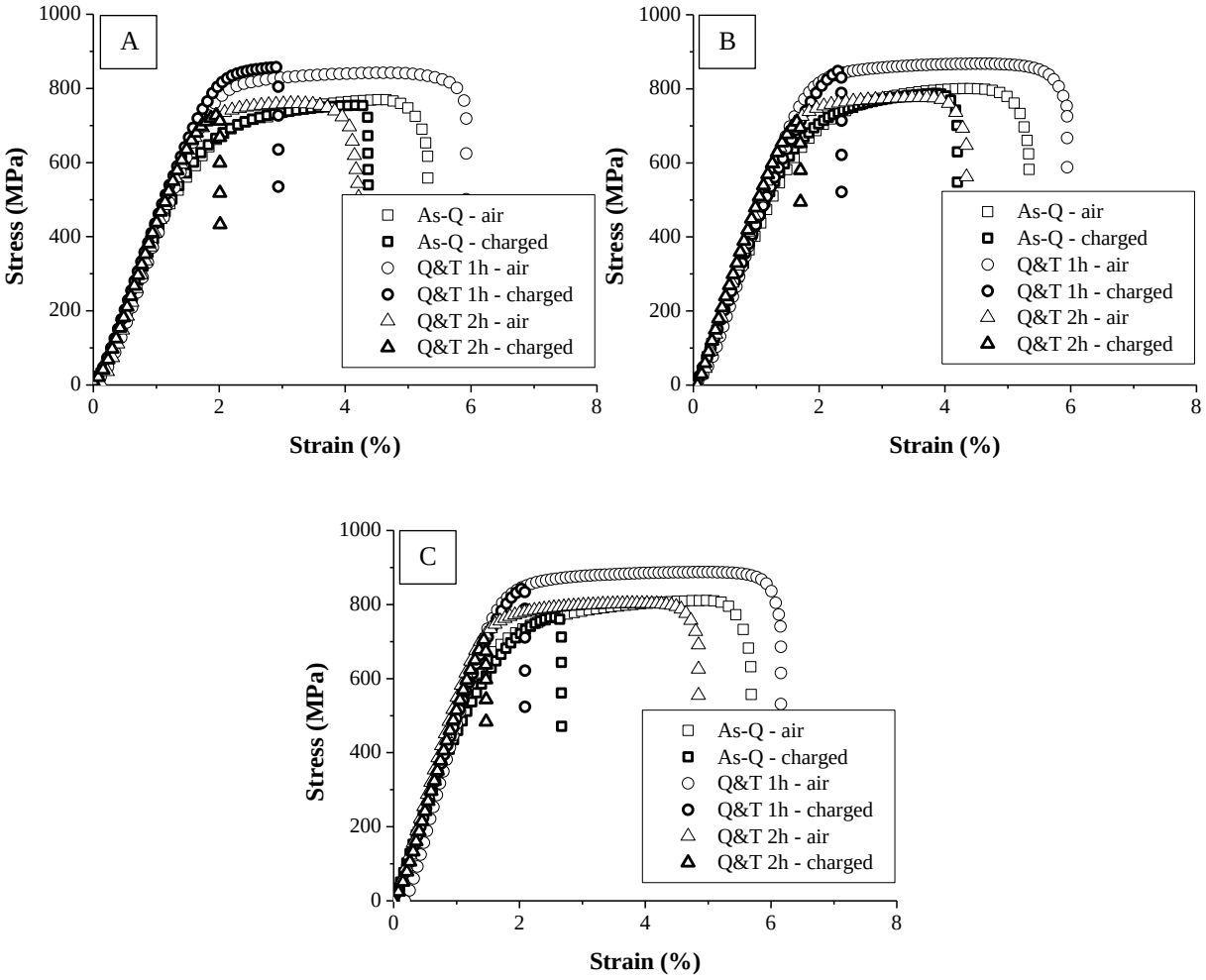

Figure V-21: Stress vs. strain curves of alloy A, B and C in the as-Q, Q&T 1h and Q&T 2h condition.

Table V-5: Summary of the HE% for alloy A, B and C in the as-Q and the 1h and 2h tempered conditions.

HE%	As-Q	Q&T 1h	Q&T 2h
Alloy A	18	50	52
Alloy B	21	60	61
Alloy C	53	66	70

The similar strength level for all alloys in the as-Q and Q&T 2h condition excludes a possible strength effect. After two hours tempering, the hydrogen induced ductility loss even slightly increased for all alloys when compared to the sample after 1h tempering, while the tensile strength was lower. Although the increase in HE% seems small, it must be emphasized that the effective elongation of the hydrogen charged specimen dropped significantly, as the elongation of the uncharged samples decreased as well. Consequently, an enhanced HE resistance was certainly not obtained by tempering for longer times, i.e. by lowering the strength of the alloy to the same strength level as the as-Q condition. In order to interpret these observations, the data obtained from TDS measurements are presented in Figure V-22 and the different determined hydrogen contents by hot extraction and TDS are summarized in Table V-6.

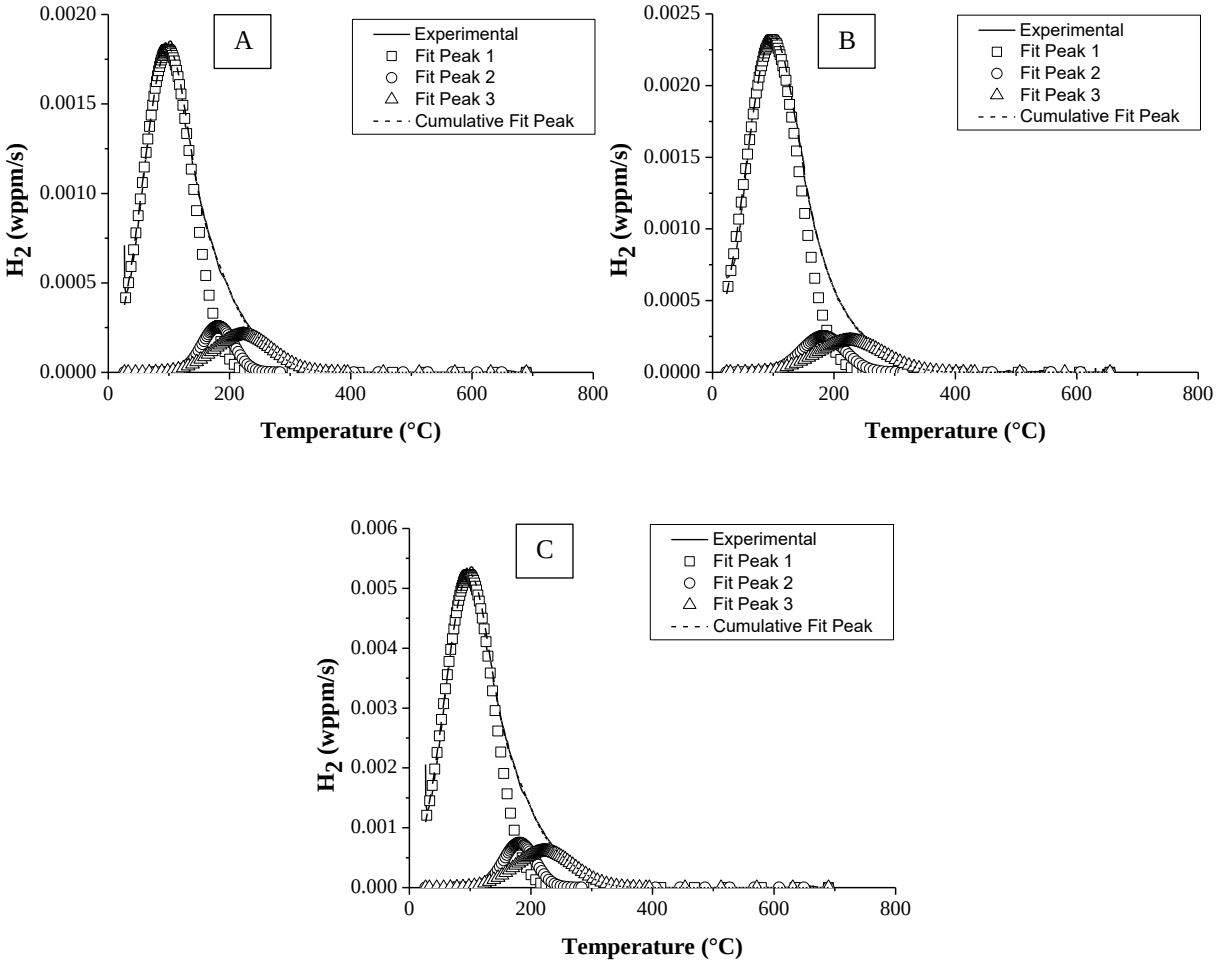

Figure V-22: TDS spectra of alloy A, B and C in the Q&T 2h condition after hydrogen charging at a heating rate of 600°C/h.

Table V-6: Summary of the hydrogen contents for alloy A, B and C in the Q&T 2h condition.

Hydrogen content (wppm)	Alloy A	Alloy B	Alloy C
diffusible hydrogen	3.60	4.10	6.14
hydrogen under TDS curves	1.30	1.78	3.75
mobile hydrogen	2.30	2.34	2.52

The TDS spectra were deconvoluted into three peaks for all materials. The fourth peak with a higher E_a (cf. Figure V-15), which was present after 1h tempering, disappeared and two TiC related peaks remained. Apparently, the corresponding carbides had grown too large and their interface with the matrix was too incoherent to trap hydrogen from an electrochemical source, which corresponds to previously reported findings [8] [47]. The two remaining peaks associated with hydrogen trapping by carbides were smaller than the corresponding peaks for the samples tempered for 1h, as shown in Table V-7. Since the amount of interface between carbides and matrix decreased when the precipitates grew and their interface became more incoherent, the present results indicated that H was trapped rather at this interface than inside the carbides. These observations are in good agreement with those obtained by Wei and Tsuzaki [8] and Pérez Escobar *et al.* [10].

Table V-7: H trapped at carbides corresponding to peak 2 and 3 for alloy A, B and C in the Q&T 1h and 2h condition.

wppm	Alloy A	Alloy B	Alloy C
Q&T 1h	0.65	0.73	2.09
Q&T 2h	0.25	0.33	0.74

When comparing the data of Table V-4 and V-6, it was observed that the amount of diffusible and mobile hydrogen did increase with an additional hour tempering, which can be correlated with the increased hydrogen induced ductility loss. Although the strength level was reduced for these longer tempered materials, the amounts of hydrogen in the microstructure had increased and resulted in a lower resistance against HE.

Next to the direct link between the amount of diffusible and mobile hydrogen, the hydrogen diffusion coefficient of the materials tempered for 2h (Figure V-23) was considerably higher as well, i.e. 8.72 x 10^{-12} m^2/s, resulting in a higher amount of hydrogen that could leave the sample in the constant time before the start of the TDS measurement (cf. Table V-6). The amount of mobile hydrogen can hence not solely be correlated to amount of hydrogen trapped at dislocations as the dislocation density decreases with tempering time [49] [50]. However, tempering also induced precipitates and thus new traps are introduced as well. Since less hydrogen got trapped by the present particles (cf. Table V-7) together with their growth and the higher amount of diffusible and mobile hydrogen in the Q&T 2h materials, the elastic stress fields in the matrix surrounding the precipitates apparently trapped a significant amount of hydrogen in the present case [8] [45] [47], as observed by hot extraction, but partly not detectable by TDS. Consequently, the amount of diffusible and mobile hydrogen increased and therefore also the HE%. This hypothesis might explain the increased intensity of the first peak as well.

As can be seen from Figure V-20, 10 minutes of tempering generated similar hardness values and therefore, these samples would allow evaluating the effect of the carbide characteristics which are discussed in the next section.

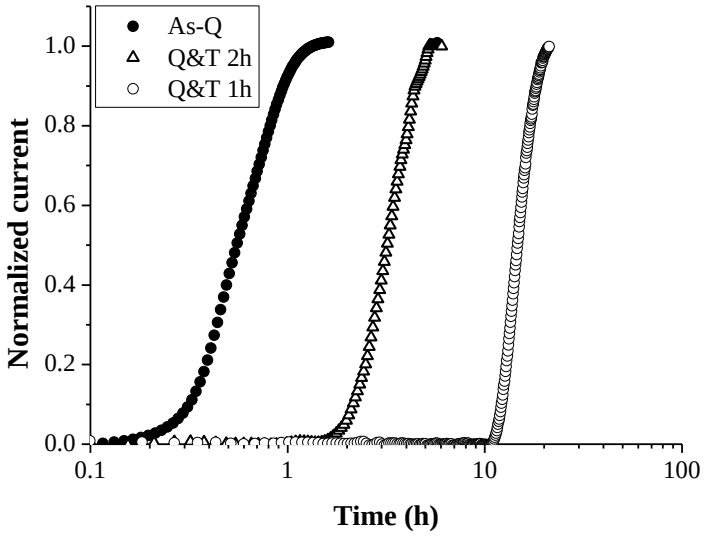

Figure V-23: Permeation curves for alloy C in the as-Q, Q&T 1h and Q&T 2h condition.

V.6.2 Influence of carbide characteristics on the trapping behavior and HE susceptibility

As shown in Figure V-20, tempering for 10 minutes resulted in similar strength level as the as-Q and Q&T 2h condition. The corresponding stress-strain curves for these samples are included in Figure V-24 and the hydrogen embrittlement degrees are summarized in Table V-8. The ductility of the uncharged specimen was located in between the elongation of the as-Q and Q&T 1h sample. An increase in ductility was observed for the hydrogen charged specimen compared to the other tempered conditions. Moreover, for alloy C even a less pronounced degree of hydrogen embrittlement was observed compared to as-Q, which is remarkable as for all other tempering conditions, the Q&T samples performed worse than the as-Q condition. As indicated above, the diffusible hydrogen content provides a first estimation of hydrogen embrittlement sensitivity, without the need of having to perform all TDS measurements. Therefore, more straightforward hot extraction measurements were performed for all alloys (Figure V-25).

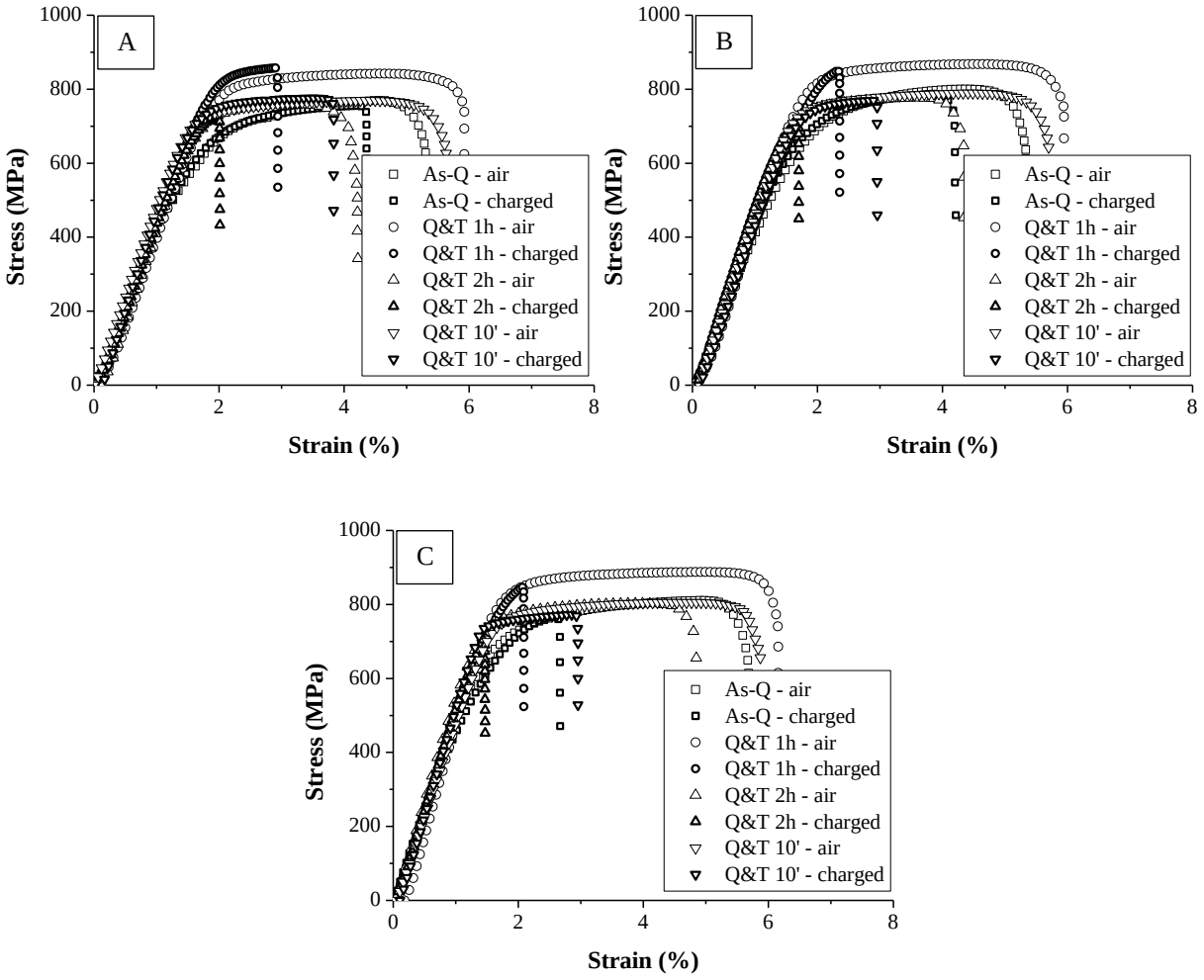

Figure V-24: Stress vs. strain curves of alloy A, B and C in the as-Q, Q&T 1h and Q&T 2h condition.

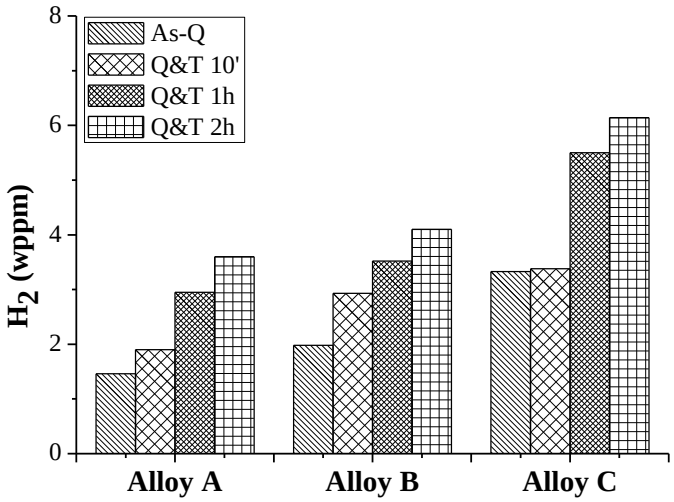

Figure V-25: The diffusible hydrogen content after electrochemical charging for alloy A, B and C in the as-Q and tempered conditions.

Generally, two main conclusions can be drawn from the hot extraction measurements. On the one hand, the hydrogen content increased when tempered and with tempering time and, on the other hand, the hydrogen content systematically augmented from alloy A over B to C. As can be seen from Table V-8, the hydrogen induced ductility loss varied in exactly the same way as the diffusible amount of hydrogen. Making the correlation between Figure V-25 and Table V-8 also supports the observation of the similar %HE for alloy C Q&T 10' as compared to the as-Q condition. For both conditions the amount of diffusible hydrogen is indeed similar. One remarkable result should be emphasized since the difference between alloy C as-Q and Q&T 10' was rather small, which was expressed in Table V-8 as well.

A carbide size distribution has been made for alloy C based on TEM bright field images for all conditions under evaluation. These results are correlated with the corresponding TDS spectra and presented in Figure V-26.

Table V-8: Summary of the HE% for alloy A, B and C in the as-Q and the tempered conditions.

HE%	**As-Q**	**Q&T 10'**	**Q&T 1h**	**Q&T 2h**
Alloy A	18	32	50	52
Alloy B	21	48	60	61
Alloy C	53	50	66	70

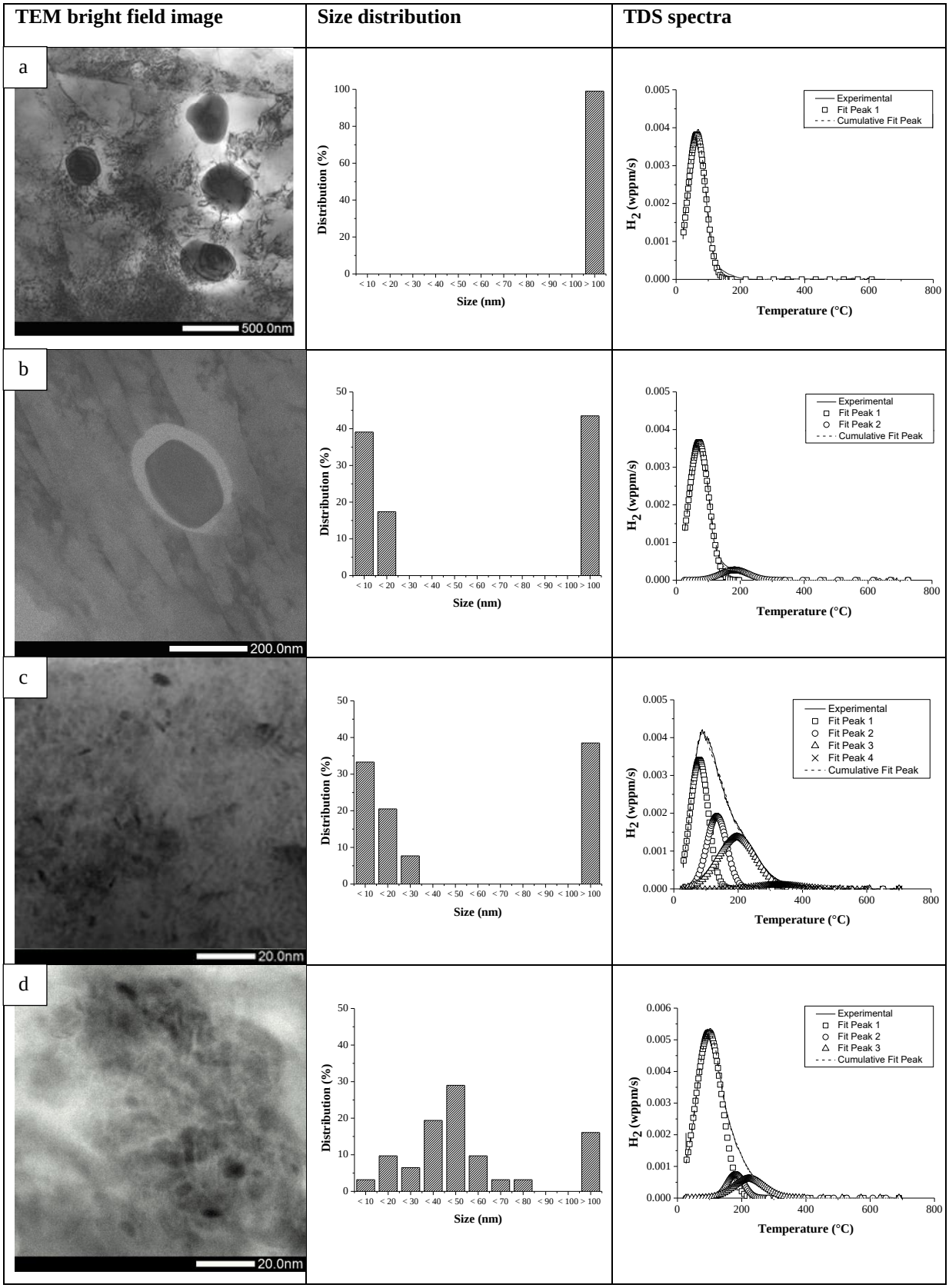

Figure V-26: Representative TEM bright field image, carbides size distribution and TDS spectrum for alloy C in the as-Q (a), Q&T 10' (b), Q&T 1h (c) and Q&T 2h (d) condition.

The as-Q condition just contained incoherent carbides from the processing with sizes above 200 nm, which were unable to trap hydrogen. The optimal trapping capacity of the TiC was achieved when the material was tempered for one hour since their highest hydrogen uptake capacity was demonstrated by the TDS measurement. This hydrogen was most likely trapped at the interface between carbides of less than 30 nm and the matrix according to the distribution maps.

For the Q&T 10' condition, a small peak appeared associated with small TiC of less than 20 nm. Although these carbides are efficient hydrogen traps, TEM analysis demonstrated that they are only in a limited amount present. This also explains the limited size of the corresponding TDS peak. Nevertheless, the limited amount of hydrogen they do trap accounts for the slightly smaller %HE of this condition for alloy C as they indeed limit the mobility of some hydrogen present in the sample.
The TEM bright field image shown in Figure V-26 (b) did, however, not reveal the presence of these small TiC particles due to resolution limits as demonstrated by Figure V-27 (a). However, their presence is confirmed by the dark field image (cf. Figure V-27 (c)) taken from the diffraction spot indicated in Figure V-27 (b). The diffraction pattern is taken from the selected area of the TEM bright field image.

While the carbides reached a maximum hydrogen trapping capacity at about one hour tempering, their trapping capacity decreased after two hours of tempering as becomes clear from the corresponding TDS spectrum. The size of the carbides indeed increased with tempering. Consequently, the total interfacial area between the particles and the matrix was reduced and the amount of trapped hydrogen decreased. One might argue that upon further tempering and increasing carbide size that the carbides might at one point reach a state in which they become too large to trap hydrogen, similarly to the very large carbides present from processing. In order to validate this theory, tempering was performed for longer times and the corresponding data analysis is presented in the next section.

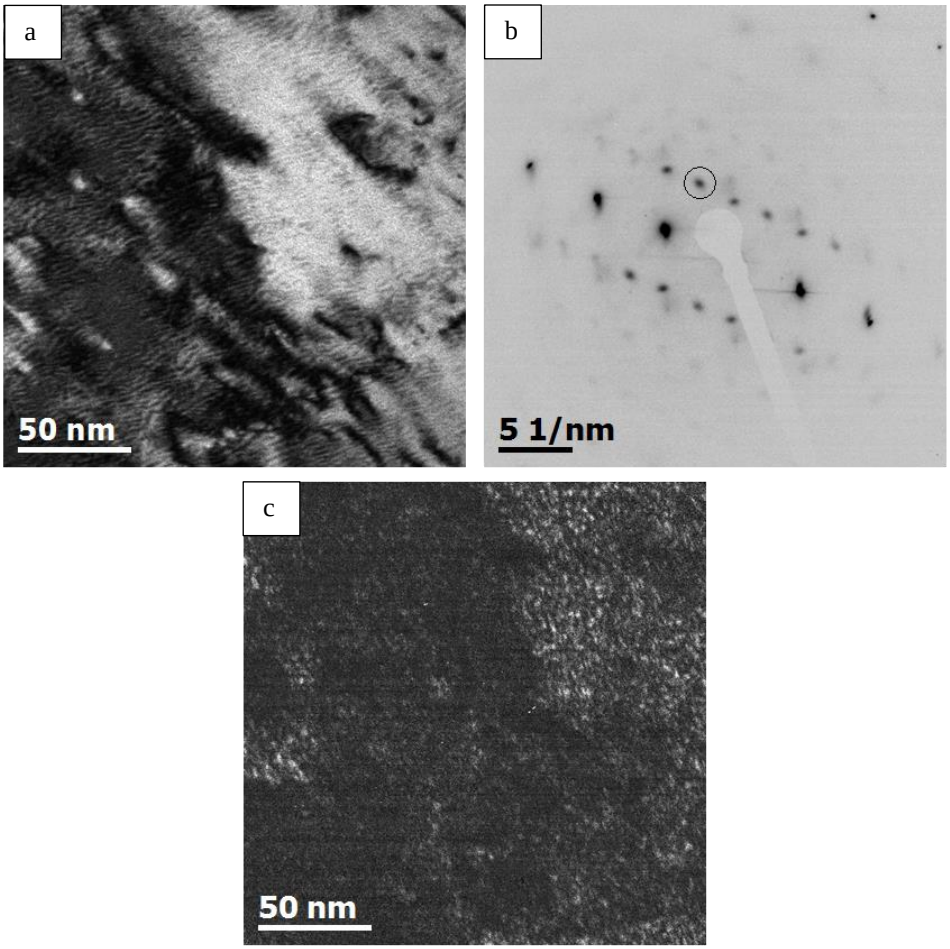

Figure V-27: TEM bright field image of alloy C Q&T 10' (a), of which a selected area diffraction pattern was taken and presented in (b). Dark field image (c) is taken from the diffraction spot indicated by the black circle in (b).

V.6.3 On the loss of trapping ability with carbide size

Tempering was performed for 10 and 20 h to further increase the carbide size and evaluate the evolution of the carbide trapping ability. TEM bright field images are presented together with the carbide size distribution and the corresponding TDS spectra in Figure V-28. The sample tempered for 10h still showed one peak corresponding to the present carbides. Approximately 0.60 wppm of H got trapped for this sample at the TiC/matrix interfaces, which were most likely those in the size range of 50 – 70 nm. The larger incoherent carbides were unable to trap electrochemically charged H. When the material got tempered for 20 h, only one peak was detected and a similar TDS spectrum as compared to the as-Q sample was observed. Consequently, TiC carbides with a size of about 70 nm or larger apparently lose their ability to trap hydrogen.

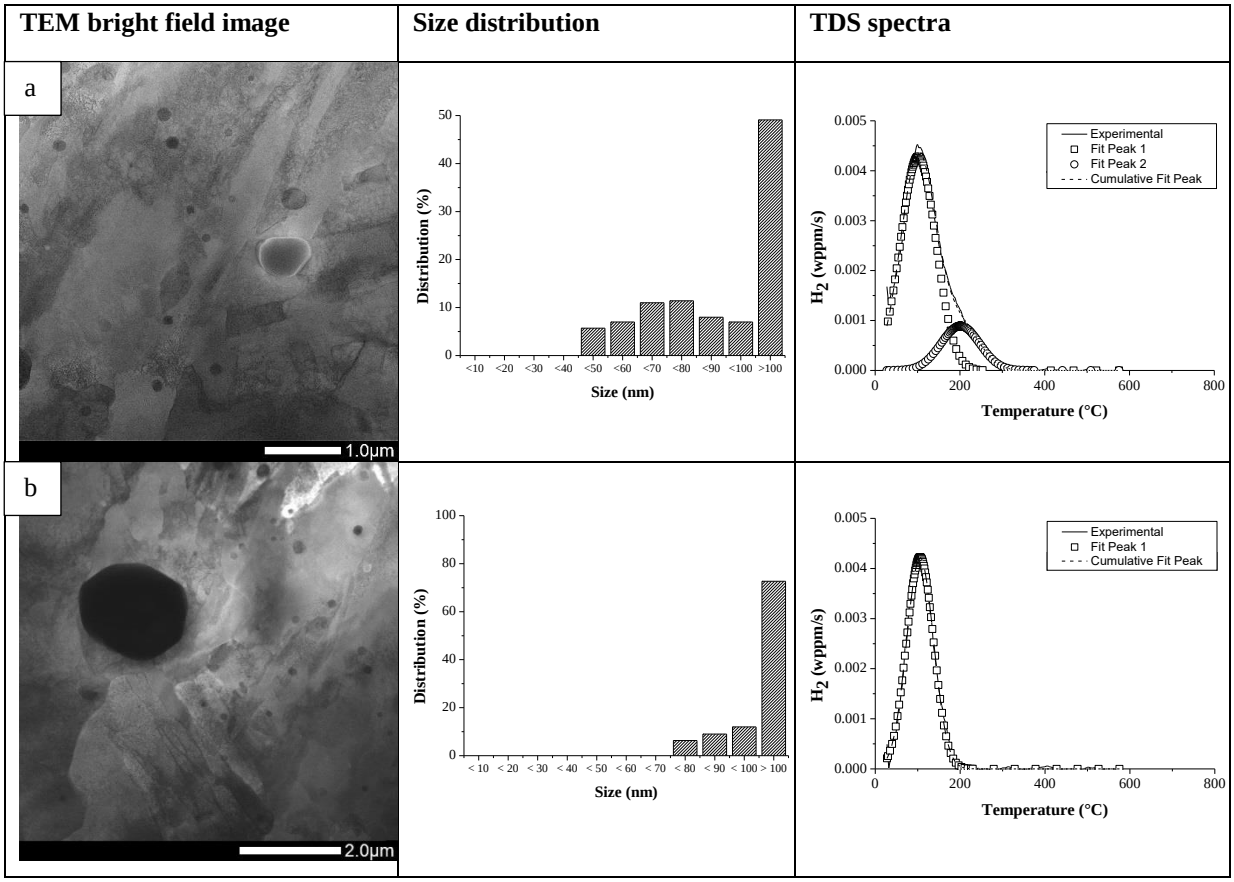

Figure V-28: Carbides size distribution maps with the according TDS spectra for alloy C in the Q&T 10h (a) and Q&T 20 h (b) condition.

V.7 On the beneficial effect of TiC in terms of hydrogen embrittlement

One important result from the present work is the higher HE sensitivity for Q&T samples although they contain a specific amount of hydrogen trapping TiC precipitates. Obviously, the question then arises whether the presence of TiC is a good strategy to enhance the resistance against hydrogen embrittlement or not. Since the discussed results presented a clear correlation between the degree of hydrogen embrittlement and the amount of hydrogen (cf. Figure V-18), an alternative charging procedure was applied as indeed so far all samples were charged till complete hydrogen saturation. Electrochemical charging was performed in such a way that a similar amount of hydrogen was charged into alloy C for all different heat treatments. This would allow evaluating the effect of the presence of carbides for samples with a constant total hydrogen content. As a reference total hydrogen content, the saturation level of the as-Q sample was chosen for alloy C. The melt extraction results vs. charging time are shown in Figure V-29.

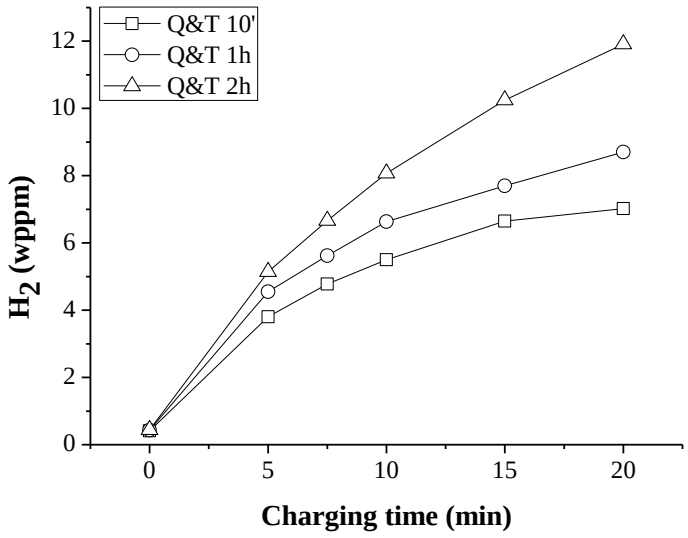

Figure V-29: Total amount of hydrogen vs. charging time for alloy C in the Q&T conditions.

The charged as-Q sample contained approximately 6.6 wppm of hydrogen (cf. Fig. V-12). This content was achieved after 7.5, 10 and 15 min of charging for the Q&T 2h, Q&T 1h and Q&T 10' material, respectively, and the corresponding samples are further referred to as 'charged*'. Tensile tests were performed after these pre-charging times and the corresponding stress-strain curves are presented in Figure V-30 and summarized in Table V-9.

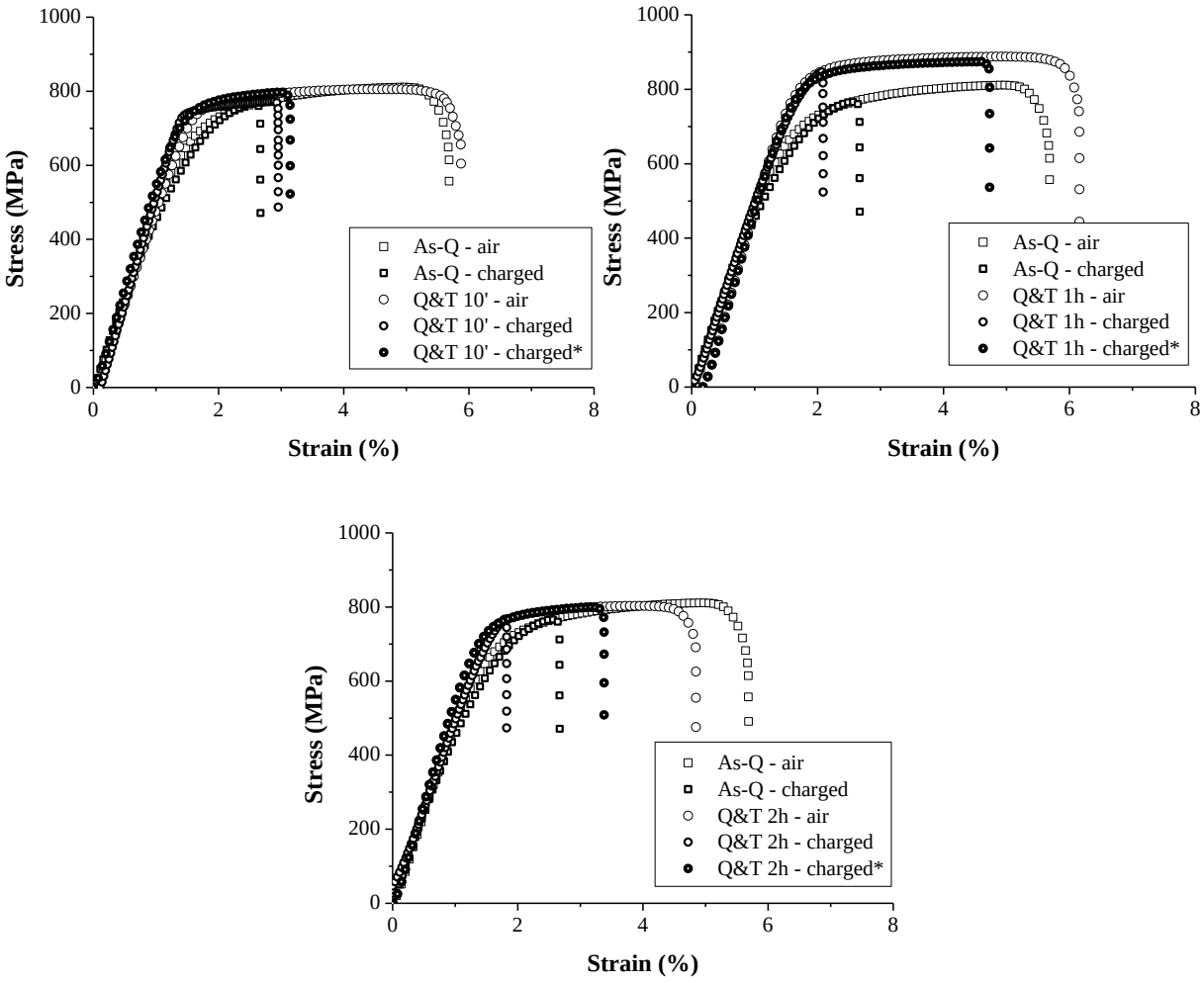

Figure V-30: Stress-strain curves for alloy C in the as-Q and tempered conditions. Charging was applied for 1 hour (charged) and until 6.6 wppm H was reached (charged*).

Table V-9: Summary of the HE% for the different conditions in alloy C, charged to similar H content.

	As-Q	Q&T 10'	Q&T 1h	Q&T 2h
HE%	53	50	66	70
HE%*	53	46	23	30

Considerable difference in HE% was observed as compared to some of the results mentioned above. Here, the material which got tempered for one hour showed the best resistance against HE, followed by the Q&T 2h condition, whereas the 10 min tempered sample showed a similar ductility loss as in the previously tested condition.

The tests discussed so far demonstrated the importance of mobile hydrogen in hydrogen induced degradation. However, all tests so far were conducted on hydrogen saturated samples. Here, samples were not saturated and moreover, all samples contained hydrogen traps to a smaller or larger extent. Therefore, a relevant next step is to evaluate the hydrogen distribution in the non-saturated samples over the different traps. TDS measurements are

performed and the spectra are shown in Figure V-31 and indicated as 'charged*'. These are compared with the TDS spectra of the samples which were hydrogen saturated.

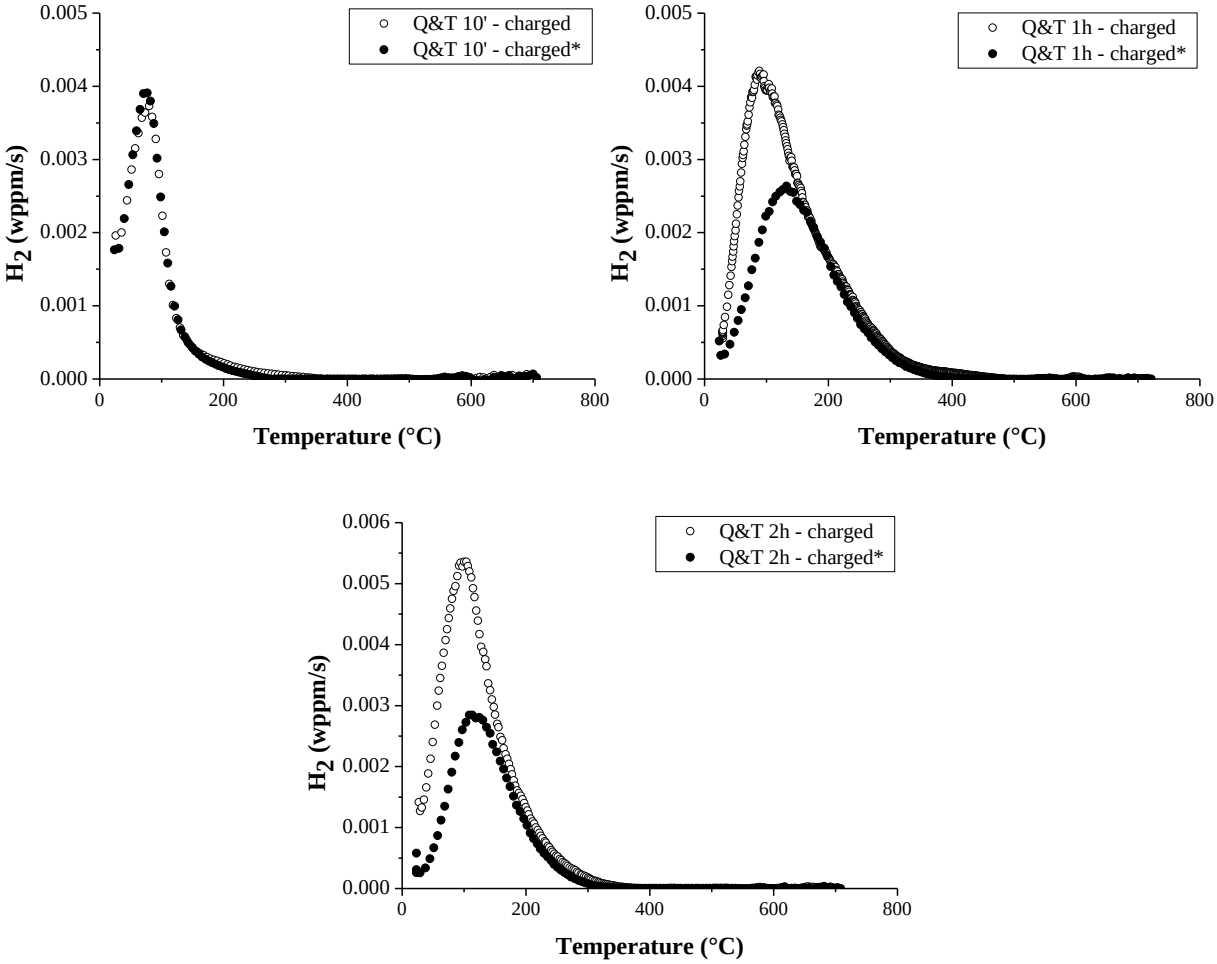

Figure V-31: TDS spectra of alloy C in the Q&T conditions, charged to similar H content as the as-Q sample (charged*) together with the TDS spectra charged for one hour (charged).

The TDS spectra indicate that the trapping sites with the higher activation energy, i.e. those correlated with H trapped at the TiC carbides, were first filled. The first peak, mainly associated with H at lath boundaries, had not yet been filled in the non-saturated samples. Consequently, hydrogen got first trapped at the deeper trapping sites, which have the higher E_a, and the samples that contained more traps were able to immobilize more hydrogen, i.e. they contained less mobile hydrogen (cf. Table V-10). This enhanced their resistance to the hydrogen induced ductility loss. As such this demonstrates that TiC are indeed beneficial for reducing the HE sensitivity.

A straightforward comparison between the different kinds of hydrogen can be made since a similar amount of hydrogen was charged into the materials. As previously shown, the amount of mobile hydrogen was dependent on the hydrogen trapping sites and of course determined by the absolute value of total hydrogen, which can now be taken out of consideration since the latter is identical for all samples. An alternative indication of the available trapping sites can be made by performing permeation tests. The hydrogen diffusivity increased from Q&T 1 h <

Q&T 2h < Q&T 10' < as-Q, which was in the opposite order as the amount of available trapping sites and hence in the same order as the mobile hydrogen content. Generally, the hydrogen diffusion coefficient decreased with increasing number of available trapping sites (cf. Figure V-23). Additionally, the degree of HE followed again the same tendency as the amount of mobile hydrogen. These results are summarized in Table V-10.

Table V-10: Summary of the hydrogen contents for the different conditions charged to similar H content together with the hydrogen diffusion coefficients.

	As-Q	**Q&T 10'**	**Q&T 1h**	**Q&T 2h**
H under TDS curves (wppm)	1.65	1.78	2.45	2.13
mobile H (wppm)	1.68	1.55	0.88	1.17
D_{app} (m^2/s)	1.14×10^{-10}	7.31×10^{-11}	3.02×10^{-12}	8.72×10^{-12}

V.8 Conclusion

The present study investigated the role of TiC in the hydrogen induced ductility loss of lab cast Fe-C-Ti alloys with an as-quenched or quench and tempered microstructure. During tempering, carbides were generated. Three alloys were cast with a variable carbon content to steer the strength level and to investigate in detail the role of the precipitates in different alloys. The impact of hydrogen was demonstrated by mechanical tests on both in-situ hydrogen charged and uncharged tensile samples. Remarkably, the results indicated a decreased resistance against embrittlement for the carbide containing tempered materials. Thermal desorption spectroscopy and hot/melt extraction were performed to understand the carbide trapping ability and capacity and hence interpret the observed tendencies. The tempered induced TiC were able to trap a significant amount of hydrogen, which was responsible for the increased hydrogen embrittlement sensitivity. Moreover, a clear correlation was obtained between the degree of hydrogen embrittlement and the amount of mobile hydrogen, assumed to be mainly trapped at dislocations.

Modified thermal treatments allowed assessing these interpretations. When the materials got tempered for longer times, the amount trapped by the TiC decreased, which suggested hydrogen was trapped at the interface of precipitate/matrix. Additionally, the trapping ability was determined to be dependent on the carbide size and no hydrogen was trapped by TiC larger than 70 nm.

A modified charging procedure was applied as well to verify if and when TiC addition was beneficial to increase the hydrogen embrittlement resistance. A similar amount of hydrogen got charged into the as-Q and tempered conditions, and the Q&T 1h material showed the lowest hydrogen induced ductility loss since, due to the highest trapping capacity of the present TiC and the lowest diffusivity, the least mobile hydrogen was present in this sample.

V.9 References

[1] Vervynckt S, Verbeken K, Lopez B, Jonas JJ, „Modern HSLA steels and role of non-recrystallisation temperature," *International Materials Reviews,* vol. 57, pp. 187-207, 2012.

[2] Depover T, Pérez Escobar D, Wallaert E, Zermout Z, Verbeken K, „Effect of in-situ hydrogen charging on the mechanical properties of advanced high strength steels," *Int Journal of Hydrogen Energy,* vol. 39, pp. 4647-4656, 2014.

[3] Hilditch TB, Lee SB, Speer JG, Matlock DK, „Response to Hydrogen Charging in High Strength Automotive Sheet Steel Products," *SAE Technical Paper,* 2003, http://dx.doi.org/10.4271/2003-01-0525.

[4] Loidl M, „Hydrogen embrittlement in HSSs limits use in lightweight body," *Adv Mat Process,* vol. 169, pp. 22-25, 2011.

[5] Asaoka T, Lapasset G, Aucouturier M, Lacombe P, „Observations of hydrogen trapping in Fe-0.15 wt. pct Ti alloy by high resolution autoradiography," *Corros NACE,* vol. 1978, pp. 39-47, 1978.

[6] Lee HG, Lee JY, „Hydrogen trapping by TiC particles in iron," *Acta Metall,* vol. 32, pp. 131-136, 1984.

[7] Pressouyre GM, Bernstein IM, „A quantitative analysis of hydrogen trapping," *Metall Trans A,* vol. 9A, pp. 1571-1580, 1978.

[8] Wei FG, Tsuzaki K, „Quantitative Analysis on hydrogen trapping of TiC particles in steel," *Met Mat Trans A,* vol. 37A, pp. 331-353, 2006.

[9] Wei FG, Hara T, Tsuzaki K, „Precise determination of the activation energy for desorption of hydrogen in two Ti-added steels by a single thermal-desorption spectrum," *Met Mat Trans B,* vol. 35B, pp. 587-597, 2004.

[10] Pérez Escobar D, Wallaert E, Duprez L, Atrens A, Verbeken K, „Thermal Desorption Spectroscopy Study of the Interaction of Hydrogen with TiC Precipitates," *Met Mater Int,* vol. 19, pp. 741-748, 2013.

[11] Asahi H, Hirakami D, Yamasaki S, „Hydrogen trapping behavior in vanadium added steel," *ISIJ Intl,* vol. 43, pp. 527-533, 2003.

[12] Li D, Gangloff RP, Scully JR, „Hydrogen trap states in ultrahigh-strength AERMET 100 steel," *Met Mat Trans A,* vol. 35, nr. 3, pp. 849-864, 2004.

[13] Wei FG, Hara T, Tsuzaki K, „Nano-precipitates design with hydrogen trapping character in high strength steels," in *Proc. of the Int. Hydrogen Conf.* , Jackson, Wyoming, 2008.

[14] Spencer GL, Duquette DJ, „The role of vanadium carbide traps in reducing the hydrogen embtrittlement susceptibility of high strength alloy steels," US army armament research, development and engineering center, Watervliet, N.Y., 1998.

[15] Depover T, Monbaliu O, Wallaert E, Verbeken K, „Effect of Ti, Mo and Cr based precipitates on the hydrogen trapping and embrittlement of Fe-C-X Q&T alloys," *Int Journal of Hydrogen Energy,* vol. 40, pp. 16977-16984, 2015.

[16] Ronevich JA, Speer JG, Matlock DK, „Hydrogen embrittlement of commercially produced advanced high strength steels," *SAE Int Journal Mater Manuf,* vol. 3, pp. 255-267, 2010.

[17] Koyama M, Tasan CC, Akiyama E, Tsuzaki K, Raabe D, „Hydrogen-assisted decohesion and localized

plasticity in dual-phase steel," *Acta Mat,* vol. 70, pp. 174-187, 2014.

[18] Pérez Escobar D, Verbeken K, Duprez L, Verhaege M, „Evaluation of hydrogen trapping in high strength steels by thermal desorption spectroscopy," *Mat Sci Eng A,* vol. 551, pp. 50-58, 2012.

[19] Duprez L, Verbeken K, Verhaege M, „Effect of hydrogen on the mechanical properties of multiphase high strength steels," in *Proc. of the Int. Hydrogen Conf.*, Jackson, Wyoming, 2008.

[20] Pérez Escobar D, Depover T, Wallaert E, Duprez L, Verbeken K, Verhaege M, „Combined thermal desorption spectroscopy, differential scanning calorimetry, scanning electron microscopy and X-ray diffraction study of hydrogen trapping in cold deformed TRIP steel," *Acta Mat,* vol. 60, pp. 2593-2605, 2012.

[21] Laureys A, Depover T, Petrov R, Verbeken K, „Characterization of hydrogen induced cracking in TRIP-assisted steels," *Int Journal of Hydrogen Energy,* vol. 40, nr. 47, pp. 16901-16912, 2015.

[22] Laureys L, Depover T, Petrov R, Verbeken K, „Microstructural characterization of hydrogen induced cracking in TRIP-assisted steel by EBSD," *Materials Characterization,* vol. 112, pp. 169-179, 2016.

[23] Depover T, Wallaert E, Verbeken K, „Fractographic analysis of the role of hydrogen diffusion on the hydrogen embrittlement susceptibility of DP steel," *Mat Sci and Eng A,* vol. 649, pp. 201-208, 2016.

[24] Pérez Escobar D, Miñambres C, Duprez L, Verbeken K, Verhaege M, „Internal and surface damage of multiphase steels and pure iron after electrochemical hydrogen charging," *Corrosion Science,* vol. 53, p. 3166–3176, 2011.

[25] Takahashi J, Kawakami K, Kobayashi Y, Tarui T, „The first direct observation of hydrogen trapping sites in TiC precipitation-hardening steel through atom probe tomography," *Scripta Mat,* vol. 63, pp. 261-264, 2010.

[26] Ren YJ, Zeng CL, „Corrosion protection of 304 stainless steel bipolar plates using TiC films produced by high-energy micro-arc alloying process," *Journal Power Sources,* vol. 171, pp. 778-782, 2007.

[27] Hirohata Y, Motojima D, Hino T, Sengoku S, „Suppresion of hydrgeon absorption to V-4Cr-4Ti alloy by TiO2/TiC coating," *Journal Nuclear Mater,* vol. 313, pp. 172-176, 2003.

[28] Todoshchenko O, Yagodzinskyy Y, Yagodzinska V, Saukkonen T, Hanninen H, „Hydrogen effects on fracture of high-strength steels with different mico-alloying," *Corros Rec,* vol. 13, p. 2, 2015.

[29] Depover T, Wallaert E, Verbeken K, „On the synergy of diffusible hydrogen and hydrogen diffusivity in the mechanical degradation of laboratory cast Fe-C alloys," *Mat Sci and Eng A,* 2016.

[30] Pérez Escobar D, Depover T, Wallaert E, Duprez L, Verhaege M, Verbeken K, „Thermal desorption spectroscopy study of the interaction between hydrogen and different microstructural constituents in lab cast Fe-C alloys," *Corrosion Science,* vol. 65, pp. 199-208, 2012.

[31] Depover T, Van den Eeckhout E, Verbeken K, „The impact of hydrogen on the ductility loss of bainitic Fe-C alloys," *Materials Science Technology,* 2016.

[32] Hadam U, Zakroczymski T, „Absorption of hydrogen in tensile strained iron and high carbon steel studied by electrochemical permeation and desorption techniques," *Int Journal of Hydrogen Energy,* vol. 34, pp. 2449-2459, 2009.

[33] Zhao MC, Liu M, Atrens A, Shan YY, Yang K, „Effect of applied stress and microstructure on sulfide stress cracking resistance of pipeline steels subject to hydrogne sulfide," *Mat Sci and Eng A,* vol. 478, pp. 43-47, 2008.

[34] Akiyama E, Matsukado K, Wang M, Tsuzaki K, „Evaluation of hydrogen entry into high strength steel under atmospheric corrosion," *Corrosion Science,* vol. 52, pp. 2758-2765, 2010.

[35] Wang M, Akiyama E, Tsuzaki K, „Effect of hydrogen on the fracture behavior of high strength steel during slow strain rate test," *Corrosion Science,* vol. 49, pp. 4081-4097, 2007.

[36] Lee SM, Lee JY, „The trapping and transport phenomena of hydrogen in nickel," *Met Trans A,* vol. 17A, pp. 181-187, 1986.

[37] Lee JY, Lee SM, „Hydrogen trapping phenomena in metals with bcc and fcc crystal structures by the desorption thermal-analysis technique," *Surface and Coatings Technology,* vol. 28, pp. 301-314, 1986.

[38] Lee JL, Lee JY, „Hydrogen trapping in AISI-4340 steel," *Metal Science,* vol. 17, pp. 426-432, 1983.

[39] Kissinger HE, „Reaction kinetics in differential thermal analysis," *Analytical Chemistry,* vol. 29, pp. 1702-1706, 1957.

[40] Devanathan MAV, Stachurski Z, „The adsorption and diffusion of electrolytic hydrogen in palladium," *Proc Roy Soc A,* vol. 270, pp. 90-101, 1962.

[41] McBreen, Nanis L, Beck W, „A method for determination of the permeation rate of hydrogen through metal membranes," *Journal of Electrochemical Society,* vol. 113, pp. 1218-1222, 1966.

[42] Irvine KJ, „Grain-refined C-Mn steels," *Journal of the Iron and Steel Insitute,* vol. 205, pp. 161-182, 1967.

[43] Thomas LSR, Li D, Gangloff RP, Scully JR, „Trap-governed hydrogen diffusivity and uptake capacity in ultrahigh strength aermet 100 steel," *Met Mat Trans A,* vol. 33A, pp. 1991-2004, 2002.

[44] Choo WY, Lee JY, „Thermal analysis of trapped hydrogen in pure iron," *Met Trans A,* vol. 13A, pp. 135-140, 1982.

[45] Pressouyre GM, „Classification of hydrogen traps in steel," *Met Trans A,* vol. 10A, pp. 1571-1573, 1979.

[46] Hirth JP, „Effects of Hydrogen on the Properties of Iron and Steel," *Met Trans A,* vol. 11A, pp. 861-890, 1980.

[47] Wei FG, Tsuzaki K, „Hydrogen Absorption of Incoherent TiC Particles in Iron from Environment at High Temperatures," *Met Mat Trans A,* vol. 35A, pp. 3155-3163, 2004.

[48] Dadfarnia M, Sofronis P, Neeraj T, „Hydrogen interaction with multiple traps: Can it be used to mitigate embrittlement?," *Int Journal of Hydrogen Energy,* vol. 36, pp. 10141-10148, 2011.

[49] Porter DA, Easterling KE, Phase transformation in metals and alloys, London, UK: Chapman & Hall, 1992.

[50] Speich GR, Leslie WC, „Tempering of steel," *Met Trans,* vol. 3, pp. 1043-1054, 1972.

[51] Gerberich WW, Livne T, Chen XF, Kaczorowski, „Crack growth from internal hydrogen-temperature and microstructural effect in 4340 steel," *Met Trans A,* vol. 19, pp. 1319-1334, 1988.

[52] Takagi S, Inoue T, Hara T, Hayakawa M, Tsuzaki K, Takahashi T, „Parameters for the evaluation of hydrogen embrittlement in high strength steel," *Tetsu-to-Hagané,* vol. 86, pp. 689-695, 2000.

CHAPTER VI

Hydrogen trapping and hydrogen induced mechanical degradation in lab cast Fe-C-Cr alloys*

VI.1 Introduction

The detrimental impact of hydrogen on steel was first discussed by Johnson in 1875 [1].The frequently cited reference works of Hirth [2], Oriani [3] and Troiano [4] describe the ductility loss as the main consequence of hydrogen embrittlement (HE). Conventional ductility features, such as elongation and reduction of area, are decreased due to the presence of hydrogen. Recently, interest has renewed in the subject due to the increasing amount of applications where hydrogen related failure may occur, i.e. hydrogen storage tanks, fuel cells, power plants, windmills, fish scale formation in enameling grades, sulfide stress corrosion cracking in pipeline steels and HE of welds [5] [6] [7]. Additionally, many industrial developments focus on steels with an increased strength level to meet the safety requirements desired by for instance the automotive industry. Alternatively, lowering the weight of vehicles is one of the main objectives to reduce the polluting emissions. These combined requests can be fulfilled by high strength steels, but unfortunately these are reported to be more prone HE [8] [9] [10] (cf. Chapter II).

Recently, these high strength steels have been investigated thoroughly [11] [12] [13] [14] [15] [16] [17] [18] [19] [20] [21]. Pérez Escobar *et al.* [13] studied the response of hydrogen charging on the damage evolution in terms of blister formation of four industrial high strength steels, i.e. a ferrite bainite (FB), dual phase (DP), transformation induced plasticity (TRIP) and high strength low alloyed (HSLA) grade. Additionally, thermal desorption spectroscopy (TDS) and hot extraction were performed to study the available trapping sites and their capacity [19]. The determined activation energies (E_a) for the different traps were in the same range, making it difficult to attribute certain microstructural features to a specific hydrogen desorption peak in the TDS spectra. In addition, those steels also contained variable amounts of total and diffusible hydrogen and the rate at which hydrogen effused from a hydrogen saturated sample was variable as well. This was also observed by Duprez *et al.* [21] as a different ductility recovery was obtained when a tensile test was performed on a sample after one week of discharging. The particular effect of hydrogen diffusion was recently visualized by a fracture surface analysis by means of scanning electron microscopy (SEM) in DP steel [14] (cf. Chapter III). The calculated diffusion distance *x*, defined as $(D \times t)^{1/2}$, was correlated with the observation of a transition between a hydrogen induced brittle fracture and a ductile mode.

An in-depth study was performed on TRIP steel which showed a high temperature peak with an E_a of about 90 kJ/mol. This was confirmed to originate from hydrogen trapped in the retained austenite. Crack analysis on this

* This chapter is based on the following publication: Depover T, Verbeken K, *Materials Science and Engineering* (2016), accepted with minor revisions.

material was done by Laureys *et al.* [17] [18], where electron backscatter detector (EBSD) analysis revealed that during crack initiation a hydrogen enhanced interface decohesion mechanism was active within the martensitic islands and that crack propagation was mainly stress driven. Finally, the hydrogen induced ductility loss was determined by performing tensile tests on both hydrogen charged and uncharged specimen [8]. The degree of HE was significant except for the HSLA steel, which was associated with the presence of Ti- and Nb- carbo-nitrides. In addition, this material also displayed the highest resistance against blister formation [13] and TDS analysis revealed that hydrogen was more strongly trapped compared to the other high strength steels [19] [22]. These findings were also attributed to the presence of carbo-nitrides.
Carbides are often quoted as beneficial in terms of both enhancing the HE resistance by trapping hydrogen preventing it from reaching more damaging sites and strengthening the material by secondary hardening [23] [24]. For instance, TiC and VC have been reported to improve HE resistance [24] [25]. However, on the other hand, M_2C (M=Cr, Fe, Mo) precipitates in ultrahigh-strength AERMET 100 steel have been found to be detrimental to the resistance of both internal hydrogen assisted cracking and hydrogen environment assisted cracking. This precipitate may act as a reversible or mobile hydrogen sink, from which the hydrogen can migrate to the stress concentration regions ahead of the crack tip [26] [27].

For some carbides, a significant amount of literature is available. The E_a for hydrogen desorption from TiC precipitates in steels depends mainly on the coherency of the carbide interface. An E_a of about 116 kJ/mol was determined by Wei and Tsuzaki [28] for coarse incoherent particles in a 0.42C-0.30Ti steel, whereas the coherent TiC present in this material showed an E_a of about 46-59 kJ/mol, depending on the tempering temperature. Furthermore, Pressouyre and Bernstein [29] [30] [31] [32] indicated that TiC trapped hydrogen more reversible when its coherency with the matrix was increased. VC in 0.25C-1.5Mn-V steels have an E_a of 33-35 kJ/mol [33]. Wei and Tsuzaki [34] also studied the trapping ability of NbC in a 0.05C-0.41Nb-2.0Ni steel and found various E_a's for detrapping increasing from 28 kJ/mol to about 56 kJ/mol, depending on the exposure time in vacuum since weakly trapped hydrogen was released more rapidly. Therefore, the E_a for hydrogen desorption from NbC depended on the total amount of remaining trapped hydrogen. Additionally, Wallaert *et al.* [35] determined that cathodic charging gave rise to hydrogen trapped near grain boundaries and at the interface of small NbC with an E_a of about 23 to 48 kJ/mol. Charging in a gaseous environment revealed a high temperature TDS peak attributed to the presence of incoherent NbC with an E_a ranging between 63 and 68 kJ/mol. On the other hand, M_2C (M=75 at% Cr, 13 Fe, and 12 Mo) in ultra-high strength AERMET 100 steel showed a binding energy of 11.4 to 11.6 kJ/mol [27].

Limited literature data are available on the hydrogen trapping behavior of chromium based particles and no information on their E_a is available yet. Hurtado-Noreña *et al.* [36] evaluated the effect of tempering temperature on the carbide type and their impact on hydrogen trapping by permeation experiments. The lowest hydrogen diffusion coefficient was obtained after tempering at 500°C and caused by the presence of coherent M_2X particles. Additionally, they reported that the trapping capacity decreased when coherency was lost.
Recently, Lee *et al.* [37] studied the role of Cr/Mo/V carbides in terms of the HE sensitivity for tempered martensitic steel. Four materials were investigated, i.e. a Cr, Cr-Mo, Mo and Cr-V based steel. Tempering was performed at 460°C for the Cr steel and unfortunately no Cr based carbides were detected. This was attributed to

the tempering temperature which was too low to induce this type of carbides [23] [38]. Consequently, the effect of Cr carbide on the hydrogen embrittlement behavior was excluded from this work. However, the addition of Cr to the other steels showed an effect on the HE resistance. Cr retarded the softening of martensite and hence Cr addition resulted in an increase of the tensile strength without deteriorating the resistance against HE [37].
Furthermore, research on the effect of Cr was also performed by Marchetti *et al.* [39]. They performed constant extension rate tests on a 9Cr-1Mo steel with constant rate of 10^{-4} s^{-1}. The samples were electrochemically charged and the hydrogen activity at the surface was varied by changing the cathodic current density. The fracture surfaces of the broken specimens were investigated by SEM to evaluate the change in the subsurface hydrogen activity on the extent of hydrogen-induced cracking. Superficial cracking was observed in the necking region of the hydrogen charged specimens and the brittle fracture zone extended when a higher hydrogen activity was achieved. Unfortunately, no carbide characterization and no hydrogen trapping analysis was performed.

As a conclusion, the presence of carbides plays a determinant role when evaluating hydrogen/material interaction, but little has been published on Cr based carbides. Therefore, the aim of this investigation was to evaluate the trapping ability of Cr-based precipitates and hence their impact on the degree of the hydrogen induced ductility loss. Generic Fe-C-Cr martensitic alloys were designed to contain only Cr carbides to specifically evaluate their interaction with hydrogen and their effect on the material's HE resistance.

VI.2 Experimental procedure

VI.2.1 Material characterization

Three laboratory Fe-C-Cr alloys with increasing carbon content were cast with a stoichiometric amount of the ternary alloying element Cr. Some Al was added to bind the present N preventing it from forming nitrides. The carbon increase will allow a consistent evaluation of the impact of the carbides with variable strength level, since this parameter is assumed to play an important role in terms of the sensitivity to hydrogen embrittlement. The chemical compositions are given in Table VI-1.

Table VI-1: Chemical composition of the used materials in wt%.

Material/Element	C	Cr	Other
Alloy A	0.097	1.300	200-300 ppm Al
Alloy B	0.143	1.800	
Alloy C	0.184	2.200	

The alloys were cast in a Pfeiffer VSG100 incremental vacuum melting and casting unit under an argon gas atmosphere and further hot rolled till 1.5 mm thickness. An appropriate heat treatment was applied on the alloys to obtain two main comparable conditions; one as-quenched (as-Q) state with as little precipitates as possible and one quenched and tempered (Q&T) state where free carbon was enabled to precipitate with Cr during tempering. The temperature vs. time graph of the used heat treatment is presented in Figure VI-1. All materials were austenitized at 1250°C for 10 minutes to obtain a full austenitic microstructure and to dissolve the carbides from previous processing steps. These materials were then quenched in brine (7wt% NaCl) to obtain a full martensitic structure. This first condition will be further referred to as as-Q (Figure VI-1 (a)).

Next to the as-Q condition, a second condition was prepared by tempering the quenched material at a certain temperature for one hour to generate, in a controlled way, Cr based precipitates, followed again by brine water quenching (Fig.VI-1 (b)). Tempering was performed at different temperatures to determine at which temperature the secondary hardening effect, due to the generation of precipitates, was optimal.

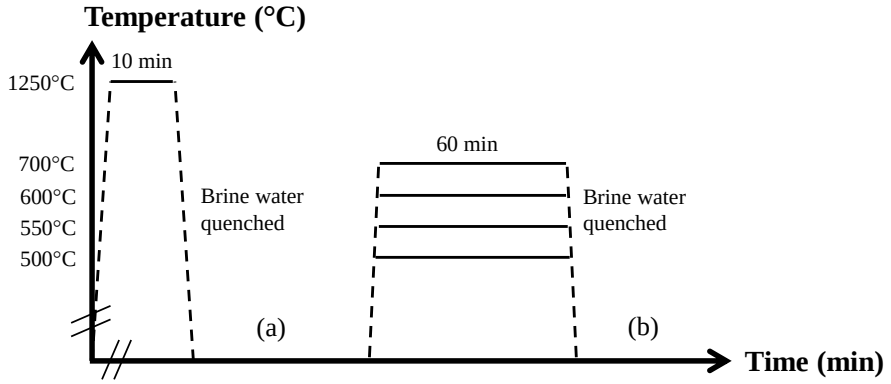

Figure VI-1: Temperature-time graphs of the heat treatments to induce: (a) as-Q and (b) Q&T condition.

Furthermore, all materials were ground and tensile specimens were machined with their tensile axis parallel to the rolling direction, for which the geometry is shown in Figure VI-2. Finally, the surface of the samples was sandblasted to remove potential oxides remaining from processing. The hardness and microstructure were investigated as described in Chapter V section V.2.1.

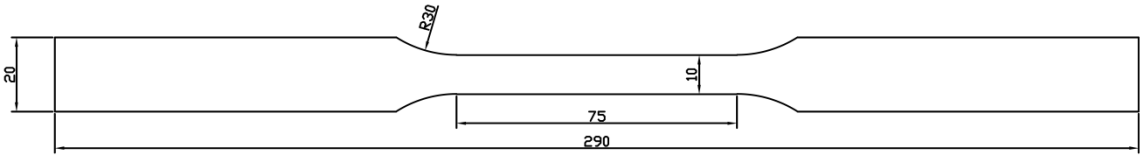

Figure VI-2: Tensile sample geometry in mm.

VI.2.2 Hydrogen induced mechanical degradation

The hydrogen induced ductility loss was determined by comparing tensile tests performed in air with tests done on hydrogen saturated samples. Hydrogen was introduced in the materials by electrochemical pre-charging using a 1g/L thiourea in a 0.5 M H_2SO_4 solution at a current density of 0.8 mA/cm² for 1 hour, while in-situ charging continued during the tensile test. The conditions were chosen based on previous work on Fe-C-Ti generic alloys (cf. Chapter V) where no blisters or internal damage was detected. The tensile tests were performed as described in Chapter V section V.2.2.

VI.2.3 Determination of the hydrogen/material interaction

The hydrogen content was determined as described in Chapter V section V.2.3, while TDS measurements were performed as explained in Chapter V section V.2.4. The hydrogen diffusion coefficient was determined as defined in Chapter V sections V.2.5.

VI.3 Material characterization

Hardness measurements were performed on the as-Q samples and on the alloys which were subsequently tempered at different temperatures to determine at which temperature secondary hardening was observed. The corresponding results are presented in Figure VI-3. A small, but recognizable secondary hardening effect can be detected after tempering at 550°C, due to the precipitation of Cr based particles. These results were in good agreement with the observations of Speich *et al.* [23] on the secondary hardening by Cr carbides. These particles tend to grow fast leading to coarse carbides and hence strengthening is minor. However, they cause a retardation of the otherwise continuous softening of the martensitic microstructure.

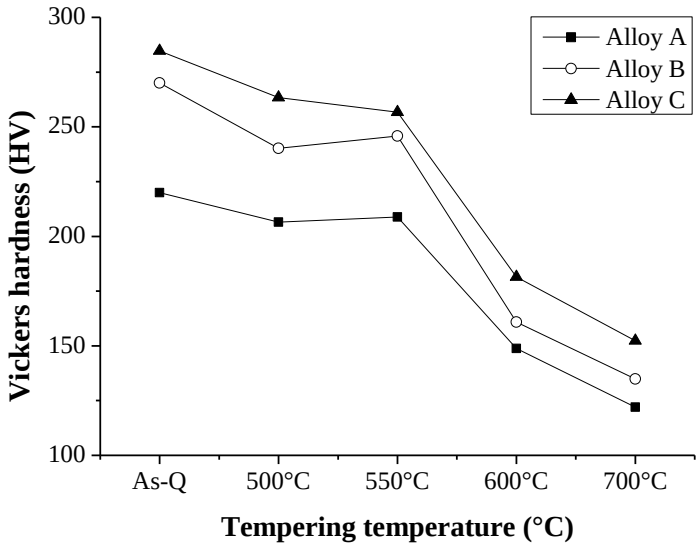

Figure VI-3: Hardness vs. tempering temperature evolution for the three Fe-C-Cr alloys.

Remarkable is the small hardness difference between alloy B and C in the as-quenched condition, since a similar carbon variation was present compared to alloy A versus B. However, the amount of dissolved carbon at an austenitization temperature of 1250°C for these stoichiometric compositions can be calculated according to the solubility product for $Cr_{23}C_6$ [40]. The thermodynamical calculations to determine the amount of dissolved carbon, as defined in Eq. VI-1, and nicely presented in Figure VI-4.

$$log_{10} \frac{M^m X^n}{MX} = -\frac{A}{T} + B \qquad \text{(VI-1)}$$

Where, M_mX_n is $Cr_{23}C_6$, M and X the alloy contents (wt%), T the temperature (K) and A and B constants of the solubility product and for $Cr_{23}C_6$ equal to 7375 and 5.36, respectively, according to Ashby [40]. In the present case, some carbon was still present in the form of carbides for alloy C in the as-Q condition. Therefore, the small difference in the amount of free carbon explains the small difference in hardness between alloy B and C.

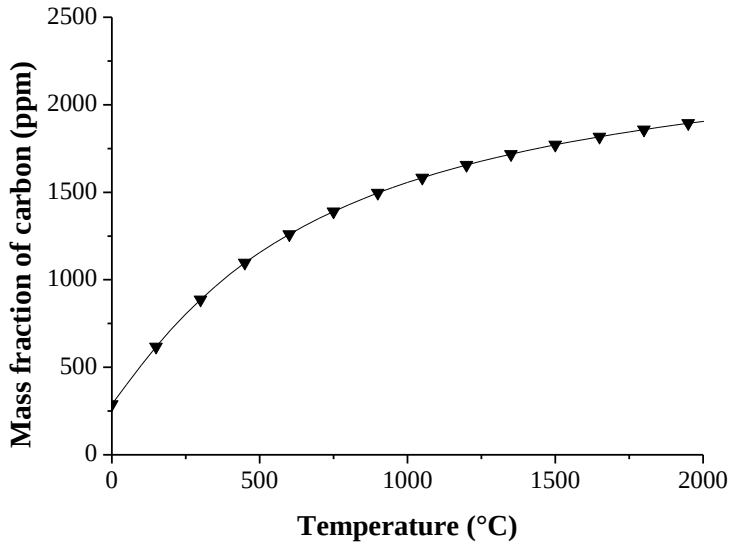

Figure VI-4: Mass fraction of carbon vs. temperature that can be kept in solid solution at each temperature for stoichiometric total contents of C and Cr

The microstructure of the materials was studied by LOM and presented in Figure VI-5 for the as-Q and the Q&T condition for materials tempered at 550°C. A martensitic and a tempered martensitic matrix can be observed. In-depth HRSEM and HRTEM were executed to analyze the Cr-based particles. Results are shown for alloy C. An HRSEM image and a forward scatter detection (FSD) image from carbon replicas are presented in Figure VI-6, whereas TEM bright field images of thin foils are given in Figure VI-7.

LOM	Alloy A	Alloy B	Alloy C
As-Q	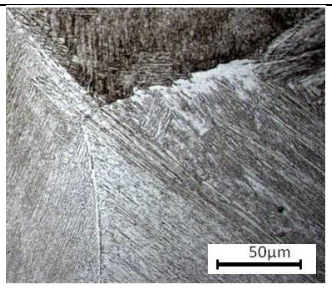	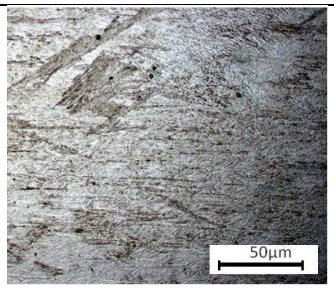	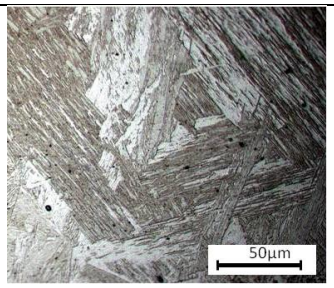
Q&T	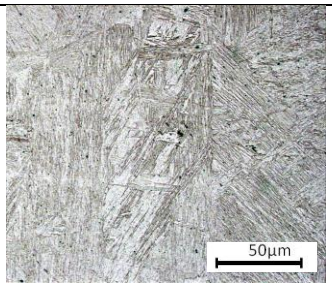	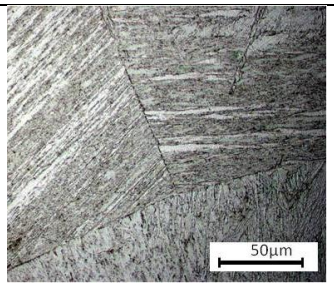	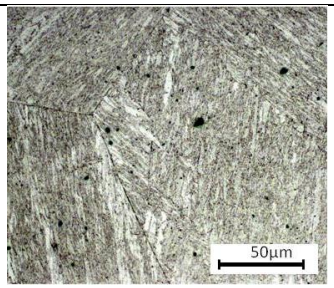

Figure VI-5: LOM images of alloy A, B and C in the as-Q and Q&T condition.

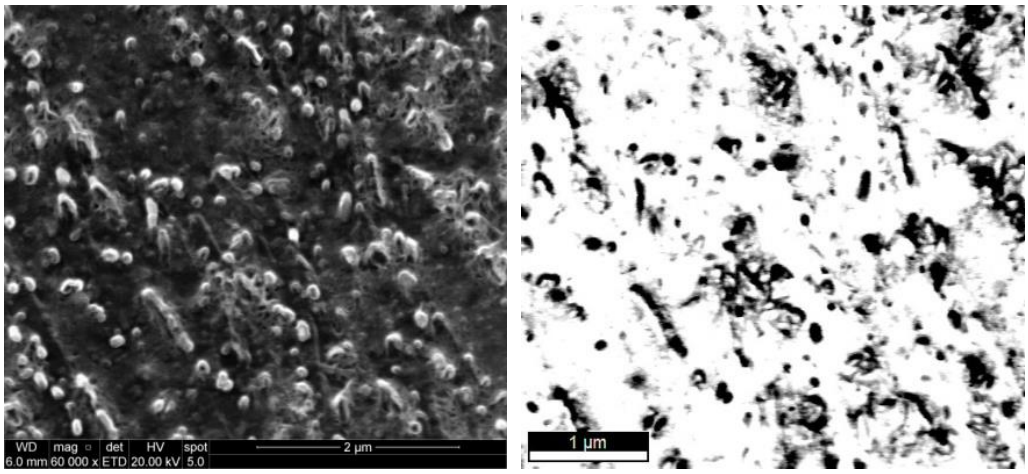

Figure VI-6: HRSEM image and FSD image of carbon replica taken from alloy C in the Q&T condition.

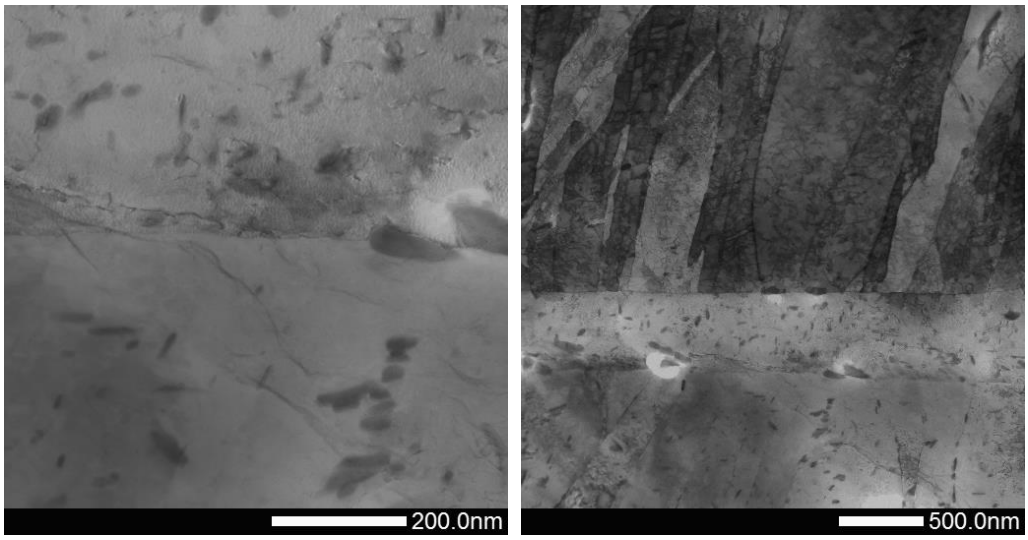

Figure VI-7: HRTEM bright field images of thin foils taken from alloy C in the Q&T condition.

Additionally, diffraction patterns from a selected area in the bright field image were taken from alloy C in the Q&T condition and analyzed to confirm $Cr_{23}C_6$ particles are indeed present in the microstructure, as shown in Figure VI-8. A match was obtained between the observed diffraction pattern and the crystal structure of $Cr_{23}C_6$. The diffraction spots were indexed and the pattern fitted with the $Cr_{23}C_6$ crystal structure with zone axis along [100]. Furthermore, other bright field images of the precipitates were taken and dark field images were made from the spots indicated on the diffraction pattern to confirm the presence of the carbides. These results are presented in Figure VI-9.

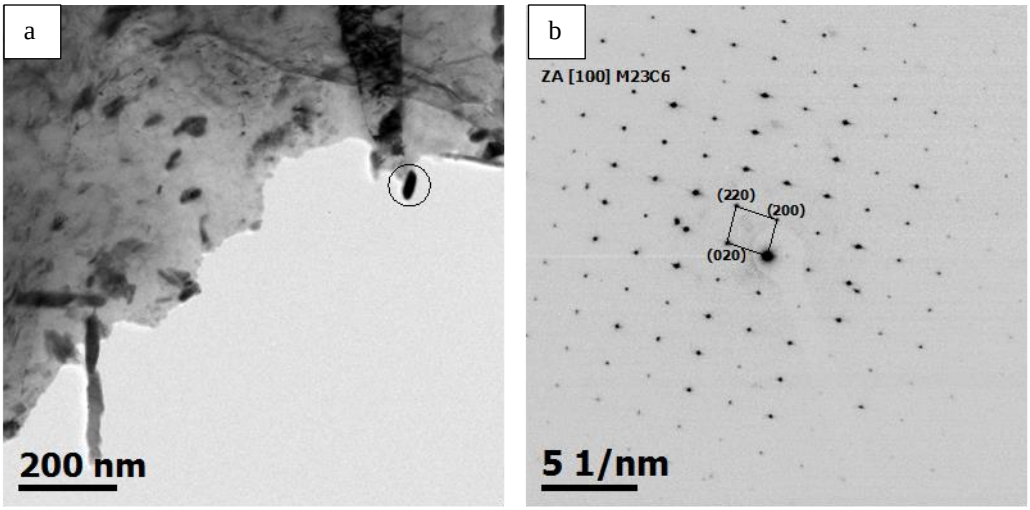

Figure VI-8: HRTEM bright field image (a) of which diffraction pattern (b) is taken from the selected area indicated by the black circle.

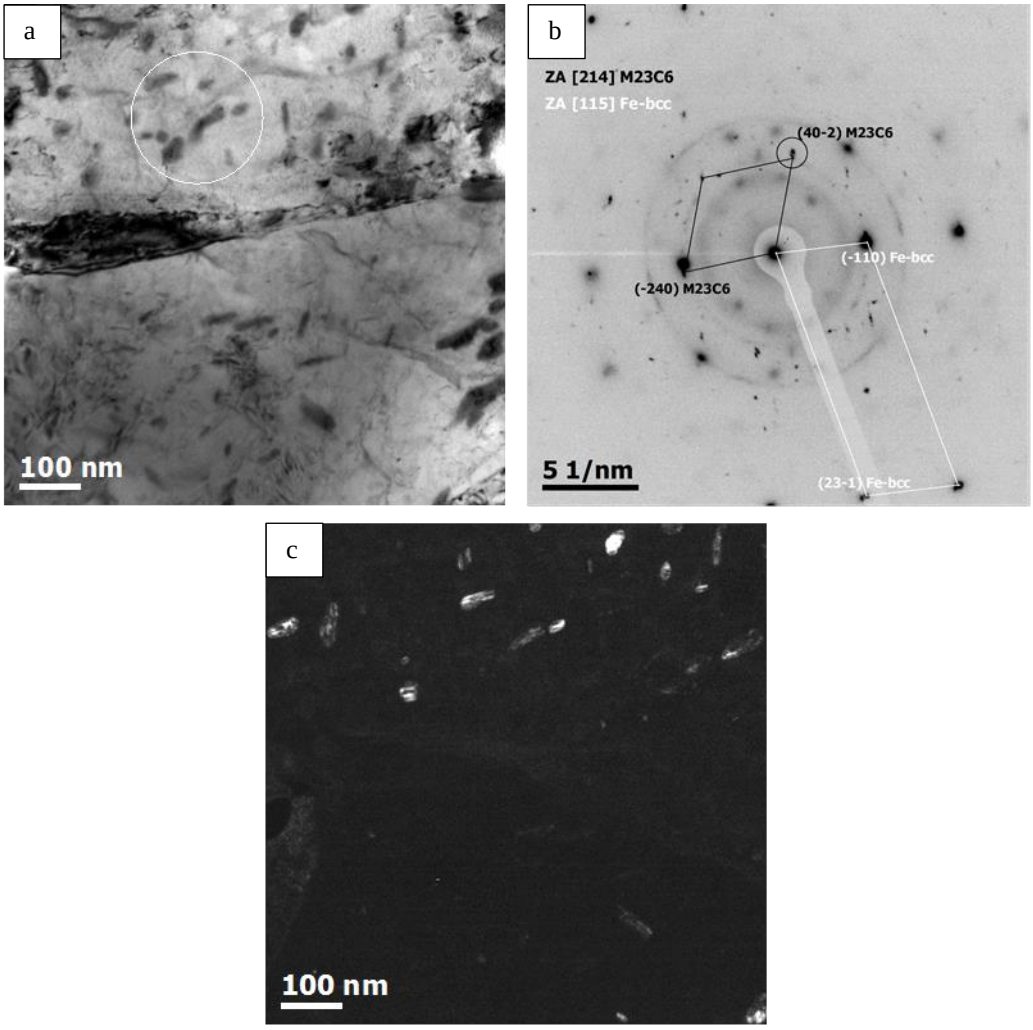

Figure VI-9: TEM bright field image (a) of which a diffraction pattern was taken from the selected area indicated by a white circle. Diffraction pattern (b) was indexed with the $Cr_{23}C_6$ crystal structure and a dark field image was taken from the indicated diffraction spots in (b) and is shown in (c).

VI.4 Hydrogen induced mechanical degradation

The tensile test results of both uncharged and hydrogen charged samples are presented in Figure VI-10 and summarized in Table VI-2. The hydrogen charged stress-strain curves are shown in bold and the two main conditions, i.e. as-Q vs. Q&T, were compared for each alloy.

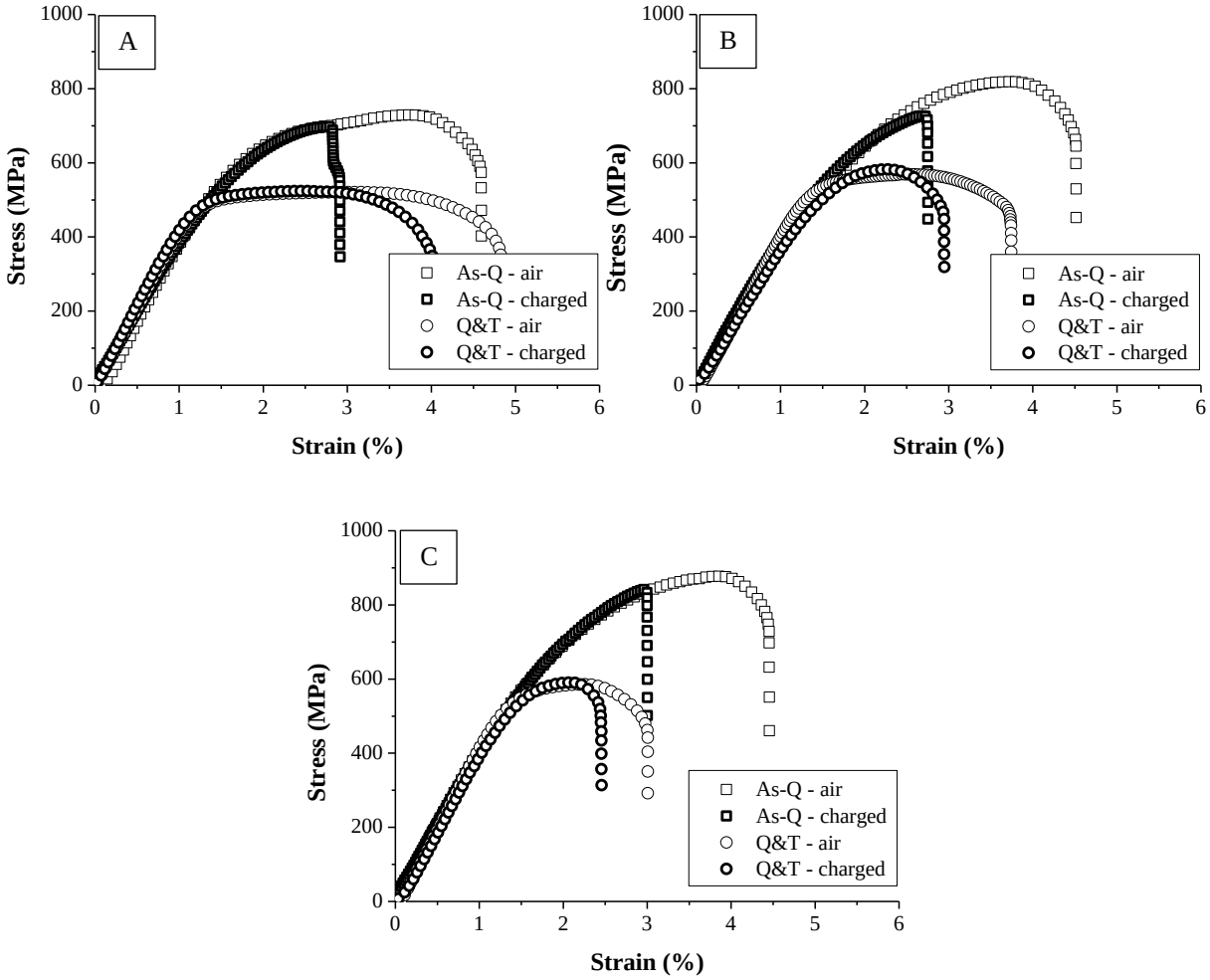

Figure VI-10: Stress-strain curves of alloy A, B and C in the as-Q and Q&T condition.

Table VI-2: Summary of the mechanical properties.

Mechanical properties	**Alloy A**		**Alloy B**		**Alloy C**	
	As-Q	Q&T	As-Q	Q&T	As-Q	Q&T
Tensile strength (MPa)	728	521	819	569	877	585
%HE	38	17	39	21	32	18

For both the as-Q and the Q&T conditions, the strength level increased with higher carbon content. Tempering resulted in a decrease of the tensile strength of the alloys, which was confirmed by the hardness measurements (cf. Figure VI-3). The precipitation of $Cr_{23}C_6$ did not cause a considerable strengthening effect due to their coarse nature [23]. Additionally, the ductility was increased for alloy A when the material got tempered, whereas the opposite was observed for alloy B and C. Furthermore, the difference in tensile strength between alloy B and

C in the as-Q state was smaller than the variation between alloy A and B, which is in good agreement with the hardness measurements.

As a general trend, tempering increased the resistance to hydrogen embrittlement. Although alloy C showed the highest as-Q strength level of all alloys, the resistance against HE slightly improved compared to alloy A and B. The correlation between HE sensitivity and strength level is, however, still under debate [8]. Also for the tempered condition of alloy C, the response to hydrogen charging did not deteriorate. In the next section, the results of these mechanical tests will be discussed based on the interaction between hydrogen and the microstructural features of the Fe-C-Cr alloys.

VI.5 Hydrogen uptake and trapping capacity

The total and diffusible hydrogen content were determined by melt/hot extraction and are shown in Figure VI-11. Identical electrochemical hydrogen charging was applied as described in section VI.2.2. A first observed tendency was that the amount of both diffusible and total hydrogen increased for alloy A over alloy B to alloy C, which can be correlated to the higher carbon content since the hydrogen uptake capacity generally increases with carbon content [41] [42] [43] [44] (cf. Chapter IV). Additionally, the potential trapping sites augmented with increasing amount of alloying elements as well.
Secondly, the amount of hydrogen trapped by the as-Q samples was similar to the content determined in the Q&T alloys. Consequently, the reduced susceptibility to HE for the tempered materials cannot be explained by differences in the total or diffusible hydrogen content of the material. Although tempering implies significant changes in the microstructural characteristics of the alloys, the overall hydrogen uptake and trapping capacity of the complete microstructure remained the same.

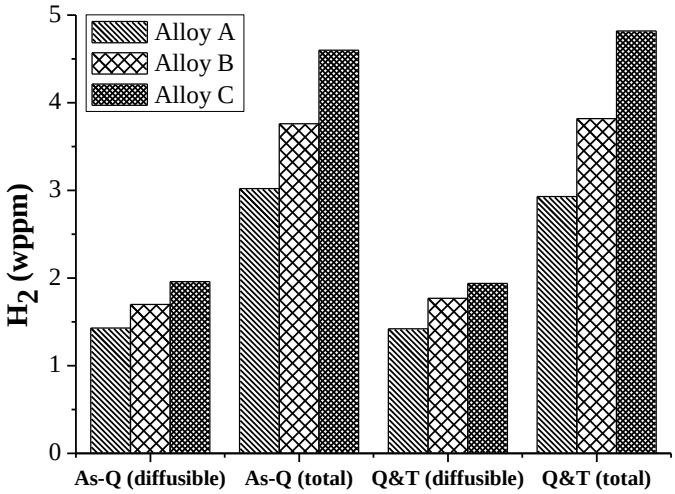

Figure VI-11: The total and diffusible amount of hydrogen after electrochemical charging for alloy A, B and C in the as-Q and Q&T condition.

To determine and interpret which trapping sites are active in both conditions for all alloys, TDS was performed. Three heating rates were applied (200°C/h, 600°C/h and 1200°C/h) to determine the activation energy of the deconvoluted peaks. Figure VI-12 represents the deconvoluted TDS spectra at a heating rate of 600°C/h and Table VI-3 summarizes the corresponding activation energies for the obtained peaks.

TDS	As-Q	Q&T
Alloy A	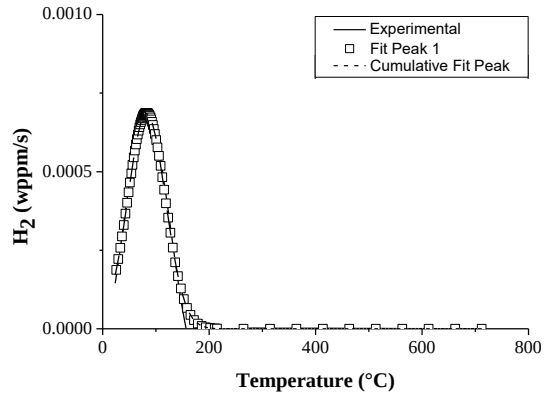	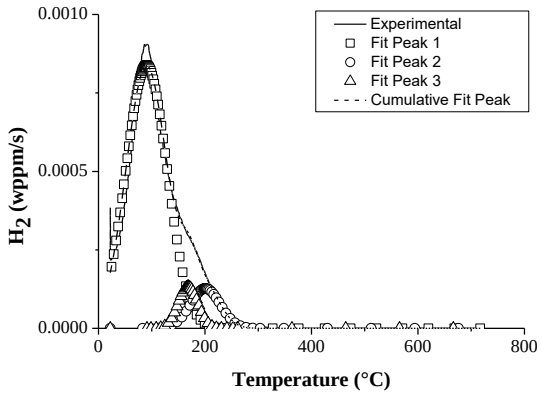
Alloy B	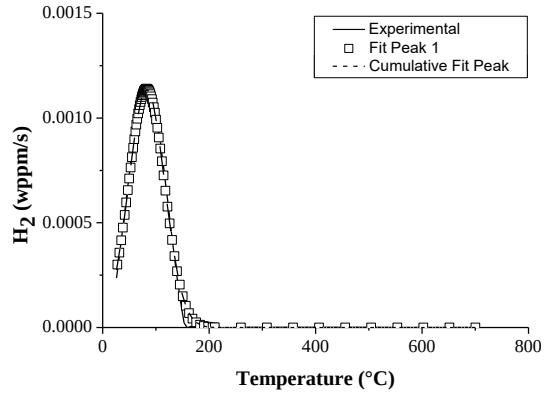	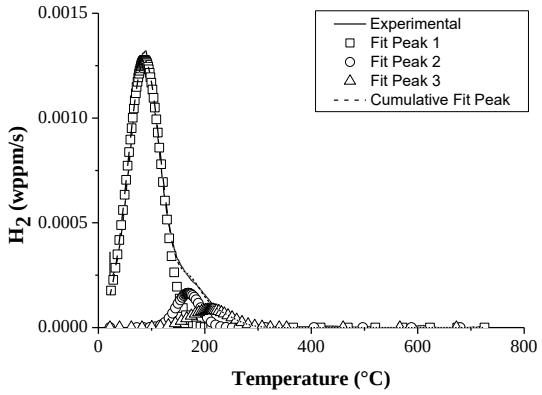
Alloy C	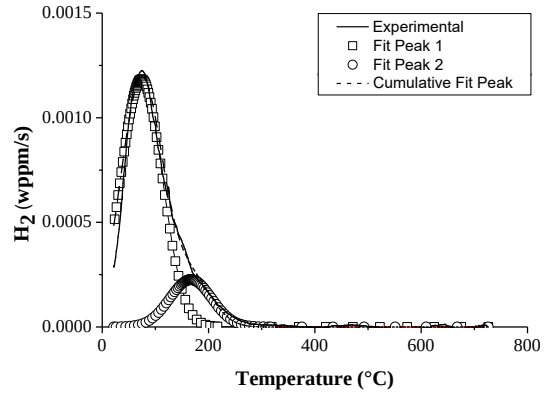	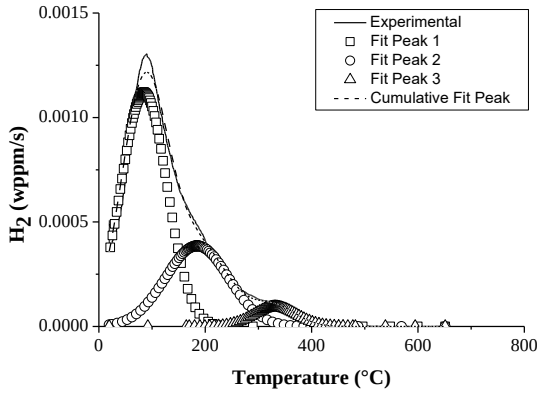

Figure VI-12: TDS spectra for alloy A, B and C in the as-Q and Q&T condition at a heating rate of 600°C/h.

Table VI-3: Summary of the corresponding activation energies for the deconvoluted peaks.

Activation energy (kJ/mol)	Alloy A		Alloy B		Alloy C	
	As-Q	Q&T	As-Q	Q&T	As-Q	Q&T
Peak 1	28	29	30	26	25	23
Peak 2	/	48	/	49	49	51
Peak 3	/	51	/	52	/	55

The TDS spectra clearly indicated that different trapping sites are available for the as-Q and the Q&T materials. When first having a look at the as-Q grades, only alloy C contained a shoulder in the experimental desorption curve, which was therefore deconvoluted into two peaks. The calculated E_a of the first peak of all the alloys was approximately 25-30 kJ/mol, which was equivalent to desorption activation energies for lath boundaries in martensite and therefore attributed to this trapping site [45]. However, hydrogen trapped by dislocations has an E_a in the same range [2] [28] [30] [46], but Pérez Escobar *et al.* [20] demonstrated that hydrogen trapped by dislocations mostly left the material before the TDS measurement could be started since it takes one hour to reach a low pressure in the analysis chamber. Although a distinction between dislocations and lath boundaries could not be made based on E_a, the first peak is therefore supposed to be largely due to hydrogen trapped at martensite lath boundaries.

Since only alloy C as-Q still contained carbides after austenitizing, as discussed in the material characterization section, the second peak was associated with hydrogen trapped at $Cr_{23}C_6$ precipitates. Moreover, the E_a of about 50 kJ/mol for this peak is in good correspondence to the E_a of TiC [28] [47]. According to [48], the kind of trapping site is still reversible since the E_a is lower than 60 kJ/mol. The (ir)reversible nature of a trap was nicely demonstrated in the work done on the Fe-C-Ti alloys (cf. Chapter V). Additionally, the peak area obtained by integrating the TDS spectra increased from A → B → C, which was in good agreement with the hot/melt extraction results (cf. Figure VI-11).

Extra peaks were observed when the materials got tempered. Since $Cr_{23}C_6$ were introduced during the tempering, these peaks were associated with hydrogen trapped at the carbides. A clear shoulder was present for all Q&T alloys and the experimental desorption curve was deconvoluted into three peaks. The first was again associated with hydrogen mainly trapped at the lath boundaries, whereas the extra peaks resulted from hydrogen at the precipitates showed an E_a of about 50-55 kJ/mol, similar to the E_a of the remaining carbides in alloy C as-Q.

In addition, more hydrogen was present in these TDS spectra compared to those of the as-Q condition and the amount increased again for A → B → C. This evolution over the different alloys is similar to the hot/melt extraction results, but the higher hydrogen content for the Q&T alloys was not confirmed by hot/melt extraction. Consequently, this observation indicates that hydrogen got trapped differently in the as-Q and Q&T material.

Although the comparison of Figure VI-11 and VI-12 showed similar tendencies in the relative evolution of the hydrogen content for the different alloys, the absolute hydrogen content was not the same. This is due to the fact that a significant amount of hydrogen was released from the sample before the start of the TDS measurement. This released hydrogen will be further referred to as mobile hydrogen. However, this hydrogen is included in the amount of diffusible hydrogen and hence detected by hot extraction since these tests were done one minute after the end of charging. The resulting values are summarized in Table VI-4. With this information, we will be able to link the results of the mechanical tests to those of the TDS and hot/melt extraction.

Table VI-4: Summary of the hydrogen contents for alloy A, B and C in the as-Q and Q&T condition.

Hydrogen content (wppm)	**Alloy A**		**Alloy B**		**Alloy C**	
	As-Q	Q&T	As-Q	Q&T	As-Q	Q&T
diffusible hydrogen	1.43	1.42	1.70	1.77	1.96	1.94
hydrogen under TDS curves	0.34	0.55	0.50	0.86	0.80	1.10
mobile hydrogen	1.09	0.87	1.20	0.91	1.16	0.89

Although a similar amount of diffusible hydrogen is present in all alloys for both conditions, a significantly different trapping occurred. Both conditions of alloy C for instance contain about 1.95 wppm of diffusible hydrogen, of which the major part is mobile for the as-Q condition, while the opposite can be observed for the Q&T state. Furthermore, the higher amount of mobile hydrogen for the as-Q samples can be linked to its higher dislocation density since hydrogen trapped at dislocations is assumed to be largely undetectable by TDS. Tempering generally reduces the dislocation density in a martensitic microstructure [23] [49]. Therefore, dislocations can be set responsible for the similar hydrogen contents which got determined for the as-Q and Q&T samples by hot/melt extraction. The elastic stress fields surrounding the carbides are less important in comparison to the TiC particles (cf. Chapter V). The Cr precipitates are coarse and induced in a softer matrix, while the introduction of TiC resulted in a significant secondary hardening.

A significant fraction of hydrogen was stronger trapped by the carbides in the Q&T sample, which explains the better response against HE for the Q&T condition. It can now also be explained why alloy C as-Q showed a better HE resistance compared to the as-Q condition for alloy A and B, as the presence of an extra hydrogen trapping peak in the TDS spectrum could be associated with the presence of $Cr_{23}C_6$ particles. Similar conclusions can be drawn for the Q&T HE values, since generally a higher HE% would be expected for alloy C because a higher hydrogen content was determined by hot/melt extraction. However, TDS analysis showed that a considerably larger amount of hydrogen was trapped in the second and third deconvoluted peak for alloy C, which can be set responsible for the decreased HE of 18%. Since a higher amount of hydrogen got trapped by the tempered induced precipitates, less mobile hydrogen was able to effuse from the material.

As the alloys contained similar amount of diffusible hydrogen in the as-Q and Q&T condition, but hydrogen showed a different ‘mobility’, this should be reflected in the hydrogen diffusion coefficients of the alloys when comparing both conditions. As hydrogen diffusivity is indeed dependent on the trapping sites in the material [42] [43] [50] [51] [52] [53] [54], hydrogen permeation experiments were done on alloy C for the as-Q and Q&T condition. The permeation curves were shown in Figure VI-13.

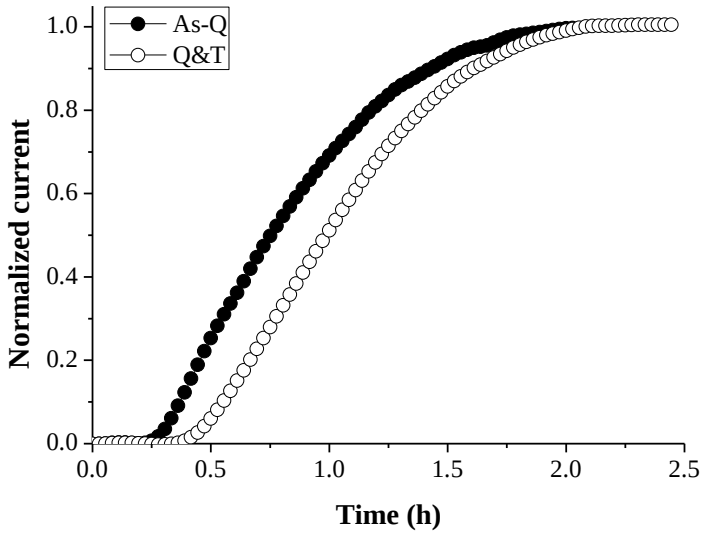

Figure VI-13: Hydrogen permeation curves for alloy C in the as-Q and Q&T condition.

The Q&T condition showed indeed a slower hydrogen permeation compared to the as-Q state with diffusion coefficients of 5.78 x 10^{-11} m^2/s and 1.71 x 10^{-10} m^2/s, respectively. The slower permeation for Q&T nicely corresponds with the presence of the carbide traps in the microstructure which hinder hydrogen diffusion [55] and with the lower amount of mobile hydrogen (cf. Table VI-4). Additionally, the higher first peak in the TDS spectra for the Q&T materials (cf. Figure VI-12) can be linked to the slower diffusion as well. Since less mobile hydrogen was able to leave the sample before the start of the measurement due to the lower diffusion coefficient, more hydrogen was still detectable in the TDS spectra.

In Figure VI-14, the degree of embrittlement is plotted with respect to the different amounts of hydrogen. Three different kinds of hydrogen were incorporated; i.e. total, diffusible and mobile and a good linear fit was achieved when HE% was correlated with the mobile hydrogen content. Apparently, this type of hydrogen, mainly considered as hydrogen trapped by dislocations, is the most important one when evaluating the susceptibility to hydrogen embrittlement.

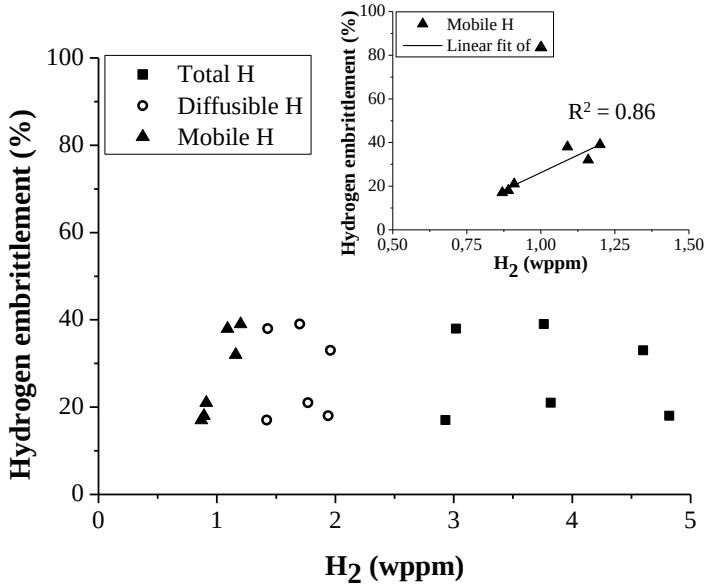

Figure VI-14: Degree of hydrogen embrittlement vs. different types of hydrogen.

As a conclusion, a particularly interesting observation was made for the present alloys. All alloys contained similar amount of diffusible hydrogen but showed a different sensitivity to HE. TDS analysis and an evaluation of the interplay between hydrogen mobility and the availability of hydrogen traps allow to explain HE differences. The presence of carbides as hydrogen traps clearly plays an important role in this discussion. Therefore, a more detailed evaluation of the carbide characteristics will be made in the next section.

VI.6 On the effect of carbide characteristics on the hydrogen trapping ability

To be able to better attribute the TDS peaks to a specific feature, carbide size distributions were made. The HRSEM and FSD images on carbon replicas are shown together with their corresponding size distributions in Figure VI-15 for alloy A and B and in Figure VI-16 for alloy C.

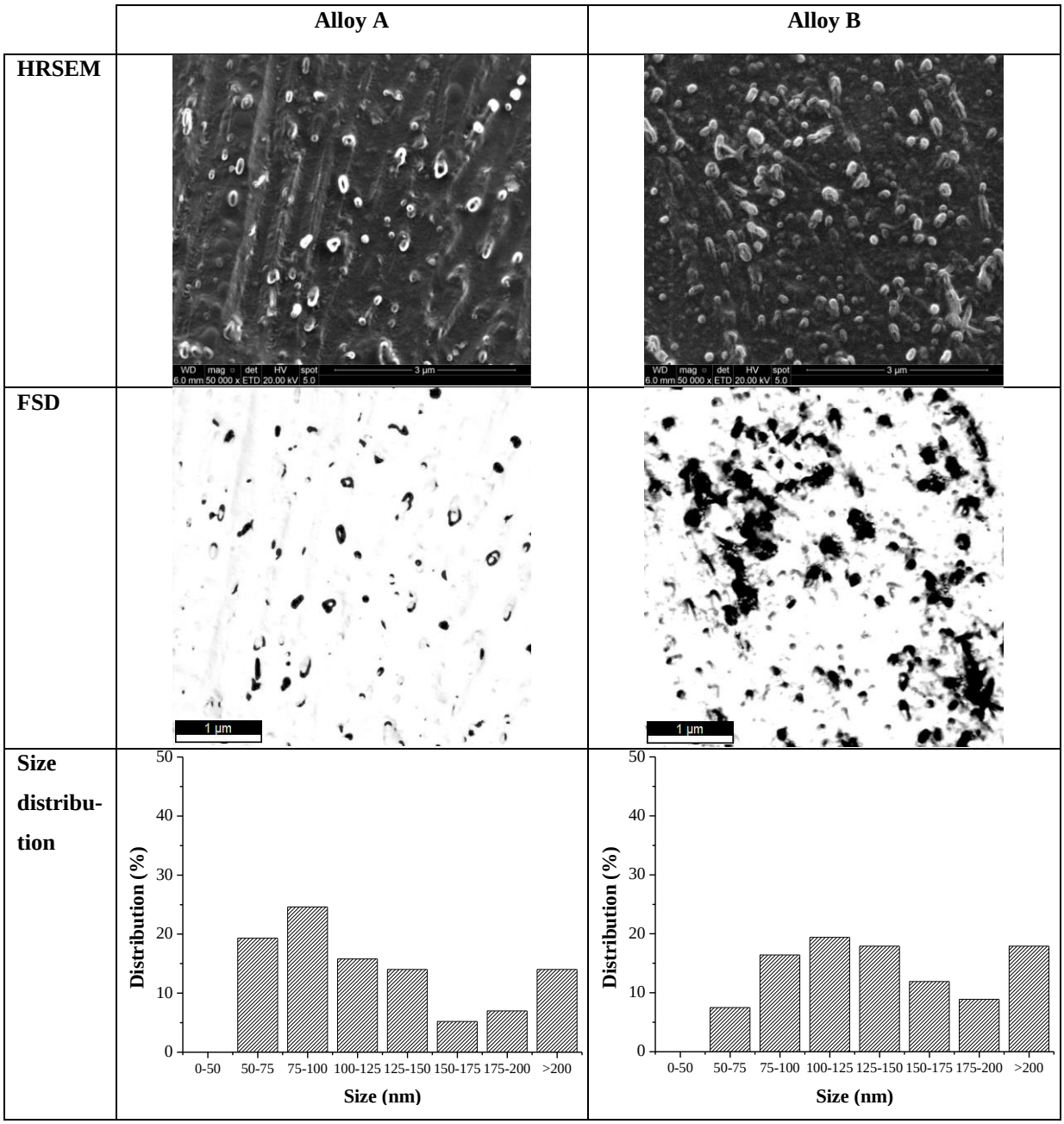

Figure VI-15: HRSEM and FSD images of carbon replicas of alloy A, B in the Q&T condition together with their corresponding size distribution maps.

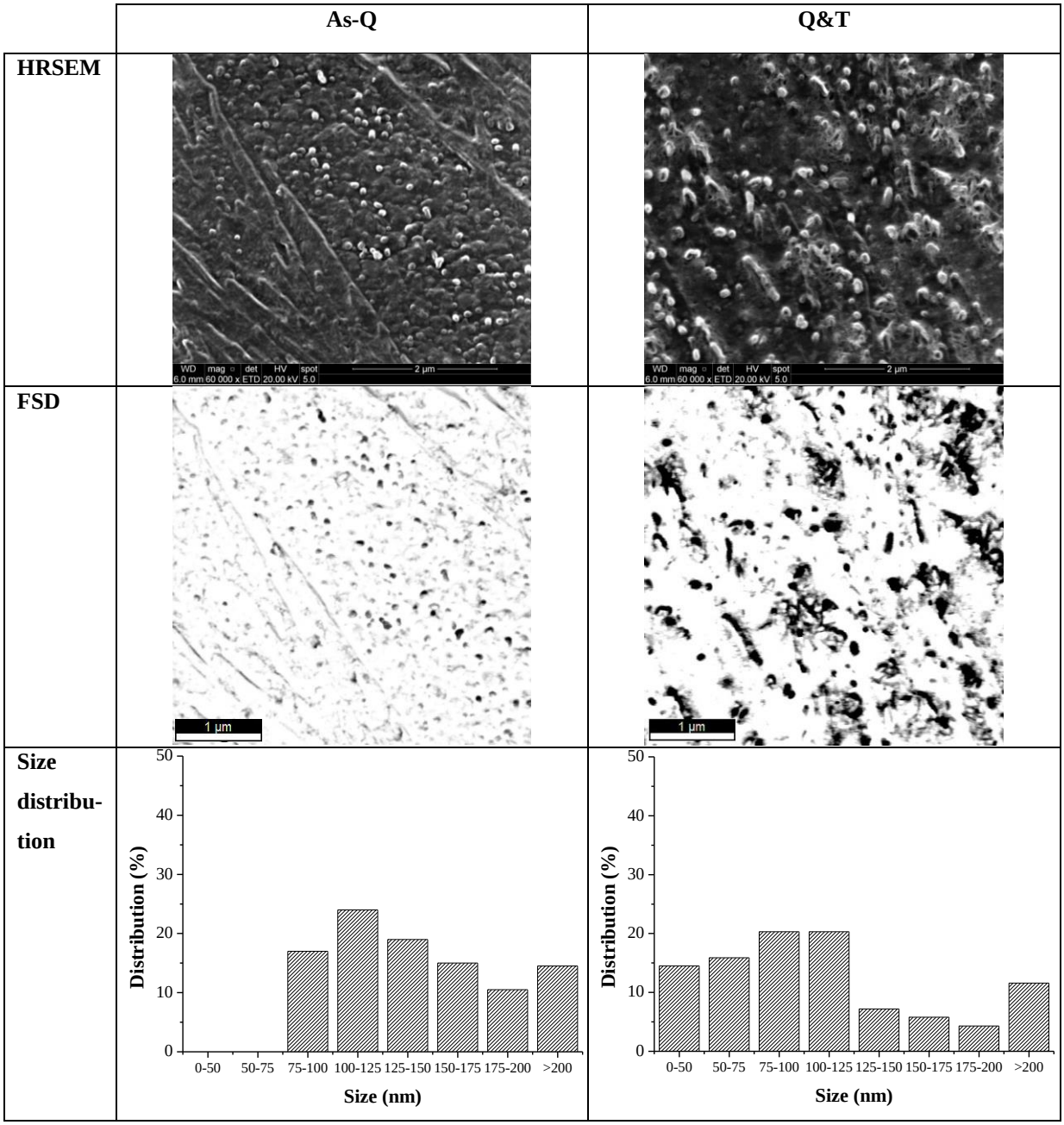

Figure VI-16: HRSEM and FSD images of carbon replicas of alloy C in the as-Q and Q&T condition together with their corresponding size distribution maps.

When considering the as-Q materials, only for alloy C a carbide size distribution map could be made since only for alloy C carbides were present as discussed in section VI-3 and VI-5. Consequently, the desorption peak of about 50 kJ/mol associated with hydrogen trapped at precipitates in Figure VI-12 can be attributed to particles > 75 nm as no smaller carbides were present in the as-Q state. These kinds of particles were also present in the Q&T samples and hence gave rise to a corresponding peak in the TDS spectra as well. The third peak for alloy C Q&T can be attributed to particles less than 75 nm, since these particles were not detected in the as-Q state.

Attributing the observed desorption peaks in Figure VI-12 for the Q&T materials to certain carbides sizes is no that straightforward. For alloy A and B, two peaks with peak temperatures around 175 - 200°C were observed,

while just one broad peak was detected for alloy C in this temperature range. Alternatively, this broad peak of alloy C could also be deconvoluted into two separate peaks, although the fit was not as good. Pérez Escobar *et al.* [56] already mentioned in their TDS methodology study that some arbitrary choices need to be made when applying a deconvolution procedure. In the present case, the peaks associated with a peak temperature of about 175 - 200°C can be linked to carbides size in the range of 50-100 nm since smaller carbides were not present for alloy A and B.

For alloy C, the peak temperature for the third peak (350°C) is considerably higher compared to alloy A and B. Additionally, the activation energy also slightly increased, which could be linked to the presence of carbides smaller than 50 nm, which were not present for alloy A and B in the Q&T condition. This might be because carbide growth and coarsening is faster in a less dense microstructure [23].

When one takes a closer look to alloy A and B in the Q&T condition, a more detailed separation in terms of carbide sizes can be proposed. The 3rd peak of alloy A contained more hydrogen compared to alloy B, whereas the amount of hydrogen for the second peak was about the same for alloy A and B (cf. Figure VI-12). Correlating this to the distribution maps, one could observe that the 2nd peak with peak temperature around 175°C can be linked to carbides of sizes 75-100 nm, while the 3rd peak with a peak temperature around 200°C can be correlated to carbides of sizes 50-75 nm since the percentage for this range was double for alloy A compared to B in this range and similar for the 75-100 nm range. In order to further evaluate these hypotheses, an alternative heat treatment, which will change the carbide size distribution, is applied as discussed in the next section.

VI.7 On the carbide trapping ability and effect on the hydrogen induced ductility loss

Instead of tempering for one hour, these samples were heat treated for two hours at 550°C which changes the carbide size distribution and allows evaluating the carbide trapping ability and capacity. TDS measurements were performed on the Q&T 2h samples and the deconvoluted peaks together with the carbide size distribution maps are shown in Figure VI-17.

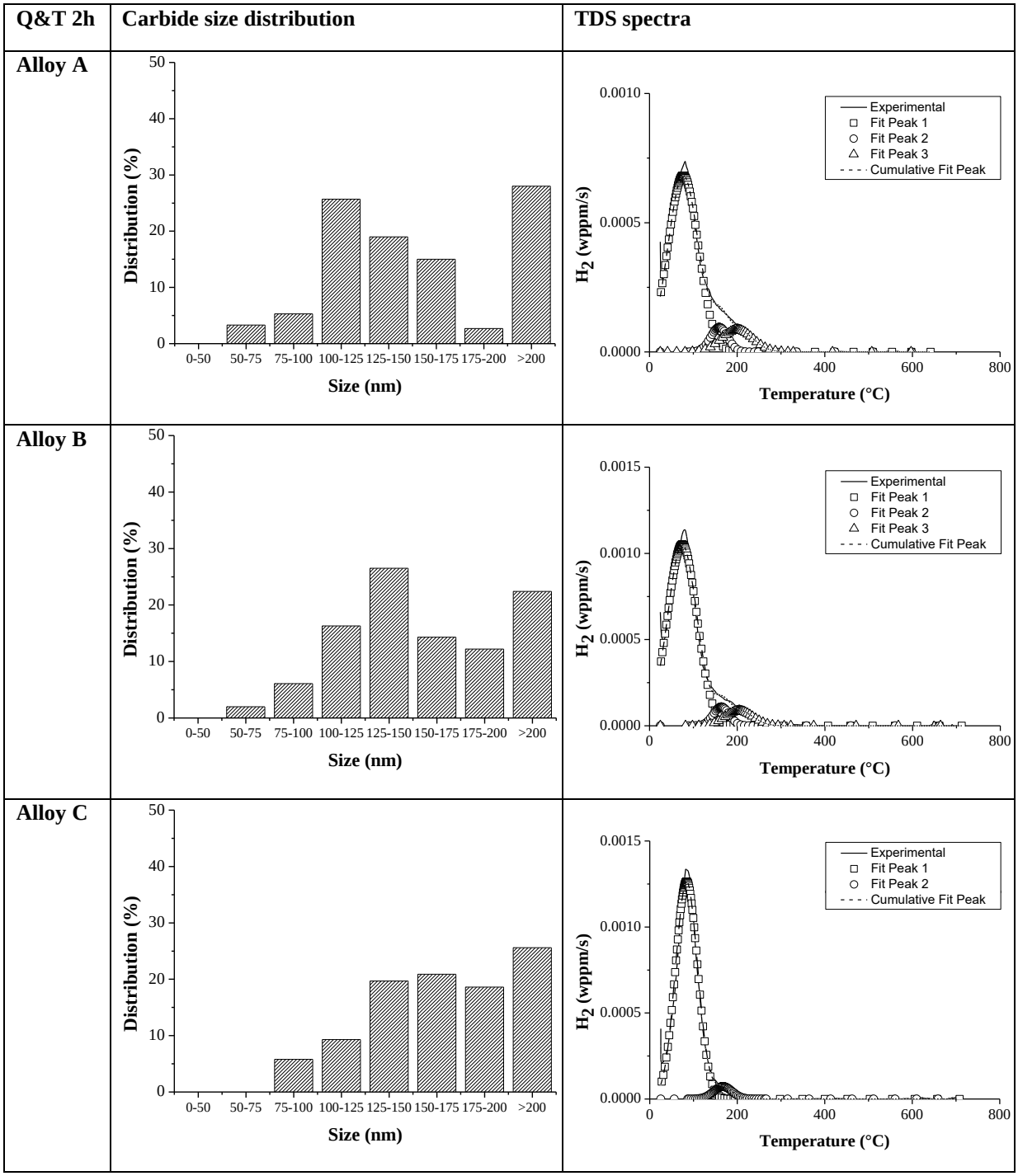

Figure VI-17: Carbide size distribution map together with the corresponding TDS spectra for alloy A, B and C in the Q&T 2h condition.

The TDS spectra were deconvoluted in three peaks for alloy A and B and in two peaks for alloy C. The amount of hydrogen detected by TDS is significantly lower compared to the Q&T 1h materials. Similar corresponding trapping sites were active for alloy A and B compared to the 1h tempered materials. However, two hours tempering made the carbides grow considerably as demonstrated by the size distributions. Consequently the amount of hydrogen trapped by the Cr-carbides, determined by integrating the corresponding peaks, decreased significantly. The total interfacial area between the precipitates and the matrix decreased accordingly with increasing carbide size. Therefore, it could be assumed that hydrogen was rather trapped in the interface than inside the carbides, which is in agreement with the observations of Wei and Tsuzaki [47] and Takahashi *et al.* [57] on TiC particles.

For alloy C, only a tiny peak associated to hydrogen trapped at carbides remained, as carbides have grown considerably for this alloy. The third peak for alloy C Q&T 1h, associated in the previous section with carbides smaller than 50 nm, disappeared in the spectrum of Q&T 2h, together with these small particles. Indeed, when this alloy got tempered for two hours, carbides became too big and their interface got more incoherent. Therefore, the precipitates were no longer able to trap hydrogen charged from the used electrochemical source.

The 2nd peak for all alloys with peak temperature around 175°C was still present for all alloys and can therefore be associated with hydrogen trapped at carbides in the range of 75-100 nm, since these were only present in alloy C. Furthermore, for alloy A and B still carbides were present in the carbide size range of 50-75 nm which resulted in a 3rd peak with a peak temperature around 200°C. Additionally, the area below this peak was again almost double for alloy A as compared to alloy B which can be correlated to the higher fraction of these kind of carbides in the size distribution maps. Consequently, the results obtained after 2h tempering confirmed the hypotheses proposed in the previous section.

The discussion on the small carbide related peak in alloy C can be confirmed by tempering this alloy for 4 h. This would demonstrate that at a certain carbide size limit, these carbides are no longer capable of trapping electrochemically charged hydrogen. The carbide size distribution together with the TDS spectra for alloy C after 4h tempering is presented in Figure VI-18.

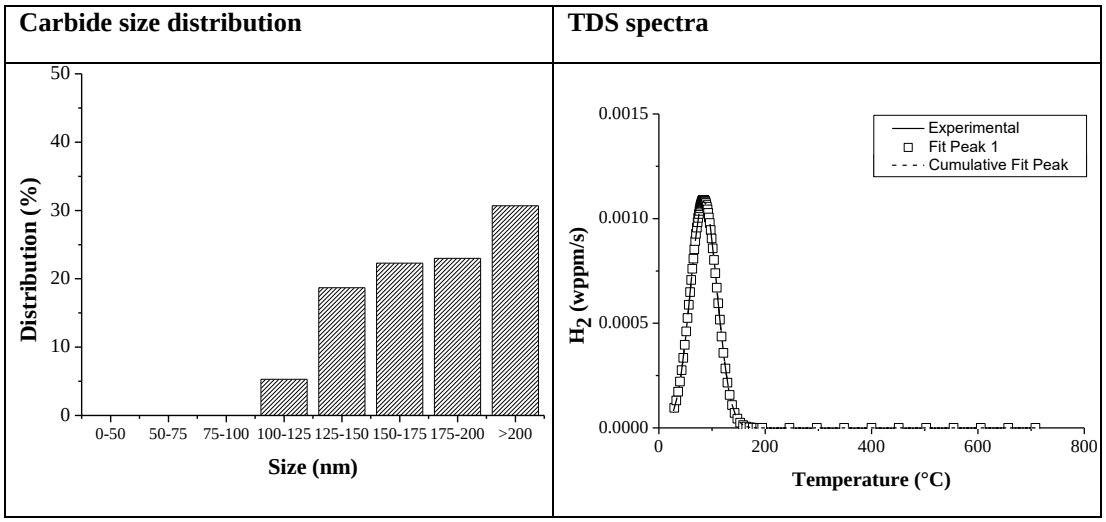

Figure VI-18: Carbide size distribution map together with the corresponding TDS spectra for alloy C in the Q&T 4h condition.

When the materials got tempered for four hours, hydrogen was indeed no longer trapped by the present carbides as they became too large and too incoherent. Therefore, the carbide size limit to trap hydrogen electrochemically can be set at 100 nm for the present materials, which indeed confirmed that the 2nd TDS peak could be attributed to carbides in the range of 75-100 nm (cf. Figure VI-17).

As the crucial amount of mobile hydrogen can be determined from the diffusible hydrogen content and the TDS spectra, hot extraction experiments were performed and the results are shown in Figure VI-19. The hot extraction results indicated that less hydrogen was trapped when the materials got tempered for two hours. This was consistent with the TDS measurements where less hydrogen got detected as well (cf. Figure VI-12 and VI-17). Additionally, the amount of mobile hydrogen decreased considerably as well to 0.21, 0.31 and 0.61 wppm for alloy A, B and C Q&T at 2h, respectively. Since the sensitivity to HE was correlated with the amount of mobile hydrogen, the hydrogen induced mechanical degradation is assumed to decrease. To confirm this hypothesis, tensile tests were performed on the Q&T 2h samples as well. The mechanical properties are presented in Figure VI-20 for alloy A, B and C and summarized in Table VI-5.

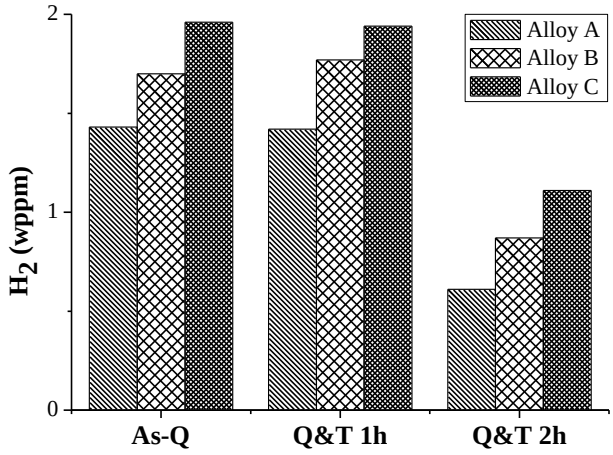

Figure VI-19: Diffusible hydrogen content vs. applied thermal treatment for alloy A, B and C.

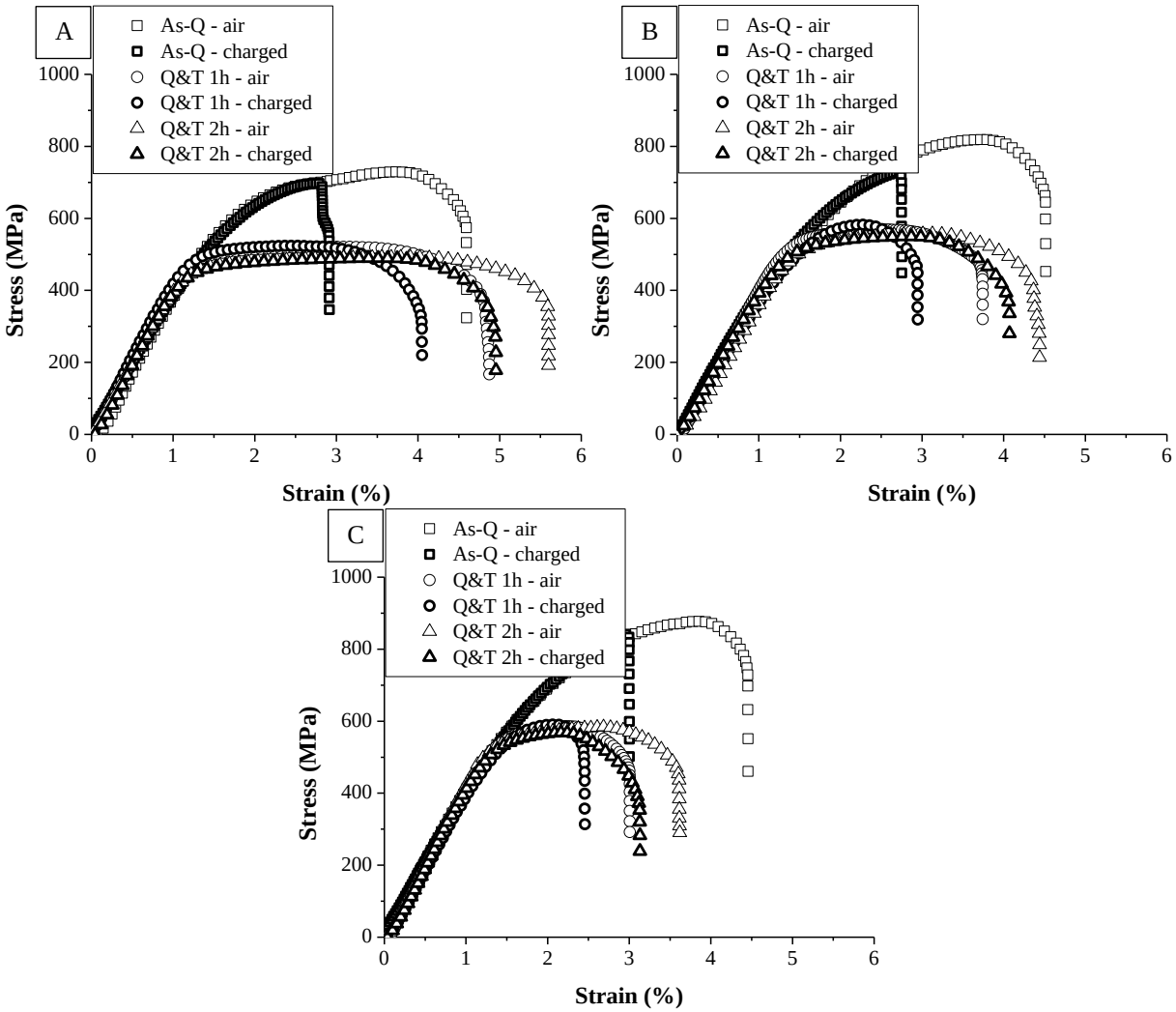

Figure VI-20: Stress-strain curves of alloy A, B and C in the as-Q, Q&T 1h and Q&T 2h condition.

Table VI-5: Summary of the HE% for alloy A, B and C in the as-Q and the tempered conditions.

HE%	As-Q	Q&T 1h	Q&T 2h
Alloy A	38	17	11
Alloy B	39	21	9
Alloy C	33	18	13

The HE% indeed decreased for all alloys when the materials got tempered for two hours, which confirms the proposed hypothesis. Although carbides trapped less hydrogen in the Q&T 2h condition (cf. Figure VI-17), the mobile hydrogen content decreased, which resulted in an enhanced resistance to HE. Additionally, the strength level was just a little lower compared to the Q&T 1h grade, which makes a comparison regardless of strength level possible. Although higher uncharged elongations were obtained, the hydrogen induced ductility loss improved when tempering for two hours was applied. Actually, the Q&T 2h condition hydrogen saturated samples had an elongation which was similar to the Q&T 1h condition without hydrogen.

In addition, alloy C Q&T 2h was slightly more prone to HE compared to alloy A and B, whereas for the as-Q and Q&T 1h condition, this alloy performed better (cf. Table VI-5). This was attributed to the amount of mobile hydrogen that was higher for alloy C compared to A and B when tempered for two hours, as opposed to the

materials which were tempered for one hour (cf. Table VI-4). The TDS results indeed also indicated the presence of only one carbide related peak for alloy C, while alloy A and B still show two carbide related peaks. Therefore, this can be considered as a confirmation of the beneficial effect of adding carbides with the right characteristics to enhance the HE resistance of a material.

VI.8 Conclusion

The present study investigated the hydrogen trapping capacity of $Cr_{23}C_6$ and hence its impact on the hydrogen induced ductility loss in laboratory Fe-C-Cr alloys. Two main conditions were compared: an as-quenched and a quenched and tempered condition containing $Cr_{23}C_6$. Three materials were cast with a variable carbon content to examine the role of the carbides in alloys with variable strength level. Mechanical tests were performed on both in-situ hydrogen charged and uncharged tensile samples. The presence of carbides decreased the susceptibility to hydrogen embrittlement. Thermal desorption spectroscopy and hot/melt extraction were done to determine the active trapping sites. A clear correlation between the degree of hydrogen induced mechanical degradation and the hydrogen mobility was confirmed by determining the hydrogen diffusivity and linking it to the available trapping sites.

A modified tempering treatment was applied to vary the carbide size and evaluate its effect on the HE resistance of the material and the trapping ability of the present carbides. The resistance to hydrogen induced mechanical degradation further improved due to the lower amount of mobile hydrogen. Additionally, it was demonstrated that hydrogen got trapped at the interface between carbide/matrix and that carbides with sizes larger than 100 nm were not able to trap electrochemically charged hydrogen.

VI.9 References

[1] Johnson WH, „On some remarkable change produced in iron and steel by the action of hydrogen and acids.," *Proceedings of the Royal Society of London,* vol. 23, pp. 168-179, 1875.

[2] Hirth JP, „Effects of Hydrogen on the Properties of Iron and Steel," *Metallurgical Transactions A,* vol. 11A, pp. 861-890, 1980.

[3] Oriani RA, Hirth JP, Smialowski M, Hydrogen degradation of ferrous alloys, New Jersey: Noyes Publications, 1985.

[4] Troiano AR, „The role of Hydrogen and Other Interstitials in the Mechanical Behaviour of Metals," *Trans. ASM,* vol. 52, pp. 54-80, 1960.

[5] Revie RW, Sastri VS, Elboujdaii M, Ramsingh RR, Lafrenière Y, „Hydrogen-induced cracking of line pipe steels used in sour service," *Corrosion,* vol. 49, pp. 531-536, 1993.

[6] Chawla KK, Rigsbee JM, Woodhouse JB, „Hydrogen-induced cracking in two linepipe steels," *Journal Mater Sci,* vol. 21, pp. 3777-3782, 1986.

[7] Maroef I, Olson DL, Eberhart M, Edwards GR, „Hydrogen trapping in ferritic steel weld metal," *Inter Mater Rev,* vol. 47, pp. 191-223, 2002.

[8] Depover T, Pérez Escobar D, Wallaert E, Zermout Z, Verbeken K, „Effect of in-situ hydrogen charging on the mechanical properties of advanced high strength steels," *Int Journal of Hydrogen Energy,* vol. 39, pp. 4647-4656, 2014.

[9] Hilditch TB, Lee SB, Speer JG, Matlock DK, „Response to Hydrogen Charging in High Strength Automotive Sheet Steel Products," *SAE Technical Paper,* 2003, http://dx.doi.org/10.4271/2003-01-0525.

[10] Loidl M, Kolk O, „Hydrogen embrittlement in HSSs limits use in lightweight body," *Advanced Materials and Processes,* vol. 169, pp. 22-25, 2011, BMW Group, Germany.

[11] Ronevich JA, Speer JG, Matlock DK, „Hydrogen embrittlement of commercially produced advanced high strength steels," *SAE Int Journal Mater Manuf,* vol. 3, pp. 255-267, 2010.

[12] Koyama M, Tasan CC, Akiyama E, Tsuzaki K, Raabe D, „Hydrogen-assisted decohesion and localized plasticity in dual-phase steel," *Acta Mat,* vol. 70, pp. 174-187, 2014.

[13] Pérez Escobar D, Miñambres C, Duprez L, Verbeken K, Verhaege M, „Internal and surface damage of multiphase steels and pure iron after electrochemical hydrogen charging," *Corrosion Science,* vol. 53, p. 3166–3176, 2011.

[14] Depover T, Wallaert E, Verbeken K, „Fractographic analysis of the role of hydrogen diffusion on the hydrogen embrittlement susceptibility of DP steel," *Mat Sci and Eng A,* vol. 649, pp. 201-208, 2016.

[15] Wang M, Akiyama E, Tsuzaki K, „Effect of hydrogen on the fracture behavior of high strength steel during slow strain rate test," *Corrosion Science,* vol. 49, pp. 4081-4097, 2007.

[16] Wang M, Akiyama E, Tzuzaki K, „Effect of hydrogen and stress concentration on the notch tensile strength of AISI 4135 steel," *Mat Sci and Eng A,* vol. 398, pp. 37-46, 2005.

[17] Laureys A, Depover T, Petrov R, Verbeken K, „Characterization of hydrogen induced cracking in TRIP-assisted steels," *Int Journal of Hydrogen Energy,* vol. 40, nr. 47, pp. 16901-16912, 2015.

[18] Laureys L, Depover T, Petrov R, Verbeken K, „Microstructural characterization of hydrogen induced cracking in TRIP-assisted steel by EBSD," *Materials Characterization,* vol. 112, pp. 169-179, 2016.

[19] Pérez Escobar D, Verbeken K, Duprez L, Verhaege M, „Evaluation of hydrogen trapping in high strength steels by thermal desorption spectroscopy," *Mat Sci and Eng A,* vol. 551, pp. 50-58, 2012.

[20] Pérez Escobar D, Depover T, Wallaert E, Duprez L, Verbeken K, Verhaege M, „Combined thermal desorption spectroscopy, differential scanning calorimetry, scanning electron microscopy and X-ray diffraction study of hydrogen trapping in cold deformed TRIP steel," *Acta Mat,* vol. 60, pp. 2593-2605, 2012.

[21] Duprez L, Verbeken K, Verhaege M, „Effect of hydrogen on the mechanical properties of multiphase high strength steels," in *Proc. of the 2008 Int. Hydrogen Conf.,* Jackson, Wyoming, USA, 2008.

[22] Pérez Escobar D, Duprez L, Atrens A, Verbeken K, „Influence of experimental parameters on thermal desorption spectroscopy measurements during evaluation of hydrogen trapping," *Journal of Nuclear Materials,* vol. 450, pp. 32-41, 2014.

[23] Speich GR, Leslie WC, „Tempering of steel," *Met Trans,* vol. 3, pp. 1043-1054, 1972.

[24] Spencer GL, Duquette DJ, „The role of vanadium carbide traps in reducing the hydrogen embtrittlement susceptibility of high strength alloy steels," US army armament research, development and engineering center, Watervliet, N.Y., 1998.

[25] Nagao A, Martin ML, Dadfarnia M, Sofronis P, Robertson M, „The effect of nanosized (Ti,Mo)C precipitates on hydrogen embrittlement of tempered lath martensitic steel," *Acta Mat,* vol. 74, pp. 244-254, 2014.

[26] Thomas RLS, Li DM, Gangloff RP, Scully JR, „Trap-governed hydrogen diffusivity and uptake capacity in ultrahigh-strength AERMET 100 steel," *Met Mat Trans A,* vol. 33A, pp. 1991-2004, 2002.

[27] Li DM, Gangloff RP, Scully JR, „Hydrogen trap states in ultrahigh-strength AERMET 100 steel," *Met Mat Trans A,* vol. 35A, pp. 849-864, 2004.

[28] Wei FG, Hara T, Tsuzaki K, „Precise determination of the activation energy for desorption of hydrogen in two Ti-added steels by a single thermal-desorption spectrum," *Met Mat Trans B,* vol. 35B, pp. 587-597, 2004.

[29] Pressouyre GM, Bernstein IM, „A quantitative analysis of hydrogen trapping," *Met Trans A,* vol. 9A, pp. 1571-1580, 1978.

[30] Pressouyre GM, „Classification of hydrogen traps in steel," *Met Trans A,* vol. 10A, pp. 1571-1573, 1979.

[31] Pressouyre GM, Bernstein IM, „A kinetic trapping model for hydrogen-induced cracking," *Acta Mat,* vol. 27, pp. 89-100, 1979.

[32] Pressouyre GM, Bernstein IM, „Example of the effect of hydrogen trapping on hydrogen embrittlement," *Met Mat Trans A,* vol. 12, pp. 835-844, 1981.

[33] Asahi H, Hirakami D, Yamasaki S, „Hydrogen trapping behavior in vanadium added steel," *ISIJ Intl,* vol. 43, pp. 527-533, 2003.

[34] Wei FG, Tsuzaki K, „Hydrogen trapping character of nano-sized NbC precipitates in tempered martensite,"

in *Proc. of the 2008 Int. Hydrogen Conf.*, Jackson, Wyoming, 2008.

[35] Wallaert E, Depover T, Arafin MA, Verbeken K, „Thermal desorption spectroscopy evaluation of the hydrogen trapping capacity of NbC and NbN precipitates," *Met Mat Trans A,* vol. 45, pp. 2412-2420, 2014.

[36] Hurtado Noreña C, Bruzzoni P, „Effect of microstructure on hydrogen diffusion and trapping in a modified 9%Cr-1%Mo steel," *Mat Sci and Eng A,* vol. 527, nr. 3, pp. 410-416, 2010.

[37] Lee J, Lee T, Kwon YJ, Mun DJ, Yoo JY, Lee CS, „Role of Mo/V carbides in hydrogen embrittlement of tempered martensitic steel," *Corros Rev,* 2015.

[38] Bhadeshia HKDH, Honeycombe R, Steels: microstructure and properties, London: Elsevier, 2011.

[39] Marchetti L, Herms E, Laghoutaris P, Chêne J, „Hydrogen embrittlement susceptibility of tempered 9%Cr-1%Mo steel," *Int Journal of Hydrogen Engery,* vol. 36, pp. 15880-15887, 2011.

[40] Ashby MF, Easterling KE, „A first report on diagrams for grain growth in welds," *Acta Mat,* vol. 30, pp. 1969-1978, 1982.

[41] Depover T, Wallaert E, Verbeken K, „On the synergy of diffusible hydrogen and hydrogen diffusivity in the mechanical degradation of laboratory cast Fe-C alloys," *Mat Sci and Eng A,* 2016.

[42] Depover T, Van den Eeckhout E, Verbeken K, „The impact of hydrogen on the ductility loss of bainitic Fe-C alloys," *Materials Science Technology,* 2016.

[43] Hadam U, Zakroczymski T, „Absorption of hydrogen in tensile strained iron and high carbon steel studied by electrochemical permeation and desorption techniques," *Int Journal of Hydrogen Energy,* vol. 34, pp. 2449-2459, 2009.

[44] Pérez Escobar D, Depover T, Wallaert E, Duprez L, Verhaege M, Verbeken K, „Thermal desorption spectroscopy study of the interaction between hydrogen and different microstructural constituents in lab cast Fe-C alloys," *Corrosion Science,* vol. 65, pp. 199-208, 2012.

[45] Thomas LSR, Li D, Gangloff RP, Scully JR, „Trap-governed hydrogen diffusivity and uptake capacity in ultrahigh strength aermet 100 steel," *Met Mat Trans A,* vol. 33A, pp. 1991-2004, 2002.

[46] Choo WY, Lee JY, „Thermal analysis of trapped hydrogen in pure iron," *Met Trans A,* vol. 13A, pp. 135-140, 1982.

[47] Wei FG, Tsuzaki K, „Quantitative Analysis on hydrogen trapping of TiC particles in steel," *Met Mat Trans A,* vol. 37A, pp. 331-353, 2006.

[48] Dadfarnia M, Sofronis P, Neeraj T, „Hydrogen interaction with multiple traps: Can it be used to mitigate embrittlement?," *Int Journal of Hydrogen Energy,* vol. 36, pp. 10141-10148, 2011.

[49] Porter DA, Easterling KE, Phase transformation in metals and alloys, London, UK: Chapman & Hall, 1992.

[50] Zakroczymski T, „Adaptation of the electrochemical permeation technique for studying entry, transport and trapping of hydrogen in metals," *Electrochemica Acta,* vol. 51, nr. 11, pp. 2261-2266, 2006.

[51] Hadzipasic AB, Malina J, Malin M, „The influence of microstructure on hydrogen diffusion and embrittlement of multiphase fine-grained steels with increased plasticity and strength," *Chem Biochem Eng Q,* vol. 25, pp. 159-169, 2011.

[52] Luppo MI, Ovejero-Garcia J, „Applicatin of the hydrogen-permeation method to the study of carbide

precipitation kinetics in a low-carbon martensite," *Materials Characterization,* vol. 40, pp. 189-196, 1998.

[53] Haq AJ, Muzaka K, Dunne DP, Calka A, Pereloma E, „Effect of microstructure and composition on hydrogen permeation in X70 pipeline steels," *Int Journal of Hydrogen Energy,* vol. 38, pp. 2544-2556, 2013.

[54] Kim SJ, Jung HG, Kim KY, „Effect of tensile stress in elastic and plastic range on hydrogen permeation of high-strength steel in sour environment," *Electrochimica Acta ,* vol. 78, pp. 139-146, 2012.

[55] Tau L, Chan SLI, Shin CS, „Hydrogen enhanced fatigue crack propagation of bainitic and tempered martensitic steels," *Corrosion Science,* vol. 38, pp. 2049-2060, 1996.

[56] Pérez Escobar D, PhD: Evaluation of hydrogen trapping in iron-based alloys by thermal desorption spectroscopy, Ghent, 2012.

[57] Takahashi J, Kawakami K, Kobayashi Y, Tarui T, „The first direct observation of hydrogen trapping sites in TiC precipitation-hardening steel through atom probe tomography," *Scripta Mat,* vol. 63, pp. 261-264, 2010.

CHAPTER VII

Evaluation of the role of Mo_2C in hydrogen induced ductility loss in Q&T Fe-C-Mo alloys*

VII.1 Introduction

The presence of hydrogen in steels is known to be detrimental for the overall performance and more specific for the ductility of the material. Unpredictable failure may occur and although it was first described by Johnson in 1875 [1], there is no full understanding of the mechanism behind so far. During the last decades, many industrial developments focus on high strength steels since they can combine a high strength level with low structural weight, which is of great interest for many applications [2]. Unfortunately, these high strength steel are more prone to hydrogen embrittlement (HE) [3] [4] and therefore applicability becomes more complicated [5].

Duprez *et al.* [6] studied the mechanical properties of four industrial high strength steels, i.e. a ferrite bainite (FB), dual phase (DP), transformation induced plasticity (TRIP) and high strength low alloyed (HSLA) steel. They observed that the hydrogen induced ductility loss was reversible as a ductility recovery occurred when the hydrogen charged tensile samples were left one week in air. This recovery was slower for the HSLA steel. Laureys *et al.* [7] [8] studied the crack behavior in TRIP steel and clearly linked the presence of stress-induced cracks to the existence of hydrogen. A hydrogen enhanced interface decohesion mechanism was active within the martensitic islands and crack propagation was mainly stress driven. Depover *et al.* [9] investigated the effect of diffusible hydrogen and hydrogen diffusivity in DP steel. They were able to visualize, by an in-depth scanning electron microscopy study, that the distance hydrogen was able to diffuse into the sample was correlated with the hydrogen induced ductility loss (cf. Chapter III). Additionally, in another work, Depover *et al.* [4] found that the HSLA steel had the highest resistance against HE of these four high strength steels (cf. Chapter II). Pérez Escobar *et al.* [10] confirmed this by demonstrating that the HSLA steel showed the lowest susceptibility to hydrogen induced damage in terms of blister formation originating from electrochemical hydrogen charging. Furthermore, thermal desorption spectroscopy (TDS) demonstrated that this material trapped hydrogen in a stronger way [11]. These observations for HSLA were all attributed to the presence of Ti- and Nb- carbo-nitrides.

The addition of nano-carbides to suppress hydrogen diffusion is one of the strategies to reduce HE [12] [13] [14] [15] [16]. Ren and Zeng [17] showed that a TiC film on stainless steel reduced the corrosion rate, while Yamasaki and Takahashi [18] studied the effect of VC and considered it an effective hydrogen trap which can reduce the HE susceptibility. Ohnuma *et al.* [19] and Wallaert *et al.* [20] showed that NbC can also act as an

* This chapter is based on the following publication: Depover T, Verbeken K, *International Journal of Hydrogen Energy* (2016), accepted with minor revisions.

effective hydrogen trap and Wei and Tsuzaki [21] determined that the NbC particles trapped the most hydrogen when tempered at 600°C with different corresponding activation energies. Asaoka *et al.* [22] observed that TiC trapped hydrogen with a binding energy larger than 61 kJ/mol and Pressouyre and Bernstein [23] found that coherent TiC precipitates were less effective hydrogen traps compared to incoherent particles. Additionally, Wei and Tsuzaki [24] [25] showed that the precipitate size determined the amount of trapped hydrogen. Since the trapped hydrogen content depended on the surface area of the carbide, they suggested that hydrogen was trapped at the TiC/matrix interface, which was later clearly confirmed by Takahashi *et al.* [26] via atom probe tomography. Furthermore, Wei *et al.* [27] described that (semi-)coherent TiC, VC and NbC particles were capable of trapping hydrogen during electrochemical charging, whereas incoherent carbides could not trap hydrogen without gaseous charging at elevated temperature. This was also reported by Escobar *et al.* [28] in their TDS study of the interaction of hydrogen with TiC precipitates. Consequently, carbides are of crucial importance in the hydrogen embrittlement subjects and may considerably alter the effect of hydrogen on the mechanical properties.

Less data are available in literature on the effect of Mo carbides. Pavlina *et al.* [29] studied the solubility products for MoC and Mo_2C. Although an effect on the susceptibility to hydrogen embrittlement by adding molybdenum was assumed in this study, there was no direct correlation with their hydrogen uptake capacity included in their work. Yamasaki and Bhadeshia investigated Fe-C-Mo steels [30] [31] and they characterized and modeled the precipitation of needle shaped Mo_2C during tempering in these generic martensitic materials. This work also stated that carbides such as Mo_2C act as hydrogen trapping sites, although unfortunately no experimental validation of this statement was present in this study. They identified the carbide size and number density as the main carbide characteristics to enhance the resistance against hydrogen embrittlement.
The research of Spencer *et al.* [32] also put emphasis on the importance of Mo_2C with respect to the degree of HE. The Mo based precipitates caused an additional beneficial effect, next to the main effect of the V carbides. Frappart *et al.* [33] studied the diffusion and trapping of hydrogen through a Fe-C-Mo quenched and tempered HSLA steel by means of electrochemical permeation experiments. They observed that the hydrogen flux was sensitive to an augmentation of the hydrogen subsurface concentration and hence that the apparent diffusion coefficient depended on this concentration. Additionally, the major trapping sites were determined to be edge dislocations and/or geometrical necessary dislocations. However, these results were based on modeling of the permeation results and they also stated that the observations should be confirmed by TDS.
On the contrary, the TDS spectra of four steels (Fe-0.05C-0.41Nb-2.0Ni, Fe-0.05C-0.20Ti-2.0Ni, Fe-0.05C-0.24V-2.0Ni, Fe-0.05C-0.84Mo-2.0Ni) tempered at 700°C which contain NbC, TiC, VC and Mo_2C precipitates respectively, were investigated [34]. Only TiC showed an additional desorption peak around 600°C. The hydrogen trapping capacity of the different carbides evolved in descending order of NbC > TiC >> VC > Mo_2C, which indicated that Mo_2C was the least promising carbide to enhance the resistance against HE. However, Lee *et al.* [35] performed recently a study on the role of Mo/V carbides in hydrogen embrittlement of tempered martensitic steel. The Mo steel possessed a good HE resistance due to the presence of Mo carbides. Unfortunately, no trapping investigation was performed nor activation energies were determined for the present precipitates.

A theoretical approach on the hydrogen interaction with multiple traps was performed by Dadfarnia *et al.* [36]. Traps with binding energy > 60 kJ/mol can be categorized as very strong or irreversible ones and those < 30 kJ/mol as weak or reversible [37]. The competition between multiple types of traps in affecting the development of hydrogen concentration near a crack was studied. They concluded that strong traps (binding energy > 60 kJ/mol) were quickly and first saturated.

The goal of this work was to evaluate the hydrogen induced ductility loss in generic Fe-C-Mo alloys in which Mo carbides are introduced by an appropriate heat treatment. The aim was to study the interaction between hydrogen and the Mo_2C particles in a quenched and tempered matrix and consequently their influence on the resistance against hydrogen embrittlement.

VII.2 Experimental procedure

VII.2.1 Material characterization

Three generic Fe-C-Mo alloys with increasing carbon content were laboratory cast with a stoichiometric amount of the ternary alloying element Mo. Al was added to bind N in order to avoid the formation of nitrides. The carbon variation will allow a trustworthy evaluation of the impact of the carbides with variable strength level of the alloys and give an opportunity to confirm their role in different Fe-C-Mo alloys. The chemical compositions are given in Table VII-1.

Table VII-1: Chemical composition of the used materials in wt%.

Material/Element	C	Mo	Other
Alloy A	0.100	1.700	200-300 ppm Al
Alloy B	0.142	2.380	
Alloy C	0.177	2.990	

The alloys were cast in a Pfeiffer VSG100 incremental vacuum melting and casting unit under an argon gas atmosphere. The materials were hot rolled till 1.5 mm. An appropriate heat treatment was applied in order to obtain two main conditions; one as-quenched (as-Q) state with as little precipitates as possible and one quenched and tempered (Q&T) state where free carbon is enabled to precipitate with Mo during tempering. Temperature vs. time graph of the used heat treatment is presented in Figure VII-1. All materials were austenitized at 1250°C for 10 minutes to obtain a fully austenitic microstructure and to dissolve the present carbides. These materials were then quenched in brine water (7wt% NaCl) to obtain a full martensitic structure. This first condition which will be further referred to as as-Q.

Next to the as-Q condition, a second condition was prepared by tempering the quenched material at a certain temperature for 1 hour to generate, in a controlled way, Mo carbides, followed again by brine water quenching. Tempering was performed at different temperatures to determine at which temperature the secondary hardening effect, due to the generation of Mo_2C, was most outspoken.

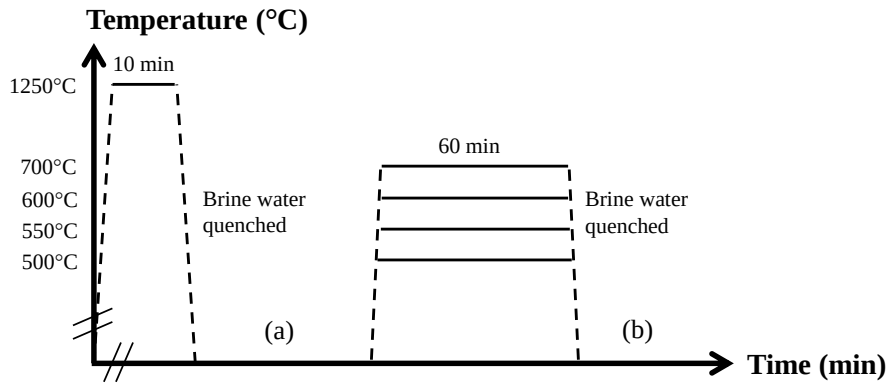

Figure VII-1: Temperature-time graphs of the heat treatments to induce: (a) as-Q, (b) Q&T condition.

All materials were further ground and tensile samples were machined with their tensile axis parallel to the rolling direction and the specimen geometry is shown in Figure VII-2. Finally, the surface of the samples was sandblasted to remove possible oxides remaining from processing. The hardness and microstructure were investigated as described in Chapter V section V.2.1.

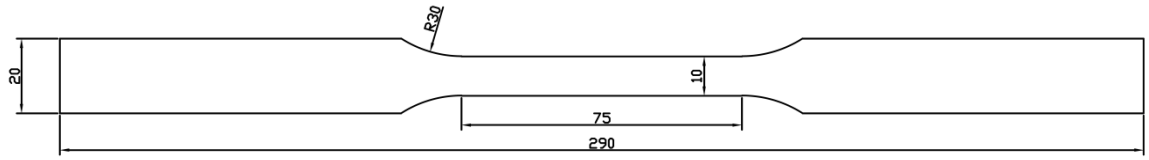

Figure VII-2: Tensile sample geometry in mm.

VII.2.2 Hydrogen induced mechanical degradation

The hydrogen induced ductility loss was determined by comparing tensile tests performed in air with tests done on hydrogen saturated samples. Hydrogen was introduced in the materials by electrochemical pre-charging using a 1g/L thiourea in a 0.5 M H_2SO_4 solution at a current density of 0.8 mA/cm² for 1 hour, while in-situ charging continued during the tensile test. The conditions were chosen in such a way that they did not create blisters or internal damage and based on previous work on Fe-C-Ti materials (cf. Chapter V). The tensile tests were performed as described in Chapter V section V.2.2.

VII.2.3 Determination of the hydrogen/material interaction

The hydrogen content was determined as described in Chapter V section V.2.3, while TDS measurements were performed as explained in Chapter V section V.2.4. The hydrogen diffusion coefficient was determined as defined in Chapter V section V.2.5.

VII.3 Material characterization

Hardness measurements were performed to determine at which temperature secondary hardening due to Mo_2C precipitation was optimal. Figure VII-3 represents the hardness results for the three alloys in the as-quenched condition and for the different tempering temperatures.

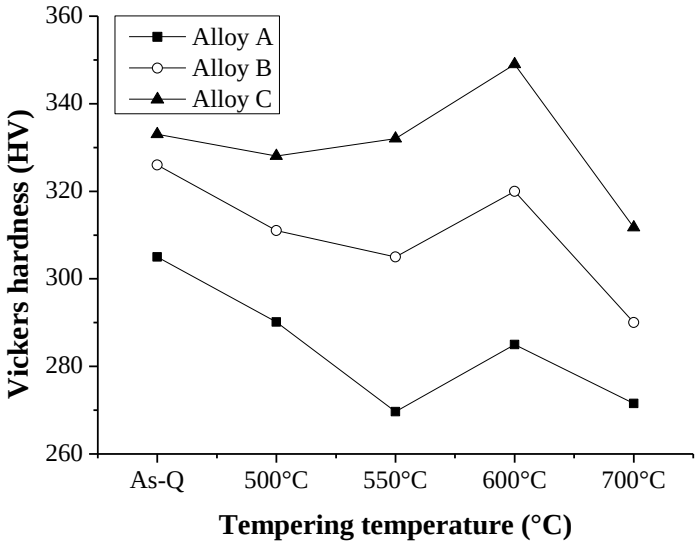

Figure VII-3: Hardness vs. temperature evolution of the three Fe-C-Mo alloys.

A distinct secondary hardening peak can clearly be observed for alloy A, B and C after 1h tempering at 600°C, which was attributed to the precipitation of Mo_2C particles. These results are in good agreement with the observations for similar alloys [30] [31]. Additionally, Speich *et al.* [38] also detected a secondary hardening peak from Mo_2C at about 600°C. Only for alloy C, the hardness after tempering was higher than the as-Q hardness.

Since the as-quenched hardness is mainly determined by the amount of dissolved carbon [38] and despite the fact that the difference in carbon content was similar between alloy A and B and between B and C, a rather small hardness difference was observed between alloy B and C in the as-quenched condition. However, the amount of dissolved carbon at an austenitization temperature of 1250°C for these stoichiometric compositions can be calculated according to the solubility product for Mo_2C [39]. Thermodynamic calculations to determine the amount of dissolved carbon, as defined in Eq. VII-1, and presented in Figure VII-4.

$$log_{10} \frac{M^m X^n}{MX} = -\frac{A}{T} + B \qquad \text{(VII-1)}$$

Where, M_mX_n is Mo_2C, M and X the alloy contents (wt%), T the temperature (K) and A and B constants of the solubility product and for Mo_2C equal to 7375 and 5.36 respectively according to Ashby [39]. In the present case, not all carbon was dissolved in the as-quenched condition for alloy C, which can be set responsible for the smaller difference in hardness between B and C. Additionally, kinetics were not incorporated in the thermodynamic calculations, which could help to explain the presence of carbides for alloy C as-Q.

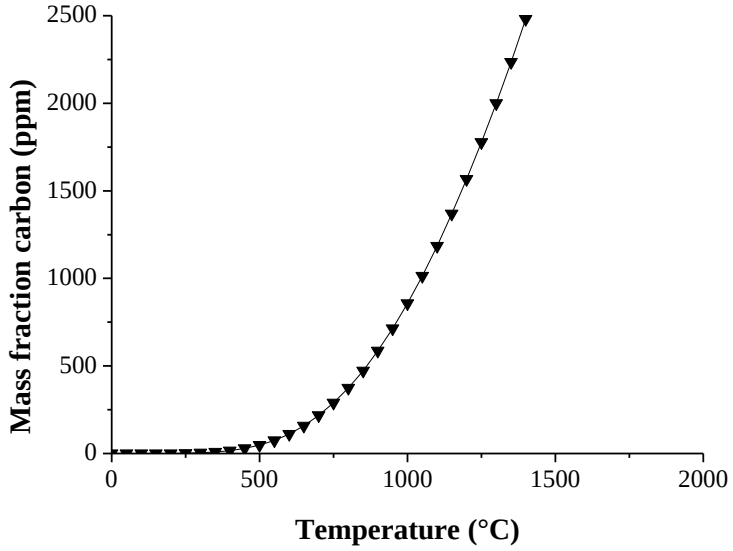

Figure VII-4: Mass fraction of carbon vs. temperature that can be kept in solid solution at each temperature for stoichiometric total content of C and Mo.

The LOM images are shown in Figure VII-5 for the as-Q and the Q&T condition when the materials got tempered at 600°C. A martensitic and a tempered martensitic microstructure can be observed. In-depth HRSEM and HRTEM was performed to analyze the Mo_2C particles. Results are shown for alloy C. A SEM image and a forward scatter detection (FSD) image of carbon replicas are represented in Figure VII-6, whereas TEM bright field images of thin foils are depicted in Figure VII-7. An elemental mapping and line scan are presented in Figure VII-8 to confirm the presence of Mo based carbides.

LOM	**Alloy A**	**Alloy B**	**Alloy C**
As-Q	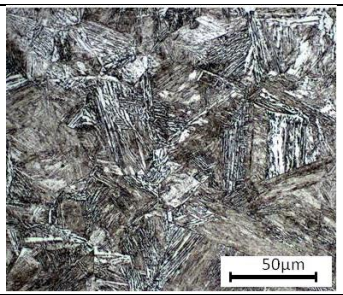	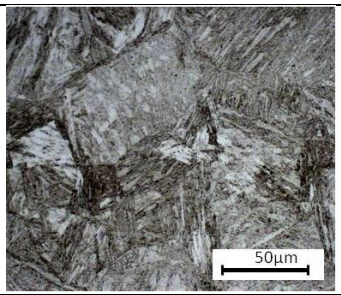	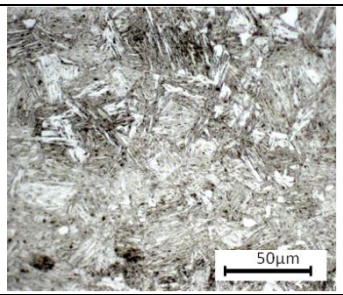
Q&T	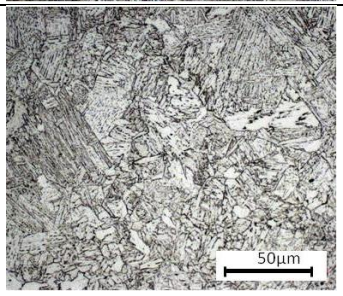	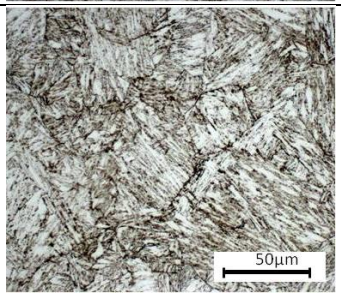	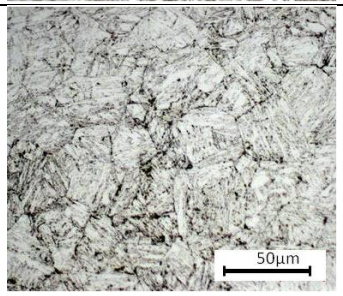

Figure VII-5: LOM images of alloy A, B and C in the as-Q and Q&T condition.

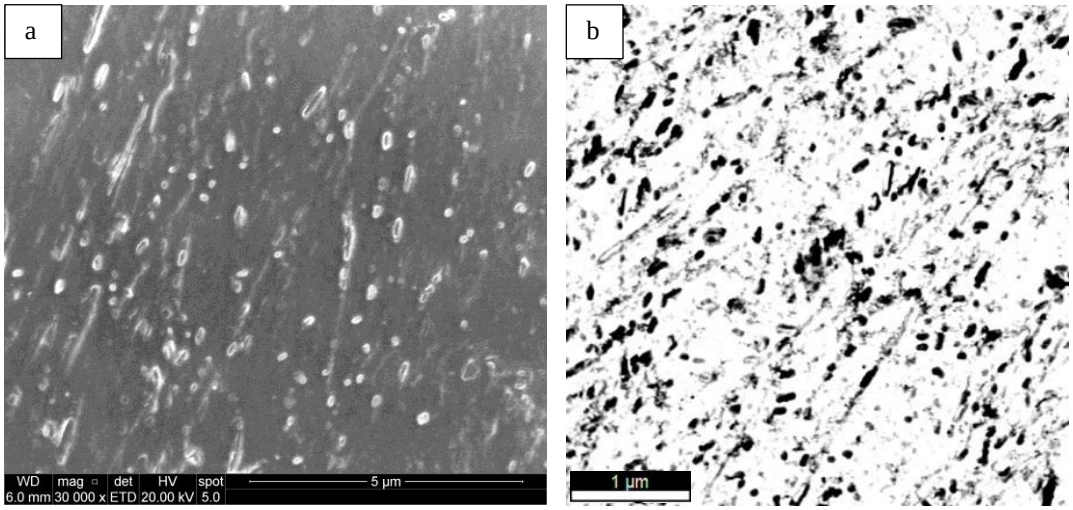

Figure VII-6: SEM image (a) and FSD image (b) of carbon replica taken from alloy C in the Q&T condition.

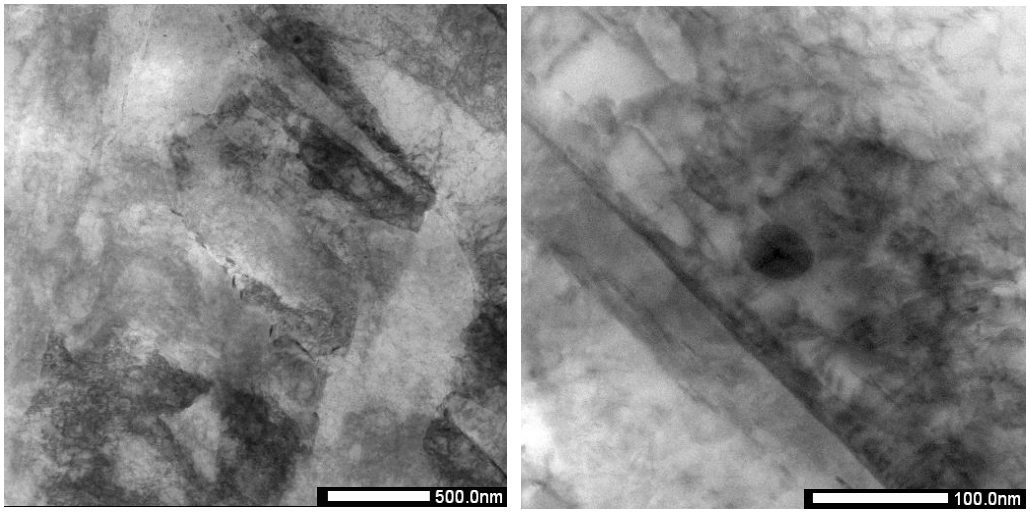

Figure VII-7: HRTEM bright field images of thin foil taken from alloy C in the Q&T condition.

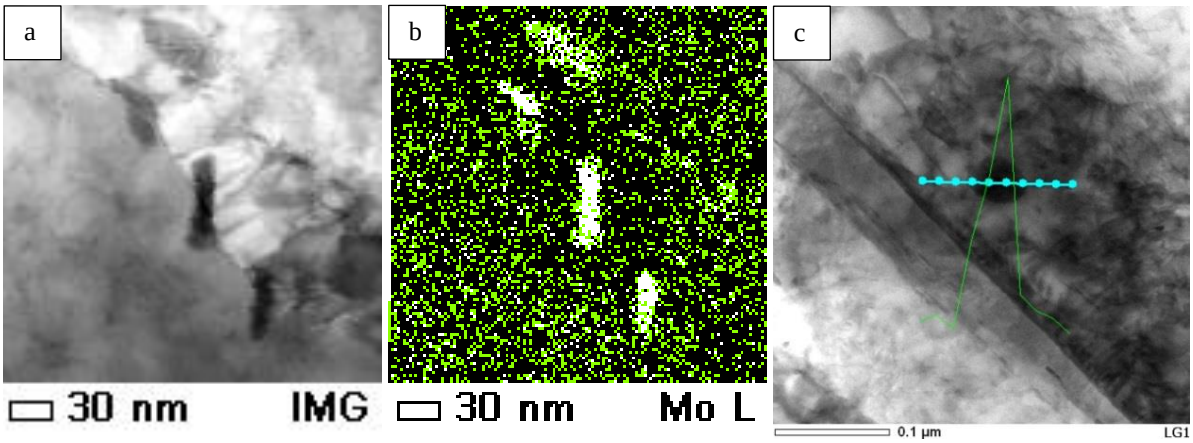

Figure VII-8: Elemental mapping (b) of HRTEM bright field image (a) and line scan (blue) taken from thin foil of alloy C in the Q&T condition (c) where the green line represents the Mo content.

Additionally, diffraction patterns from a selected area in the bright filed image were taken from alloy C in the Q&T condition and analyzed to confirm Mo_2C particles are indeed present in the microstructure. A match was obtained between the observed diffraction pattern and the crystal structure of Mo_2C. Diffraction spots from the (0-11) and (1-1-5) directions were indexed and the pattern fitted with the Mo_2C crystal structure with zone axis [611]. Furthermore, dark field images were taken from the spots indicated on the diffraction pattern to check the presence of the carbides. These results are presented in Figure VII-9.

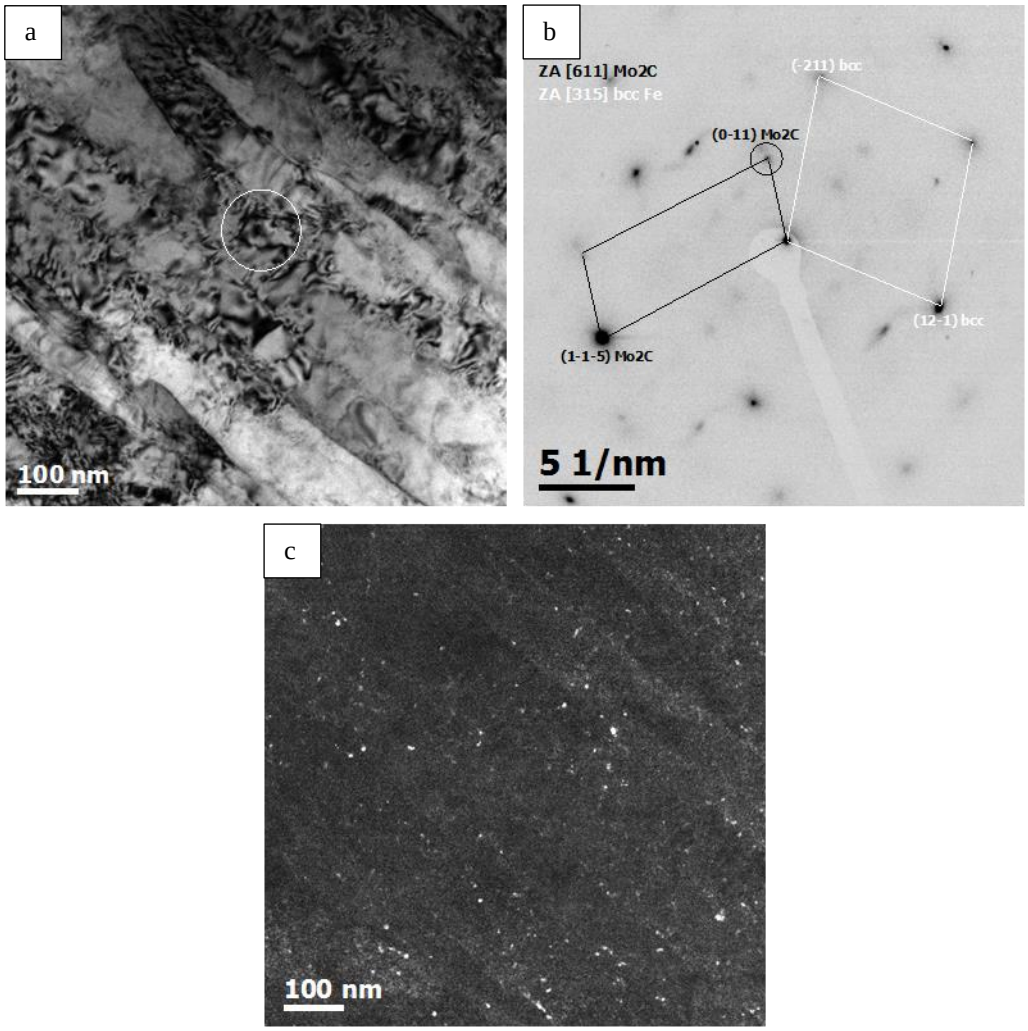

Figure VII-9: HRTEM bright field image (a) of which a diffraction pattern was taken from the selected area indicated by a white circle. Diffraction pattern (b) was indexed with the Mo_2C crystal structure and a dark field image was taken from the indicated diffraction spots in (b) and shown in (c).

VII.4 Hydrogen induced mechanical degradation

The results of the tensile tests performed on both charged and uncharged specimen are presented in Figure VII-10 and summarized in Table VII-2. The hydrogen charged tests are shown in bold and two main conditions, i.e. as-Q vs. Q&T, are compared to each other for each alloy.

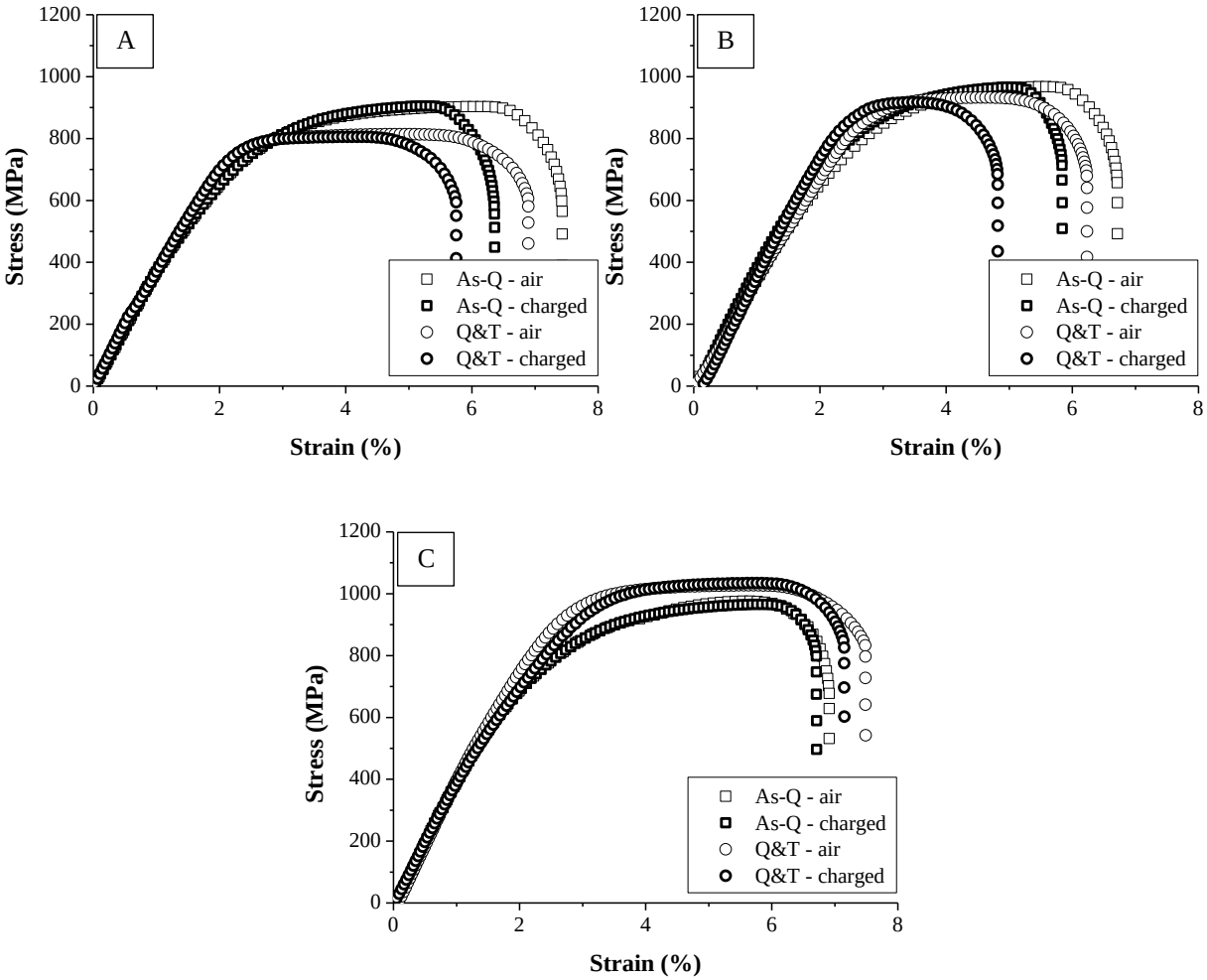

Figure VII-10: Stress-strain curves of alloy A, B and C in the as-Q and Q&T condition.

Table VII-2: Summary of the mechanical properties.

Mechanical properties	**Alloy A**		**Alloy B**		**Alloy C**	
	As-Q	Q&T	As-Q	Q&T	As-Q	Q&T
Tensile strength (MPa)	903	814	966	932	976	1034
%HE	14	17	13	23	3	5

The strength level of the materials increased with increasing carbon content. Tempering reduced the strength level for alloy A and B, whereas the opposite can be observed for alloy C. This is in good agreement with the hardness measurements (cf. Figure VII-3). Although the secondary hardening peak was still most outspoken at 600°C for alloy A and B, the as-Q hardness remained a bit higher. Additionally, the difference in strength level between alloy B and C in the as-Q condition was rather small, which was explained above.

Since the strength levels were not identical for these materials, a small additional comment should be made. In general, the susceptibility to hydrogen embrittlement increases with strength level, although contradictory observations have been reported as well (Chapter II). However, in this case, the strongest alloy showed the highest resistance against HE. Additionally, the as-Q conditions of alloy A and B were less prone to HE compared to the corresponding tempered state, whereas their strength level was each time higher.
Moreover, the ductility followed exactly the same trend as the strength evolution for all alloys; only for alloy C an increased elongation was detected for the Q&T condition compared to the as-Q state. Rather low percentages of hydrogen induced ductility loss were observed while tempering lead to a slight increase in susceptibility to the hydrogen induced mechanical degradation. Remarkable are the very low HE% for alloy C, which was hardly affected by the presence of hydrogen in both as-Q and Q&T condition. In order to further develop understanding of these observations; a detailed evaluation of the interaction between hydrogen and the different alloys is made in the next section.

VII.5 Determination of the hydrogen uptake and trapping capacity

The diffusible and total hydrogen content, after electrochemical hydrogen charging under identical conditions as for the tensile tests, are shown in Figure VII-11. Two major tendencies are observed. First of all, an increase of hydrogen content, both total and diffusible, can be observed when the materials were tempered. Secondly, the amount of total hydrogen clearly increased from A → B → C, which can be linked to a higher amount of possible trapping sites since a higher amount of carbon and molybdenum was present. However, a somewhat different behavior was observed for the amount of diffusible hydrogen. Whereas in the as-Q condition, similar amounts were observed for all alloys, a slight increase with increasing carbon content was detected for the Q&T condition.

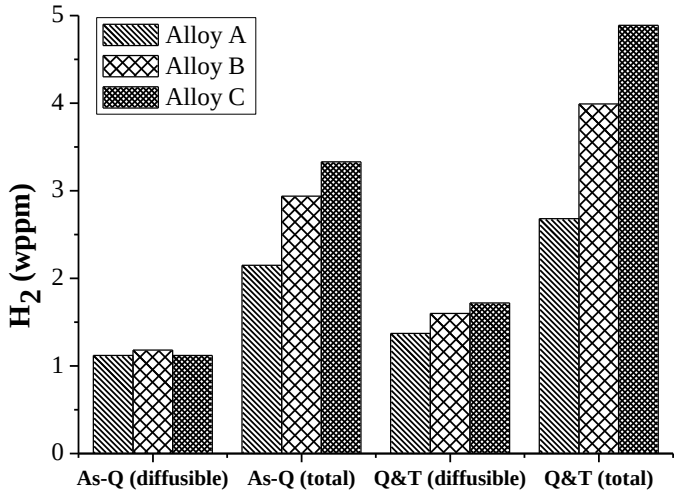

Figure VII-11: The total and diffusible amount of hydrogen after electrochemical charging for alloy A, B and C in the as-Q and Q&T condition.

The mechanical tests indicated that tempering lead to a reduced resistance against HE, which might be linked to the higher total amount of hydrogen in the Q&T material. However, the total hydrogen content only gives a first indication and to increase understanding on the results of the mechanical tests, evaluation of the trapping behavior of the precipitates via TDS analysis is required. Three heating rates were applied (200°C/h, 600°C/h

and 1200°C/h) to calculate the activation energy of the observed peaks. Figure VII-12 represents the deconvoluted TDS spectra at a heating rate of 600°C/h and Table VII-3 summarizes the corresponding activation energies.

TDS	As-Q	Q&T
Alloy A	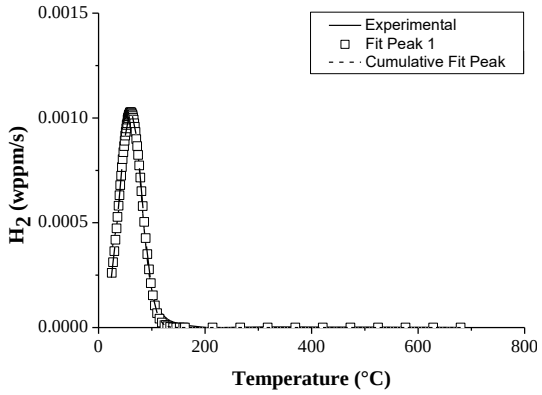	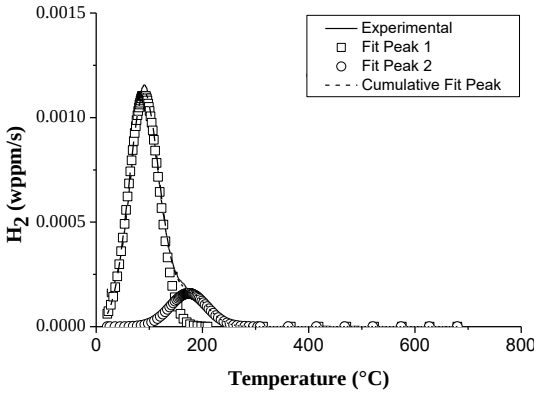
Alloy B	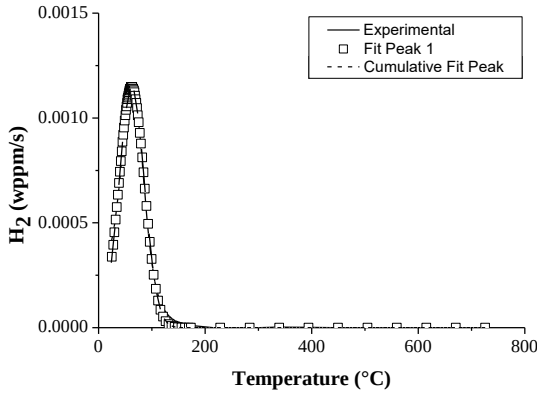	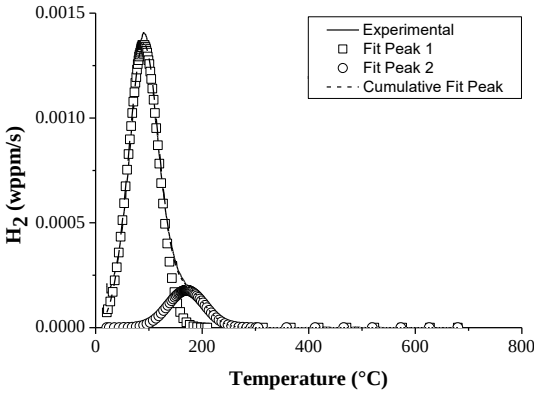
Alloy C	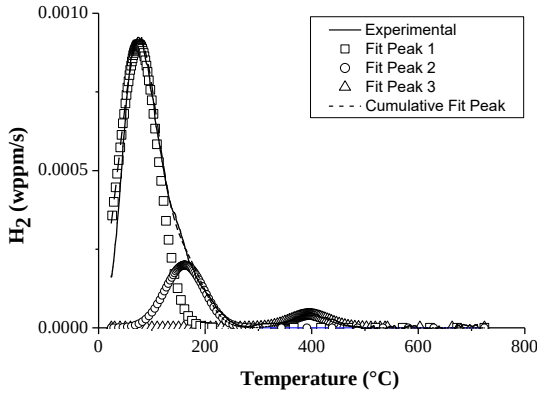	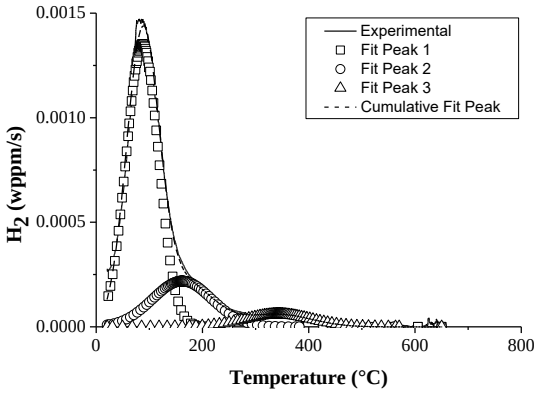

Figure VII-12: TDS spectra for alloy A, B and C in the as-Q and Q&T condition at a heating rate of 600°C/h.

Table VII-3: Summary of the corresponding activation energies for the different peaks.

Activation energy (kJ/mol)	**Alloy A**		**Alloy B**		**Alloy C**	
	As-Q	Q&T	As-Q	Q&T	As-Q	Q&T
Peak 1	25	27	27	28	30	27
Peak 2	/	41	/	42	36	34
Peak 3	/	/	/	/	75	84

When considering the as-Q conditions, only one peak appeared for alloy A and B with a corresponding E_a of about 25-30 kJ/mol, which was attributed to hydrogen trapped at the lath boundaries of martensite [40]. Also the first peak of alloy C showed an E_a in this range and was hence correlated to this trapping site. Dislocations can trap hydrogen in the same range of E_a [24] [41] [42] [43], but Pérez Escobar *et al.* [44] showed that hydrogen trapped at dislocations largely left the material before the TDS measurement could be started. Although a distinction between dislocations and lath boundaries could not be made based on the activation energy, the first peak is assumed to be largely related to hydrogen trapped by martensite lath boundaries.

The TDS spectrum of alloy C showed three peaks. The two extra peaks were attributed to hydrogen trapped at the Mo_2C particles as for this alloy not all carbides were dissolved during austenitizing (cf. section VII.3). The second peak showed an activation energy of 36 kJ/mol. Although this value is close to the one of the lath boundaries, the extra peak is clearly visible for alloy C by the shoulder of the first peak, which was not present for alloy A and B. The higher temperature peak had an E_a of 75 kJ/mol, which is in the irreversible hydrogen trap range. The border between reversible and irreversible trapping has been reported to be 60 kJ/mol [36]. In order to validate if this hydrogen is really trapped irreversibly, a TDS spectrum after 72 hours of vacuum was performed as well. This would allow the reversibly trapped hydrogen to leave the sample. The result is depicted in Figure VII-13 (a) together with the corresponding 3rd peak of the original TDS measurement (cf. Figure VII-12). All reversibly trapped hydrogen was gone after 72 hours of vacuum whereas the irreversible peak remained present. Additionally, the total amount of detected hydrogen by TDS increased for alloy A → B → C, which was in good agreement with the hot/melt extraction results.

For the Q&T condition, an extra peak was observed for alloy A and B compared to the as-Q condition which represented the hydrogen trapped at Mo_2C induced during tempering. The activation energies were 41 and 42 kJ/mol, respectively. The first peak for all three alloys can again be ascribed to hydrogen trapped at the martensite lath boundaries with a similar activation energy compared to the as-Q samples. Since the dislocation density decreases with tempering [38], the possibility that hydrogen trapped at dislocations contribute to this peak is even smaller than in the as-Q state. Alloy C showed again two peaks related to hydrogen trapped at carbides with similar activation energies compared to the as-Q condition of alloy C. Additionally, the amount of detected hydrogen by TDS increased when the materials were tempered due to the precipitation of Mo_2C and also for alloy A – B – C, which is in good agreement to the hot/melt extraction results (cf. Figure VII-11).

In Figure VII-13 (b) the TDS spectra of the Q&T sample after 72 hours of vacuum is presented together with the corresponding 3rd peak of the original TDS measurement (cf. Figure VII-12). The reversible trapping sites disappeared after 72 hours of vacuum while the irreversibly trapped hydrogen remained here visible as well. A more detailed look on the TDS spectra and the variation in activation energy for Mo_2C will be given below when they are correlated with the carbide size distributions.

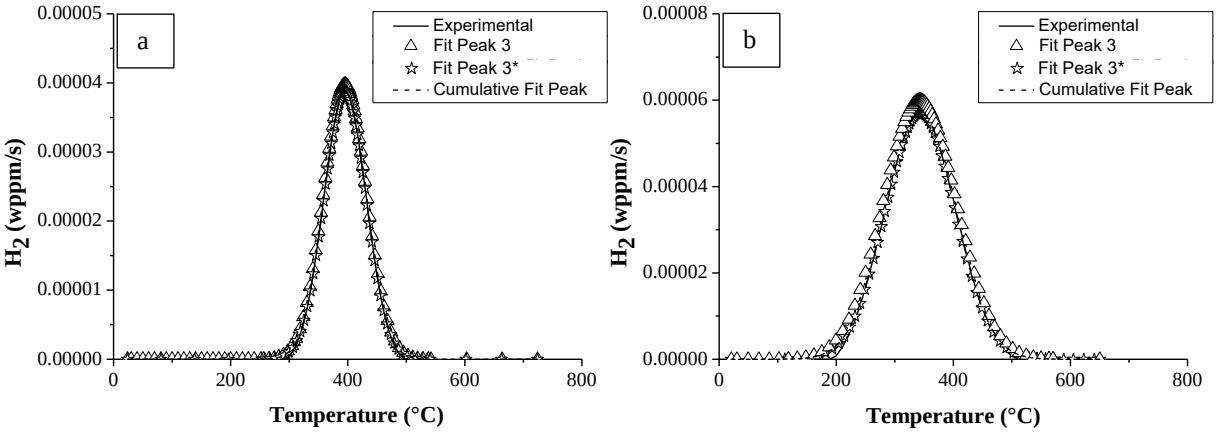

Figure VII-13: TDS curves of alloy C in the as-Q (a) and Q&T (b) condition where only peak 3 is shown from Figure VII-12 for the regular TDS measurements and where the TDS spectra after one weekend of vacuum (experimental curve) is added as peak 3*.

With the available information from the hot/melt extraction and TDS measurements further interpretation of the mechanical tests can be performed. When considering the as-Q condition for all alloys, alloy C, which had the best HE-resistance, clearly showed a different trapping behavior compared to alloy A and B. In alloy C, carbides were available and able to trap hydrogen, even in an irreversible way (cf. Figure VII-13). This emphasizes the beneficial effect of Mo_2C in terms of suppressing the hydrogen induced ductility loss, as an effect of their presence was noticeable in the mechanical tests despite the fact that the limited amount of hydrogen that they trapped in a partially reversible (2^{nd} peak), partially irreversible (3^{rd} peak) way.

Although the comparison of Figure VII-11 and VII-12 showed mostly similar tendencies, there is an important difference due to the fact that a specific amount of hydrogen is able to leave the materials before the start of the TDS measurement as one hour is necessary to obtain a low pressure in the analysis chamber. This specific amount of hydrogen, further referred to as mobile hydrogen, cannot be detected by TDS, but is included in the hot extraction measurements which are started one minute after charging. Since the amount of diffusible hydrogen has been determined by hot extraction and the amount of hydrogen under the TDS spectra is available as well, one can calculate the amount of mobile hydrogen. These calculations are summarized in Table VII-4.

Table VII-4: Overview of the different hydrogen contents for alloy A, B and C in the as-Q and Q&T condition.

Hydrogen content (wppm)	**Alloy A**		**Alloy B**		**Alloy C**	
	As-Q	Q&T	As-Q	Q&T	As-Q	Q&T
diffusible hydrogen	1.12	1.37	1.18	1.60	1.12	1.72
hydrogen under TDS curves	0.32	0.56	0.39	0.67	0.50	1.17
mobile hydrogen	0.80	0.81	0.79	0.93	0.68	0.61

For all alloys, the integrated amount of hydrogen under the TDS curves was higher for the Q&T condition, which is amongst others due to the presence of Mo_2C. The very low amounts of mobile hydrogen for alloy C

were in contrast to the overall increasing trend for the other values along the A → B → C sequence. The amount of mobile hydrogen was even lower for the Q&T condition although a higher amount of diffusible hydrogen was present.

Apart from the amount of hydrogen in the sample, the hydrogen diffusion coefficient also plays an important role in the hydrogen induced mechanical degradation. Depover *et al.* [4] [9] [45] indeed demonstrated the combined effect of the amount and diffusivity of hydrogen on the HE susceptibility (cf. Chapter II, III and IV). Additionally, Escobar *et al.* [11] showed that, depending on the microstructural features of the material, a different amount of mobile hydrogen left the material before the start of the TDS measurement, which is an important parameter when interpreting the mechanical test data. For sure, the amount of mobile H is also related to the hydrogen diffusion coefficient as the time between the end of charging and the start of the TDS measurement is constant for all alloys. Therefore, hydrogen permeation experiments were performed to determine the hydrogen diffusion coefficient for alloy C and the results were shown in Figure VII-14.

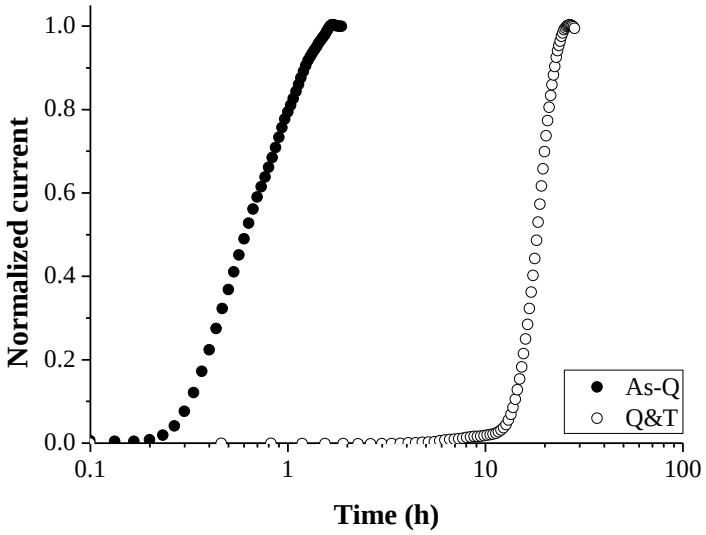

Figure VII-14: Hydrogen permeation curves for alloy C in the as-Q and Q&T condition.

The Q&T sample of alloy C clearly showed a distinct lower hydrogen diffusivity (2.26 x 10^{-12} m^2/s) compared to the as-Q material (9.91 x 10^{-11} m^2/s). The slower hydrogen permeation for the tempered grade was linked to the presence of Mo_2C, hindering hydrogen diffusion and slowing down the apparent hydrogen diffusivity. The amount of mobile hydrogen which effused out of the material in the Q&T condition can be correlated to the low hydrogen diffusion coefficient. Additionally, the lower hydrogen diffusion of the Q&T materials can be set responsible for the increase of the first peak in the TDS spectra compared to the as-Q materials. Since less hydrogen was able to effuse out of the sample ahead of the TDS measurement due to the lower diffusion, more hydrogen was detected under this first peak.

For the as-Q condition of alloy C, a little lower amount of diffusible hydrogen was present compared to alloy B as mentioned previously, but a higher amount of hydrogen was trapped by the available carbides, which were not present for alloy A and B. Consequently, the amount of mobile hydrogen remained very low for alloy C as-Q as well, which can explain the low obtained HE%.

Finally, as it is important to correlate the susceptibility to hydrogen embrittlement with the amount of hydrogen and three different kinds of hydrogen were determined in this section, the HE% vs. the different hydrogen contents is summarized in Figure VII-15. In general, the resistance against HE decreased with total and diffusible hydrogen, as determined by melt and hot extraction, respectively. However, the correlation between the HE% and the amount of mobile hydrogen was most outspoken and gave the best fit, which is noticeably demonstrated in the enlarged part of Figure VII-15. Hence, this kind of hydrogen was assumed to play a more crucial role in the hydrogen induced mechanical degradation of these materials.

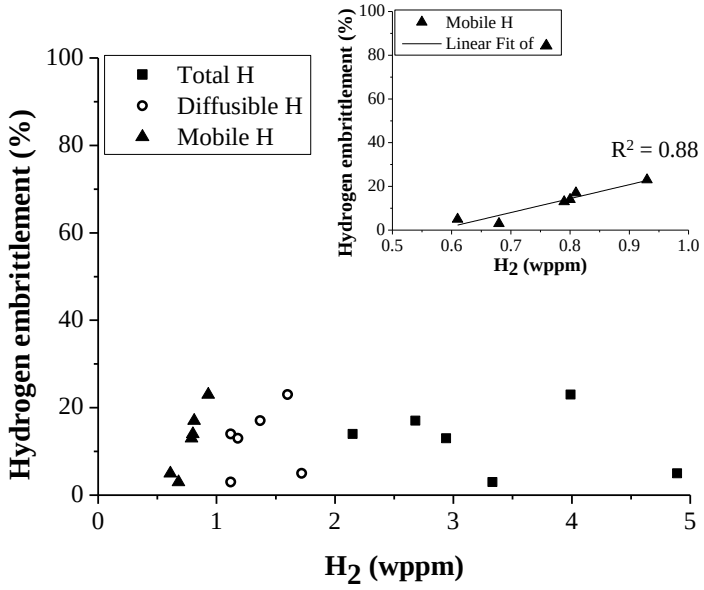

Figure VII-15 : Hydrogen embrittlement percentages vs. different types of hydrogen.

As a conclusion, this section demonstrated that the importance of the presence of Mo_2C precipitates. They were able to trap hydrogen and were responsible for the decreased hydrogen diffusivity. In order to explore their function in more detail, the carbide characteristics and their role in the hydrogen trapping process will be elaborated in the next section.

.

VII.6 The effect of carbide size on the trapping ability

Carbide size distributions were made to link the observed TDS peaks to a specific origin. The HRSEM and FSD images on carbon replicas are shown together with their corresponding distribution map in Figure VII-16 for alloy A and B in the Q&T condition and in Figure VII-17 for alloy C for both conditions.

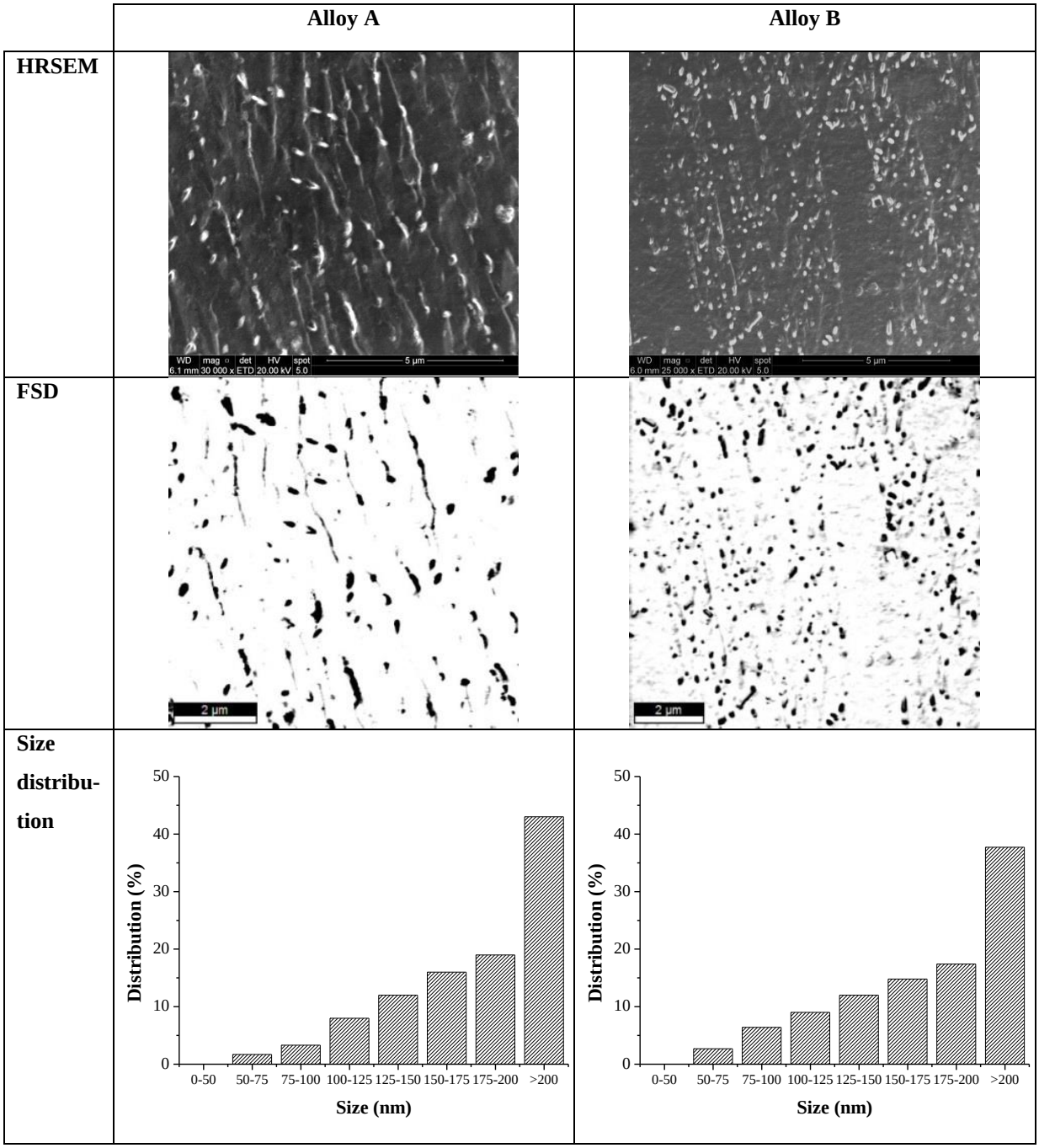

Figure VII-16: HRSEM and FSD images of carbon replicas of alloy A, B in the Q&T condition together with their corresponding size distribution maps.

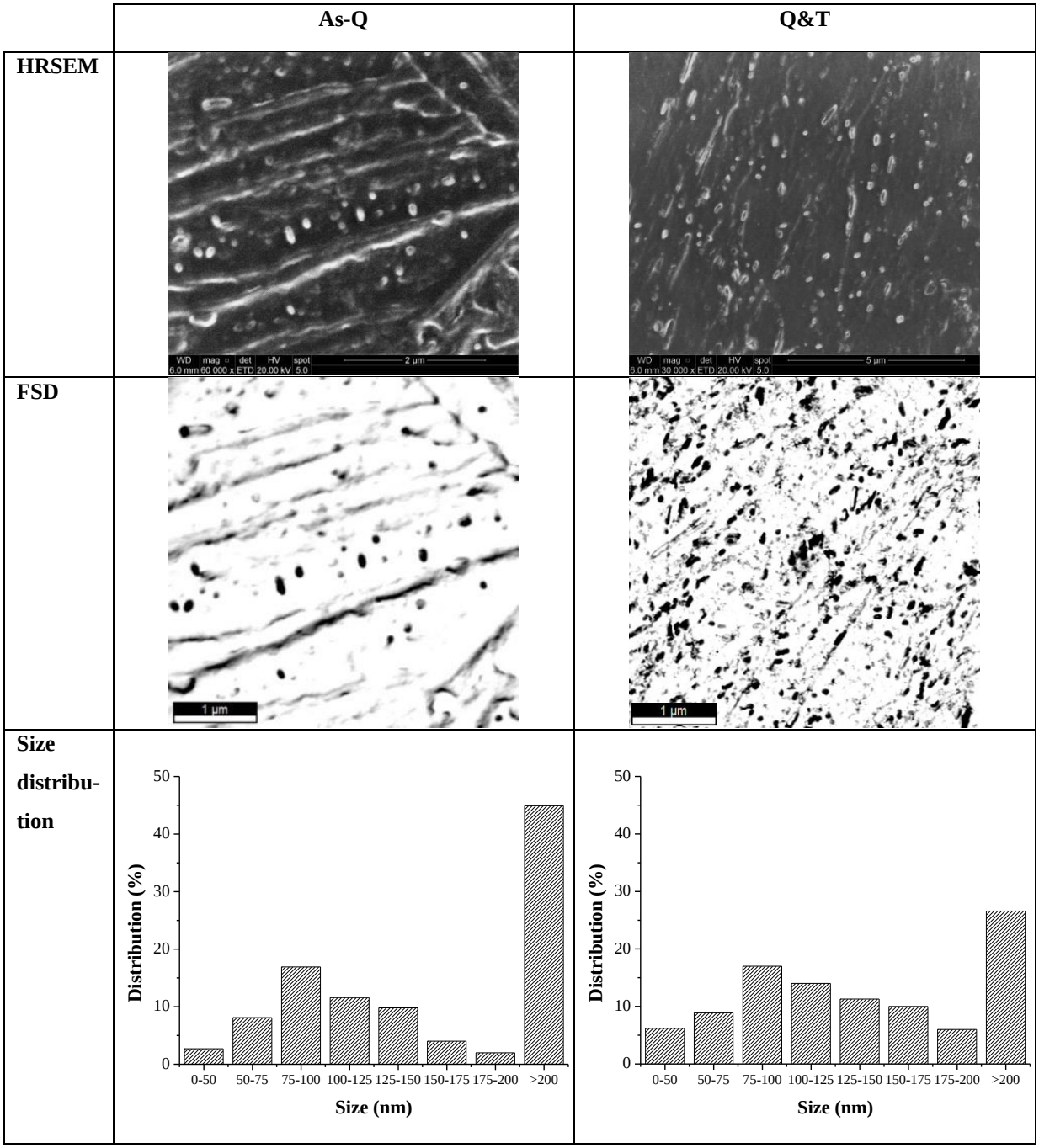

Figure VII-17: HRSEM and FSD images of carbon replicas of alloy C in the as-Q and Q&T condition together with their corresponding size distribution maps.

Tempering only resulted in a small increase in carbide size for alloy C, while alloy A contained the largest fraction of large precipitates in the Q&T condition. Since only alloy C contained Mo_2C with sizes smaller than 50 nm in length, the higher temperature peak in the TDS spectra was attributed to this kind of precipitates. These particles trap hydrogen in an irreversible way with an E_a above 60 kJ/mol. These very small carbides have a needle-shape (cf. Figure VII-8) [30] [38], whereas in the tempered conditions for alloy A and B the carbides have grown and apparently lose their needle-shape during growing evolving into rather coarse long particles (cf.

Figure VII-16 and VII-17). This geometry change might explain the irreversible trapping behavior of the smallest carbides.

The TDS spectra for alloy A and B, in the Q&T condition, showed a second peak which could be attributed to the presence of precipitates. The corresponding second peak was also present for alloy C and contained twice as much hydrogen. Precipitates in the range of 50-125 nm might be set responsible for this peak since the percentage of these precipitates is twice as large for alloy C. Alternatively, the percentage of particles larger than 125 nm is higher for alloy A and B compared to alloy C. If these precipitates were responsible for this 2nd peak, this would be in contradiction with the bigger second peak in the TDS spectrum for alloy C. Precipitates larger than 125 nm were considered to be too large to trap hydrogen via electrochemical charging. Confirmation and possible further refinement for these clear peak attributions will be searched for by changing the carbide size distribution in the next section.

VII.7 On the effect of carbide trapping ability and impact on the resistance against hydrogen embrittlement

To change the carbide size and hence their trapping ability, tempering was applied for two hours. The trapping ability was investigated by TDS and presented together with the corresponding carbide size distributions in Figure VII-18.

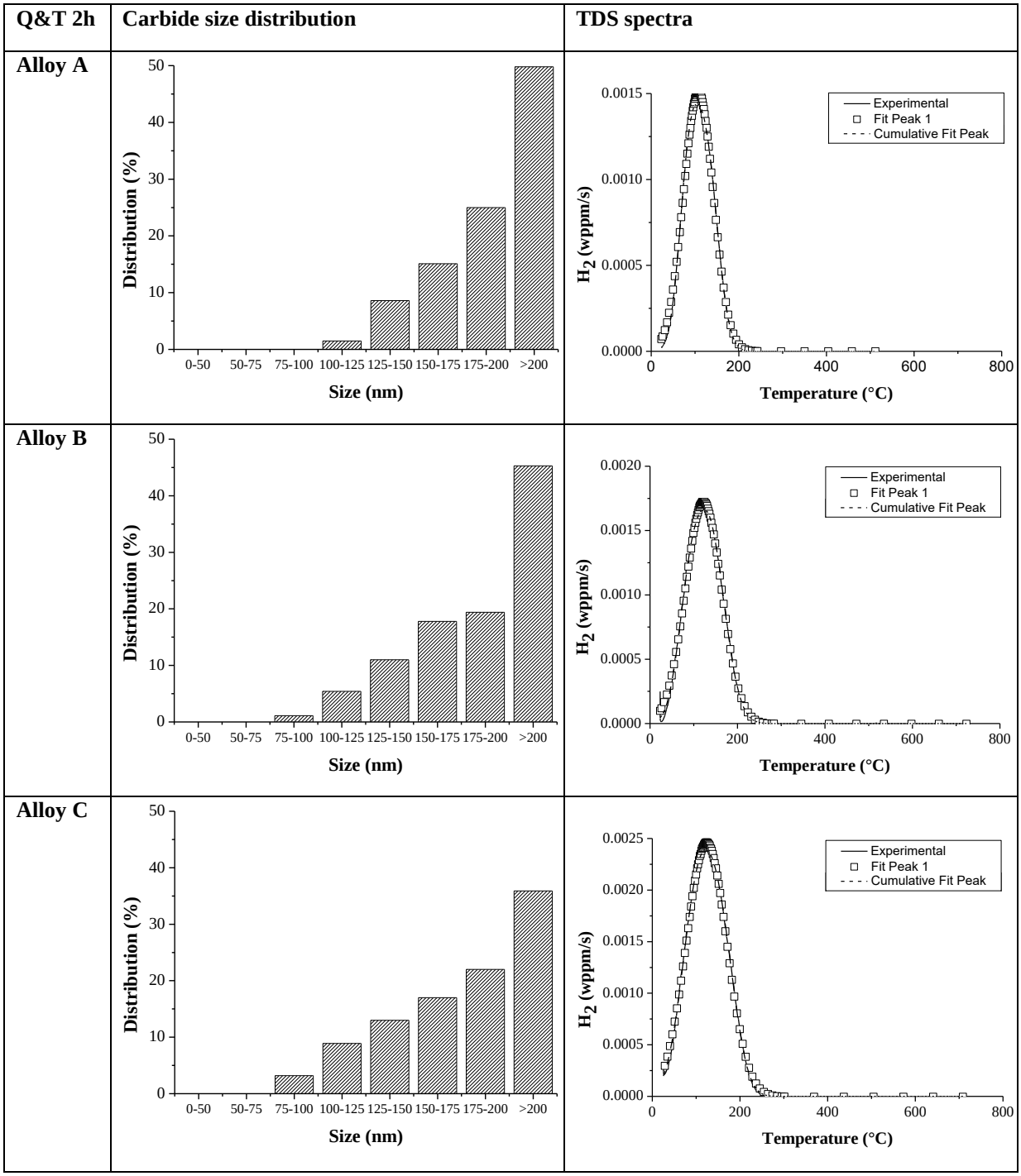

Figure VII-18: Carbide size distribution map together with the corresponding TDS spectra for alloy A, B and C in the Q&T 2h condition.

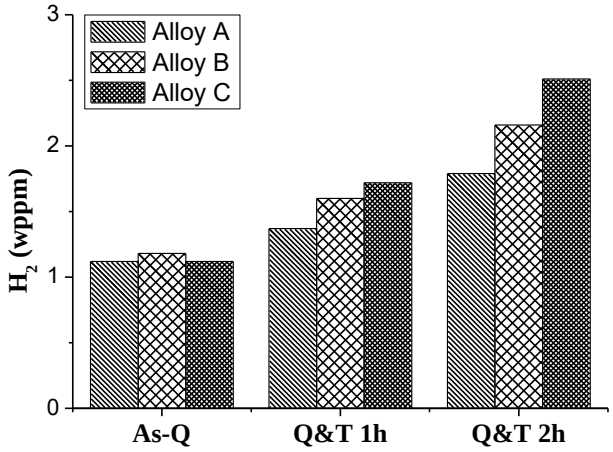

Figure VII-19: Diffusible hydrogen content vs. applied thermal treatment for alloy A, B and C.

One peak was observed in all TDS spectra with increasing peak area for alloy A → B → C. Additionally, the area beneath the peak was higher compared to the materials tempered for one hour. These observations were in good agreement to the hot extraction results presented in Figure VII-19, but are rather remarkable since no carbide related peak was present. Carbides have grown too large and were hence not capable anymore of trapping hydrogen efficiently by electrochemical hydrogen charging. Therefore, the carbide size upper limit to trap hydrogen can be set at 75 nm and the carbide related peak in the TDS spectra, as discussed in the previous section (cf. Figure VII-12), can now be attributed to carbides with sizes in the range of 50-75 nm instead of 50-125 nm.

However, an extra hour of tempering did both the diffusible hydrogen content and the first peak in the TDS spectrum increase. A similar observation was actually made when the as-Q and the Q&T 1h condition were compared (cf. Figure VII-12). The latter observation was attributed to the hydrogen diffusivity since the tempered material showed a considerably lower diffusion coefficient compared to the as-Q grade. However, in the present case, the hydrogen diffusivity of Q&T 2h is approximately the same as the Q&T 1h grade as also determined by a hydrogen permeation test. Consequently, this cannot explain the increase of the first peak in Figure VII-18. Some other feature should play a role here.

As the carbides have grown very large by two hours tempering, this may cause increasing elastic strain fields around the Mo_2C particles, as reported by Wei and Tsuzaki [25] and described in Chapter V on TiC. These can trap hydrogen as well [42] [46] and this hydrogen might, due to the low diffusion coefficient, still partly contribute to this first broad TDS peak. This would both explain the increase in diffusible hydrogen and the amount of detected hydrogen by TDS. In order to verify this assumption, tempering was applied for four hours on alloy C to further increase the carbide size and hence evaluate the corresponding evolution in hydrogen trapping. The TDS measurement on alloy C after 4h tempering is presented in Figure VII-20 and confirmed the assumption as the area below the first peak increased again. Since the carbides were not able to trap hydrogen, as they grew too large, the elastic stress fields around the precipitates can be set responsible for the increased hydrogen contents.

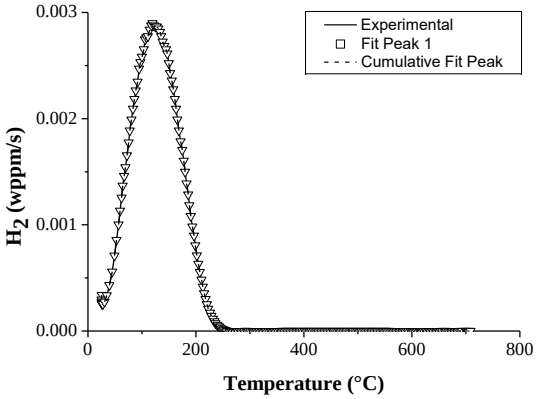

Figure VII-20: TDS spectrum of alloy C in the Q&T 4h condition.

The amount of mobile hydrogen (1.05, 1.11 and 0.85 wppm for alloy A, B and C Q&T 2h, respectively), associated with hydrogen trapped by dislocations, also increased when tempered for two hours in comparison to the Q&T 1h condition (cf. Table VII-4). Since generally tempering leads to a decrease in dislocation density, hydrogen got trapped at the elastic stress fields around the precipitates, as mentioned above and demonstrated by the rather low E_a as well [25] [47] [48]. As the impact of hydrogen on the mechanical performance is an important issue in the context of this study and to confirm the previously addressed correlation between mobile hydrogen and the HE%, tensile tests were performed. The stress-stress curves of the tensile tests are shown in Figure VII-21 and the corresponding HE% are summarized in Table VII-5. When the materials were tempered for two hours, they all got more prone the hydrogen embrittlement and the highest resistance to HE remained for alloy C. This confirms the statement made above that the amount of mobile hydrogen was indeed crucial as it was the lowest for alloy C. Since a similar strength level was obtained after 1h and 2h tempering, this observation can be considered to be independent of any possible strength related effect.

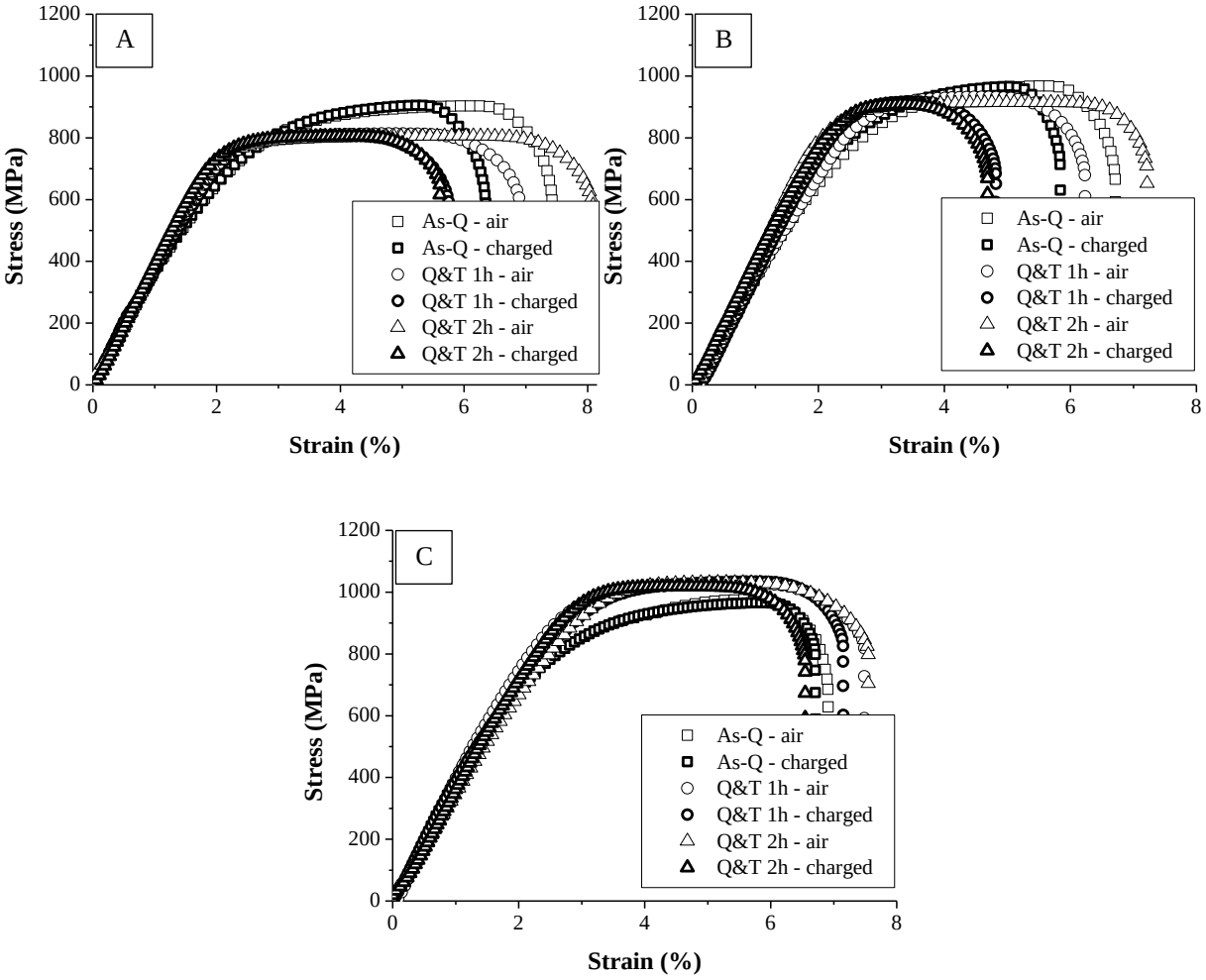

Figure VII-21: Stress-strain curves of alloy A, B and C in the as-Q, Q&T 1h and Q&T 2h condition.

Table VII-5: Summary of the HE% for alloy A, B and C in the as-Q and the tempered conditions.

HE%	As-Q	Q&T 1h	Q&T 2h
Alloy A	14	17	31
Alloy B	13	23	35
Alloy C	3	5	13

VII.8 On the effect of hydrogen diffusion on hydrogen embrittlement

Alloy C shows a really low susceptibility to embrittle due to the presence of hydrogen. In addition, the present work also demonstrated the importance of hydrogen mobility and hydrogen diffusion. So far, all tensile tests were performed at a cross-head deformation speed of 5 mm/min. Hydrogen embrittlement, on the other hand, should be more pronounced when hydrogen is enabled to diffuse to a certain hydrogen induced micro-crack or stress region and hence accelerate the crack propagation during the tensile test. The limited amount of HE in alloy C makes this alloy extremely suitable to verify this, and therefore, tensile tests were performed at a cross-head deformation speed of 0.05 mm/min, i.e. 100 times slower. The corresponding stress-strain curves for the as-Q (a) and Q&T (b) condition of alloy C are depicted in Figure VII-22.

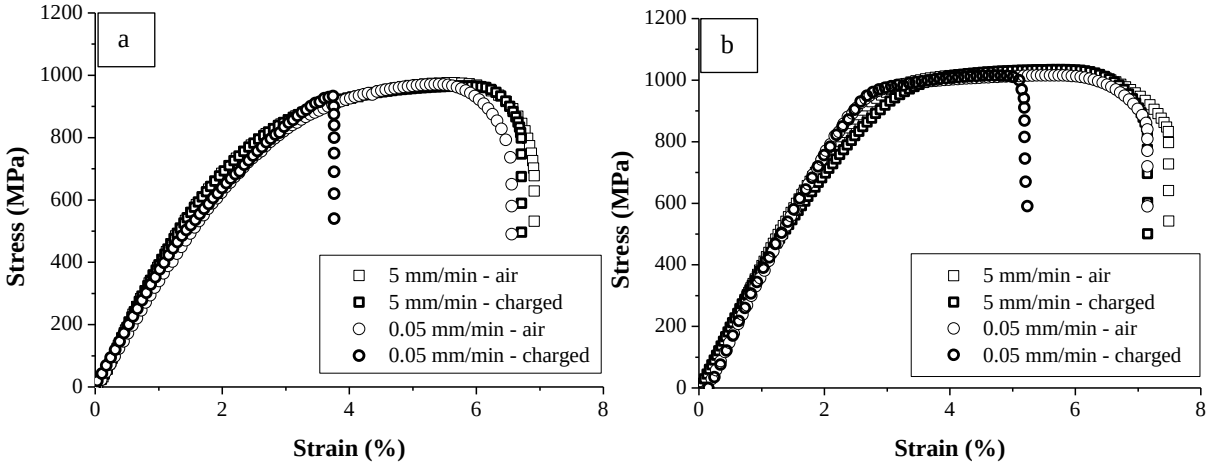

Figure VII-22: Stress-strain curves of alloy C in the as-Q (a) and Q&T 1h (b) condition at different cross-head displacement speeds of 5 and 0.05 mm/min.

At the decreased cross-head deformation, the HE% of the as-Q material increased from 3 to 43%, whereas the Q&T sample went from 5 to 28%. The increase in the hydrogen induced ductility loss was clearly much more pronounced for the as-Q condition, although the amount of diffusible hydrogen was higher for the tempered material (cf. Figure VII-11). Due to the significantly higher diffusion coefficient for the as-Q condition, as shown in Figure VII-14, hydrogen could cover a larger distance during the test and could diffuse to critical stress zones ahead of a crack tip in the as-Q condition. This combined impact of both the amount and diffusivity of hydrogen when interpreting HE% has already been reported before [4] [9] [45] [49] (cf. Chapter II, III and IV).

So far all tensile tests were performed on samples that were hydrogen saturated before the test. Therefore, tensile tests were also performed on specimens that were not pre-charged to verify the impact of the hydrogen penetration depth in samples with a variable microstructure. In-situ hydrogen charging was started together with the actual tensile test. The stress-strain curves are shown in Figure VII-23. Due to the higher diffusion coefficient of the as-Q sample, the in-situ hydrogen induced ductility loss is higher compared to the Q&T 1h grade, with embrittlement percentages of 33 and 21%, respectively. These values were lower than for the pre-charged samples as the material was only partially affected by hydrogen in the present case. The hydrogen effect was larger for the as-Q microstructure as hydrogen penetrated faster into this microstructure. To get some

quantitative information on this, the hydrogen distance x (cm) was be calculated by taking the square root of the product of the diffusion coefficient D (cm^2/s) and the test time t (s), i.e. $x = (D\,x\,t)^{1/2}$ [50]. The calculated hydrogen diffusion distances in the as-Q and Q&T matrix were 630 and 110 μm, respectively. Consequently, the tempered Mo_2C particles effectively limited hydrogen diffusion and slowed down the chance to hydrogen induced failure when samples come into contact with a hydrogen containing environment. This particular effect of the hydrogen penetration depth on the HE degree was reported by Ronevich *et al.* [51] and discussed in Chapter III [9].

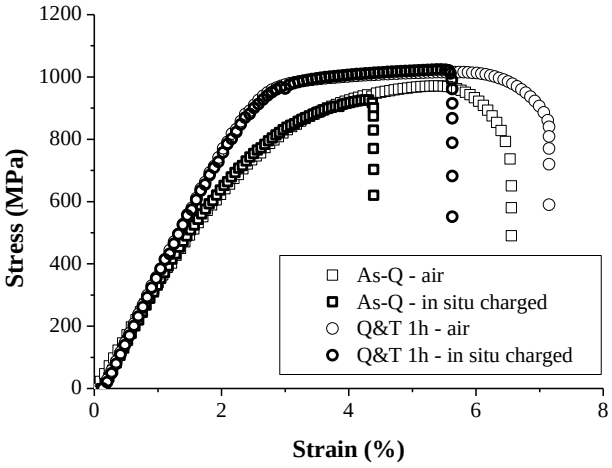

Figure VII-23: Stress-strain curves of alloy C at a cross-head displacement speed of 0.05 mm/min without pre-charging. In-situ hydrogen charging was applied together with the actual tensile test.

VII.9 On the beneficial effect of Mo_2C on the hydrogen induced ductility loss

Finally, the question remains whether the addition of Mo_2C precipitates was beneficial to enhance the HE resistance. The tempered conditions indeed showed an increased HE susceptibility, although a higher amount of hydrogen got trapped by these materials as well. Since a clear correlation has been established between the degree of HE and the amount of hydrogen, no decisive conclusions upon the beneficial effect of Mo_2C could be drawn so far. Therefore, a modified hydrogen charging procedure was performed to introduce a similar amount of hydrogen in the Q&T sample compared to the as-Q material. Hence, it can be verified whether the effect of the addition of Mo_2C was beneficial or not in terms of the materials' mechanical behavior under hydrogen loading. Alloy A and B were chosen for this particular study because these alloys showed the highest differences in HE% and a clear evaluation of the effect of tempered induced Mo_2C can be performed as no carbides were present in the as-Q state of these grades. The as-Q conditions were compared with the Q&T 1h states since carbides were too big to trap hydrogen when tempered for two hours.

First, the materials got charged for different charging times to achieve a similar hydrogen level as the as-Q grade. The melt extraction results are presented in Figure VII-24. Electrochemical hydrogen charging for about 30 minutes was sufficient for both materials to contain a hydrogen content similar to the as-Q state. Tensile tests

were performed after these hydrogen charging times and the corresponding stress-strain curves are shown in Figure VII-25 and summarized in Table VII-6. These results are indicated with "*".

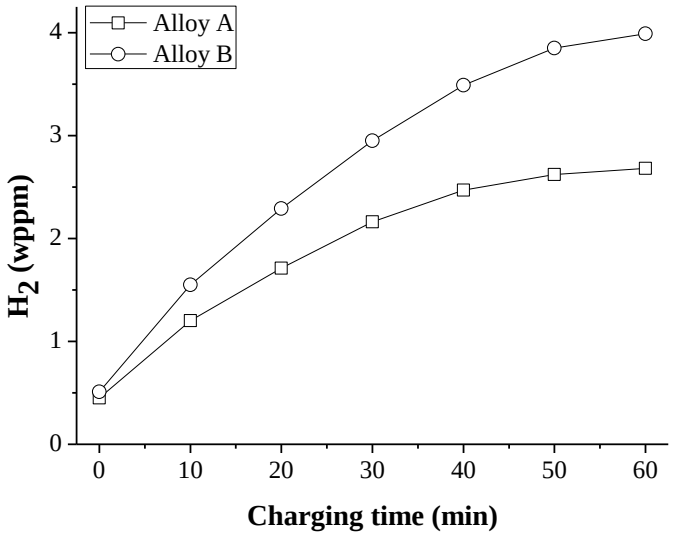

Figure VII-24: Total amount of hydrogen vs. charging time for alloy A and B in the Q&T conditions.

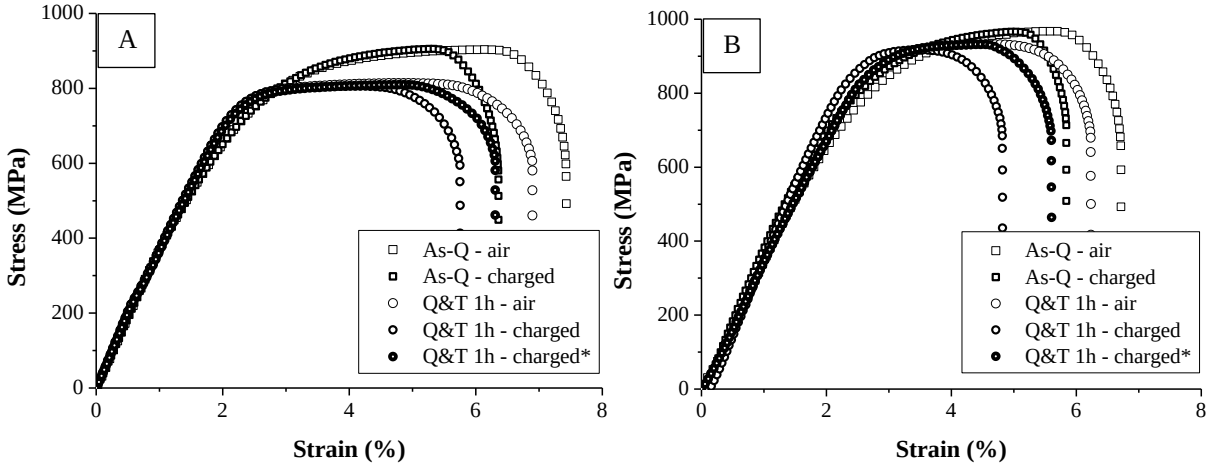

Figure VII-25: Stress-strain curves for alloy A and B in the as-Q and Q&T 1h condition. Charging was applied for 1 hour (charged) and until a similar as-Q hydrogen content was reached (charged*).

Table VII-6: Summary of the HE% for alloy A and B in the as-Q and Q&T 1h condition. Charging was applied for 1 hour and until a similar as-Q hydrogen content was reached (indicated with "*").

HE%	As-Q	Q&T 1h	Q&T 1h*
Alloy A	14	17	8
Alloy B	13	23	10

The response to hydrogen presence improved when a similar amount of hydrogen was introduced in the materials in both conditions. Consequently, the addition of Mo_2C clearly was beneficial for these materials. To determine where hydrogen is trapped after the modified charging procedure, TDS measurements are performed after 30 minutes of hydrogen charging as well. The spectra are shown in Figure VII-26 and indicated as

'charged*'. These are presented together with the TDS spectra of the samples charged for one hour (cf. Figure VII-12), indicated as 'charged', to verify which trapping sites will first trap hydrogen.

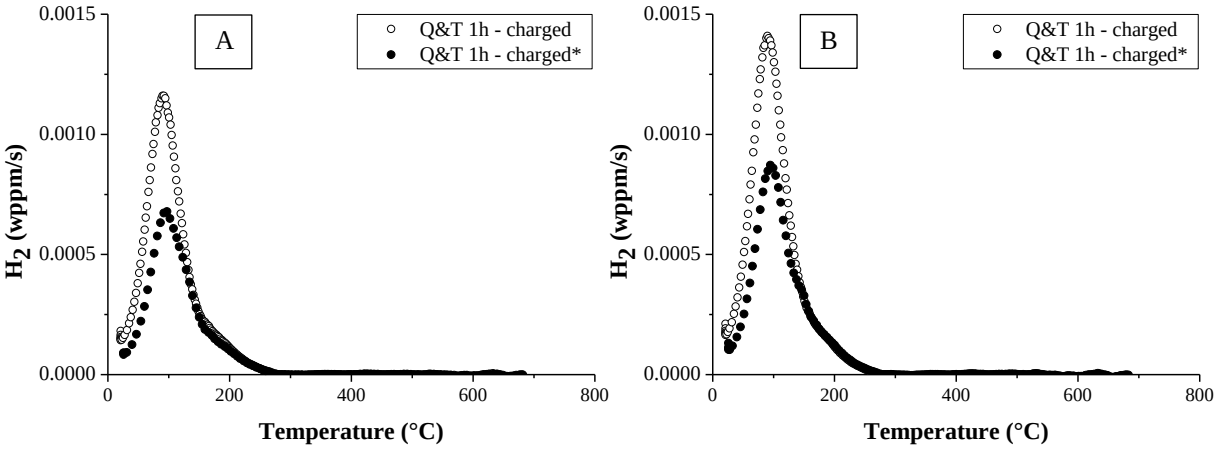

Figure VII-26: TDS spectra of alloy A and B in the Q&T 1h condition, charged to similar H content as the as-Q sample (charged*), together with the TDS spectra (cf. Figure VII-12) charged for one hour (charged).

The TDS spectra indicated that the trapping sites with the highest activation energy, i.e. those associated with hydrogen trapped at the Mo_2C precipitates, were first filled. The first peak, correlated with H trapped mainly by the lath boundaries with an E_a of about 25-30 kJ/mol, was not yet saturated compared to the TDS spectra obtained on hydrogen saturated samples. Consequently, the Mo_2C related trapping sites enhanced the response to the susceptibility to HE. A straightforward comparison, regardless the total amount of hydrogen which got introduced, can now be obtained. Similarly to the lower amount of H trapped by the lath boundaries, it may be assumed that the corresponding trapping sites for mobile hydrogen, i.e. those with the lowest E_a, and associated with dislocations, were not completely occupied either. Hence, the amount of mobile hydrogen decreased resulting in a reduced HE%. The observation that the trapping sites associated with a higher E_a were first filled is in good agreement with findings of Dadfarnia *et al.* [36].

VII.10 Conclusion

The hydrogen induced ductility loss was evaluated for three Fe-C-Mo alloys and correlated with the hydrogen interaction with the Mo_2C precipitates. Two thermal treatments were applied to compare two main conditions; i.e. an as-quenched and a quenched and tempered state in which Mo_2C particles had precipitated. The susceptibility to hydrogen embrittlement was determined by performing tensile tests on both uncharged and in-situ hydrogen charged tensile specimens. Tempering appeared to reduce the resistance against hydrogen embrittlement. Hot/melt extraction and thermal desorption spectroscopy were subsequently performed to determine the role of the Mo_2C precipitates. Tempering induced Mo_2C particles trapped a considerable amount of hydrogen and a correlation between the hydrogen embrittlement susceptibility and the hydrogen mobility was confirmed.

Carbide size distributions together with a slightly modified thermal treatment allowed to further elaborate these observations and hypotheses put forward. Carbides with sizes less than 50 nm were responsible for the irreversibly trapped hydrogen, while carbides with sizes larger than 75 nm were not able to trap hydrogen

electrochemically. An adjusted charging procedure allowed demonstrating the beneficial effect of Mo_2C addition on the HE resistance in a partially charged sample. The deeper traps, associated with the carbides, were first filled and hence the amount of mobile hydrogen decreased, together with the hydrogen embrittlement sensitivity. Moreover, the crucial role of hydrogen diffusion was demonstrated by performing tests at lower strain rate on hydrogen pre-charged and non-pre-charged specimens. Although the amount of diffusible hydrogen was higher for the Q&T materials, the HE effect was more pronounced for the as-Q material due to its higher hydrogen diffusivity.

VII.11 References

[1] Johnson WH, „On some remarkable change produced in iron and steel by the action of hydrogen and acids.," *Proceedings of the Royal Society of London,* vol. 23, pp. 168-179, 1875.

[2] Michler T, Naumann J, „Microstructural aspects upon hydrogen environment embrittlement of various bcc steels.," *Int Journal of H Energy,* vol. 35, pp. 821-832, 2010.

[3] Hilditch TB, Lee SB, Speer JG, Matlock DK, „Response to Hydrogen Charging in High Strength Automotive Sheet Steel Products," *SAE Technical Paper,* 2003, http://dx.doi.org/10.4271/2003-01-0525.

[4] Depover T, Pérez Escobar D, Wallaert E, Zermout Z, Verbeken K, „Effect of in-situ hydrogen charging on the mechanical properties of advanced high strength steels," *Int Journal of Hydrogen Energy,* vol. 39, pp. 4647-4656, 2014.

[5] Loidl M, Kolk O, „Hydrogen embrittlement in HSSs limits use in lightweight body," *Advanced Materials and Processes,* vol. 169, pp. 22-25, 2011, BMW Group, Germany.

[6] Duprez L, Verbeken K, Verhaege M, „Effect of hydrogen on the mechanical properties of multiphase high strength steels," in *Proc. of the 2008 Int. Hydrogen Conf.*, Jackson, Wyoming, USA, 2008.

[7] Laureys A, Depover T, Petrov R, Verbeken K, „Characterization of hydrogen induced cracking in TRIP-assisted steels," *Int Journal of Hydrogen Energy,* vol. 40, nr. 47, pp. 16901-16912, 2015.

[8] Laureys L, Depover T, Petrov R, Verbeken K, „Microstructural characterization of hydrogen induced cracking in TRIP-assisted steel by EBSD," *Materials Characterization,* vol. 112, pp. 169-179, 2016.

[9] Depover T, Wallaert E, Verbeken K, „Fractographic analysis of the role of hydrogen diffusion on the hydrogen embrittlement susceptibility of DP steel," *Mat Sci and Eng A,* vol. 649, pp. 201-208, 2016.

[10] Pérez Escobar D, Miñambres C, Duprez L, Verbeken K, Verhaege M, „Internal and surface damage of multiphase steels and pure iron after electrochemical hydrogen charging," *Corrosion Science,* vol. 53, p. 3166–3176, 2011.

[11] Pérez Escobar D, Verbeken K, Duprez L, Verhaege M, „Evaluation of hydrogen trapping in high strength steels by thermal desorption spectroscopy," *Mat Sci and Eng A,* vol. 551, pp. 50-58, 2012.

[12] Akiyama E, „Evaluation of delayed fracture property of high strength bolt steels," *ISIJ Int,* vol. 52, pp. 307-315, 2012.

[13] Kang HJ, Yoo JS, Park JT, Ahn ST, Kang N, Cho KM, „Effect of nano-carbide formation on hydrogen-delayed fracture for quenching and tempering steels during high-frequency induction heat treatment," *Mat Sci and Eng A,* vol. 543, pp. 6-11, 2012.

[14] Li S, Akiyama E, Kimura Y, Tsuzaki K, Ini N, Zhang B, „Hydrogen embrittlement property of a 1700 MPa class ultrahigh-strength tempered martensitic steel," *Sci Technol Adv Mater,* p. 11:025005, 2010.

[15] Liu Y, Wang M, Liu G, „Effect of hydrogen on ductility of high strength 3Ni-Cr-Mo-V steels," *Mat Sci and Eng A,* vol. 594, pp. 40-47, 2014.

[16] Nagao A, Martin ML, Dadfarnia M, Sofronis P, Robertson M, „The effect of nanosized (Ti,Mo)C precipitates on hydrogen embrittlement of tempered lath martensitic steel," *Acta Mat,* vol. 74, pp. 244-254, 2014.

[17] Ren YJ, Zeng CL, „Corrosion protection of 304 stainless steel bipolar plates using TiC films produced by high-energy micro-arc alloying process," *Journal Power Sources,* vol. 171, pp. 778-782, 2007.

[18] Yamasaki S, Takahashi T, „Evaluation method of delayed fracture property of high strength steels," *Tetsu-to-Hagane,* vol. 83, pp. 454-459, 1997.

[19] Ohnuma M, Suzuki JI, Wei FG, Tsuzaki K, „Direct observation of hydrogen trapped by NbC in steel using small-angle neutron scattering," *Scripta Mat,* vol. 58, pp. 142-145, 2008.

[20] Wallaert E, Depover T, Arafin MA, Verbeken K, „Thermal desorption spectroscopy evaluation of the hydrogen trapping capacity of NbC and NbN precipitates," *Met Mat Trans A,* vol. 45, pp. 2412-2420, 2014.

[21] Wei FG, Tsuzaki K, „Hydrogen trapping character of nano-sized NbC precipitates in tempered martensite," in *Proc. of the 2008 Int. Hydrogen Conf.,* Jackson, Wyoming, USA, 2008.

[22] Asaoka T, Lapasset G, Aucouturier M, Lacombe P, „Observations of hydrogen trapping in Fe-0.15 wt. pct Ti alloy by high resolution autoradiography," *Corros NACE,* vol. 1978, pp. 39-47, 1978.

[23] Pressouyre GM, Bernstein IM, „A quantitative analysis of hydrogen trapping," *Met Trans A,* vol. 9A, pp. 1571-1580, 1978.

[24] Wei FG, Hara T, Tsuzaki K, „Precise determination of the activation energy for desorption of hydrogen in two Ti-added steels by a single thermal-desorption spectrum," *Met Mat Trans B,* vol. 35B, pp. 587-597, 2004.

[25] Wei FG, Tsuzaki K, „Quantitative Analysis on hydrogen trapping of TiC particles in steel," *Met Mat Trans A,* vol. 37A, pp. 331-353, 2006.

[26] Takahashi J, Kawakami K, Kobayashi Y, Tarui T, „The first direct observation of hydrogen trapping sites in TiC precipitation-hardening steel through atom probe tomography," *Scripta Mat,* vol. 63, pp. 261-264, 2010.

[27] Wei FG, Hara T, Tsuzaki K, „Nano-precipitates design with hydrogen trapping character in high strength steels," in *Proc. of the 2008 Int. Hydrogen Conf,* Jackson, Wyoming, USA, 2008.

[28] Pérez Escobar D, Wallaert E, Duprez L, Atrens A, Verbeken K, „Thermal Desorption Spectroscopy Study of the Interaction of Hydrogen with TiC Precipitates," *Met Mater Int,* vol. 19, pp. 741-748, 2013.

[29] Pavina EJ, Speer JG, Van Tyne CJ, „Equilibrium solubility products of molybdenum carbide and tungsten carbide in iron," *Scripta Mat,* vol. 66, pp. 243-246, 2012.

[30] Yamasaki S, Bhadeshia HKDH, „Modelling and characterisation of Mo2C precipitation and cementie dissolution during tempering of Fe-C-Mo martensitic steel," *Materials Science and Technology,* vol. 19, pp. 723-731, 2003.

[31] Yamasaki S, PhD: Modelling precipitation of carbides in martensitic steels, Cambridge, 2004.

[32] Spencer GL, Duquette DJ, „The role of vanadium carbide traps in reducing the hydrogen embtrittlement susceptibility of high strength alloy steels," US army armament research, development and engineering center, Watervliet, N.Y., 1998.

[33] Frappart S, Feaugas X, Creus J, Thebault F, Delattre L, Marchebois H, „Study of the hydrogen diffusion and segregation into Fe-C-Mo martensitic HSLA steel using electrochemical premeation test," *Journal of*

Physics and Chemistry of Solids, vol. 71, pp. 1467-1479, 2010.

[34] Wei FG, Tsuzaki K, „Hydrogen trapping phenomena in martensitic steels," in *Gaseous HE of materials in energy technologies,* Woodhead, 2012, pp. 493-525.

[35] Lee J, Lee T, Kwon YJ, Mun DJ, Yoo JY, Lee CS, „Role of Mo/V carbides in hydrogen embrittlement of tempered martensitic steel," *Corros Rev,* 2015.

[36] Dadfarnia M, Sofronis P, Neeraj T, „Hydrogen interaction with multiple traps: Can it be used to mitigate embrittlement?," *Int Journal of Hydrogen Energy,* vol. 36, pp. 10141-10148, 2011.

[37] Gibala R, Kumnick AJ, „Hydrogen trapping in iron and steels," in *Hydrogen embrittlement and stress corrosion cracking,* American Society for Metals, 1984, pp. 61-77.

[38] Speich GR, Leslie WC, „Tempering of steel," *Met Trans,* vol. 3, pp. 1043-1054, 1972.

[39] Ashby MF, Easterling KE, „A first report on diagrams for grain growth in welds," *Acta Mat,* vol. 30, pp. 1969-1978, 1982.

[40] Thomas LSR, Li D, Gangloff RP, Scully JR, „Trap-governed hydrogen diffusivity and uptake capacity in ultrahigh strength aermet 100 steel," *Met Mat Trans A,* vol. 33A, pp. 1991-2004, 2002.

[41] Choo WY, Lee JY, „Thermal analysis of trapped hydrogen in pure iron," *Met Trans A,* vol. 13A, pp. 135-140, 1982.

[42] Pressouyre GM, „Classification of hydrogen traps in steel," *Met Trans A,* vol. 10A, pp. 1571-1573, 1979.

[43] Hirth JP, „Effects of Hydrogen on the Properties of Iron and Steel," *Met Trans A,* vol. 11A, pp. 861-890, 1980.

[44] Pérez Escobar D, Depover T, Wallaert E, Duprez L, Verbeken K, Verhaege M, „Combined thermal desorption spectroscopy, differential scanning calorimetry, scanning electron microscopy and X-ray diffraction study of hydrogen trapping in cold deformed TRIP steel," *Acta Mat,* vol. 60, pp. 2593-2605, 2012.

[45] Depover T, Van den Eeckhout E, Verbeken K, „The impact of hydrogen on the ductility loss of bainitic Fe-C alloys," *Materials Science Technology,* 2016.

[46] Wei FG, Tsuzaki K, „Hydrogen Absorption of Incoherent TiC Particles in Iron from Environment at High Temperatures," *Met Mat Trans A,* vol. 35A, pp. 3155-3163, 2004.

[47] Gerberich WW, Livne T, Chen XF, Kaczorowski, „Crack growth from internal hydrogen-temperature and microstructural effect in 4340 steel," *Met Trans A,* vol. 19, pp. 1319-1334, 1988.

[48] Takagi S, Inoue T, Hara T, Hayakawa M, Tsuzaki K, Takahashi T, „Parameters for the evaluation of hydrogen embrittlement in high strength steel," *Tetsu-to-Hagané,* vol. 86, pp. 689-695, 2000.

[49] Toh T; Baldwin WM, Stress Corrosion Cracking and Embrittlement, New York, 1956, pp. 176-186.

[50] Koyama M, Tasan CC, Akiyama E, Tsuzaki K, Raabe D, „Hydrogen-assisted decohesion and localized plasticity in dual-phase steel," *Acta Mat,* vol. 70, pp. 174-187, 2014.

[51] Ronevich JA, Speer JG, Matlock DK, „Hydrogen embrittlement of commercially produced advanced high strength steels," *SAE Int Journal Mater Manuf,* vol. 3, pp. 255-267, 2010.

CHAPTER VIII

Evaluation of the effect of V_4C_3 precipitates on the hydrogen induced mechanical degradation in Fe-C-V alloys*

VIII.1 Introduction

The mechanical degradation due to the impact of hydrogen has been reported to impede the application of newly developed high strength alloys [1]. Carbides play an important role while dealing with the hydrogen embrittlement (HE) issue since they can, on the one hand, realize a mechanical strengthening effect and, on the other hand, they are quoted to be beneficial to reduce the susceptibility to the hydrogen induced ductility loss by trapping hydrogen. Carbides such as TiC, NbC, V_4C_3, $Cr_{23}C_6$, and Mo_2C are indeed known to cause secondary hardening [2] and some of them, TiC and VC, have been reported to be beneficial for improving the resistance to HE due to hydrogen trapping [3] [4] [5] [6] [7].

Thermal desorption spectroscopy (TDS) can be used to study the hydrogen trapping sites in a material. The hydrogen trapping capacity was for instance investigated by means of TDS on four steels in which Nb, Ti, V and Mo was introduced as carbide forming element [8]. Only TiC showed an additional desorption peak around 600°C and the hydrogen trapping capacity of the alloy carbides varied in descending order of NbC > TiC >> VC > Mo_2C. Asahi *et al.* [9] studied the hydrogen trapping behavior in vanadium-added steel. The VC precipitate in 0.25C-1.5Mn-V steels had a desorption activation energy (E_a) of 33-35 kJ/mol. A theoretical approach on the hydrogen interaction with multiple traps was performed by Dadfarnia *et al.* [10]. Traps with binding energy > 60 kJ/mol can be categorized as very strong or irreversible ones and those < 30 kJ/mol as weak and reversible [11]. Trapping of hydrogen by VC in Fe-C-Mn steel was studied by small angle neutron scattering in [12] and it was estimated that the precipitates trapped approximately 5 wppm of hydrogen. They concluded that VC precipitates are effective irreversible hydrogen trapping sites for moderate hydrogen concentrations up to a few wppm hydrogen. It was concluded that the hydrogen trapping was homogeneously within the precipitates rather than at the precipitate/matrix interface.

Zhang *et al.* [13] investigated the diffusion coefficient by means of the hydrogen permeation technique and the reduction of area after hydrogen charging during a slow strain rate test (SSRT). They concluded that the diffusion coefficient of hydrogen in V or Nb added alloys was lower than without alloying. The combined effect of V and Nb on the hydrogen diffusion coefficient was not larger than when only Nb was added, which was attributed to the fact that the VC precipitates were too big to trap hydrogen. V or Nb addition reduced the susceptibility of hydrogen induced fracture when comparing air and hydrogen pre-charged samples in SSRT. In

* This chapter is based on the following publication: Depover T, Verbeken K, *Materials Science and Engineering A* (2016), submitted.

this case, the combined effect of V and Nb on the hydrogen induced delayed fracture resistance was better than only Nb. Additionally, intergranular fracture along prior austenitic grain boundaries and cleavage fracture of the non-alloyed material was more visible compared to the Nb-steel and Nb-V steel, where a mixture of quasi-cleavage, transgranular and intergranular was obtained. Micro-alloyed additions give rise to a strengthening effect due to a reduction in grain size. The resistance to delayed fracture was correlated to the tendency for intergranular fracture along prior austenitic grain boundaries. If the tendency is higher, the resistance to delayed fracture is better according to Zhang *et al.* [13]. These observations enhance the interest of introducing carbides into steel grades in order to reduce their susceptibility to HE.

Other investigation on the role of vanadium was performed by Spencer *et al.* [4]. They refer to previous work of Raymond [14] in order to motivate their goals. Raymond [14] already suggested that addition of Si or V could reduce the susceptibility to hydrogen embrittlement. Alloying elements can act as effective traps and these are able to limit hydrogen migration to stressed regions in a material, where it can initiate cracks or assist their growth. Experimental analysis by Spencer *et al.* [4] was done on quenched and tempered steels, which were heat treated to approximately the same yield and tensile strength and a variation of carbon and vanadium content was studied. They concluded that carbon did not cause a difference in the hydrogen embrittlement susceptibility. The V-alloyed steel, on the contrary, did change significantly since a lower hydrogen induced ductility loss was obtained, which demonstrated that the addition of vanadium carbides was beneficial. In addition, an extra improved ductility was observed for some materials which was attributed to the presence of molybdenum and consequently the precipitation of Mo_2C in these alloys. Consequently, this is a good example of how addition of carbide-forming elements can enhance the resistance to hydrogen embrittlement. A hydrogen extraction study was done as well and the main conclusion was that vanadium carbides act as beneficial hydrogen traps for diffusible hydrogen.

Lee *et al.* [15] investigated the role of Mo/V carbides in hydrogen embrittlement of tempered martensitic alloys. The V containing material showed the largest peak of diffusible hydrogen, indicating that V carbides were capable of trapping a high amount of hydrogen. This was attributed to the high chemical affinity of V for hydrogen. Ideally, vanadium carbide should be present as VC, however in most cases, V_4C_3 predominates in steel [2]. The empty carbon sites of the V_4C_3 can act as a physical trap for hydrogen. V has five electrons in its outer shell, able to make a bonding with four carbon valence electrons. An extra vanadium electron is left, this may be an attractive hydrogen trap site as also reported by Pressouyre [16]. The presence of fine V_4C_3 particles of less than 50 angstroms in diameter were investigated in steels with 0.2% C and more than 0.10% V by means of transmission electron microscopy (TEM) by Aoki and Tanino [2] [17]. The carbides had a coherent interface and according to Yoshino [2] [18], these helped to promote the resistance to stress corrosion cracking.

An extensive study about modeling and characterization of V based precipitates was elaborated by Yamasaki and Bhadhesia [5], although they did not perform a hydrogen related experimental study. The precipitation and Ostwald ripening behavior of V_4C_3 (plate shaped) particles during the tempering of a ternary Fe – C –V martensitic steel was studied. TEM was used to validate the proposed theory. When carbides, such as V_4C_3, are introduced into the steel, they can behave as hydrogen trapping sites in order to enhance the resistance to static

fracture. The mechanical and hydrogen trapping properties depend on many parameters but the two most significant terms are the carbide size and number density according to the authors. V_4C_3 played a more important role in enhancing the resistance to hydrogen embrittlement owing to its much higher hydrogen trapping capacity than Mo_2C. Modeling of V_4C_3 precipitation was therefore a useful tool for the development of hydrogen resistant steels as it was possible to estimate the average length, volume fraction, and number density of particles in a manner consistent with experimental observations. Unfortunately, the effective correlation with their interaction with hydrogen was not made, it is only emphasized that this carbide can enhance the resistance to hydrogen embrittlement.

The present study aims to correlate the effect of V_4C_3 precipitates on the trapping ability and consequently on the hydrogen induced ductility loss of steels with increased strength. Focus was put on generic quenched and tempered alloys in which the possible trapping sites were limited to verify the trapping capacity of the carbides.

VIII.2 Experimental procedure

VIII.2.1 Material characterization

Three laboratory Fe-C-V alloys with increasing carbon content were produced with a stoichiometric amount of the ternary alloying element V. Al was added to bind the present nitrogen avoiding it from forming nitrides. The carbon increase allows a reliable estimation of the impact of the carbides with variable strength level and to confirm their role in different Fe-C-V alloys. The chemical compositions are given in Table VIII-1.

Table VIII-1: Chemical composition of the used materials in wt%.

Material/Element	C	V	Other
Alloy A	0.100	1.000	200-300 ppm Al
Alloy B	0.190	1.090	
Alloy C	0.286	1.670	

The alloys were cast in a Pfeiffer VSG100 incremental vacuum melting and casting unit under an argon gas atmosphere. The materials were hot rolled till 1.5 mm. An appropriate heat treatment was applied in order to obtain two main conditions; one as quenched (as-Q) state with as little precipitates as possible and one quenched and tempered (Q&T) state where free carbon is enabled to precipitate with V during tempering. Temperature vs. time graph of the used heat treatment is presented in Figure VIII-1. All materials were austenitized at 1250°C for 10 minutes to obtain a fully austenitic microstructure and to dissolve the carbides from the processing. These materials were then quenched in brine (7wt% NaCl) to obtain a fully martensitic structure. This condition will further be referred to as as-Q (Figure VIII-1 (a)).

Next to the as-Q condition, a second condition was prepared by tempering the quenched material at a certain temperature for one hour to generate, in a controlled way, V carbides, followed again by brine quenching (Figure VIII-1 (b)). Tempering was performed at different temperatures to determine at which temperature the secondary hardening effect, due to the generation of small V_4C_3, was most outspoken.

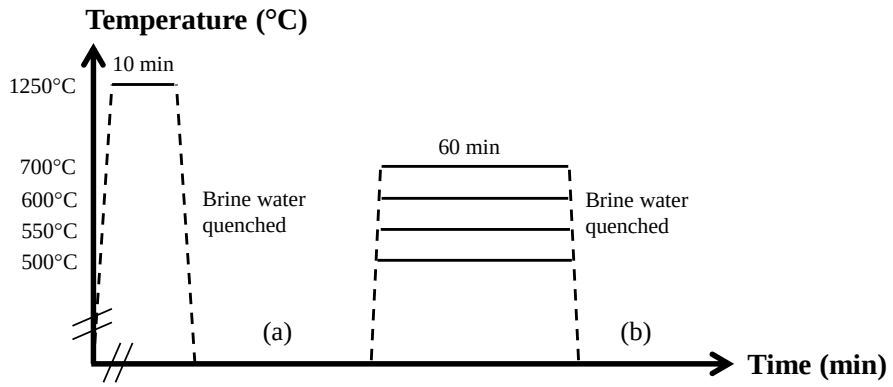

Figure VIII-1: Temperature-time graph of the heat treatments to induce: (a) as-Q, (b) Q&T condition.

All materials were further ground and tensile samples were machined with their tensile axis parallel to the rolling direction and the specimen geometry is shown in Figure VIII-2. Finally, the surface of the samples was sandblasted to remove possible oxides remaining from processing. The hardness and microstructure were investigated as described in Chapter V section V.2.1.

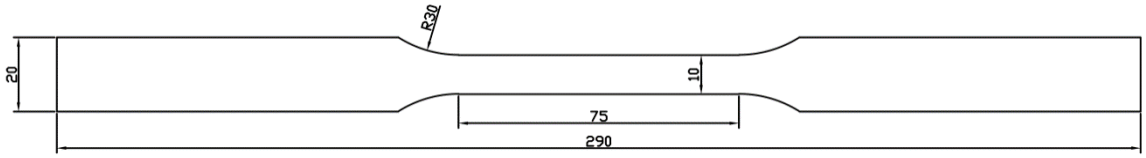

Figure VIII-2: Tensile sample geometry in mm.

VIII.2.2 Hydrogen induced mechanical degradation

The hydrogen induced ductility loss was determined by comparing tensile tests performed in air with tests done on hydrogen saturated samples. Hydrogen was introduced in the materials by electrochemical pre-charging using a 1g/L thiourea in a 0.5 M H_2SO_4 solution at a current density of 0.8 mA/cm² for 1 hour, while in-situ charging continued during the tensile test. The conditions were chosen in such a way that they did not create blisters or any internal damage and based on the results on Fe-C-Ti materials (cf. Chapter V). The tensile tests were performed as described in Chapter V section V.2.2.

VIII.2.3 Determination of the hydrogen/material interaction

The hydrogen content was measured as defined in Chapter V section V.2.3, while TDS measurements were performed to determine the hydrogen trapping ability as explained in Chapter V section V.2.4. The hydrogen diffusion coefficient was determined as described in Chapter V section V.2.5.

VIII.3 Material characterization

Material characterization was started by measuring the hardness of the samples in order to determine at which temperature the secondary hardening effect was most efficient. These results are presented in Figure VIII-3. A distinct secondary hardening peak can clearly be observed after tempering at 600°C, which can be attributed to the precipitation of small V_4C_3 particles. These results are in good agreement with the findings of Speich on similar alloys [2].

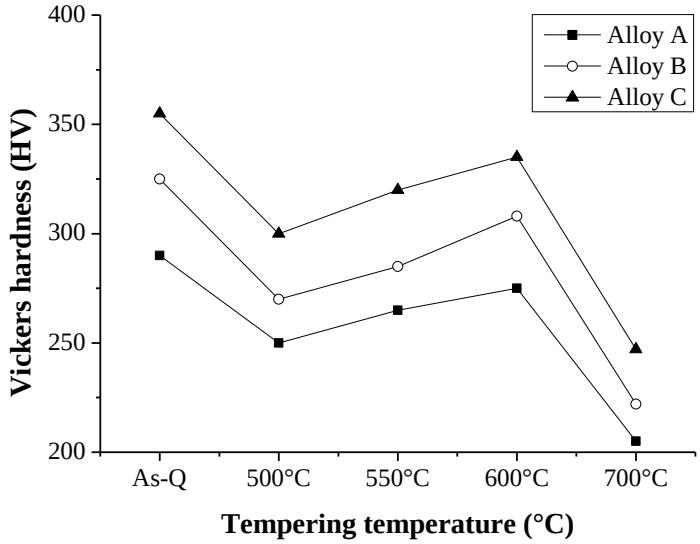

Figure VIII-3: Hardness vs. tempering temperature evolution for the three Fe-C-V alloys.

Similar HV differences were detected between the three alloys in the as-Q state due to the increased carbon content. When calculating the amount of dissolved carbon at an austenitization temperature of 1250°C for these stoichiometric compositions according to the solubility product for V_4C_3 [19], all carbon is found to be dissolved in the as quenched condition for alloy A, B and C, which accounts for the similar differences in hardness. These conclusions were based on the thermodynamical calculations to determine the amount of dissolved carbon based on Eq. VIII-1, and illustrated in Figure VIII-4.

$$log_{10} \frac{M^m X^n}{MX} = -\frac{A}{T} + B \qquad \text{(VIII-1)}$$

Where, M_mX_n is V_4C_3, M and X the alloy contents (wt%), T the temperature (K) and A and B constants of the solubility product and for V_4C_3 equal to 8000 and 5.36 respectively according to Ashby [19].

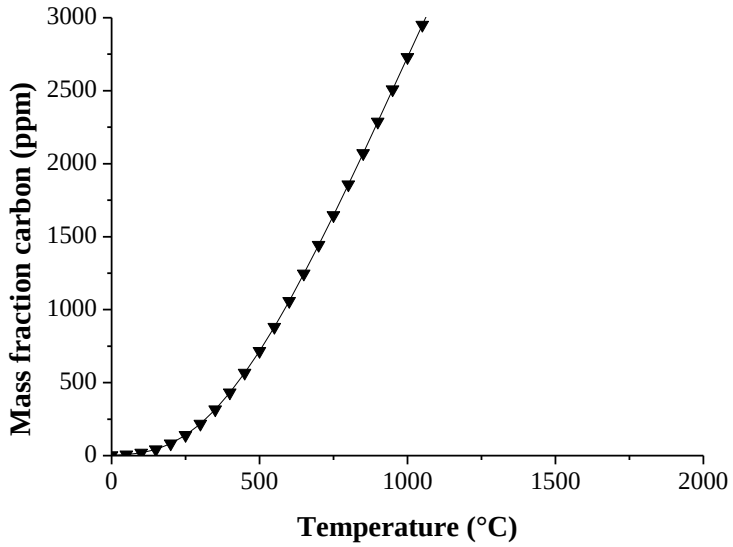

Figure VIII-4: Mass fraction of carbon (ppm) vs. temperature (°C) that can be kept in solid solution at each temperature for stoichiometric total contents of C and V.

The LOM images are shown in Figure VIII-5 for the as-Q and the Q&T condition for materials tempered at 600°C. A martensitic matrix can be observed and in-depth HRSEM and HRTEM analysis were performed to characterize the precipitates. Results are shown for alloy C. TEM bright field images of thin foils are depicted in Figure VIII-6 and a line scan to determine the elemental composition was also taken in order to proof V based particles are indeed present in the microstructure.

LOM	Alloy A	Alloy B	Alloy C
As-Q	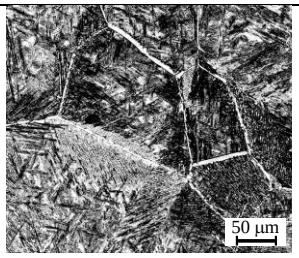	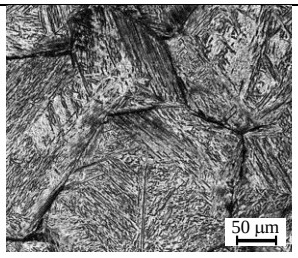	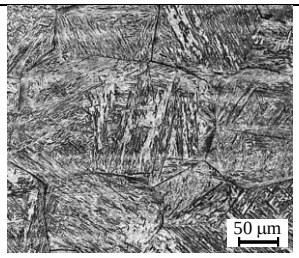
Q&T	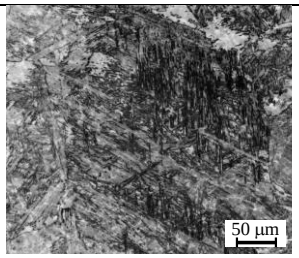	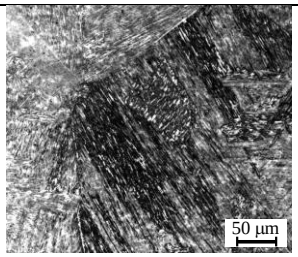	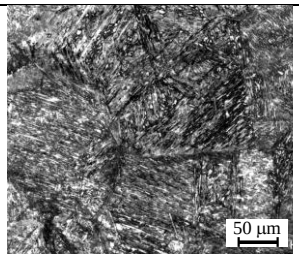

Figure VIII-5: LOM images of alloy A, B and C in the as-Q and Q&T condition.

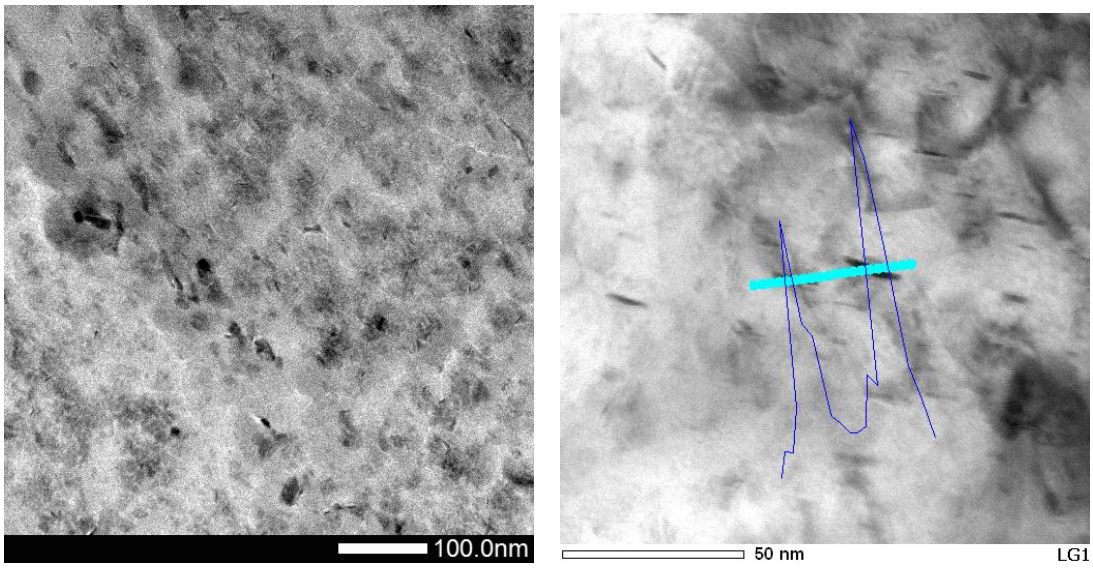

Figure VIII-6: TEM bright field images of alloy C Q&T with an elemental line scan analysis (V content in dark blue)

Additionally, a diffraction pattern was taken from a selected area in the bright field image, shown in Figure VIII-7 (a), to determine the carbide morphology. The selected area diffraction pattern is presented in Figure VIII-7 (b) and revealed the existence of the V_4C_3 face centered cubic crystal structure with a zone axis along [001]. The corresponding directions of the diffraction spots are designated in the diffraction pattern as well. Dark field images were recorded using the diffraction spots circled in black to confirm V_4C_3 were present. Carbides indicated as ‘a’, ‘b’ and ‘c’ are depicted in both the bright field and dark field images.

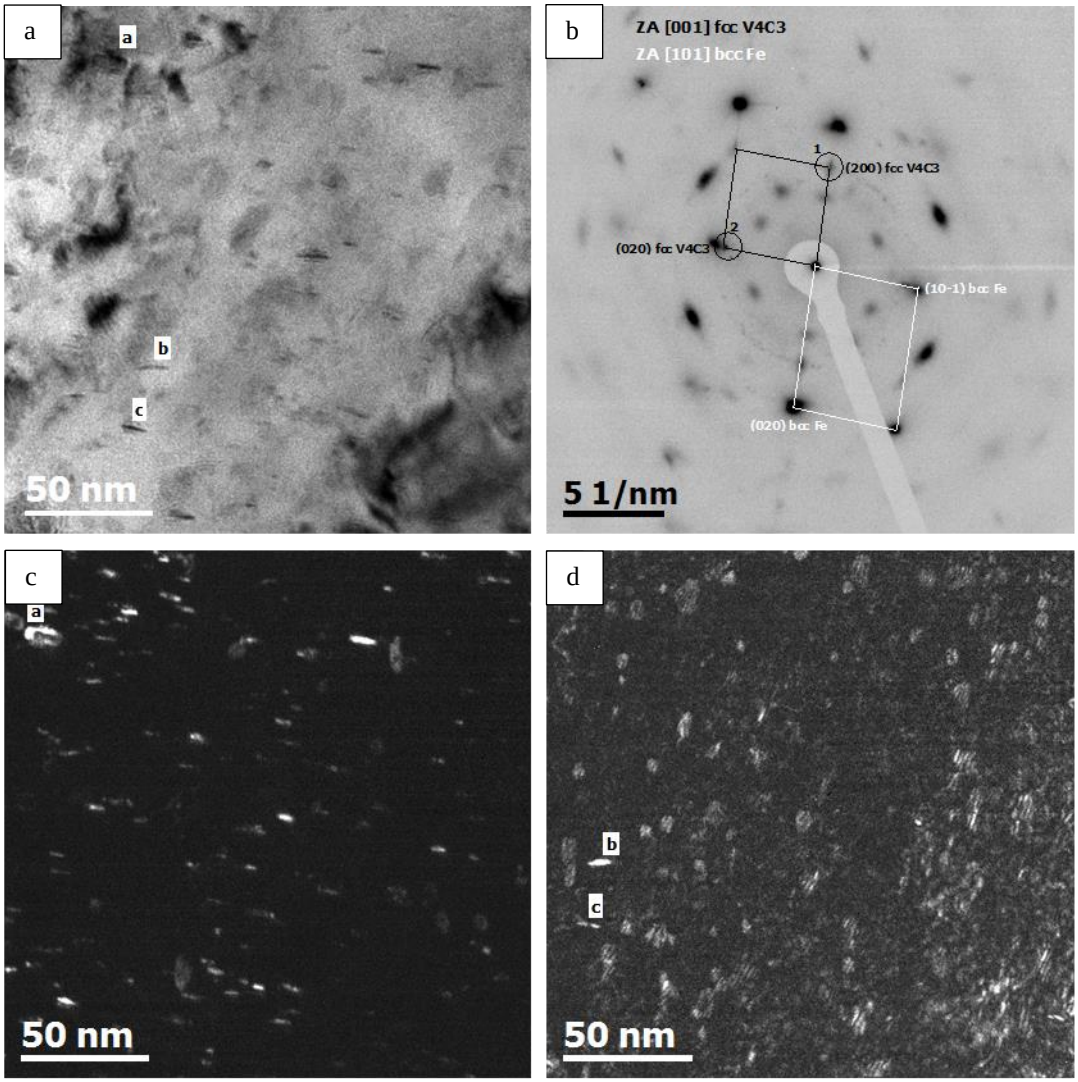

Figure VIII-7: TEM bright field image of alloy C Q&T (a), of which a selected area diffraction pattern was taken and presented in (b). The fcc crystal structure of V_4C_3 is shown in black with a zone axis along [001], while the bcc iron crystal structure is indicated in white with a zone axis along [101]. The dark field images (c) and (d) were taken from the corresponding diffraction spots (1) and (2) indicated by the black circles in (b).

VIII.4 Hydrogen induced mechanical degradation

The tensile test results performed on both uncharged and hydrogen charged samples are presented in Figure VIII-8 and summarized in Table VIII-2. The hydrogen charged stress-strain curves are shown in bold and two main conditions, i.e. as-Q vs Q&T, are compared for each alloy.

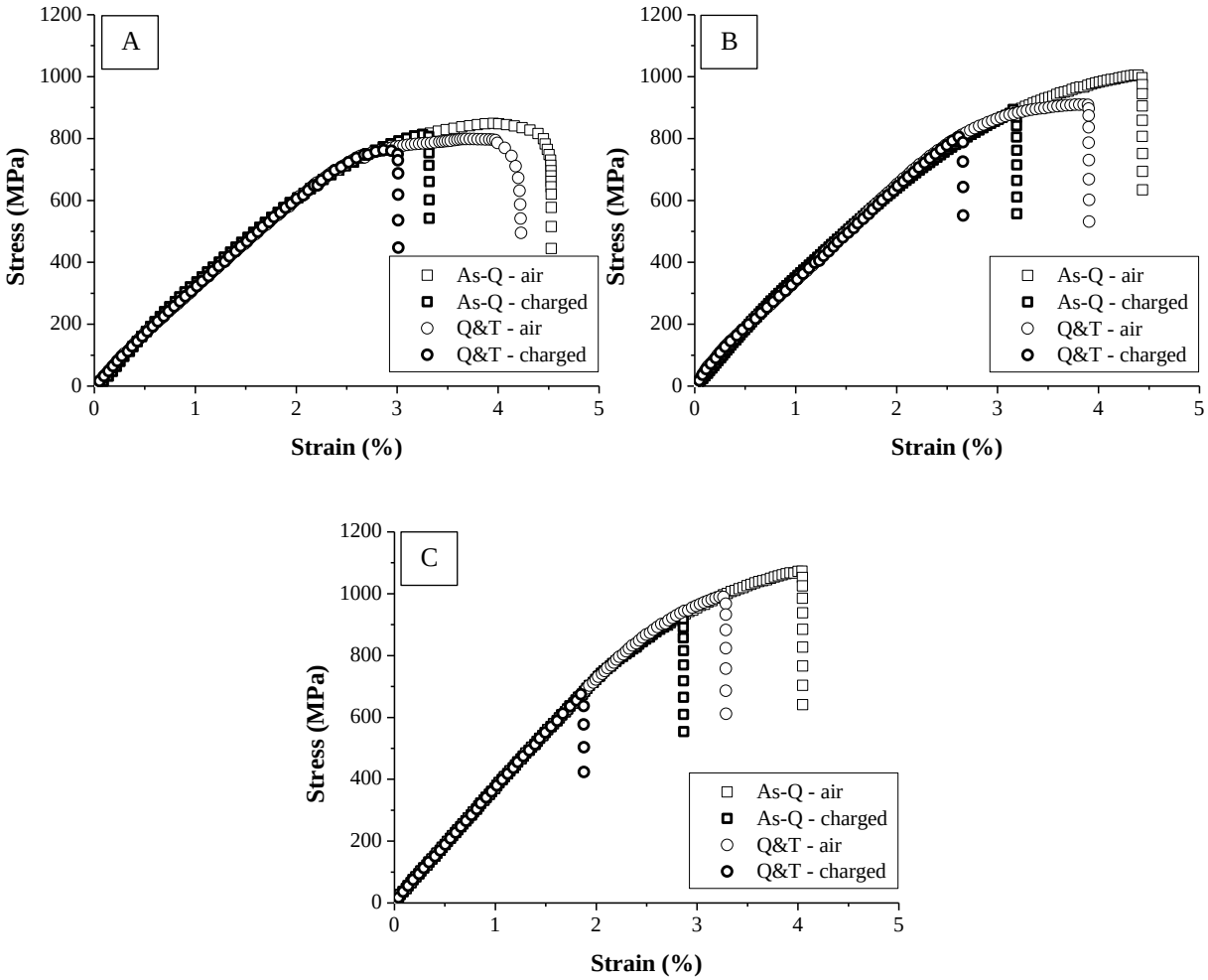

Figure VIII-8: Stress-strain curves of alloy A, B and C in the as-Q and Q&T condition.

Table VIII-2: Summary of the mechanical properties.

Mechanical properties	**Alloy A**		**Alloy B**		**Alloy C**	
	As-Q	Q&T	As-Q	Q&T	As-Q	Q&T
Tensile strength (MPa)	850	800	1000	908	1070	990
%HE	26	29	28	32	29	43

The strength level increased for alloy A → B → C and although tempering induced a secondary hardening effect due to the precipitation of V_4C_3, a decrease of the tensile strength can be observed. This is in good agreement with the hardness measurements (cf. Figure VIII-3). For both conditions the increase can be linked to the higher amount of carbon content [2].

A rather similar hydrogen induced ductility loss was observed for all as-Q materials, whereas tempering slightly decreased the resistance against HE for all alloys. The degree of HE% also slightly increased for alloy A – B –

C. Unfortunately, despite the confirmed presence of V_4C_3 precipitates, the response to hydrogen charging did not improve. It is definitely remarkable that the actual strain at fracture was rather low for these alloys and the tensile specimen of the Q&T condition for alloy B and C already broke in the elastic region of the stress-strain curve. Consequently, an in-depth look into the hydrogen related characteristics of these materials is needed to further elaborate these observations.

VIII.5 Hydrogen uptake and trapping capacity

The amount of diffusible and total hydrogen was determined by hot/melt extraction after hydrogen charging under the same conditions as the tensile tests. These results are presented in Figure VIII-9. The temper induced V_4C_3 precipitates were able to trap a lot of hydrogen. The amount of hydrogen increased for alloy A – B – C in the as-Q condition, which was attributed to the higher carbon content [20] [21] [22]. The increase when the materials were tempered was consistently higher when more carbides had precipitated, i.e. thus increasing for alloy A – B – C (cf. Table VIII-1).

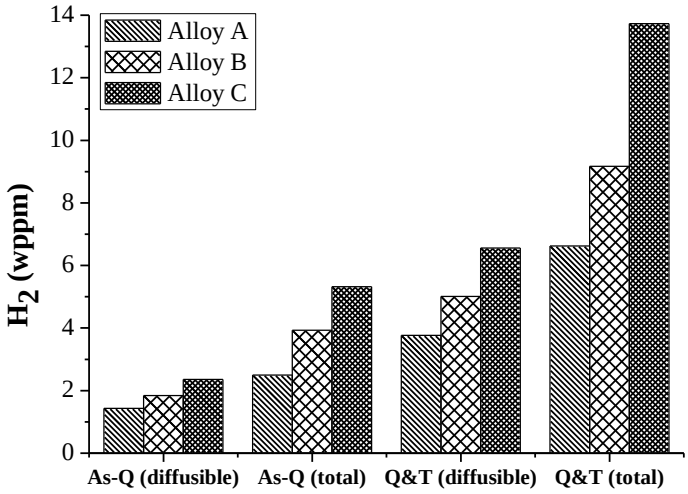

Figure VIII-9: The total and diffusible amount of hydrogen after electrochemical charging for alloy A, B and C in the as-Q and Q&T condition.

These results correspond nicely to the obtained degrees of the hydrogen induced mechanical degradation as the HE susceptibility increased for alloy A –B – C. Additionally, tempering resulted in an increased sensitivity to HE and an increased hydrogen saturation level as seen by the hot/melt extraction results.

A noteworthy observation from Figure VIII-9 is the relatively high amount of hydrogen for alloy C in the Q&T condition. To verify whether internal damage had occurred during hydrogen charging, an additional test was performed, i.e. a tensile test was performed after discharging a charged tensile specimen for 72 hours in vacuum. This result is shown in Figure VIII-10. A clear though not complete ductility recovery was obtained for the Q&T material, which indicated that some hydrogen-related detrimental effect is still active. This will be further elaborated in section VIII-7.

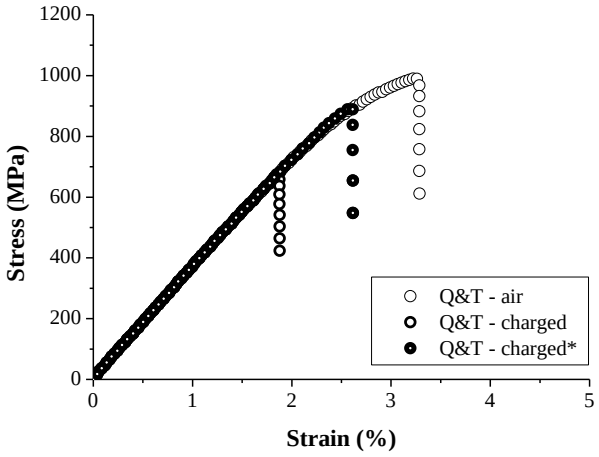

Figure VIII-10: Stress-strain curves of alloy C in the Q&T condition (cf. Figure VIII-8), both uncharged and charged, together with the test performed after hydrogen charging and subsequently 72 hours of vacuum (charged*).

In order to determine the hydrogen trapping sites and identify the specific microstructural constituent, TDS measurements were done for all alloys. These results are presented in Figure VIII-11 and the corresponding activation energies for the different peaks are summarized in Table VIII-3.

TDS	As-Q	Q&T
Alloy A	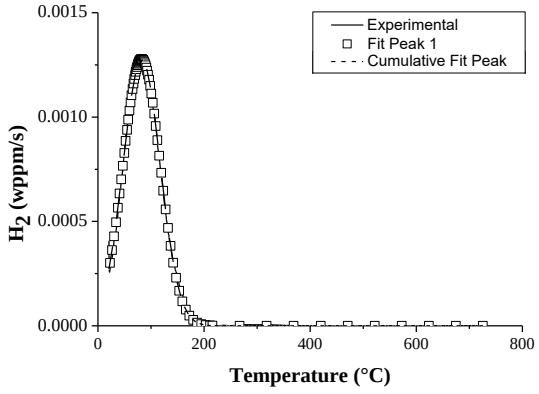	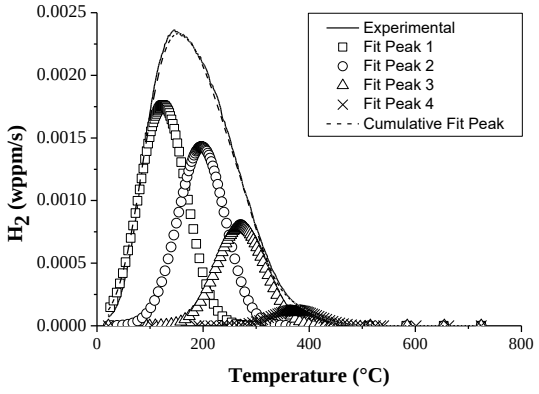
Alloy B	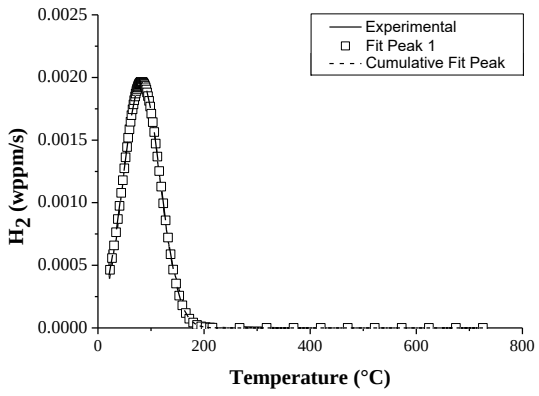	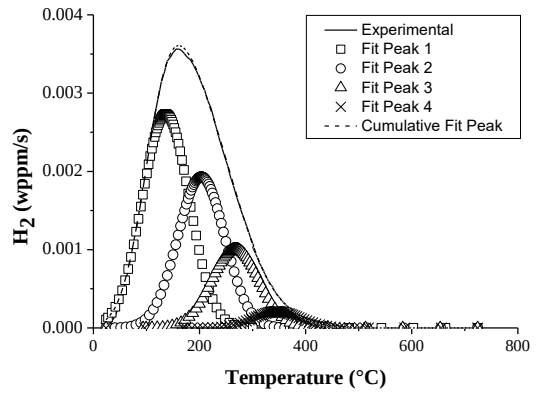

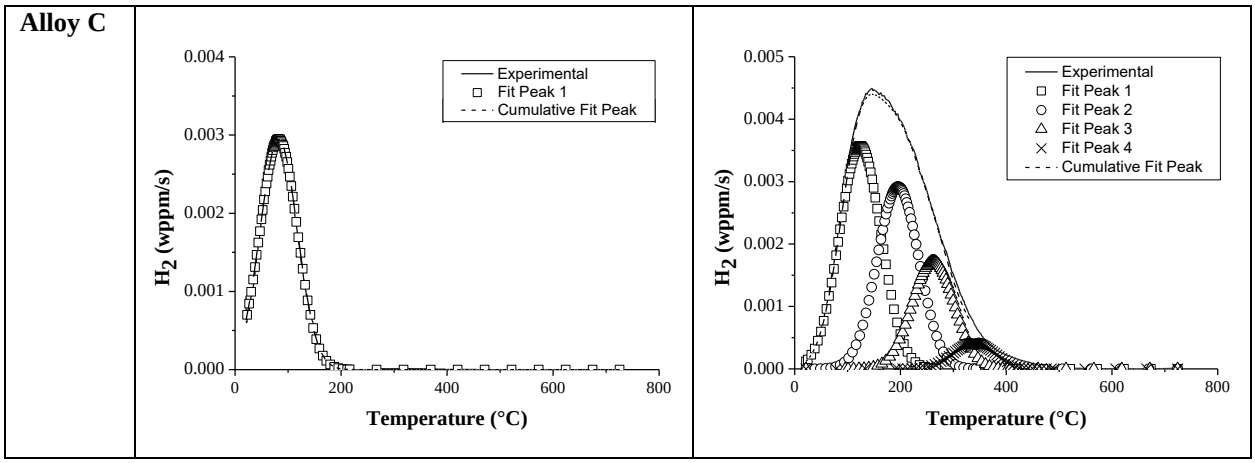

Figure VIII-11: TDS spectra for alloy A, B and C in the as-Q and Q&T condition at a heating rate of 600°C/h.

Table VIII-3: Summary of the corresponding activation energies for the deconvoluted peaks.

Activation energy (kJ/mol	Alloy A		Alloy B		Alloy C	
	As-Q	Q&T	As-Q	Q&T	As-Q	Q&T
Peak 1	26	30	27	31	28	33
Peak 2	/	52	/	52	/	53
Peak 3	/	55	/	58	/	57
Peak 4	/	67	/	65	/	62

The TDS spectra clearly revealed differences in trapping sites before and after tempering. When V_4C_3 precipitates were induced by tempering, extra peaks were obtained compared to the as-Q condition, which were therefore associated with the presence of these carbides. Moreover, the Q&T condition contained a lot more hydrogen compared to the as-Q state, which was already clear from the hot/melt extraction results (cf. Figure VIII-9) and is confirmed here.

One peak was detected for the as-Q condition for all alloys. This peak corresponded to an activation energy of about 26-28 kJ/mol, which can be related to hydrogen trapped at martensitic lath boundaries [23]. However, hydrogen trapped at dislocations has an E_a in the same range [3] [16] [24] [25], but Pérez Escobar *et al.* [26] demonstrated that hydrogen trapped by dislocations mostly left the sample before the TDS measurement started. Although a distinction between dislocations and lath boundaries could not be established based on the activation energies, the first peak is supposed to be mainly associated to hydrogen trapped at martensitic lath boundaries. Furthermore, the increasing amount of hydrogen detected for alloy A → B → C was in good agreement to the hot/melt extraction results (cf. Figure VIII-9).

The Q&T materials all showed broad desorption spectra and were deconvoluted into four peaks. The first represented again hydrogen mainly trapped at martensite lath boundaries with an E_a of about 30-33 kJ/mol, similarly as above. Three additional peaks were present in the Q&T condition, which were attributed to hydrogen trapped at the tempered induced V_4C_3 precipitates. Both the interface between carbide and matrix and the carbon vacancies in the V_4C_3 precipitate can act as a trapping site [16], which will be further elaborated. The activation energies varied from 52-67 kJ/mol. These were higher compared to the E_a determined for hydrogen trapped at vanadium carbides by Asahi *et al.* [9]. Moreover, the 4th peak showed an E_a higher than 60 kJ/mol,

which was therefore correlated to irreversibly trapped hydrogen according to the definition of reversible/irreversible hydrogen proposed by Dadfarnia *et al.* [10]. In addition, the evolution of the amount of detected hydrogen corresponded nicely to the hot/melt extraction results (cf. Figure VIII-9).

It is worth mentioning that the first peak in the Q&T material, associated with hydrogen at lath boundaries, was a little higher compared to the as-Q sample for all alloys. As the dislocation density generally decreases with tempering and dislocations were not likely to have a large contribution to this peak, dislocations cannot explain this increased peak height. Since some hydrogen is able to leave the sample ahead of the TDS measurement, this difference can be attributed to a change in hydrogen diffusivity for the Q&T samples as carbides are reported to decrease the hydrogen mobility in steels [20] [22] [27] [28] [29] [30]. Therefore, hydrogen permeation tests were performed to determine the hydrogen diffusion coefficients. These results are shown in Figure VIII-12 and the corresponding diffusion coefficients were 8.53 x 10^{-11} and 1.16 x 10^{-12} m^2/s for the as-Q and Q&T material, respectively. This confirmed that more hydrogen could leave the sample for the as-Q condition. V_4C_3 precipitates present after tempering lowered the hydrogen diffusivity, and consequently more hydrogen remained at the lath boundaries at the start of the TDS measurement which explained the slightly higher first peak for the Q&T materials.

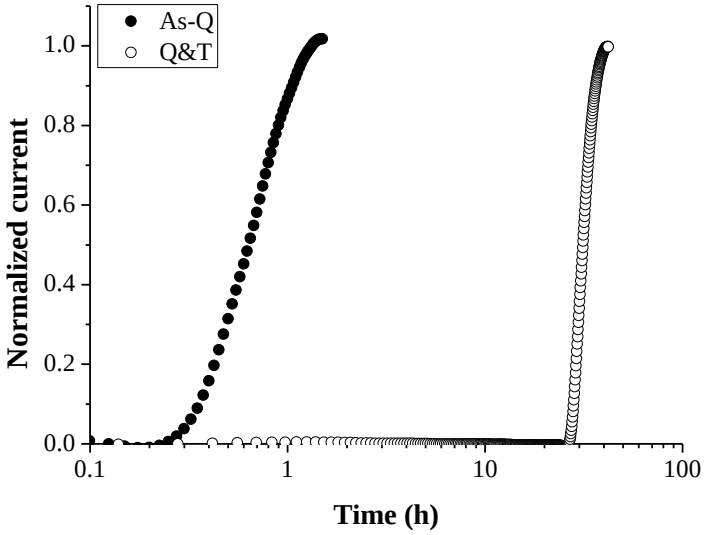

Figure VIII-12: Hydrogen permeation curves of alloy C in the as-Q and Q&T condition.

The as-Q samples contained less hydrogen compared to the Q&T materials as determined by hot/melt extraction and confirmed by TDS (cf. Figure VIII-9 and VIII-11). Although tempering induced V_4C_3 precipitates which were able to trap a significant amount of hydrogen, the hydrogen embrittlement susceptibility increased when the materials got tempered. Therefore, the degree of HE can be correlated to some extent to the amount of charged hydrogen. However, an important difference has to be noted for these hydrogen determination techniques. Hot/melt extraction differs from TDS analysis as one hour is needed before the TDS measurement to guarantee a low pressure in the analysis chamber. During this hour, the pressure is continuously lowered and a certain amount of hydrogen is released from the material and thus no longer present in the TDS spectra. This type of hydrogen will be further referred to as mobile hydrogen, similarly as defined in previous chapters. The amount of diffusible hydrogen, determined by hot extraction, and the integrated hydrogen content under the TDS peaks together with the calculated amount of mobile hydrogen are summarized in Table VIII-4.

Table VIII-4: Summary of the hydrogen contents for alloy A, B and C in the as-Q and Q&T condition.

Hydrogen content (wppm)	Alloy A		Alloy B		Alloy C	
	As-Q	Q&T	As-Q	Q&T	As-Q	Q&T
diffusible hydrogen	1.43	3.77	1.84	5.01	2.36	6.56
hydrogen under TDS curves	0.65	2.75	1.00	3.88	1.50	5.28
mobile hydrogen	0.78	1.25	0.84	1.45	0.86	1.75

A link between the HE% and the amount of hydrogen was already proposed when the hot/melt extraction results were discussed. The correlation between the different types of hydrogen and the degree of hydrogen embrittlement was studied in more detail. When plotting the HE% vs. the amount of hydrogen, as presented in Figure VIII-13, the total, diffusible and mobile hydrogen content is considered. R^2-values are added to evaluate the correlations.

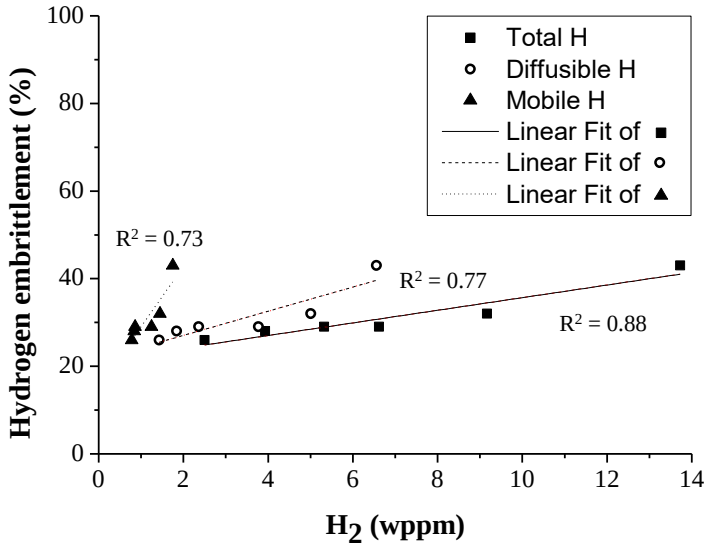

Figure VIII-13: Degree of hydrogen embrittlement vs. different types of hydrogen.

In contrast to what was observed for the Fe-C-Ti, Cr and Mo materials (cf. Chapter V, VI and VII), no better fit was observed when the amount of mobile hydrogen was considered. This type of hydrogen was found to be crucial to explain the observed HE% for the Ti, Cr and Mo alloyed materials. Although a reasonable correlation can be detected between the different types of hydrogen and the degree of HE for the Fe-C-V alloys, this correlation did not improve going from total – diffusible – mobile, on the contrary. Since the mobile hydrogen content is associated with hydrogen trapped by dislocations, and the HELP (hydrogen enhanced local plasticity) mechanism, which implies an increased dislocation mobility due to the presence of hydrogen, is a frequently proposed theory for explaining HE, this might seem a contradiction. However, for the Fe-C-V materials no or hardly any plastic deformation was observed before fracture when charged with hydrogen (cf. Figure VIII-8), meaning that dislocation movement is not active in these materials. Consequently, the mobile hydrogen, associated with hydrogen trapped by dislocations, can be expected to play a at maximum just a minor role in the observed hydrogen induced ductility loss, as opposed to previous results (cf. Chapter V-VI-VII).

The results so far demonstrate therefore a particular interesting observation for the Fe-C-V alloys. The HE differences were correlated with the present amount of hydrogen but mobile hydrogen was not a determining

factor. The V_4C_3 precipitates were apparently able of to trap a significant amount of hydrogen, but their role needs to be further elaborated, which will be done in the next section where the effect of the carbide characteristics on the hydrogen trapping capacity will be discussed.

VIII.6 On the effect of tempering time on carbide size and HE susceptibility

Tempering was applied for two hours instead of one hour to stimulate further carbide growth and hence evaluate the evolution in their hydrogen trapping ability. TDS was performed and results are shown in Figure VIII-14. Additionally, melt extraction was performed as presented in Figure VIII-15. The hydrogen content decreased for all alloys as observed in Figure VIII-15 and out of comparison of Figure VIII-11 and VIII-14. It can be assumed that some carbides have grown too large and were hence not able to trap hydrogen electrochemically due to the high energy barrier to get trapped (cf. Figure I-5). This was also reported by Wei and Tsuzaki [31] and Pérez Escobar *et al.* [32] and is in good agreement to the findings of the Fe-C-Ti alloys. The TDS spectra already offer a confirmation as the fourth peak, associated with irreversibly trapped hydrogen, disappeared in the spectra. Furthermore, the peak area of the second and third peak decreased significantly compared to the materials tempered for one hour (cf. Figure VIII-11). These peaks correspond to hydrogen trapped at the interface between carbides and matrix, but this interfacial area decreased due to the carbide growth.

In order to further clarify the observed TDS peaks with the evolution of the carbide characteristics during tempering, carbide size distributions were made for alloy C in the Q&T 1h and 2h condition. These are presented, together with their corresponding TDS spectrum, in Figure VIII-16.

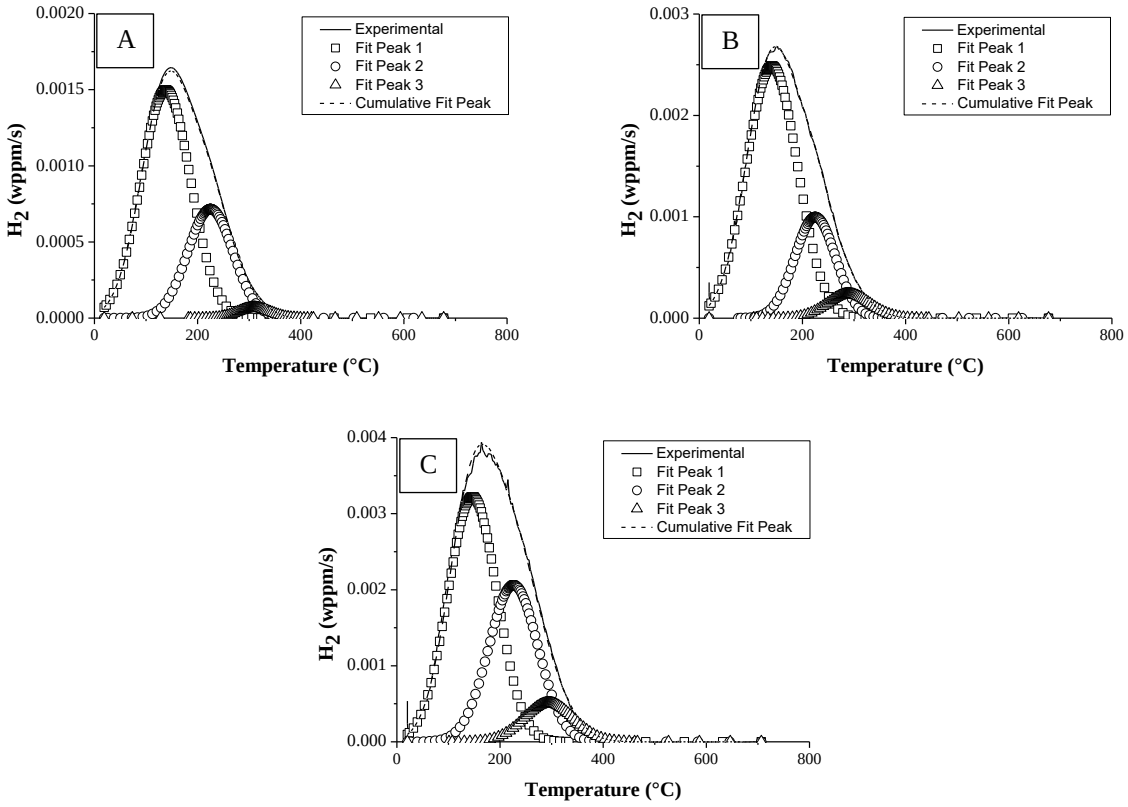

Figure VIII-14: TDS spectra of alloy A, B and C in the Q&T 2h condition at heating rate of 600°C/h.

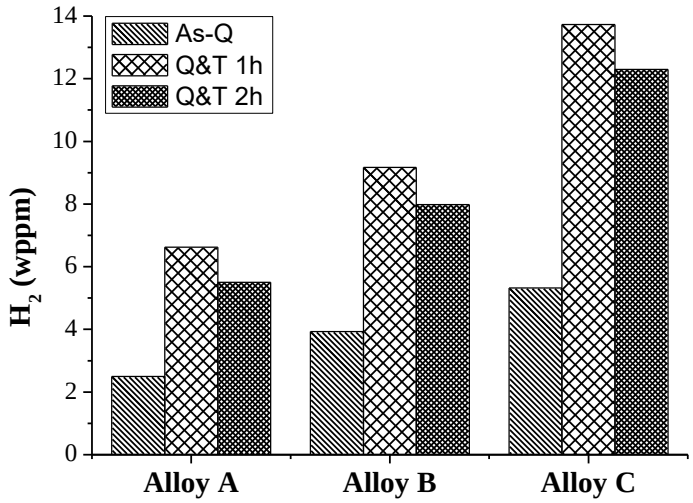

Figure VIII-15: Total hydrogen content for alloy A, B and C in the as-Q, Q&T 1h and Q&T 2h condition.

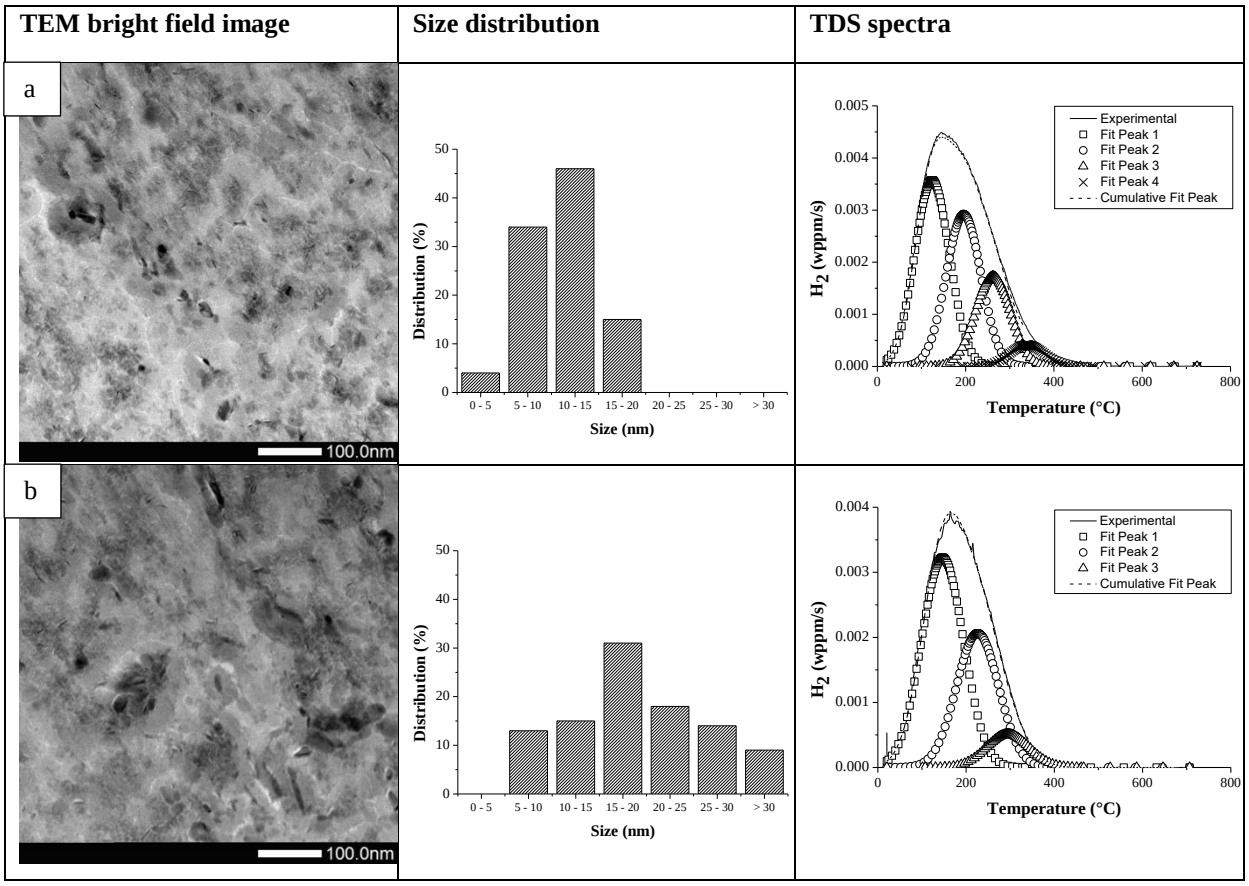

Figure VIII-16: Carbide size distributions together with their corresponding TDS spectrum for alloy C in the Q&T 1h (a) and Q&T 2h (b) condition.

As expected, tempering for two hours resulted in an increase of the carbide sizes as indicated by the size distributions. This was reflected in the TDS spectra since the carbide related peaks decreased in intensity or even disappeared in the case of the 4th peak. When correlating both conditions with each other, the 4th peak might be

related to carbides with sizes smaller than 5 nm since these were only present after one hour of tempering. Furthermore, the amount of detected carbides in the range of 5-20 nm decreased significantly when the alloys were tempered for two hours, which was reflected in the TDS spectra as well. Carbides with sizes above 20 nm were assumed not to play a determinant role in hydrogen trapping. This type of carbides was only present when the material was tempered for two hours, and no corresponding new peak was observed in the TDS spectrum for the 2h tempered material.

A particular interesting observation was made when performing mechanical tests on alloy C Q&T 2h. The corresponding stress-strain curves are shown in Figure VIII-17. Although less hydrogen was measured for this condition (cf. Figure VIII-15), the HE% slightly increased for Q&T 2h (50%) compared to Q&T 1h (43%). Since the first peak in the TDS spectra for both conditions trapped a similar amount of hydrogen, the decreased hydrogen content was attributed to the fact that the V_4C_3 precipitates trapped less hydrogen in the Q&T 2h condition (cf. Figure VIII-16). The decrease in total hydrogen was approximately 1 wppm hydrogen, which was exactly the difference in the amount of trapped hydrogen by the V_4C_3 precipitates, as determined by the area below the corresponding TDS peaks. The carbides formed after for two hours tempering were less effective in terms of trapping hydrogen, resulting in a lower total hydrogen content.
However, the HE% increased when tempered for two hours, which is rather contradictory to the obtained correlations in Figure VIII-13. This might be linked to hydrogen saturated larger carbides in the Q&T 2h material. As described in the section VIII.1 and VIII.5, the empty carbon sites of the V_4C_3 can act as an attractive hydrogen trap site [16]. When the amount of hydrogen exceeds a critical barrier, H_2 might be formed in these vacancies. This might induce cracks in the brittle carbides upon charging. As the carbides in the Q&T 2h condition are bigger, a larger crack length can be provoked. On the other hand, the cracks in the carbides might also be induced when straining is applied. When considering the TDS spectrum, the carbon vacancy hydrogen trap might be included in the 2nd and 3rd TDS peak which remains present as the total volume of the carbdes does not change with tempering time. The decrease of these two carbide related peaks can still be correlated to hydrogen trapped at the interface between carbide and matrix, which still shows a decreasing fraction upon carbide growth. Both trapping sites are thus possible for V_4C_3 and to further investigate this, electron backscatter diffraction analysis should be performed on samples which are tensile tested at intermediate strain levels to evaluate crack initiation and propagation, as done by Laureys *et al.* [33] [34]. First principle calculations based on density functional theory would also allow to verify the exact trapping location of hydrogen at V_4C_3 precipitates on a more theoretical base.

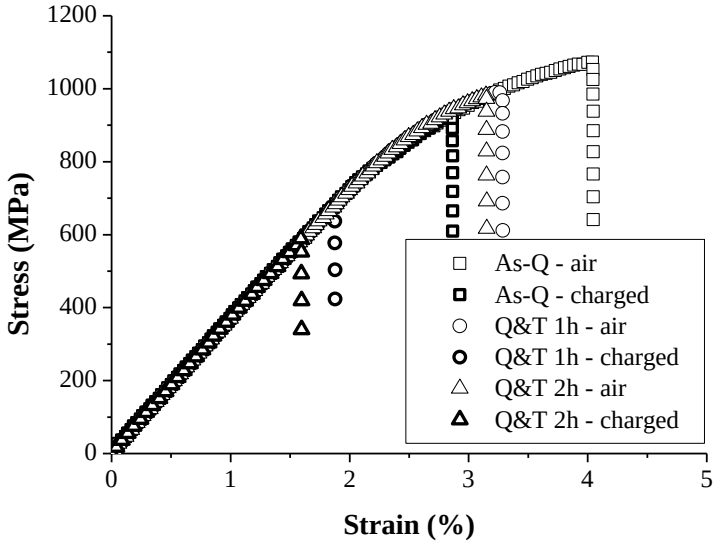

Figure VIII-17: Stress-strain curve for alloy C in the as-Q, Q&T 1h and Q&T 2h condition.

As a conclusion, the trapping ability of the V_4C_3 precipitates is of crucial importance to evaluate the HE sensitivity. The E_a of the carbide related peaks was on the border of reversible and irreversible trapping (cf. Table VIII-3). Moreover, no full ductility recovery was observed when the tensile specimen was left 72 hours in vacuum (cf. Figure VIII-10), meaning that hydrogen still has an effect, which confirms the importance of the total amount of hydrogen. More attention is paid to these issues to understand the role of hydrogen after 72 hours of vacuum in the next section.

VIII.7 On the effect of irreversible hydrogen on the HE degree

When discussing the possible link between the high amount of hydrogen detected for alloy C Q&T and the presence of internal damage after hydrogen charging in section VIII-5, tensile tests were performed on specimens which were discharged for 72 hours in vacuum. The response to HE improved, although no full ductility recovery was obtained. This kind of tensile test was performed on the as-Q material as well and there a full ductility recovery was detected, as presented together in Figure VIII-18.

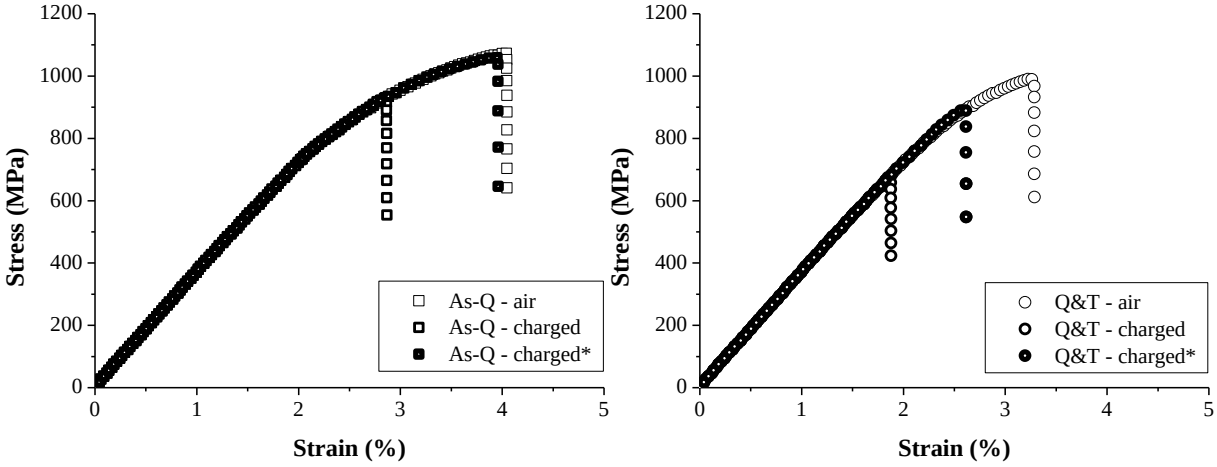

Figure VIII-18: Stress-strain curves of alloy C in the as-Q and Q&T 1h condition, both uncharged and charged, together with the test performed after hydrogen charging and subsequently 72 hours of vacuum (charged*).

In order to interpret these observations, a correlation was made with TDS. These measurements were also performed after 72 hours of vacuum to verify if any hydrogen was still present in the sample for both conditions. Furthermore, this allows to validate the irreversible character of the high temperature peaks of the Q&T material in Figure VIII-11. These results are shown in Figure VIII-19, together with the TDS spectra of the regular TDS measurements, i.e. after one hour of vacuum.

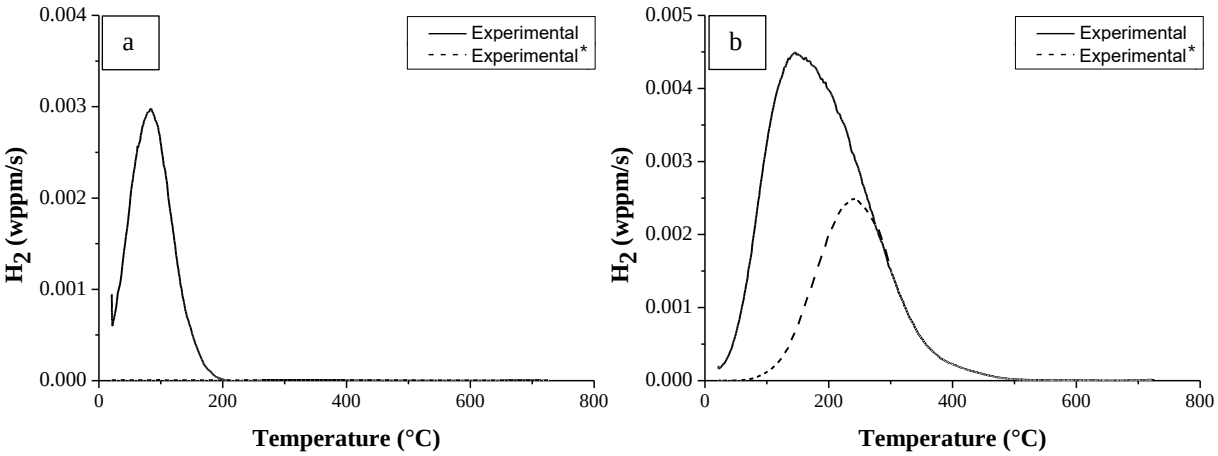

Figure VIII-19: TDS spectra of alloy C in the as-Q (a) and Q&T (b) condition after one hour (experimental) and 72 hours of desorption time in vacuum (experimental*).

No hydrogen was detected after 72 hours of desorption time in the as-Q material, which can be linked to the full ductility recovery as no hydrogen is present anymore in the sample (cf. Figure VIII-18). For the Q&T material, still 1.40 wppm of hydrogen was detected under the higher temperature TDS peaks after 72 hours of desorption time in vacuum. This can be correlated to the corresponding high activation energy of this trap which are in the range of irreversible hydrogen trapping. Moreover, generally irreversibly trapping is associated with E_a higher than 60 kJ/mol. However, in the present case, only the 4th peak showed an E_a > 60 kJ (cf. Table VIII-3), whereas after 72 hours of vacuum still hydrogen was present which was detected in the 2nd and 3rd peak of the regular TDS measurement (cf. Figure VIII-11). These carbide related peak showed an E_a of about 52-58 kJ/mol, which is for these materials assumed to be rather irreversible since hydrogen was still present after 72 hours of vacuum. This indicates that the border of 60 kJ/mol is an arbitrary choice to distinguish reversible vs. irreversible trapping. Moreover, the detected amount of hydrogen is assumed to be partly associated to hydrogen trapped at the carbon vacancies of the V_4C_3 precipitates.

However, although this kind of hydrogen got trapped with a rather high E_a, it still had an impact on the HE susceptibility since no full ductility recovery was obtained for the Q&T materials after 72 hours of discharging. Consequently, the hydrogen trapped by the V_4C_3 precipitates was responsible for the observed loss of ductility. One should take into consideration that this failure occurred in the elastic region of the stress-strain curve, where no dislocation movement was possible. Hence, the amount of reversible hydrogen, which effused from the sample during the 72 hours of discharging, was not able to play a significant role. Therefore, an increase in ductility is observed, confirming the role of reversible hydrogen as no hydrogen was present in the matrix of the material. However, no complete ductility recovery was obtained, which can be correlated to present amount of

hydrogen, assumed to be trapped at the carbon vacancies in the V_4C_3 precipitates. Therefore, crack initiation was linked to the presence of hydrogen at these sites, whereas crack propagation was not influenced by hydrogen as hydrogen from the matrix left the material during the 72 hours of vacuum. Consequently, an intermediate behavior was observed. In the hydrogen saturated sample, both hydrogen trapped by the carbides and hydrogen present in the matrix were able to affect the mechanical behavior. Alternatively, during the tensile test, stresses are developed which might release hydrogen from its trapping site due to the mechanical applied load, resulting in some hydrogen induced ductility loss as well.

To further elaborate on these interpretations, a fracture surface analysis was done by SEM on the Q&T tensile specimens which were hydrogen charged, tested in air and tested after hydrogen charging and subsequently leaving the sample for 72 hours in vacuum. The corresponding fracture surfaces are shown in Figure VIII-20, VIII-21 and VIII-22. The fracture surface of the hydrogen charged specimen showed a brittle cleavage surface with neither any ductile features nor necking (Figure VIII-20). Additionally, some intercrystalline fracture zones can be observed at the edge of the sample. Although only little plastic deformation occurred for test performed in air (cf. Figure VIII-18), some ductile features can be detected at the edges (Figure VIII-21). Moreover, no intercrystalline fracture zones were present without hydrogen charging. When the material was charged with hydrogen and subsequently left for 72 hours in vacuum, a combination of both can be observed since some ductile features can be noticed at the edges together with intercrystalline features in the fracture surface. Since, in the latter, only hydrogen (1.40 wppm) was present with a rather high E_a (Figure VIII-19 (b)), the observed intercrystalline fracture features can be linked to this kind of hydrogen. However, for all conditions, the fracture surface was very brittle, which is in good agreement to the low obtained elongations in the stress-strain curves.

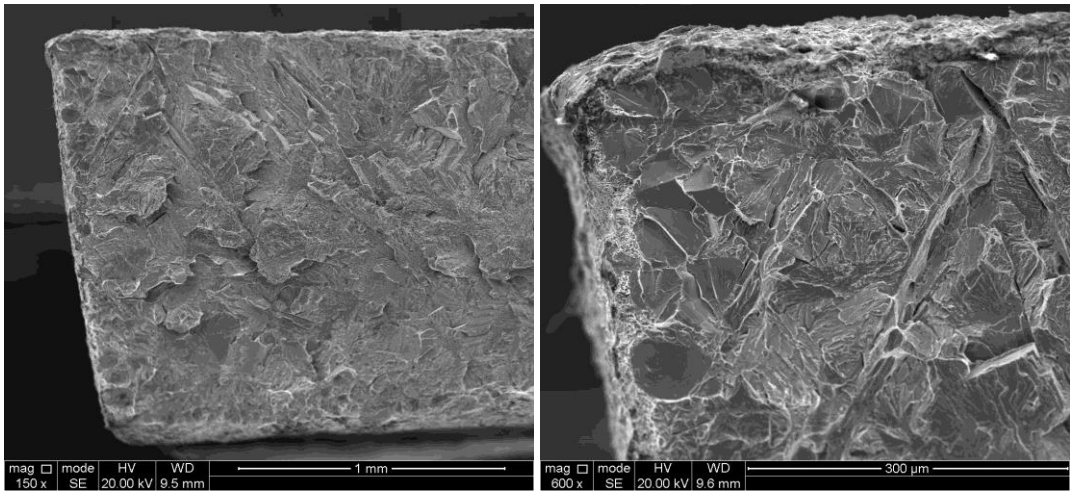

Figure VIII-20: Fracture surface of alloy C Q&T tensile tested in the hydrogen charged condition.

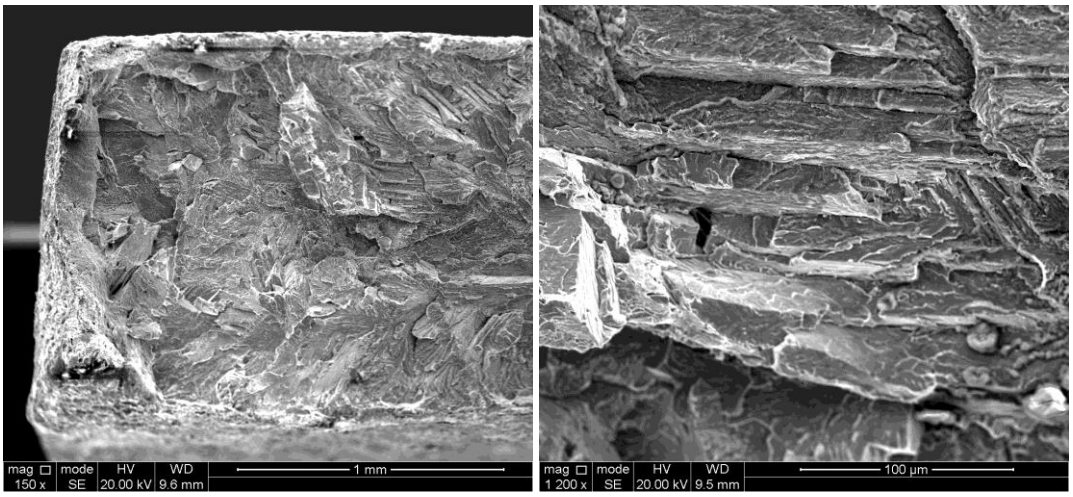

Figure VIII-21: Fracture surface of alloy C Q&T tensile tested in air.

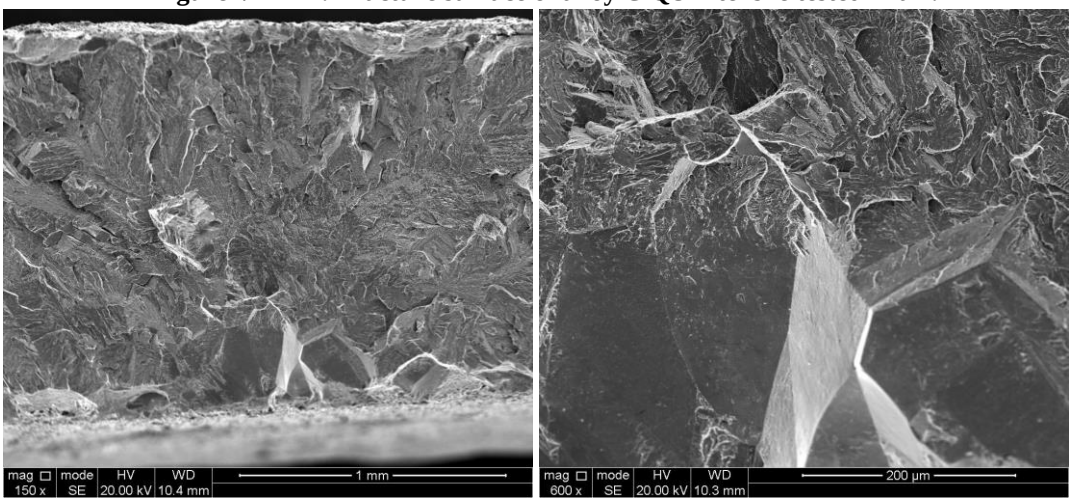

Figure VIII-22: Fracture surface of alloy C Q&T tensile tested after hydrogen charging and subsequently 72 hours of vacuum time.

VIII.8 Conclusion

The impact of V_4C_3 precipitates on the sensitivity to hydrogen embrittlement was evaluated in this work. Two main conditions were compared with each other, i.e. an as-quenched and a quenched and tempered condition in which carbides have precipitated. Tensile tests were performed on both uncharged and hydrogen charged specimen and a correlation with the amount of charged hydrogen was made by hot/melt extraction. The tempered induced carbides trapped a significant amount of hydrogen which explained why the degree of hydrogen embrittlement increases for the quenched and tempered condition. To verify at which trapping sites hydrogen was located, thermal desorption spectroscopy is performed. A considerable amount of hydrogen was trapped in a rather irreversibly way, which still had an effect on the degree of hydrogen embrittlement.

Additionally, a slightly modified temper treatment was applied to vary the carbide size and hence evaluate the impact of the hydrogen induced ductility loss. Hydrogen was trapped at the interface of the carbide and the matrix and at the carbon vacancies in the V_4C_3 precipitates. Carbides with sizes above 20 nm were assumed not to play a determinant role in terms of trapping. The beneficial effect of carbide addition was confirmed as the degree of hydrogen embrittlement increased when less hydrogen was trapped by the carbides.

Furthermore, the samples were kept 72 hours in vacuum to evaluate the irreversible nature of the precipitates. A rather high amount of hydrogen was still detectable by TDS after 72 hours, which was therefore categorized as irreversible hydrogen. This type of hydrogen was available in such a significant amount that it still showed an influence of the HE degree. Moreover, intercrystalline fracture zones were spotted on the fracture surfaces and correlated to the presence of this irreversibly trapped hydrogen.

VIII.9 References

[1] Loidl M, Kolk O, „Hydrogen embrittlement in HSSs limits use in lightweight body," *Advanced Materials and Processes,* vol. 169, pp. 22-25, 2011, BMW Group, Germany.

[2] Speich GR, Leslie WC, „Tempering of steel," *Met Trans,* vol. 3, pp. 1043-1054, 1972.

[3] Wei FG, Hara T, Tsuzaki K, „Precise determination of the activation energy for desorption of hydrogen in two Ti-added steels by a single thermal-desorption spectrum," *Met Mat Trans B,* vol. 35B, pp. 587-597, 2004.

[4] Spencer GL, Duquette DJ, „The role of vanadium carbide traps in reducing the hydrogen embtrittlement susceptibility of high strength alloy steels," US army armament research, development and engineering center, Watervliet, N.Y., 1998.

[5] Yamasaki S, PhD: Modelling precipitation of carbides in martensitic steels, Cambridge, 2004.

[6] Kang HJ, Yoo JS, Park JT, Ahn ST, Kang N, Cho KM, „Effect of nano-carbide formation on hydrogen-delayed fracture for quenching and tempering steels during high-frequency induction heat treatment," *Mat Sci and Eng A,* vol. 543, pp. 6-11, 2012.

[7] Nagao A, Martin ML, Dadfarnia M, Sofronis P, Robertson M, „The effect of nanosized (Ti,Mo)C precipitates on hydrogen embrittlement of tempered lath martensitic steel," *Acta Mat,* vol. 74, pp. 244-254, 2014.

[8] Wei FG, Tsuzaki K, „Hydrogen trapping phenomena in martensitic steels," in *Gaseous HE of materials in energy technologies*, Woodhead, 2012, pp. 493-525.

[9] Asahi H, Hirakami D, Yamasaki S, „Hydrogen trapping behavior in vanadium added steel," *ISIJ Intl,* vol. 43, pp. 527-533, 2003.

[10] Dadfarnia M, Sofronis P, Neeraj T, „Hydrogen interaction with multiple traps: Can it be used to mitigate embrittlement?," *Int Journal of Hydrogen Energy,* vol. 36, pp. 10141-10148, 2011.

[11] Gibala R, Kumnick AJ, „Hydrogen trapping in iron and steels," in *Hydrogen embrittlement and stress corrosion cracking,* American Society for Metals, 1984, pp. 61-77.

[12] Malard B, Remy B, Scott C, Deschamps A, Chêne J, Dieudonné T, Mathon MH, „Hydrogen trapping by VC precipitates and structural defects in a high strength Fe-Mn-C steel studied by small-angle neutron scattering," *Mat Sci and Eng A,* vol. 536, pp. 110-116, 2012.

[13] Zhang CL, Liu YZ, Jiang C, Xiao JF, „Effects of niobium and vanadium on hydrogen-induced delayed fracture in high strength spring steel," *Journal of iron and steel research,* vol. 18, pp. 49-53, 2011.

[14] Raymond L, "Proceedings of the Tri-Services Conference on Corrosion," Orlando, 1985.

[15] Lee J, Lee T, Kwon YJ, Mun DJ, Yoo JY, Lee CS, „Role of Mo/V carbides in hydrogen embrittlement of tempered martensitic steel," *Corros Rev,* 2015.

[16] Pressouyre GM, „Classification of hydrogen traps in steel," *Met Trans A,* vol. 10A, pp. 1571-1573, 1979.

[17] Aoki K, Tanino M, Yawata, „Technical report no. 225, pp. 159-161".

[18] Yoshino Y, *Corrosion,* vol. 38, p. 156, 1982.

[19] Ashby MF, Easterling KE, „A first report on diagrams for grain growth in welds," *Acta Mat,* vol. 30, pp. 1969-1978, 1982.

[20] Hadam U, Zakroczymski T, „Absorption of hydrogen in tensile strained iron and high carbon steel studied by electrochemical permeation and desorption techniques," *Int Journal of Hydrogen Energy,* vol. 34, pp. 2449-2459, 2009.

[21] Pérez Escobar D, Depover T, Wallaert E, Duprez L, Verhaege M, Verbeken K, „Thermal desorption spectroscopy study of the interaction between hydrogen and different microstructural constituents in lab cast Fe-C alloys," *Corrosion Science,* vol. 65, pp. 199-208, 2012.

[22] Depover T, Van den Eeckhout E, Verbeken K, „The impact of hydrogen on the ductility loss of bainitic Fe-C alloys," *Materials Science Technology,* 2016.

[23] Thomas LSR, Li D, Gangloff RP, Scully JR, „Trap-governed hydrogen diffusivity and uptake capacity in ultrahigh strength aermet 100 steel," *Met Mat Trans A,* vol. 33A, pp. 1991-2004, 2002.

[24] Hirth JP, „Effects of Hydrogen on the Properties of Iron and Steel," *Met Trans A,* vol. 11A, pp. 861-890, 1980.

[25] Choo WY, Lee JY, „Thermal analysis of trapped hydrogen in pure iron," *Met Trans A,* vol. 13A, pp. 135-140, 1982.

[26] Pérez Escobar D, Depover T, Wallaert E, Duprez L, Verbeken K, Verhaege M, „Combined thermal desorption spectroscopy, differential scanning calorimetry, scanning electron microscopy and X-ray diffraction study of hydrogen trapping in cold deformed TRIP steel," *Acta Mat,* vol. 60, pp. 2593-2605, 2012.

[27] Hadzipasic AB, Malina J, Malin M, „The influence of microstructure on hydrogen diffusion and embrittlement of multiphase fine-grained steels with increased plasticity and strength," *Chem Biochem Eng Q,* vol. 25, pp. 159-169, 2011.

[28] Luppo MI, Ovejero-Garcia J, „Applicatin of the hydrogen-permeation method to the study of carbide precipitation kinetics in a low-carbon martensite," *Materials Characterization,* vol. 40, pp. 189-196, 1998.

[29] Zakroczymski T, „Adaptation of the electrochemical permeation technique for studying entry, transport and trapping of hydrogen in metals," *Electrochemica Acta,* vol. 51, nr. 11, pp. 2261-2266, 2006.

[30] Kim SJ, Jung HG, Kim KY, „Effect of tensile stress in elastic and plastic range on hydrogen permeation of high-strength steel in sour environment," *Electrochimica Acta ,* vol. 78, pp. 139-146, 2012.

[31] Wei FG, Tsuzaki K, „Hydrogen Absorption of Incoherent TiC Particles in Iron from Environment at High Temperatures," *Met Mat Trans A,* vol. 35A, pp. 3155-3163, 2004.

[32] Pérez Escobar D, Wallaert E, Duprez L, Atrens A, Verbeken K, „Thermal Desorption Spectroscopy Study of the Interaction of Hydrogen with TiC Precipitates," *Met Mater Int,* vol. 19, pp. 741-748, 2013.

[33] Laureys A, Depover T, Petrov R, Verbeken K, „Characterization of hydrogen induced cracking in TRIP-assisted steels," *Int Journal of Hydrogen Energy,* vol. 40, nr. 47, pp. 16901-16912, 2015.

[34] Laureys L, Depover T, Petrov R, Verbeken K, „Microstructural characterization of hydrogen induced cracking in TRIP-assisted steel by EBSD," *Materials Characterization,* vol. 112, pp. 169-179, 2016.

CHAPTER IX

Effect of Ti, Cr, Mo and V based precipitates on the hydrogen trapping and embrittlement of Fe-C-X Q&T alloys*

IX.1 Introduction

Carbides are often mentioned to have a positive effect on the HE susceptibility [1] [2] [3] [4] [5]. Detailed literature studies on Ti, Cr, Mo and V based precipitates were included in the previous chapter (cf. Chapter V, VI, VII and VIII). This PhD work discussed in the previous chapters a set of specifically designed alloys containing carbide forming elements. An in-depth evaluation on the hydrogen/material interactions and the effect of hydrogen on the mechanical properties was presented. However, each chapter focused on one specific type of carbide forming element. The present chapter aims at comparing the different carbides. As creating alloys with the highest possible strength combined with a good ductility is of high relevance from both industrial and scientific point of view, the alloys with the highest strength were selected for all carbide containing materials and are compared in this chapter.

IX.2 Materials and Methods

IX.2.1 Material processing

Four different steel grades with a stoichiometric amount of ternary alloying element X (Table IX-1) were cast and processed. Besides carbon and the alloying element, also some Al was added to bind with N, and as such avoiding nitride formation.

Table IX-1: Chemical compositions of the Fe-C-X materials.

Alloy Fe-C-X	wt.% C	wt.% X	Other elements
Fe-C-Ti	0.313	1.34	Al: 200-300 wt. ppm
Fe-C-Cr	0.184	2.20	Other elements traces
Fe-C-Mo	0.177	2.99	
Fe-C-V	0.286	1.67	

The Fe-C-X alloys were cast and hot rolled as previously discussed. Subsequently, they were austenitized at 1250°C for 10 minutes followed by a brine water quenching. A tempering treatment of one hour was applied to introduce carbides in the martensitic microstructure. Since the size, coherency and distribution of the carbides all determine the degree of secondary hardening [6] and the hydrogen de-trapping energy [7], an appropriate tempering treatment is of key importance. The tempering temperature at which secondary hardening, due to carbide precipitation, was found to be maximal, was 600°C for Fe-C-Ti, Fe-C-Mo and Fe-C-V and 550°C for Fe-

* This chapter is based on the following publication: Depover T, Monbaliu O, Wallaert E, Verbeken K, *International Journal of Hydrogen Energy*, vol. 40, pp. 16977-16984, 2015.

C-Cr [6] [7] [8] (cf. Chapter V, VI, VII and VIII). A distinct secondary hardening peak was observed for the Ti-, Mo- and V-alloys, whereas for Cr-alloy retardation in the otherwise continuous softening as a function of tempering temperature was found. Details were discussed in the corresponding chapters. In this work, alloy C of all Fe-C-X alloys were studied in the as-Q and Q&T condition to compare the difference kind of precipitates.

IX.2.2 Material characterization

The microstructure and composition of the alloys were studied by means of optical microscopy, high resolution scanning electron microscopy (HRSEM) and transmission electron microscopy (TEM). Carbon replica samples and thin foils were used for the last two methods.

IX.2.3 Determination of the hydrogen/material interaction

The hydrogen content was determined as described in Chapter V section V.2.3, while TDS measurements were determined as described in Chapter V section V.2.4. Mechanical characterization was performed as discussed in Chapter V sections V.2.1 and V.2.2.

IX.3 Results and Discussions

IX.3.1 Material characterization

The optical microscopy images are depicted in Figure IX-1. A clear martensitic and Q&T microstructure can be observed. In depth HRSEM and TEM analysis was also performed on all materials in both the as-Q and Q&T condition. TEM bright field images are presented in Figure IX-2, while more microstructural details can be found in the corresponding chapters.

	As-Q	**Q&T**
Fe-C-Ti	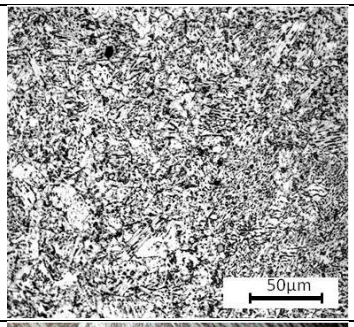	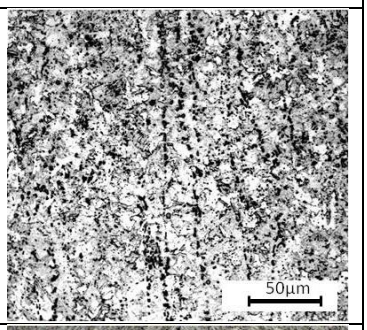
Fe-C-Cr	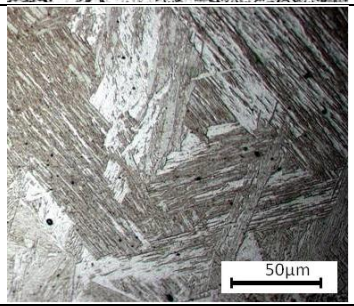	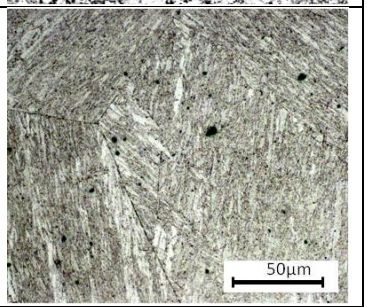

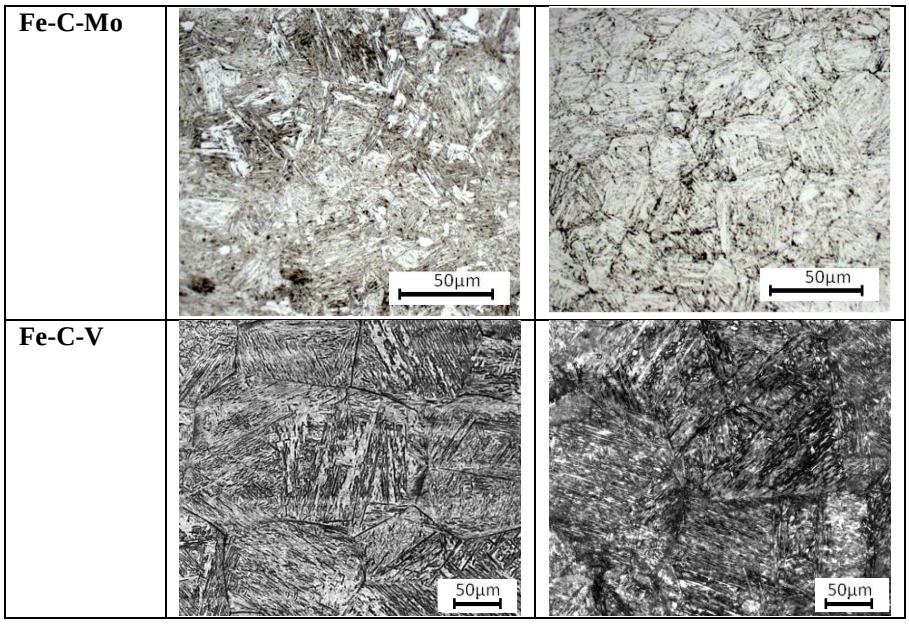

Figure IX-1: Optical microscopy images of the Fe-C-X materials in the as-Q and Q&T condition.

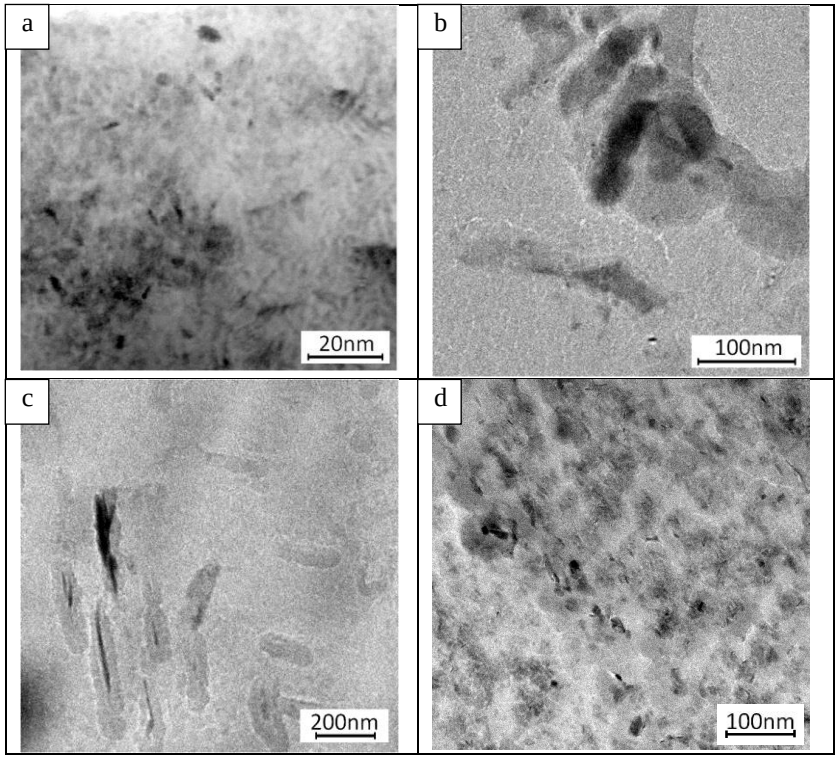

Figure IX-2: TEM bright field images of X-based carbides of the Fe-C-X alloys in Q&T condition, with X = Ti (a), Cr (b), Mo (c) and V (d).

Fe-C-Ti in the as-Q condition contains large carbides of approximately 300-500 nm, which are still present in the Q&T condition. The latter also contains a fine distribution of small TiC of about 2-5 nm as observed in the TEM image. The detected carbides for the Fe-C-Mo alloy show in both conditions a coarse needle-like shape of about 200 nm in length, while smaller ones (< 50 nm) are induced as well (cf. Chapter VII). For Fe-C-Cr, the carbides are rather coarse, resulting in a lower impact on the strength level. Finally, the Fe-C-V material contains no carbides in the as-Q condition, while small V_4C_3 precipitates with sizes below 20 nm are detected when

tempered. It was observed that only for the V-containing material, the carbides appear to be fully dissolved in the as-Q condition. For Fe-C-Ti, Fe-C-Cr and Fe-C-Mo, carbides are still detected in the as-Q condition since the solubility temperature for these materials is above the austenitization temperature of 1250°C [9] [10]. More details on the carbide characteristics and their morphology can be found in the corresponding chapters.

IX.3.2 Determination of the hydrogen content

The results of the hot and melt extraction, which show the diffusible and total hydrogen content of the hydrogen saturated samples, are given in Figure IX-3. Some important differences between the different materials and conditions could be observed.

For the Fe-C-Ti and Fe-C-V materials, the diffusible and total hydrogen content of the charged samples nearly or more than doubled when the sample was tempered. Consequently, the microstructural changes that occurred during tempering, including the formation of a considerable amount of small Ti or V-carbides, provided an important increase in both weak and stronger hydrogen trapping sites in the material. The Mo- and Cr-alloys showed a significantly lower hydrogen content, both diffusible and total, while the amount of diffusible hydrogen was the lowest for the Fe-C-Mo alloy. Moreover, the difference between as-Q and Q&T was also rather small, especially for Fe-C-Cr. Although tempering induced significant changes in the microstructure and therefore, as discussed in the next section, also in the potential trapping sites in the alloy, the total hydrogen trapping capacity of the material appeared to be the same in as-Q and Q&T condition.

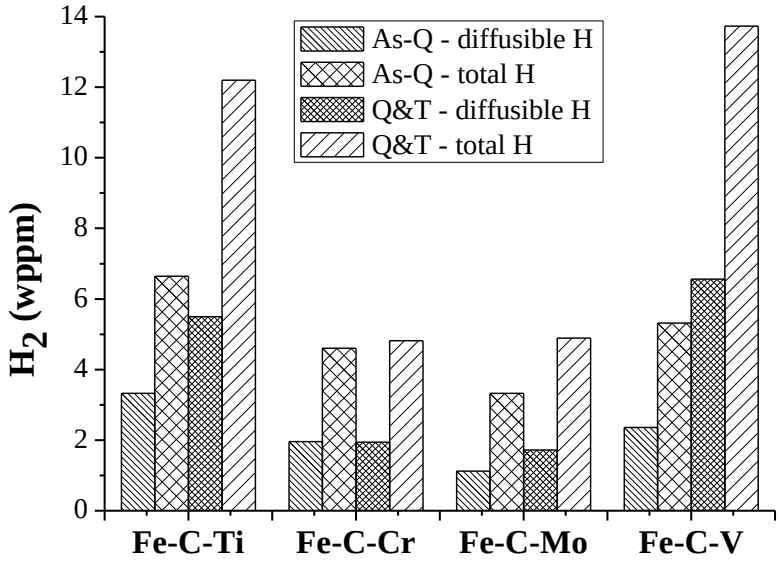

Figure IX-3: Diffusible and total hydrogen content for charged Ti-, Cr-, Mo- and V-alloys in the as-Q and Q&T condition.

IX.3.3 Thermal desorption spectroscopy

TDS measurements were performed on all Fe-C-X materials in both the as-Q and Q&T condition as summarized in Figure IX-4 and an overview of the hydrogen contents for the different measurements is given in Table IX-2. One kind of trap was identified for Fe-C-Ti as-Q with an E_a for detrapping of 33 kJ/mol. As demonstrated in our previous work (cf. Chapter V), this peak and corresponding E_a can be attributed to hydrogen trapped at lath boundaries [11] [12]. The experimental TDS curve of Fe-C-Ti Q&T can be deconvoluted in four peaks, with E_a's

of 48, 53, 47 and 60 kJ/mol, respectively. The first peak can again be attributed to hydrogen trapped at the lath boundaries, whereas the second and the third peak correspond to the values found in literature [7] [11] for hydrogen trapped at (semi-)coherent TiC. The fourth peak can be linked to hydrogen trapped at more irreversible trapping sites [11]. It must also be mentioned that the material also contains other possible traps which do not seem to be available for hydrogen pick-up during charging, such as dislocations. However, as demonstrated by Table IX-2, there is a clear difference between the amount of hydrogen as determined by hot extraction and the total area under the TDS curve. Indeed, hydrogen was able leave the sample before the TDS measurement. As was also demonstrated in our previous work [16], traps such as dislocations indeed trap hydrogen, but loose this hydrogen before the TDS measurement is started. During the tensile tests, this disappearing hydrogen will be very relevant as discussed below.

The TDS curves of Fe-C-Cr as-Q and Q&T can be deconvoluted in two and three peaks, respectively, with E_a's of 25 and 49 kJ/mol for the as-Q condition and 23, 51 and 55 kJ/mol for the Q&T sample. Peak one is again attributed to hydrogen trapped at lath boundaries, whereas peak two and three correspond to hydrogen trapped at the chromium carbides. Although a similar hydrogen pick-up was measured, a higher hydrogen content under the TDS curves was present when the material got tempered as again the features of the traps and their corresponding hydrogen uptake capacity are affected by tempering resulting in a higher hydrogen pick-up in the second TDS peak and a third peak with a higher E_a, which was absent in the as-Q state. Therefore, more hydrogen was able to effuse out of the sample for the as-Q sample during the vacuum time. Consequently, the as-Q material contained more highly mobile hydrogen and tempering resulted in a modification of the trapping behavior.

The TDS spectra for the Fe-C-Mo alloys look quite similar and could both be deconvoluted into three peaks. E_a of 30, 36 and 75 kJ/mol for the as-Q and 27, 34 and 84 kJ/mol for the Q&T grade are calculated for peak one, two and three, respectively. Again, peak one corresponds to hydrogen trapped at lath boundaries while peak two is attributed to reversibly trapped hydrogen by small carbides. Since the third peak has an E_a higher than 60 kJ/mol, it represents hydrogen trapped irreversibly by the molybdenum carbides. However, the as-Q sample contains less hydrogen and consequently, although similar traps are present, a different amount of hydrogen got trapped as the trap characteristics changed during tempering. Additionally, a low and similar amount of hydrogen effused during the hour of vacuum.

The as-Q condition of the Fe-C-V alloy shows one peak, with a corresponding E_a of 28 kJ/mol, which is attributed to hydrogen trapped at lath boundaries. The TDS spectrum of the Q&T condition can be deconvoluted into four peaks, of which the first peak can again be linked to hydrogen at lath boundaries with an E_a of 33 kJ/mol. The three additional peaks are correlated to hydrogen trapped by V-carbides with corresponding E_a of 53, 57 and 62 kJ/mol, which is on the border of reversible/irreversible trapping.

Also no hydrogen was irreversibly trapped up to 600°C. The incoherent carbides do not trap hydrogen during cathodic charging because the energy barrier is too high [7] [13]. A heat treatment at elevated temperature is required for hydrogen to get trapped at these trapping sites. More details on the interpretation of the TDS spectra can be found in the corresponding chapters.

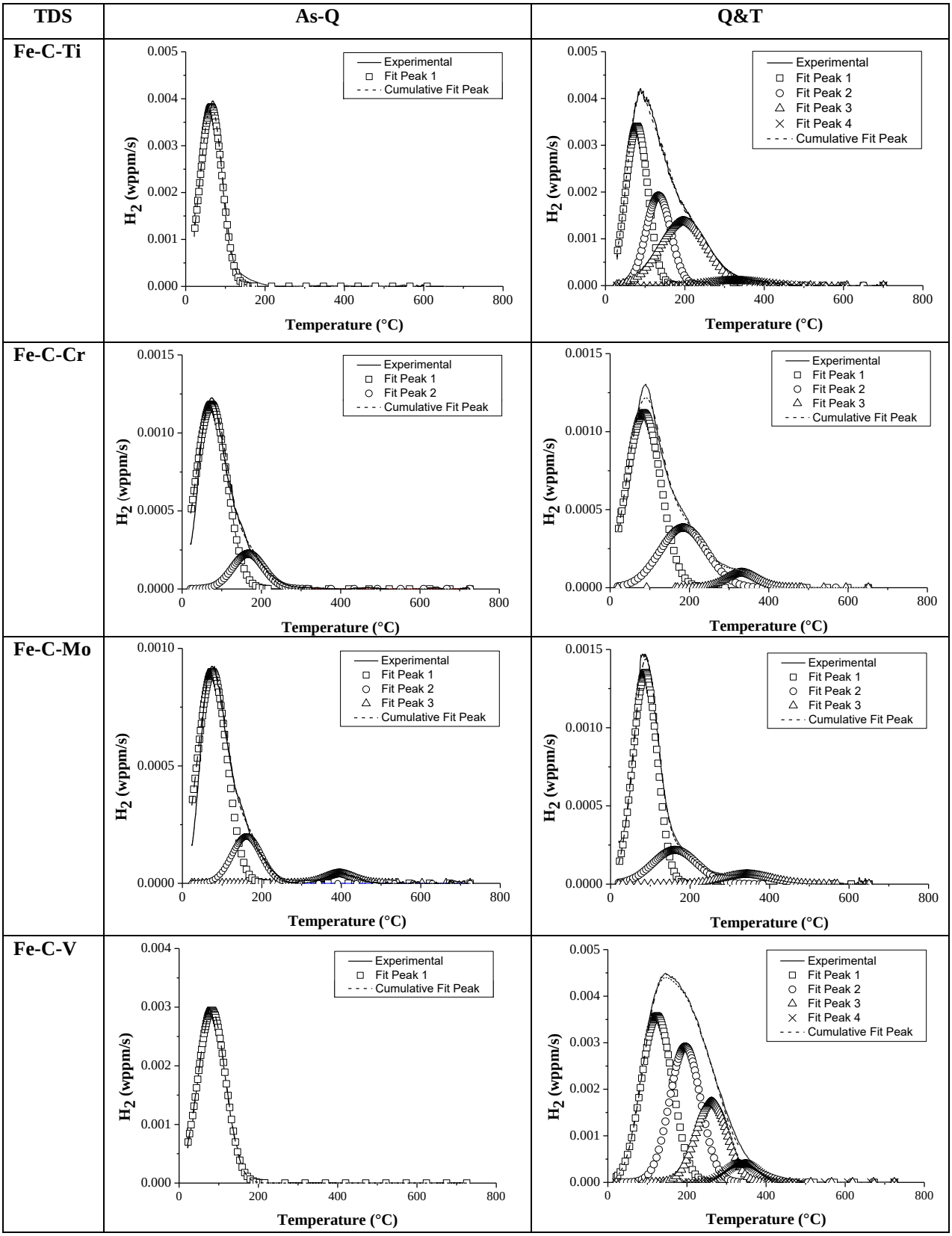

Figure IX-4: TDS curves of Fe-C-X alloys in the as-Q and Q&T condition for tests performed at 600°C/h.

Table IX-2: Summary of the hydrogen contents of the Fe-C-X alloys in the as-Q and Q&T condition.

Hydrogen content (wppm)	Fe-C-Ti		Fe-C-Cr		Fe-C-Mo		Fe-C-V	
	As-Q	Q&T	As-Q	Q&T	As-Q	Q&T	As-Q	Q&T
diffusible hydrogen	3.33	5.50	1.96	1.94	1.12	1.72	2.36	6.56
hydrogen under TDS curves	1.65	3.90	0.80	1.10	0.50	1.17	1.50	5.28
mobile hydrogen	1.68	1.79	1.16	0.89	0.68	0.61	0.86	1.75

IX.3.4 Hydrogen induced mechanical degradation

The stress-strain curves for Ti-, Cr-, Mo- and V-alloy in the as-Q and Q&T condition are depicted in Figure IX-5 and the degree of HE is given in Table IX-3. Tempering leads to an increase in strength level for the Ti- and Mo-alloy, while for the Cr and V grade a decrease was observed, as also noticed by hardness measurements (cf. Chapter V-VIII) [6] [8]. These differences in strength level should be taken into consideration since generally the susceptibility to HE increases with strength level [14] [15]. However, results in the previous chapters showed that this is not always the case since suitable trapping sites might reduce the amount of mobile hydrogen and hence the hydrogen induced ductility loss [1]. A significantly different HE-susceptibility was observed for the four alloys.

The HE-susceptibility is very high for the Fe-C-Ti materials due to the combined effect of a high amount of hydrogen and a low E_a for detrapping. Additionally, both Ti-alloys contained a similar amount of mobile hydrogen. This weakly trapped hydrogen is surely present in the material during the in-situ tensile tests. Moreover, it likely is, at least, partially located near dislocations, as demonstrated elsewhere [16], and therefore could be expected to play an important role during the tensile test. Tempering even increased the HE to 66%. This could be attributed to the small TiC precipitates formed during tempering, which not only increased the hydrogen trapping capacity as compared to the as-Q samples, but also introduced a lot of weakly trapped hydrogen into the material. This was confirmed by hot/melt extraction and TDS measurements, respectively. Consequently, this combined impact had a detrimental effect on the ductility properties of the alloy.

The Cr-alloy as-Q embrittles more than the Q&T material although a similar amount of diffusible hydrogen was measured. However, more mobile hydrogen was present in the as-Q material, which could effuse from the sample before the TDS tests. Just as for the other alloys, there is a clear correlation between the amount of mobile hydrogen and the hydrogen induced ductility loss. The tensile test results for Fe-C-Cr Q&T alloy show a rather low HE. The trapping capacity of the carbides introduced during tempering seems to have a positive effect on the HE resistance since less hydrogen was able to effuse from the material and more was trapped by the carbides.

The Fe-C-Mo alloys show a much better resistance to HE, as almost no ductility loss is observed. First of all, the lower hydrogen content can account for this observation (cf. Table IX-2). Moreover, the amount of mobile hydrogen, which is able to effuse from the sample before the TDS measurement, is the lowest for this grade, underlining again the importance of mobile hydrogen in the hydrogen induced ductility loss. Additionally, the precipitate shape might also have to be taken into account as the diffusion of mobile hydrogen during the tensile test might be hindered by the presence of the randomly distributed needle-shaped carbides, as discussed in Chapter VII. Furthermore, the high energy traps only have a minor effect on the HE%, since only a small amount of hydrogen is trapped irreversibly. Besides, also the Ti-Q&T alloy contains such a high energy trap whereas it embrittled significantly.

The Fe-C-V alloys show rather low strain levels and the hydrogen charged specimen broke in the elastic region of the stress-strain curve. Tempering increased the sensitivity to HE since the degree of hydrogen induced mechanical degradation went from 29 to 43%. The higher amount of hydrogen, trapped by the V-carbides, in the Q&T condition can explain this observation (cf. Figure IX-4 and Table IX-2). Since no or hardly any plastic deformation occurred for these materials, the effect of mobile hydrogen, trapped at dislocations, is assumed to be minimal.

To confirm this hypothesis and to evaluate the relation between the different types of hydrogen (i.e. total, diffusible and mobile) and the HE degree, a linear fitting comparison is applied on these correlations as presented in Figure IX-6. When all materials are included, the correlation improves for total – diffusible – mobile hydrogen, emphasizing the importance of the latter type of hydrogen. Moreover, when the Fe-C-V materials are excluded from the analysis, a relation of 98% between the HE% and the amount of mobile hydrogen is obtained, as presented in Figure IX-6 as well. This confirmed the crucial importance of the amount of hydrogen trapped by dislocations and the enhancement of the dislocation mobility by the presence of hydrogen as proposed by the HELP mechanism.

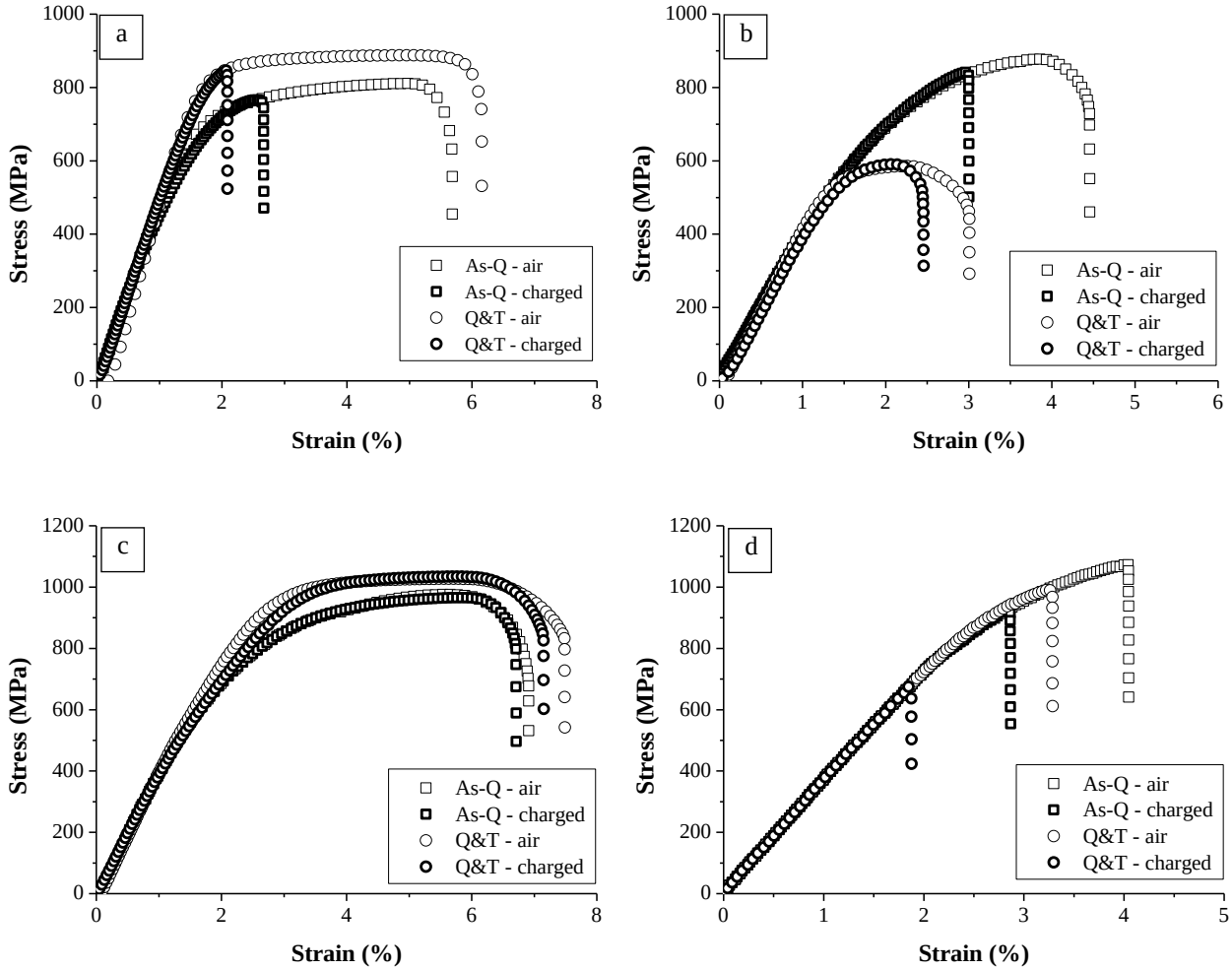

Figure IX-5: Stress-strain curves for (a) Fe-C-Ti, (b) Fe-C-Cr, (c) Fe-C-Mo and (d) Fe-C-V at a cross-head deformation speed of 5 mm/min of uncharged and hydrogen charged specimens.

Table IX-3: Summary of the HE indices (%HE) of Fe-C-X alloys in the as-Q and Q&T conditions.

%HE	Fe-C-Ti		Fe-C-Cr		Fe-C-Mo		Fe-C-V	
	As-Q	Q&T	As-Q	Q&T	As-Q	Q&T	As-Q	Q&T
	53	66	33	18	3	5	29	43

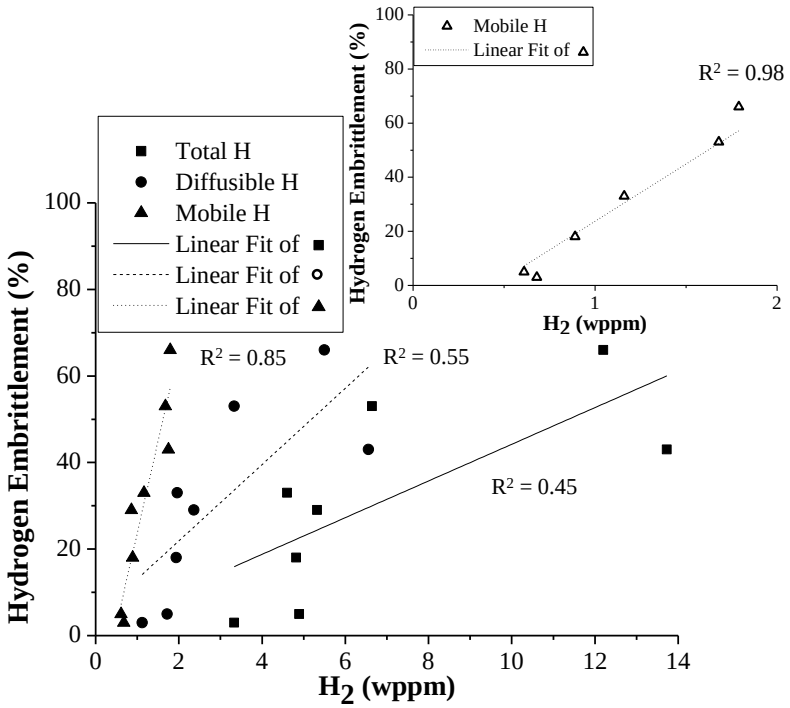

Figure IX-6: Degree of hydrogen embrittlement vs. the total, diffusible and mobile hydrogen content for Fe-C-X alloys. The Fe-C-V materials were excluded from the analysis in the right upper corner.

IX.4 Conclusions

Four lab cast Fe-C-X materials (with X = Ti, Cr, Mo or V) were investigated in both as-Q and Q&T conditions. Tempering was performed to achieve maximal secondary hardening. The effect of the present carbides on the hydrogen trapping and hydrogen induced embrittlement was evaluated. Only when plastic deformation occurred and thus when dislocation mobility was relevant, the amount of mobile hydrogen, associated with hydrogen trapped at the dislocations, plays a determinant role in the induced mechanical degradation. This was nicely illustrated by the clear correlation between the degree of hydrogen embrittlement and the amount of mobile hydrogen.

Additionally, it is worth mentioning that the Q&T condition, in which carbides were induced, often showed a decreased HE-resistance. However, these materials were saturated with hydrogen and mostly contained a higher amount of hydrogen as compared to the as-Q state. When these materials were not fully saturated with hydrogen and when the present carbides had suitable characteristics in terms of trapping, their beneficial effect on the hydrogen induced ductility loss was demonstrated in the different chapters.

IX.5 References

[1] Depover T, Pérez Escobar D, Wallaert E, Zermout Z, Verbeken K, „Effect of in-situ hydrogen charging on the mechanical properties of advanced high strength steels," *Int Journal of Hydrogen Energy,* vol. 39, pp. 4647 4656, 2014.

[2] Duprez L, Verbeken K, Verhaege M, „Effect of hydrogen on the mechanical properties of multiphase high strength steels," in *Proc. of the 2008 Int. Hydrogen Conf.*, Jackson, Wyoming, USA, 2008.

[3] Spencer GL, Duquette DJ, „The role of vanadium carbide traps in reducing the hydrogen embrittlement susceptibility of high strength alloy steels," US Army Armament Research, Development and Engineering Center, N.Y., 1998.

[4] Kang HJ, Yoo JS, Park JT, Ahn ST, Kang N, Cho KM, „Effect of nano-carbide formation on hydrogen-delayed fracture for quenching and tempering steels during high-frequency induction heat treatment," *Mat Sci and Eng A,* vol. 543, pp. 6-11, 2012.

[5] Nagao A, Martin ML, Dadfarnia M, Sofronis P, Robertson M, „The effect of nanosized (Ti,Mo)C precipitates on hydrogen embrittlement of tempered lath martensitic steel," *Acta Mat,* vol. 74, pp. 244-254, 2014.

[6] Speich G, Leslie W, „Tempering of steel," *Met Trans,* vol. 3, pp. 1043-1054, 1972.

[7] Wei FG, Tsuzaki K. „Quantitative analysis on hydrogen trapping of TiC particles in steel," *Met Mat Trans A,* vol. 37A, pp. 331-353, 2006.

[8] Depover T, Van den Eeckhout E, Wallaert E, Zermout Z, Verbeken K, „Evaluation of the effect of TiC precipitates on the hydrogen trapping capacity of Fe-C-Ti alloys," *Adv Mat Research,* vol. 922, pp. 102-107, 2014.

[9] Ashby MF, Easterling KE, „A first report on diagrams for grain growth in welds," *Acta Mat,* vol. 30, pp. 1969-1978, 1982.

[10] Irvine KJ, „Grain-refined C-Mn Steels," *Journal of the iron and steel institute,* vol. 250, pp. 161-182, 1967.

[11] Wei FG, Hara T, Tsuzaki K „Precise determination of the activation energy for desorption of hydrogen in two Ti-added steels by a single thermal-desorption spectrum," *Met Mat Trans B,* vol. 35B, pp. 587-97, 2004.

[12] Wallaert E, Depover T, Arafin M, Verbeken K, „Thermal desorption spectroscopy of NbC and NbN precipitates," *Met Mat Trans A,* vol. 45, pp. 2412-2420, 2014.

[13] Pérez Escobar D, Wallaert E, Duprez L, Atrens A, Verbeken K, „Thermal desorption spectroscopy study of the interaction of hydrogen with TiC precipitates," *Metall Mater Int,* vol. 19(4), pp. 741-748, 2013.

[14] Hilditch TB, Lee SB, Speer JG, Matlock DK, „Response to Hydrogen Charging in High Strength Automotive Sheet Steel Products," *SAE Technical Paper,* 2003, http://dx.doi.org/10.4271/2003-01-0525.

[15] Loidl M, „Hydrogen embrittlement in HSSs limits use in lightweight body," *Adv Mat Process,* pp. 22-25, 2011, BMW Group Germany.

[16] Pérez Escobar D, Depover T, Wallaert E, Duprez L, Verbeken K, Verhaege M, „Combined thermal desorption spectroscopy, differential scanning calorimetry, scanning electron microscopy and X-ray diffraction study of hydrogen trapping in cold deformed TRIP steel," *Acta Mat,* vol. 60, p. 2593, 2012.

CHAPTER X

General conclusions

X.1 Introduction

To have a complete overview of all the studied materials in this work, the hydrogen induced mechanical degradation was correlated with the strength level in Figure X-1 for all materials tested. No clear tendency was observed when linking the degree of HE to the strength level. This observation was already demonstrated in several chapters, as the %HE mainly depends on both the amount of hydrogen and the hydrogen diffusivity, which is not always linked to the strength level of a material but mainly to the available trapping sites.

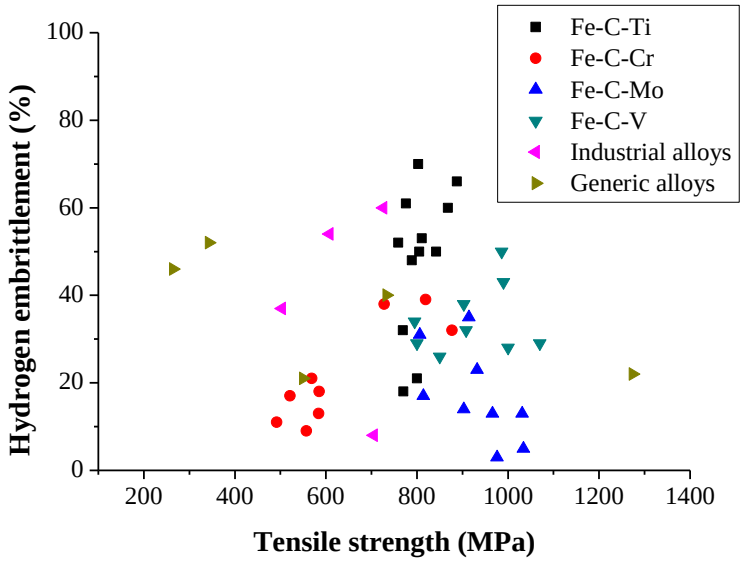

Figure X-1: Hydrogen embrittlement (%) vs tensile strength (MPa) of all studied materials.

The impact of hydrogen charging on the mechanical properties of four industrial high strength steels was investigated in **Chapter II**. An increase in HE sensitivity was obtained with strength level, except for the HSLA steel. The latter showed an enhanced resistance to HE, while the ductility loss was considerable for DP, TRIP and FB steel. Lowering the cross-head deformation speed resulted in an increase in the HE sensitivity as hydrogen had more time to diffuse to critical stress zones ahead of the crack tip. This increase was more pronounced for DP compared to TRIP, which was indeed attributed to its hydrogen diffusion coefficient. This phenomenon was elaborated thoroughly in DP steel as described in **Chapter III**. The diffusion distance of hydrogen into the sample was visualized by performing an in-situ tensile test on non-pre-charged tensile specimen. As such, the effective diffusion distance of hydrogen was visualized by a fractography study. The transition barrier between a hydrogen induced brittle fracture and a ductile zone was clearly observed at similar distances than hydrogen could diffuse during the test. Additionally, the degree of hydrogen embrittlement increased with higher pre-charging times until saturation was obtained.

Due to their complex multiphase microstructure, it was hard to correlate a certain obtained hydrogen related effect to a specific microstructural feature of the material. Therefore, lab cast Fe-C alloys were designed in which different constituents, i.e. pearlite, bainite and martensite, were induced (**Chapter IV**). Pure iron was used as a reference material and the effect of an increase in carbon content was evaluated for the bainite material. The pearlitic material showed a low resistance against hydrogen embrittlement compared to the bainitic and martensitic alloy, which was linked to the amount of diffusible hydrogen and the hydrogen diffusivity. Also pure iron underwent a high hydrogen induced ductility loss, which was linked to some possible internal damage due to charging and the high diffusivity of hydrogen in ferrite. When lowering the cross-head deformation speed, an increase of HE sensitivity was observed as hydrogen is more enabled to diffuse to critical stress areas ahead of a crack tip. Special attention was given to the bainitic materials with variable carbon content. Both bainitic materials showed an increased sensitivity to hydrogen charging, however, the increase was more pronounced for the lower carbon bainite. This was correlated to its higher hydrogen diffusion coefficient in comparison with the higher carbon grade. This again confirmed the synergy between both the amount of diffusivity of hydrogen when interpreting HE results.
As carbides were often mentioned to be beneficial to enhance the response to hydrogen charging, a carbide forming element was added to the Fe-C lab cast materials and a martensitic matrix was chosen as this guaranteed a higher alloy strength level.

X.2 On the correlation between HE% and the amount of mobile hydrogen

Ti, Cr, Mo and V were added to the Fe-C alloys and three different chemical compositions were cast and studied in **Chapter V-VIII**. Different degrees of hydrogen induced mechanical degradation were obtained for all alloys. When interpreting these HE% by determining the amount of total and diffusible hydrogen by melt/hot extraction or by evaluating the available trapping sites with their corresponding activation energies by thermal desorption spectroscopy, a clear correlation was presented between the HE% and the amount of mobile hydrogen, which is the hydrogen that left the sample before the start of the TDS measurement. It was verified that this type of hydrogen was linked to the hydrogen diffusivity as well by performing hydrogen permeation tests. Additionally, due to the mobile nature of this type of hydrogen, it was assumed to be mainly associated to hydrogen trapped at dislocations or also to elastic stress fields around the precipitates. This correlation was confirmed for all different Fe-C-X alloys. Only for the Fe-C-V alloy, the correlation was worse for the mobile hydrogen than for the diffusible/total hydrogen content.

However, to verify the relevance of this statement, a first comparison was made in Chapter IX and here the correlation between the degree of HE and the amount of mobile hydrogen is presented for all Fe-C-X alloys in the as-Q and Q&T 1h condition (Figure X-2(a)). The Q&T 1h condition was chosen as this time resulted in the largest amount of hydrogen trapped by carbides for all alloys. One particular case were the Fe-C-V alloys which hardly showed any plastic deformation before fracture. As dislocations trap the mobile hydrogen, these materials were left out of consideration in Figure X-2(b). Hence, the correlation between the hydrogen induced mechanical degradation and the amount of mobile hydrogen was 96%, very clearly demonstrating proving its crucial impact and nicely supporting the HELP mechanism which attributes an increased dislocation mobility in the presence of hydrogen.

As verified in **Chapter V and VII**, the deepest traps sites, associated with carbides, were first filled. Consequently, it can be concluded that the amount of mobile hydrogen, and thus the HE%, can be decreased by designing materials with carbides with appropriate characteristics. Moreover, when a similar amount of hydrogen was present in the as-Q and Q&T, the Q&T material always showed a better resistance against HE compared to the as-Q alloy. This confirms the beneficial effect of carbide addition. Nevertheless, the different carbides trapped significantly variable amounts of hydrogen, as discussed in the next section.

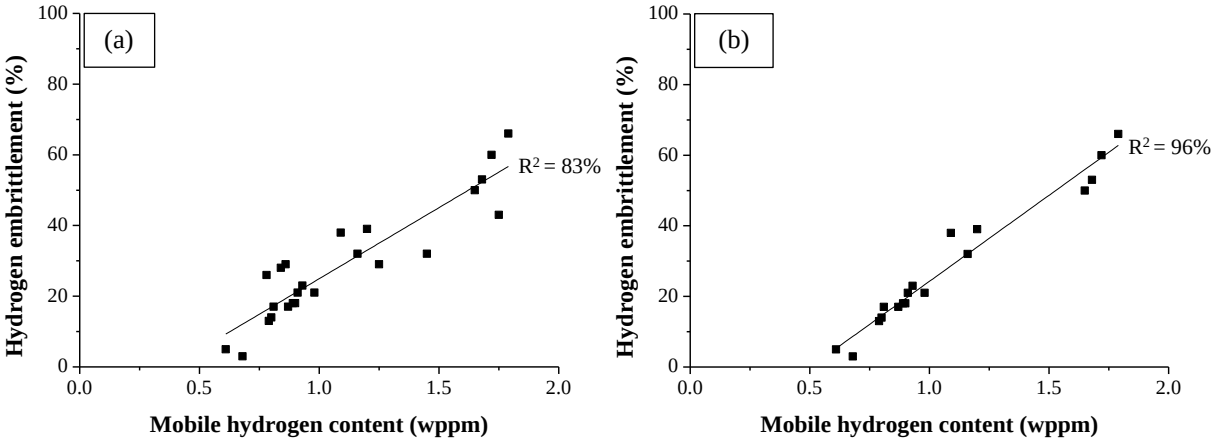

Figure X-2: Hydrogen embrittlement (%) vs the mobile hydrogen content of all studied Fe-C-X alloys in the as-Q and Q&T 1h condition (a). Fe-C-V was left out of consideration in (b).

X.3 On the trapping behavior of the tempered induced carbides

The Fe-C-Ti and Fe-C-V Q&T materials were able to trap more hydrogen than the Fe-C-Cr and Fe-C-Mo alloys. This was first due to their higher amount of carbon, and secondly to their smaller carbides, which were able of trapping more hydrogen as hydrogen is mainly trapped at the carbide/matrix interface. Quite large carbides were detected for Cr and Mo, which were therefore unable to trap a significant amount of hydrogen as revealed by TDS.

Here, Alloy A was selected for each Fe-C-X alloy as it contained approximately a similar amount of carbon, i.e. 0.1 wt% C. Carbides were subsequently induced by tempering and the optimal temper time for carbides to trap hydrogen was for all alloys the same, i.e. one hour. Consequently, the trapping behavior of the different carbides (TiC, $Cr_{23}C_6$, Mo_2C and V_4C_3) can be compared by plotting the TDS spectra of the corresponding Fe-C-X alloy A in the Q&T 1h condition on one figure as shown in Figure X-3. The trapping ability of the carbides can be ranked as: $V_4C_3 > TiC > Cr_{23}C_6 \geq Mo_2C$.

When enlarging the lower left part of the figure, a clear order was achieved regarding the hydrogen content that was detected at first; i.e. a decreasing initial hydrogen signal was obtained from Fe-C-Cr > Fe-C-Ti > Fe-C-Mo > Fe-C-V. This was exactly in the same order as the determined diffusion coefficient, i.e. 5.78×10^{-11}, 3.02×10^{-12}, 2.26×10^{-12} and 1.16×10^{-12} for the corresponding Fe-C-Cr, Fe-C-Ti, Fe-C-Mo and Fe-C-V alloy C respectively. This confirmed again the role of hydrogen diffusivity, even when interpreting TDS data.

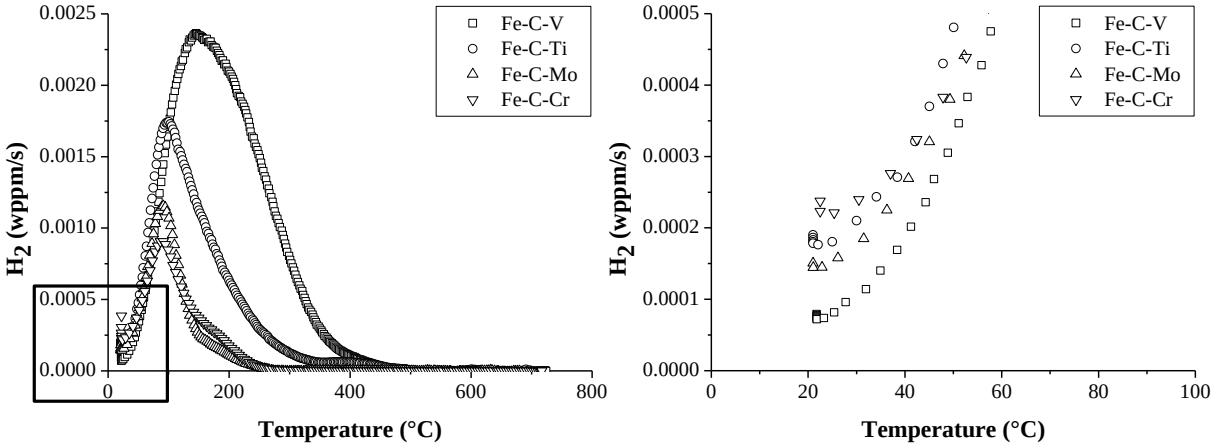

Figure X-3: TDS spectra of alloy A for all Fe-C-X alloys in the Q&T 1h condition.

X.4 Suggestions for further research

Many hydrogen related data was presented and several important insights and conclusions were drawn in this work. However, when interpreting new results, one comes always up with new issues and ideas for further study on the hydrogen/material interaction. In this section, some suggestions for further research are formulated.

- Atom probe tomography might be useful to confirm the exact trapping site of hydrogen by carbides. Experimentally, it was shown that hydrogen was most likely located at the interface between the precipitate and the matrix for most alloys. However, one can never visualize the presence of hydrogen at the exact moment of the test as hydrogen might have diffused again. This makes is hard to determine the exact position of hydrogen in a microstructure. Performing TDS is one way to evaluate the different trapping sites, although it is a destructive technique as hydrogen is released from its trapping site by heating up the sample. Atom probe tomography might be an opportunity, although the experimental challenge is big as only one publication of hydrogen visualization at TiC was reported and they needed to use deuterium instead of hydrogen working at liquid nitrogen temperatures.
- First principle calculations based on density functional theory would add more theoretical insights on the topic. Additional information can be obtained for instance to determine whether the carbides/matrix interface can act as an efficient hydrogen trap. Additionally, one can calculate the cohesive strength of the interface and the effect of hydrogen on it. This would give us information if these interfaces become more sensitive to crack initiation in the presence of hydrogen. Furthermore, the weakening of interatomic bonds can be linked to a decreased surface energy and hence a faster crack growth.
- Electron backscatter diffraction analysis of initiating cracks could give us additional information on the mechanisms of hydrogen induced cracking. Additionally, it could be verified whether hydrogen trapped by precipitates plays an important role when stresses are applied. Furthermore, the influence of orientation on the crack propagation can be evaluated as well.
- The trapping ability of the present carbides can be enhanced by modifying the thermal treatment. Additionally, a ferritic matrix could be induced as well to establish a certain amount of ductility in for instance the Fe-C-V materials. The chemical composition could be changed as the main part of the carbides in the Fe-C-Ti alloys could not be dissolved.